Synthesis and characterisation of potential multiferroic materials

Thesis submitted in accordance with the requirements of the University of Liverpool for the degree of Doctor in Philosophy by Helen Hughes

March 2008

Synthesis and characterisation of potential multiferroic materials

The synthesis and characterisation of a number of novel bismuth based perovskite materials are presented in this thesis that were made in the search for a multiferroic material. Details are also given of the numerous other attempts made to prepare one of these elusive materials.

Chapter One gives an introduction into the properties of a multiferroic material and their uses, it also highlights the reasoning behind what structure types were selected for investigation in this thesis. Chapter Two describes the experimental methods used to synthesise and characterise the materials presented in this thesis.

The later chapters deal with the synthetic trials and materials prepared during this thesis. Chapter Three describes the synthesis and characterisation of the novel bismuth perovskite, $Bi_2Mn_{4/3}Ni_{2/3}O_6$, early results looked promising for this being a multiferroic material. However on further investigation it was proven not to be, although this material was still very interesting as $Bi_2Mn_{4/3}Ni_{2/3}O_6$ along with $BiFeO_3$ are the only known bismuth perovskites to be synthesised under ambient conditions. Chapter Four describes a lanthanum doping study carried out on $Bi_2Mn_{4/3}Ni_{2/3}O_6$, demonstrating that it was possible to tune the temperature of transitions in the material with lanthanum content. Chapter Five details the other synthetic attempts, some successful, to prepare bismuth based perovskites. Chapter Six illustrates the use of other structure types in the search for a multiferroic, and finally Chapter Seven summarises all of the work carried out in this thesis.

Acknowledgements

Firstly I would like to thank Prof. Matthew Rosseinsky and Dr. John Claridge for all of their help and support during my three years of research. Your ideas and encouragement have kept me very busy over the last three years, particular thanks to Matt for providing me with the opportunity to learn as much as I have over the three years.

Next I would like to thank all of technical members of staff both in university and outside, particularly the beamline scientists whose help was invaluable during those long days and nights. Rob, your help was most appreciated in keeping the MJR labs and equipment up and running; Barbara and Pat thank you for always having the time for a good chat!

I would also like to thank all members of the MJR group, past and present, in particular I would like to thank Amy, Ben, Carlos, Chris, French Matthew, American Matthew.

Last but not least I would like to say a very special to all of my family, especially Paul, Mum, Dad and Lorna for all of their love and support. Thank You

The work presented in this thesis was carried out by myself, except where stated, at the Chemistry Department, University of Liverpool between October 2004 and October 2007 under the supervision of Prof. Matthew J. Rosseinsky and Dr. John B. Claridge. This work has not been submitted for any other degree at this or any other university.

_____ _____

Helen Hughes Date

Contents

Chapter 1: Introduction

1.1 Introduction

Multiferroic materials are an uncommon class of materials, and the rarity of them has led to numerous reviews on this topic[1-5]. The term multiferroic is used to describe systems where ferroelectricity, ferromagnetism and ferroelasticity occur in the same phase; my work has focused on magnetoelectric multiferroics. The magnetoelectric effect is when coupling occurs between magnetic and ferroelectric ordering. A recent review[6] stated that the possibility of the magnetoelectric effect was first speculated back in 1894, but that the first theoretical predictions were not made until 1959 and the first experimental observation was not reported until 1960. Since then much research has been carried out on this topic, both theoretical and experimentally.

The ability to control the magnetic ordering of a material with an electric field and vice-versa is extremely attractive and would be very useful for applications such as multiple state memory devices where data can be electronically written and magnetically read[7]. The design of materials with both ferroelectricity and ferromagnetism is complicated by the conflicting requirements of the two properties[1], as discussed later magnetism requires the presence of d-electrons whereas ferroelectricity is often coupled with empty d-orbitals; as a result the occurrence of these materials is rare. Since research began back in 1958, no material has been synthesised that could be used for practical application the interactions

between the two properties has been too weak and / or the working temperature of the material is too low. My thesis has centred on the attempt to design and synthesis of one of these elusive materials.

This introduction will address the two properties required for a magnetoelectric multiferroic material, ferroelectricity and ferromagnetism, as well as giving an overview as to what is known about multiferroic materials and some examples.

1.2 Magnetism in Solids

Magnetic effects[8,9] are observed within a solid when unpaired electron spins are present, these have magnetic dipole moments that arises from the coupling between the spin of the electron and the orbital angular momentum. Unpaired electrons are usually located on transition metals and lanthanides; it is the interactions of these spins that give rise to overall magnetic ordering. Several magnetic ordering combinations are possible when unpaired electrons orient randomly, this is known as the paramagnetic state. When the spins align parallel the material possesses an overall magnetic moment and the material is said to be ferromagnetically ordered. Spins can also align anti-parallel, giving rise to a net zero magnetic moment, in this case the material is said to be antiferromagnetically ordered. In some materials the spins are aligned anti-parallel but there is an unequal number of spins in one of the two directions resulting in a net magnetic moment, the material in this case is said to be a ferrimagnet.

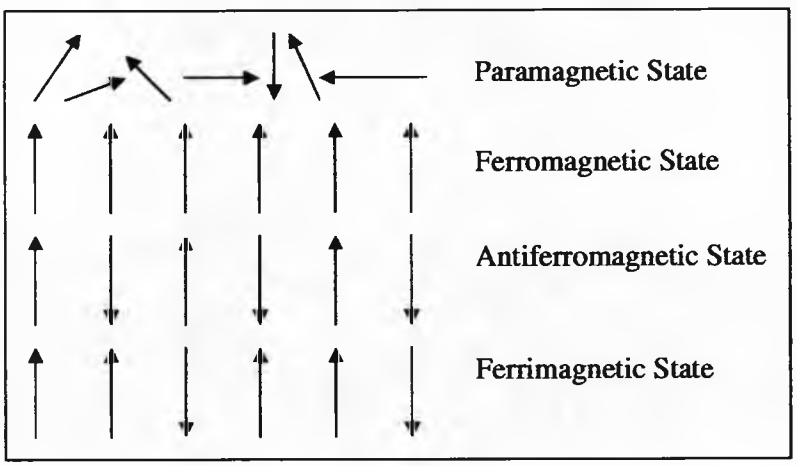

Figure 1.1: *Schematic of possible magnetic spin ordering within a 1-D crystal*

Consider a solid in the absence of an applied magnetic field (H), with no interactions between spins. The spins adopt a random direction in space that optimises the entropy of the material, giving rise to a total magnetic dipole moment of zero (M = 0). The material is said to be in the paramagnetic state.

As a field (H) is applied, a magnetic moment (M) can be induced in the material as the spins within the material align with the field. A number of parameters can be calculated and used to distinguish between the types of magnetic behaviour the material is exhibiting.

Susceptibility: $\kappa = \frac{M}{H}$ ***Equation 1.1***

Molar Susceptibility: $\chi = \kappa \frac{F}{d}$ ***Equation 1.2***

Equations 1.1 – 1.2: *Equations used to calculate the susceptibility of the material. (F = formula weight and d = density of the sample)*

Susceptibility values in this thesis will be quoted with respect to electromagnetic units (emu); this is a unit with volume dimensions (cm^3). The magnetic susceptibility is quoted with the units emu / cm^3 i.e. dimensionless; this is due to the fact that susceptibility according to *Equation 1.1* is the ratio of two fields. The molar susceptibility is quoted using the units emu / mol.

Table 1.1 provides information on the average susceptibility values for the different types of magnetic behaviour.

Type of magnetic behaviour	Molar Susceptibility Value / emu mol^{-1}
Diamagnetism	-1×10^{-6}
Paramagnetism	$0 - 10^{-2}$
Ferromagnetism	$10^{-2} - 10^{6}$
Antiferromagnetism	$0 - 10^{-2}$

Table 1.1: *Average values of susceptibility for materials with different types of magnetic behaviour.*

The type of magnetic behaviour a material exhibits can also be distinguished using the temperature dependency of the susceptibility.

1.2.1 Paramagnetism

As already stated, paramagnetism arises when the moments of the electron spins within a material arrange randomly; it is one of the simplest forms of magnetic behaviours. A key feature of paramagnetism is that the magnetisation measured as a

function of the applied field is linear. The temperature dependency of a paramagnetic material obeys the simple Curie-Weiss Law.

$$\chi = \frac{C}{T - \vartheta}$$ ***Equation 1.3: Curie - Weiss Law***

In *Equation 1.3* 'C' is known as the Curie constant, which contains information about the effective magnetic moment of the ions within the solid. This can be used for providing information on the spin and oxidation state of the ions present.

Also in *Equation 1.3* 'ϑ' is the Weiss constant which provides information on the nature of the spin interactions within the solid, i.e. what magnetic ordering will occur below the transition temperature. For a true paramagnet the Weiss constant 'ϑ' is equal to zero.

1.2.2 Magnetic Ordering

In some materials the moments of the electron spins orient themselves in an ordered arrangement to give a magnetically ordered material. Ferromagnetism arises when the spins align parallel to give an overall net magnetic moment, whereas when they align anti-parallel antiferromagnetism arises giving a net zero magnetic moment across the material. Although the Curie-Weiss Law can provide an idea regarding the nature of the magnetic ordering that can occur, the law cannot be used to describe the temperature dependency of ferro- and antiferro- magnetic materials. Ferromagnetic materials display paramagnetic behaviour up to the transition temperature (T_c), but below this temperature the susceptibility rapidly increases as the temperature decreases. This is because as the temperature decreases the thermal

energy of the spins also decreases making it easier to align parallel at the lower temperatures. A Curie-Weiss fit of the paramagnetic region of the susceptibility data reveals a positive Weiss constant (ϑ).

In contrast antiferromagnetic materials display a decrease in the susceptibility with decreasing temperature below the transition temperature (T_N). The susceptibility decreases as the material becomes ordered, because in the fully ordered state the anti-parallel alignment cancels out any net polarisation giving a low susceptibility value. Thermal energy of the spins decreases with falling temperature making them easier to align. A Curie-Weiss fit of the paramagnetic region of the susceptibility data reveals a negative Weiss constant (ϑ).

Magnetic properties of materials are often expressed in terms of the magnetic moment (μ) of the material. In general we describe the size of the magnetic moment in Bohr magnetons (μ_B). 1 Bohr magneton is equal to 9.274×10^{-24} A m^2 it is derived from the magnetic moment induced from the electron orbiting the nucleus of a hydrogen atom (one proton)[9]. The magnetic moment can be calculated directly from the magnetic susceptibility of the material using the relationship:

$$\chi = \frac{N\beta^2\mu^2}{3kT} \qquad \textit{Equation 1.4}$$

This simplifies to: $\mu = 2.83\sqrt{\chi T}$ ***Equation 1.5***

(N = Avogadro's number; β = Bohr Magneton; k = Boltzmann's constant)

It can also be estimated from the Curie constant (C) calculated from fitting the paramagnetic behaviour using the Curie-Weiss Law:

$$\mu = \sqrt{8C} \qquad \textit{Equation 1.6}$$

This observed magnetic moment is often compared with the estimated moment calculated from the sum of the spins of the unpaired electrons present in the material *(Equation 1.7).*

$$\mu_B = 2\sqrt{S(S+1)} \qquad \textit{Equation 1.7}$$

($S = n \times \frac{1}{2}$, where n is the number of unpaired electrons in the magnetic ions present in the material)

1.2.2.1 Driving force for magnetic ordering

Ferro- and antiferro- magnetic materials undergo spontaneous phase transitions from a high temperature phase with no magnetic ordering (paramagnetic state) to a low temperature phase were the spins become aligned even in the absence of an applied field. A driving force must be present that causes the spin alignment in either a parallel or anti-parallel fashion. Several types of driving force are known; namely direct, indirect and double exchange[8]. Direct exchange involves the electrons on neighbouring atoms to interact directly, no intermediary is required, and in general this does not occur as there is often insufficient overlap between the neighbouring atom orbitals. Indirect exchange involves the electrons of magnetic ions exchanging through a non-magnetic ion which is positioned between the two ions. When this

occurs over a long range this is known as superexchange. Double exchange occurs when the magnetic ion exhibits mixed valency.

Superexchange is considered as the most important type of exchange for the work carried out in this thesis as it generates long range magnetic order and the mediating ion is often oxygen. Therefore, as this thesis focuses on the synthesis of oxide materials the most significant contribution to the magnetic ordering is likely to be superexchange. For example it is superexchange that causes the antiferromagnetic ordering that it is observed in NiO. The nickel in this material is present in the 2+ oxidation state hence there are eight d-electrons present. This means that there are two unpaired electrons present in the e_g orbitals. The e_g orbitals are oriented parallel to the axis of the unit cell and so are orientated directly facing the p-orbital of the oxide ions. Therefore in order to complete the coupling Ni – O – Ni, the electron spin in the next nickel orbital must align anti-parallel to allow the full orbital mixing.

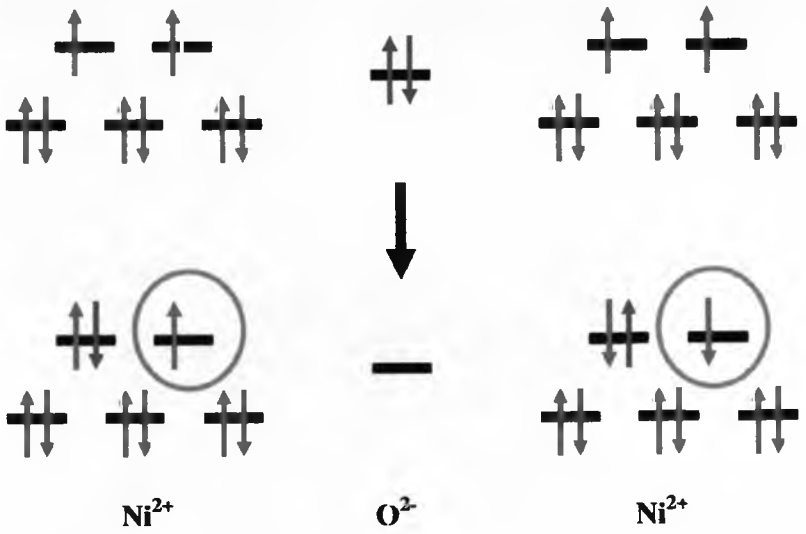

Figure 1.2: *Schematic showing the antiferromagnetic coupling in NiO, the d-orbitals of the nickel are represented, along with the p-orbital of the oxygen. To allow mixing between the nickel and oxygen orbitals throughout the material, the spin of the electron in each adjacent nickel must aligned anti-parallel as highlighted to allow full mixing.*

In the opposite case, ferromagnetic ordering occurs through the superexchange interactions between unoccupied and occupied e_g orbitals and the oxygen orbitals which give rise to the parallel alignment of the unpaired electron spins.

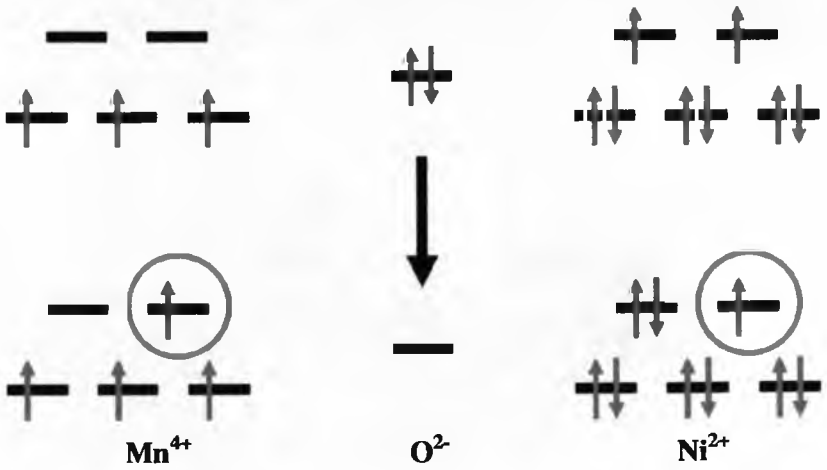

Figure 1.3: *Schematic showing the ferromagnetic coupling in a Mn-Ni-O, the d-orbitals of the nickel and manganese are represented, along with the p-orbital of the oxygen. To allow mixing between the nickel, manganese and oxygen orbitals throughout the material, the spin of the electron in each adjacent metal aligns parallel as highlighted to allow full mixing.*

1.2.2.2 Spiral magnetic ordering

Spiral magnetic ordering arises due to the layered nature of the atoms within the structure, the ordering generally occurs along one layer of the material with the direction of each adjacent moment slightly different to the previous to form a spiral of moments along one direction. In spiral magnets the magnetic ordering is often coupled with a structural distortion which causes the position of the magnetic ion to be distorted slightly, generating a polarised (ferroelectric) structure. Hence, spiral magnetic ordering has recently been the focus of many reviews due to the link between the spiral magnetic structure and ferroelectricity[10-15]

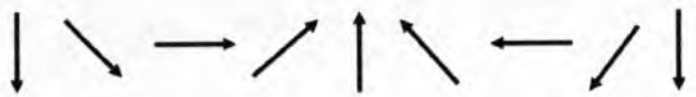

Figure 1.4: *Direction of the magnetic moments through one layer of a material with a spiral magnetic structure.*

1.2.2.3 Magnetic Structures

When talking about magnetic structures vectors are often used to describe the magnetic structure with respect to the crystal structure, i.e. how the ordering of the magnetic ions affects the size of the unit cell along each crystallographic direction. The vector ('k') used to describe the magnetic order is quoted with respect to the chemical structure (or nuclear structure) and is described using reciprocal space. Reciprocal space describes the directions and distance that the diffracted beams follow in diffraction experiments, it is inversely proportional to the real space in which the actual crystal structure exists[8]. Therefore the moduli of the k-vector are inversely proportional to the actual size of the magnetic unit cell with respect to the nuclear cell (*Figure 1.5*). For example a k-vector of 0,0,0 means that the magnetic and nuclear unit cells are identical, whereas a k-vector of $\frac{1}{2}$,0,0 means that the magnetic unit cell is double the length of the nuclear unit cell along the a-direction. A ferromagnetically ordered material where the spins align parallel in all directions throughout the unit cell would have a magnetic k-vector of 0,0,0 Whereas an anitferromagnet with spins aligned anti-parallel along each direction, resulting in a

magnetic structure that is twice the size of the crystal structure in each direction would have a vector of $\frac{1}{2},\frac{1}{2},\frac{1}{2}$.

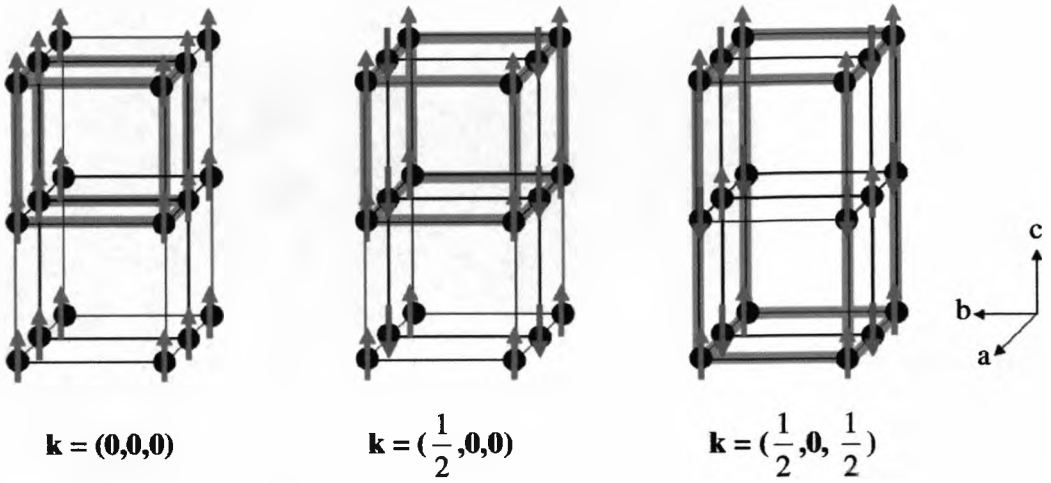

Figure 1.5: *Schematic showing the effect of the magnetic ordering k-vector on the size of the magnetic cell in comparison to the fundamental structure. The fundamental unit cell is depicted with black lines; the direction of the electron spins on the magnetic ions are show as red arrows (up spin) and blue arrows (down spin; the magnetic unit cell is represented with a green line.*

1.2.2.4 Spin Glass Materials

This thesis, along with discussing the conventional magnetically ordered materials also discusses the magnetic phenomena of a spin glass[9,16]. Spin glasses occur when there is a random distribution of magnetic moments throughout a structure. They undergo a phase transition at a particular temperature (known as the freezing temperature, T_f) to a low temperature state that although does not have any long range ordering is distinctly different to the fully disordered, high temperature state.

An important requirement for a spin glass material to form is the randomness (i.e. disorder) of either the position or alignment of the spins with respect to its nearest coupling partner. The main evidence for a spin glass material is that although what looks like a magnetic transition is observed in the magnetic susceptibility data, neutron diffraction data collected below the transition temperature displays no extra scattering with respect to the data collected above the transition, revealing that there is no long range ordering within the material. In order to confirm this AC susceptibility data is collected.

Alternating Current (AC) measurements provide extra information on the magnetisation of the sample in comparison to Direct Current (DC) measurements[17]. DC measurements determine the average magnetization value of the material using a constant applied magnetic field. Whereas in AC measurements a small AC field is superimposed over the DC field; when high frequencies are used the magnetisation lags behind the applied field resulting in the generation of a real (in-phase) and imaginary (out-of-phase) component to the measured susceptibility. When AC susceptibility is carried out on a spin glass the location of the maxima is frequency dependent, the T_f reduces with decreasing frequency. Also the T_f in a spin glass is irreversible, due to the random nature of both the 'ordered' and 'disordered' state; this causes the out-of-phase susceptibility component to always be non zero.

1.3 Electrical Properties of Solids

Oxide materials consist of a repeating array of ions, the material is stabilised by short range repulsions between adjacent electron clouds of the ions. The presence and absence of ferroelectricity is determined by the balance between these short-range electron cloud repulsions and bonding that favours the non-centrosymmetric, polarised ferroelectric form[1,18].

1.3.1 Types of electrical properties

In solids different types of electrical properties can occur; in particular dielectric, ferroelectricity, pyroelectricity and piezoelectricity[8]. Although ferroelectricity is the main focus of this research, an introduction to each of these properties will also be given.

1.3.1.1 Dielectric Materials

The main feature of dielectric materials is that they are insulators; a good dielectric material is one that can withstand high voltages without degrading and becoming conductive. Another favourable feature is that the material exhibits low dielectric loss, this means that the amount of electrical energy lost through heat is minimised. Dielectric properties are defined by the behaviour of the material between two parallel plates, however firstly we have to consider when a vacuum is between the plates the capacitance of the material is given by *Equation 1.8.*

$$C_0 = \frac{\varepsilon_0 A}{d} \qquad \textit{Equation 1.8}$$

Where: ε_o = *permittivity of free space* = 8.854×10^{-12} Fm^{-1}

A = *surface area of the plates* / m^2

d = *distance between the two plated* / *m*

When a voltage (V) is applied across the two plates, a charge (Q) becomes stored in the material between the plates, for the vacuum case this is given by *Equation 1.9.*

$$Q_o = C_o V \qquad \textit{Equation 1.9}$$

Now, when an actual dielectric material is placed between the two plates the amount of charge (Q_1) stored between the plates increases from the vacuum case (Q_0). The ratio of the charge stored in the dielectric material in comparison to the vacuum can be used to determine the materials ability to hold a charge, i.e. how polarisable the material is. This ratio is known as the dielectric constant and is given by *Equations 1.10 and 1.11.*

$$\varepsilon' = \frac{Q_1}{Q_0} = \frac{C_1}{C_0} \qquad \textit{Equation 1.10}$$

When the equation for C_0 *(Equation 1.10) is substituted in this becomes:*

$$\varepsilon' = \frac{C}{8.854 \times 10^{-12}} \times \frac{d}{A} \qquad \textit{Equation 1.11}$$

Dielectric measurements carried out for this thesis were made over a range of frequencies with a superimposed AC field. At low frequencies the polarisation within the material can occur before the field reverses and so creating an alternating current through the material. As the frequency is increased the polarisation in the material can no longer keep up with the alternating field, therefore the current that is

induced by the polarisation lags behind the applied voltage, the angle by which it lags is known as δ. This results in the dissipation of energy from the sample in the form of heat, otherwise known as dielectric loss. Therefore the polarisation (or induced current) can be considered to have a real (in-phase) and imaginary (out-of-phase) part to it, as a result both real and imaginary values of the capacitance and charge can be measured. The amount of dielectric loss can be calculated this known as ε'' and is calculated using *Equation 1.11*, just using the imaginary capacitance component. The dielectric loss is often reported with respect to the dielectric constant, it is given the term 'tan delta' and is calculated using *Equation1.12*.

$$\tan\delta = \frac{\varepsilon''}{\varepsilon'} \qquad \textbf{\textit{Equation 1.12}}$$

1.3.1.2 Ferroelectric Materials

Ferroelectric materials are distinguished from a dielectric material through the properties defined in *Equations 1.8 – 1.12*. According to *Equation 1.9* it is normal to observe that as the voltage is increased across a dielectric material the charge stored increases. However when the material is ferroelectric this is not the case instead a hysteresis loop is observed and the material saturates. Typical value for the saturation of the well known ferroelectric $BaTiO_3$ is 0.26C m^{-2} [8]. This occurs because the material has undergone a phase transition from the dielectric form to a phase that undergoes spontaneous polarisation, the direction of which can be switched using the applied electric field.

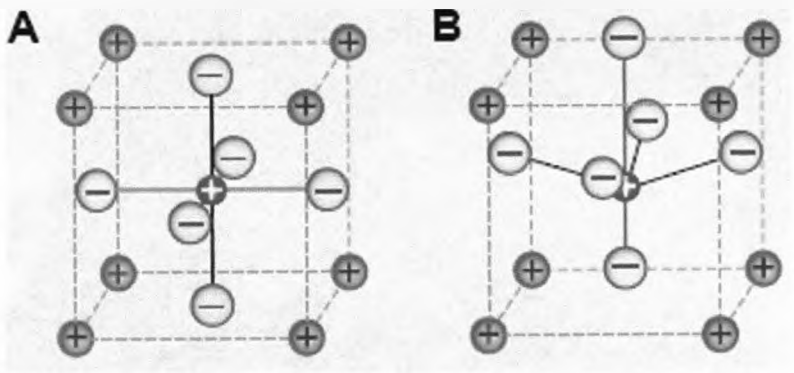

Figure 1.6[18]: *Perovskite structure, ABO_3. Part A shows the perovskite in the dielectric form with no net polarisation as all charges cancel. Part B shows the ferroelectric form with a distorted perovskite structure, the charges no longer cancel and so a net polarisation occurs. (A cation is represented by the red sphere; B cation is represented by the blue sphere; Oxygen anions are represented by the grey spheres)*

The most technologically important ferroelectrics are considered to be those adopting a perovskite structure, such as $BaTiO_3$ which has a typical perovskite structure including a TiO_6 octahedra surrounded by a cube of Ba ions. Above 120°C a symmetrical structure *(Figure 1.6 (A))* is adopted, the ionic charges cancel and so the structure is un-polarised. Below 120°C a structural transition occurs where the titanium ions are displaced off centre *(Figure 1.6 (B))*, creating a dipole in the structure.

1.3.1.3 Pyroelectric Materials

This is another type of electrical property which can be exhibited by a material. The spontaneous polarisation in pyroelectric materials cannot be reversed by an applied

field and in general it is temperature dependent. This arises because on heating the expansion of the material results in a change in the size of the dipole.

1.3.1.4 Piezoelectric Materials

This type of electrical property arises when the material is put under a form of mechanical stress. As the stress is applied the site geometry of the ions within the material distorts creating a dipole resulting in a polarised structure.

1.3.1.5 Driving force for ferroelectricity

For a material to exhibit ferroelectricity (as well as Pyro- and Piezo- electricity) the space group must be non-centrosymmetric[19] so the charges on the ions within the structure no longer cancel out. The Landolt-Börnstein series[20] list hundreds of ferroelectric materials each with a non-centrosymmetric space group. Many of these materials have B-site cations which have empty d-orbitals, such as Ti^{4+} (d^0) in $BaTiO_3$. When the structure distorts to the ferroelectric structure it is stabilised through coupling between the filled oxygen orbitals and the empty orbital on the metal. It can therefore be considered that vacant orbitals on the small B cation are a requirement for ferroelectricity. It is also thought having cations on the A-site with lone pairs contributes to the stabilisation of the distorted ferroelectric structure, in $PbTiO_3$ hybridization occurs between the lone pair on the lead and the oxygen orbitals stabilising the distorted ferroelectric structure.

1.4 Multiferroic Materials

Multiferroic materials, as already stated, are materials where ferroelectricity, ferromagnetism and ferroelasticity occur in the same phase, the occurrence of which is very rare. My work has centred on the magnetoelectric multiferroics, taking forward conclusions from the two previous sections that ferroelectricity generally requires B-site metals with no d-electrons whereas ferromagnetism requires d-electrons to generate the magnetic moments. Therefore combining the two in a magnetoelectric multiferroic material is very difficult due to the conflicting requirements, and so explains why there are so few multiferroic materials.

Recently a number of theoretical studies[3-5] have been carried out identifying three main areas for the investigation of multiferroic behaviour. (i) Systems which are designed by incorporating elements that promote ferroelectricity (e.g Bi^{3+} atoms – the $6s^2$ lone pair stabilise the off-centre distortion of the atom through Bi-O orbital mixing[21]) and elements that promote ferromagnetism (e.g. Fe^{3+} and Cr^{3+} ions – coupling between the empty chromium e_g orbital and occupied iron e_g orbital causes ferromagnetic Fe – O – Cr coupling[22]). An example would be $BiFeO_3$[23]. (ii) Systems that exhibit a spiral magnetic structure which causes the breakdown in symmetry resulting in ferroelectricity, for example in the material $TbMnO_3$[10]. (iii) Systems made of two composites, a ferromagnetic one and a ferroelectric one, are moulded together such as alternating layers in a thin film, the elastic interface between these two composites gives rise to multiferroic behaviour[24,25].

The work reported in this thesis focused mainly on the first type of multiferroic design, using a system which incorporates elements that promote ferroelectricity and ferromagnetism. However the final chapter *(Chapter Six)* investigates the use of spiral magnets for multiferroicity.

1.4.1 Examples of multiferroic materials

The following is a list of known multiferroic materials are grouped in their structure types.

Boracites: $Ni_3B_7O_{13}I$[26]

Fluorides: $BaMF_4$ (M = Mn, Fe, Co, Ni)[27-29]

Magnetite: Fe_3O_4[30]

Hexagonal Manganites: $YMnO_3$[31,32], $HoMnO_3$[33], $TbMn_2O_5$[34]

Perovskites: $BiFeO_3$[23,35], $BiMnO_3$[36-38]

Sulphides: $CdCr_2S_4$[39]

Hexagonal ferrites: $LuFe_2O_4$[40]

In all of the above cases the ferroelectric transition occurs at a much higher temperature than the ferromagnetic transition, thus the origins of the ordering have no relation to one another, and leads to only weak coupling between the two. To date a multiferroic material has not been synthesised with coupling between the two properties occurring at a practical working temperature. One of the main barriers to creating new multiferroic materials lies in the understanding of what causes multiferroicity in the known materials. Recently a lot of controversy has surrounded the materials $BiMnO_3$[36-38] and $CdCr_2S_4$[39] and the origin of multiferroicity in them;

questions are being raised as to whether the ferroelectricity in $BiMnO_3$ is actually caused by a structural distortion to a non-centrosymmetric structure[37] and what is the relationship of the spiral magnetic structure in $CdCr_2S_4$ with ferroelectricity[39]?

1.5 Thesis Aim: Designing a Multiferroic Material

The aim of this thesis has focused on the design and synthesis of a multiferroic material. A number of approaches can be taken when designing a multiferroic, as discussed in *section 1.4*. The main approach taken in this thesis was to incorporate two sets of elements that each favoured either ferromagnetism or ferroelectricity in a structure. To generate the ferroelectricity, bismuth was used as the $6s^2$ lone pair is known[23] to stabilise the off-centre distortion that gives rise to a ferroelectric structure. To generate the magnetism magnetically active transition metal ions were used such as chromium, cobalt, copper, iron, manganese, and nickel. The primary focus of the thesis was on the perovskite structure type, as this is a particularly favourable structure due to the fact that there are two cation sites within the structure, one for ferromagnetism and the other for ferroelectricity. However other structure types were investigated such as the garnets and spinels; the reasoning behind each of these structure types is discussed in each individual section.

1.5.1 Perovskites

A recent article[41] reported that the mineral perovskite was first described in 1830 and was named after the Russian mineralogist A.Von Perovskji. However it was not until the 1940's that the perovskite structure type began to be investigated thoroughly for its chemical, physical and structural properties. The perovskite, with the formula $A^{3+}B^{3+}O_3$, has two metal sites A and B when in its simplest form it has a cubic structure made up of BO_6 octahedra.

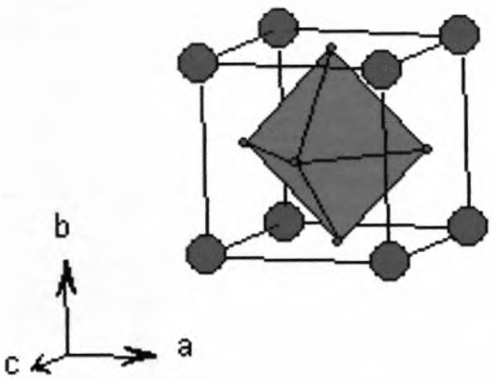

Figure 1.7: *Structure of a simple perovskite, $BaTiO_3$[42]. Blue spheres are the A-site cations; the purple octahedron represents the BO_6 environment.*

Many perovskite materials however do not have structures as simple as this a number of distortions of the BO_6 octahedra give rise to more complex structures. What makes this structure favourable for multiferroic materials is the presence of two cation environments.

As the aim of this thesis was the synthesis of a multiferroic material, the idea was to take the perovskite structure type and design a multiferroic material around it.

Bismuth was placed on the A-site of the perovskite as it has been known to stabilise the distorted ferroelectric structure through hybridisation of its lone pair with the oxygen orbitals[21]. Magnetic transition metal ions such as chromium, manganese, iron, cobalt, nickel and copper were placed on the B-site, in order to favour ferromagnetism two transition metal ions were used in the oxidation states 4+ and 2+. This meant that if ordering did occur it would give rise to ferromagnetic ordering as the coupling would be between an empty and an occupied e_g orbitals and so would result in parallel M_1^{4+} - O – M_2^{2+} superexchange.

A literature search soon revealed that these bismuth based perovskite materials required artificial methods to form, such as high pressures or thin film substrates[43]; the only known bismuth based perovskite, up until the work carried out in this thesis, that could be made under ambient conditions was $BiFeO_3$[23,44-46]. This is not a true multiferroic as although it exhibits both ferroelectricity and antiferromagnetism the two properties do not couple as the ferroelectric ordering temperature is at 1123K and the magnetic ordering temperature is 650K. Using high pressures typically 6GPa, all of the first row transition metals and more can be incorporated into a bismuth based perovskite, $BiMO_3$ were M = Sc[47], Ti, V, Cr[48,49], Mn[36-38], Co[50], Ni[51], Al[52], Ga[52], Y[53] and In[54]. Many of these materials exhibited ferroelectricity, however out of these only $BiMnO_3$ exhibits true ferromagnetic ordering (T_c = 100K) and exhibits ferroelectricity at room temperature, it is considered as the only multiferroic in the bismuth based perovskite series. However, currently there is a great deal of controversy surrounding this material and the origin of the ferroelectricity[37]. Up until

recently it was thought that the material exhibited a non-centrosymmetric structure and that was used to explain the occurrence of ferroelectricity. However latest studies have revealed that $BiMnO_3$ exhibits a centrosymmetric structure and so even now the origin of ferroelectricity (and multiferroicity) remains unclear in the only known multiferroic in the bismuth based perovskite series.

As already stated the aim of this work was to take the studies carried out with the $BiMO_3$ perovskites and expand on them by introducing another magnetic ion on the B-site, in the attempt to generate ferromagnetic ordering within the material. This work focused on using the transition metals chromium, manganese, iron, cobalt and nickel attempting to make a perovskite at ambient pressure, proving successful with $Bi_2Mn_{4/3}Ni_{2/3}O_6$[55]. A literature search was also carried out on these bismuth based double perovskites, revealing that these have also been extensively researched incorporating Mn-Ni[56], Zn-Ti[57], Fe-Cr[58], Ni-Ti[59] and Mg-Ti[60] however again high pressures were required.

Although the main body of this research focused on the perovskite structure type and the different substitutions possible on the B-site at ambient pressure (*Chapters Three, Four and Five)*, other structure types were investigated in *Chapter Six* and a brief introduction to these are provided in the following sections.

1.5.2 Garnets

The garnet structure is essentially a cubic structure with the general formula $(A^{3+})_3(B^{3+})_5O_{12}$; the A-site is a dodecahedral environment and is generally occupied

by the large lanthanides. The B site, generally occupied by a metal ion such as iron, is made up of two types of environments octahedral and tetrahedral. The garnet structure is very versatile and is known to incorporate many different elements within the structure[61,62], making this material attractive for designing a multiferroic material.

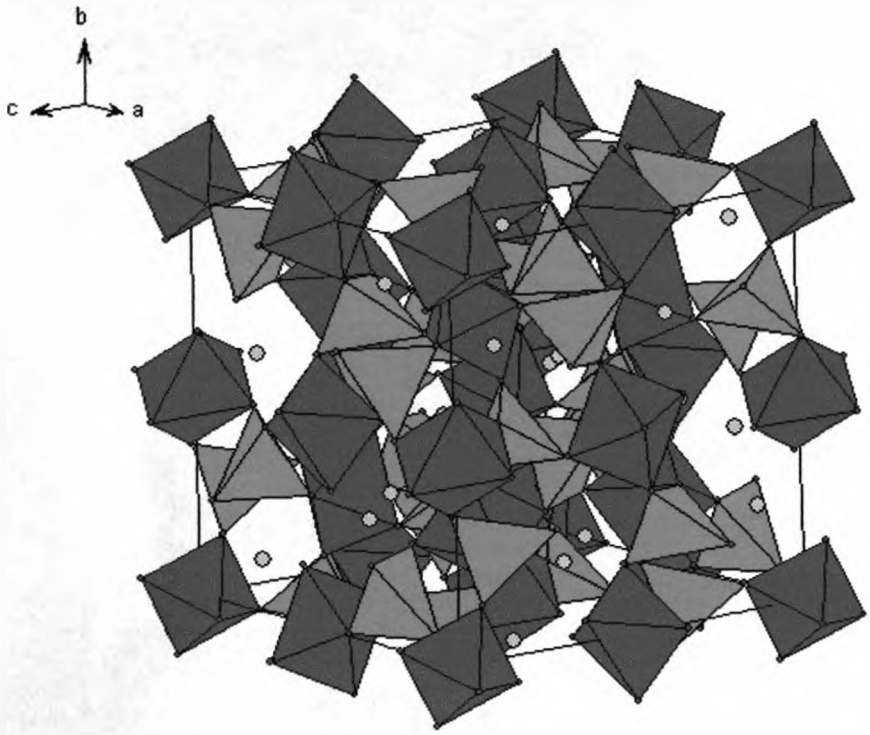

Figure 1.8: *Garnet structure[63] ($Y_3Fe_5O_{12}$) highlighting the two iron sites, light blue represents the tetrahedral iron site and the dark blue represents the octahedral iron environment. The grey spheres represent the dodecahedral yttrium site.*

This structure type was selected for a number of reasons, the first one being the similarity between the Y^{3+} ions that generally occupy the A-site and Bi^{3+} ions,

opening up the possibility to substitute bismuth onto this site and generate ferroelectricity within this structure. Also the two environments that make up the B-site are favourable with the possibility of incorporating site selective transition metal ions into the structure, generating an ordered material and so forming a magnetically ordered material. Although the main driving force for using the garnet structure was the fact that the iron containing garnets $A_3Fe_5O_{12}$ exhibited ferrimagnetic ordering, with high magnetic ordering temperatures[64-66], which would overcome the problem seen in the perovskites of high ferroelectric transition temperatures and low ferromagnetic transition temperatures, making it very difficult to couple the two.

The idea behind using the garnet structure type was to introduce Bi^{3+} ions onto the A-site and investigate the effect of this on the electrical properties of the material. The pure bismuth iron garnet, $Bi_3Fe_5O_{12}$ is reported to form only through the use of thin film substrates[67] reports using standard solid state routes suggest that maximum amount of bismuth that can be doped into the system is $Y_{1.8}Bi_{1.2}Fe_5O_{12}$[68,69]. Dielectric studies carried on the maximum bismuth doped solid state materials report that a maximum is observed in the relative permittivity with temperature, suggesting the possibility of inducing polarisation within the material. The focus of the work carried out on this structure type has been on attempting to dope more bismuth into the material through substitutions on the iron site.

1.5.3 Spinel

Spinels have the general formula $(A^{2+})(B^{3+})_2O_4$ the A and B cations can be a variety of elements. The structure consists of a cubic closed packed array of oxide ions with the A-cations in tetrahedral site and the B site cations occupying the octahedral sites.

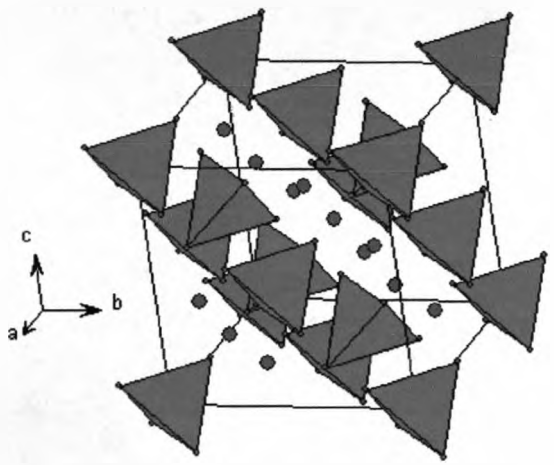

Figure 1.9: *Schematic of the spinel[70] (AB_2O_4) structure, the pink tetrahedra represent the environment of the A-cation co-ordinated with four oxygen ions (red spheres); the blue spheres represent the B-cation site which co-ordinates with six oxygen ions.*

This structure type was selected after a literature search into materials which exhibited a spiral magnetic structure, of which spinels featured the most. Interest in these types of materials for use as multiferroics was inspired by recent reviews discussing the link between a spiral magnetic structure and ferroelectricity[10-15]. They state that when a material with a spiral magnetic structure enters a magnetically ordered state it can induce an electric polarisation within the material; this is

particularly favourable for the design of multiferroic materials as it overcomes the problem of high magnetic and low electrical transition temperatures preventing the two properties from coupling, as in these materials the onset of the magnetic ordering induces ferroelectric ordering. Examples of these materials include $CoCr_2O_4$[71,72], RMn_2O_5 (R = Rare Earth Element e.g. Tb / Dy / Ho)[73-75], $RMnO_3$ (R = Gd / Tb / Dy)[76-78], $CuFeO_2$[79] and $MnWO_4$[13].

A material with known spiral magnetic behaviour (the spinel $ZnFe_2O_4$ Tc ~ 100K[80]) was taken and doped with a material that exhibited ferromagnetic ordering (another spinel $NiFe_2O_4$ Tc ~ 850K[81]). This was with the aim to synthesis a material with a spiral magnetic structure but with a higher ordering temperature as ferrimagnets often order at high temperatures.

1.5.4 Summary

The aim of the work reported in this thesis was the attempted synthesis of multiferroic materials; the design of a multiferroic has centred on the incorporation of elements that promote ferroelectricity and ferromagnetism in perovskite structures. However later chapters do go on to discuss the use of other structure types, such as garnets and spinels.

1.6 References

(1) Hill, N. A. *J. Phys. Chem. B* **2000**, *104*, 6694-6709.

(2) Hill, N. A.; Filippetti, A. *J. Magnetism and Magnetic Materials* **2002**, *242-245*, 976 - 979.

(3) Khomskii, D. I. *Journal of Magnetism and Magnetic Materials* **2006**, *306*, 1-8.

(4) Schmid, H. *Ferroelectrics* **1994**, *162*, 317 - 338.

(5) Fiebig, M. *J. Physics D: Applied Physics* **2005**, *38*, R123 - R152.

(6) Kimura, T. *Annual Review of Materials Research* **2007**, *37*, 387-413.

(7) Scott, J. F. *Nat Mater* **2007**, *6*, 256 - 257.

(8) West, A. R. *Solid State Chemistry and its Applications*; John Wiley & Sons, 1984.

(9) Blundell, S. J. *Magnetism in condensed matter*; Oxford University Press: Oxford, 2001.

(10) Cheong, S.-W.; Mostovoy, M. *Nat Mater* **2007**, *6*, 13-20.

(11) Mostovoy, M. *Physical Review Letters* **2006**, *96*, 067601-4.

(12) Radaelli, P. G.; Chapon, L. C. *Condensed Matter* **2006**, 1 - 22.

(13) Heyer, O.; Hollmann, N.; Klassen, I.; Jodlauk, S.; Bohat, L.; Becker, P.; Mydosh, J. A.; Lorenz, T.; Khomskii, D. *Journal of Physics: Condensed Matter* **2006**, *18*, L471 - L475.

(14) Przenioslo, R.; M., R.; Sosnowska, I. *J Phys Soc Jpn* **2006**, *75*, 084718.

(15) Sergienko, I. A.; Dagotto, E. *Physical Review B (Condensed Matter and Materials Physics)* **2006**, *73*, 094434-5.

(16) Mydosh, J. A. *Spin Glasses: an experimental introduction* London, Washington and DC, 1993.

(17) Martien, D. *Introduction to AC susceptibility, Quantum Design, www.qdusa.com*.

(18) Spaldin, N. A. *Science* **2004**, *304*, 1606-1607.

(19) Halasyamani, P. S.; Poeppelmeier, K. R. *Chem. Mater.* **1998**, *10*, 2753-2769.

(20) Landolt-Bornstein *Ferroelectrics and Related Substances*, 2001; Vol. III / 36 / A / Part 1.

(21) Seshadri, R.; Hill, N. A. *Chem. Mater.* **2001**, *13*, 2892 - 2899.

(22) Baettig, P.; Ederer, C.; Spaldin, N. A. *Physical Review B (Condensed Matter and Materials Physics)* **2005**, *72*, 214105.

(23) Mazumder, R.; Devi, P. S.; Bhattacharya, D.; Choudhury, P.; Sen, A.; Raja, M. *Applied Physics Letters* **2007**, *91*, 062510.

(24) Ramesh, R.; Spaldin, N. A. *Nat Mater* **2007**, *6*, 21-29.

(25) Testino, A.; Mitoseriu, L.; Buscaglia, V.; Buscaglia, M. T.; Pallecchi, I.; Albuquerque, A. S.; Calzona, V.; Marre, D.; Siri, A. S.; Nanni, P. *J. European Ceramic Society* **2006**, *26*, 3031 - 3036.

(26) Ascher, E.; Rieder, H.; Schmid, H.; Stossel, H. *Journal of Applied Physics* **1966**, *37*, 1404-1405.

(27) Fox, D. L.; Scott, J. F. *Journal of Physics C: Solid State Physics* **1977**, *10*, L329-31.

(28) Fox, D. L.; Tilley, D. R.; Scott, J. F.; Guggenheim, H. J. *Physical Review B* **1980**, *21*, 2926.

(29) Fabbrici, S.; Montanari, E.; Righi, L.; Calestani, G.; Migliori, A. *Chem. Mater.* **2004**, *16*, 3007-3019.

(30) Kato, K.; Iida, S.; Yanai, K.; Mizushima, K. *Journal of Magnetism and Magnetic Materials* **1983**, *31-34*, 783-784.

(31) Huang, Z. J.; Cao, Y.; Sun, Y. Y.; Xue, Y. Y.; Chu, C. W. *Physical Review B* **1997**, *56*, 2623.

(32) Filippetti, A.; Hill, N. A. *Journal of Magnetism and Magnetic Materials* **2001**, *236*, 176-189.

(33) Lottermoser, T.; Lonkai, T.; Amann, U.; Hohlwein, D.; Ihringer, J.; Fiebig, M. *Nature* **2004**, *430*, 541-544.

(34) Hur, N.; Park, S.; Sharma, P. A.; Ahn, J. S.; Guha, S.; Cheong, S. W. *Nature* **2004**, *429*, 392-395.

(35) Teague, J. R.; Gerson, R.; James, W. J. *Solid State Communications* **1970**, *8*, 1073-1074.

(36) Belik, A. A.; Iikubo, S.; Yokosawa, T.; Kodama, K.; Igawa, N.; Shamoto, S.; Azuma, M.; Takano, M.; Kimoto, K.; Matsui, Y.; Takayama-Muromachi, E. *J. Am. Chem. Soc.* **2007**, *129*, 971-977.

(37) Baettig, P.; Seshadri, R.; Spaldin, N. A. *J. Am. Chem. Soc.* **2007**, *129*, 9854-9855.

(38) Hill, N. A.; Rabe, K. M. *Physical Review B* **1999**, *59*, 8759.

(39) Hemberger, J.; Lunkenheimer, P.; Fichtl, R.; Krug von Nidda, H. A.; Tsurkan, V.; Loidl, A. *Nature* **2005**, *434*, 364-367.

(40) Ikeda, N.; Ohsumi, H.; Ohwada, K.; Ishii, K.; Inami, T.; Kakurai, K.; Murakami, Y.; Yoshii, K.; Mori, S.; Horibe, Y.; Kito, H. *Nature* **2005**, *436*, 1136-1138.

(41) Raveau, B. *Progress in Solid State Chemistry* **2007**, *35*, 171 - 173.

(42) Waesche, R.; Denner, W.; Schulz, H. *Materials Research Bulletin* **1981**, *16*, 497 - 500.

(43) Gajek, M.; Bibes, M.; Fusil, S.; Bouzehouane, K.; Fontcuberta, J.; Barthelemy, A.; Fert, A. *Nat Mater* **2007**, *6*, 296-302.

(44) Michel, C.; Moreau, J. M.; Achenbach, G. D.; Gerson, R.; James, W. J. *Solid State Communications* **1969**, *7*, 701 - 704.

(45) Kumar, M. M.; Palkar, V. R.; Srinivas, K.; Suryanarayana, S. V. *Applied Physics Letters* **2000**, *76*, 2764 - 2766.

(46) Kubel, F.; Schmid, H. *Acta Cryst. B* **1990**, *46*, 698 - 702.

(47) Belik, A. A.; Iikubo, S.; Kodama, K.; Igawa, N.; Shamoto, S.; Maie, M.; Nagai, T.; Matsui, Y.; Stefanovich, S. Y.; Lazoryak, B. I.; Takayama-Muromachi, E. *J. Am. Chem. Soc.* **2006**, *128*, 706-707.

(48) Niitaka, S.; Azuma, M.; Takano, M.; Nishibori, E.; Takata, M.; Sakata, M. *Solid State Ionics* **2004**, *172*, 557 - 559.

(49) Hill, N. A.; Battig, P.; Daul, C. *J. Phys. Chem. B* **2002**, *106*, 3383-3388.

(50) Belik, A. A.; Iikubo, S.; Kodama, K.; Igawa, N.; Shamoto, S.; Niitaka, S.; Azuma, M.; Shimakawa, Y.; Takano, M.; Izumi, F.; Takayama-Muromachi, E. *Chem. Mater.* **2006**, *18*, 798-803.

(51) Ishiwata, S.; Azuma, M.; Takano, M.; Nishibori, E.; Takata, M.; Sakata, M.; Kato, K. *J. Mater. Chem.* **2002**, *12*, 3733 - 3737.

(52) Belik, A. A.; Wuernisha, T.; Kamiyama, T.; Mori, K.; Maie, M.; Nagai, T.; Matsui, Y.; Takayama-Muromachi, E. *Chem. Mater.* **2006**, *18*, 133-139.

(53) Tomashpol'skii, Y. Y.; Venevtsev, Y. N. *Soviet Physics - Crystallography* **1972**, *16*, 905 - 908.

(54) Belik, A. A.; Stefanovich, S. Y.; Lazoryak, B. I.; Takayama-Muromachi, E. *Chem. Mater.* **2006**, *18*, 1964-1968.

(55) Hughes, H.; Allix, M. M. B.; Bridges, C. A.; Claridge, J. B.; Kuang, X.; Niu, H.; Taylor, S.; Song, W.; Rosseinsky, M. J. *J. Am. Chem. Soc.* **2005**, *127*, 13790-13791.

(56) Azuma, M.; Takata, K.; Saito, T.; Ishiwata, S.; Shimakawa, Y.; Takano, M. *J. Amer. Chem. Soc.* **2005**, *127*, 8889-8892.

(57) Suchomel, M. R.; et.al. *Chem. Mater.* **2006**, *18*, 4987-4989.

(58) Suchomel, M. R.; et.al. *Applied Physics Letters* **2007**, *90*, 112909-112911.

(59) Inaguma, Y.; Miyaguchi, A.; Yoshida, M.; Katsumata, T.; Shimojo, Y.; Wang, R.; Sekiya, T. *Journal of Applied Physics* **2004**, *95*, 231-235.

(60) Suchow, L. *Journal of Inorganic and Nuclear Chemistry* **1968**, *30*, 87 - 95.

(61) Euler, F.; Bruce, J. A. *Acta Cryst.* **1965**, *19*, 971 - 978.

(62) Gilleo, M. A. *Ferromagnetic Insulators: Garnets*; North-Holland Publishing Company, 1980; Vol. 2.

(63) Nakatsuka, A.; Yoshiasa, A.; Takeno, S. *Acta Crystallographica B* **1995**, *51*, 737 - 745.

(64) Landolt-Bornstein *Magnetic and Other Properties of Oxides and Related Compounds*, 1978; Vol. III / 12 / A

(65) Gilleo, M. A. *J. Phys. Chem. Solids* **1960**, *13*, 33 - 39.

(66) Rodic, D.; Mitric, M.; Tellgren, R.; Rundlof, H.; Kremenovic, A. *Journal of Magnetism and Magnetic Materials* **1999**, *191*, 137-145.

(67) Lux, R.; Heinrich, A.; Leitenmeier, S.; Korner, T.; Herbort, M.; Stritzker, B. *Journal of Applied Physics* **2006**, *100*, 113511.

(68) Takeuchi, H. *Japanese Journal of Applied Physics* **1975**, *14*, 1903 - 1910.

(69) Zhao, H.; Zhou, J.; Bai, Y.; Gui, Z.; Li, L. *J. Magnetism and Magnetic Materials* **2004**, *280*, 208 - 213.

(70) Hirota, K.; Inoue, T.; Mochida, N.; Ohtsuka, A. *Nippon Seramikkusu Kyokai Gakujutsu Ronbunshi* **1990**, *98*, 976 - 986.

(71) Yamasaki, Y.; Miyasaka, S.; Kaneko, Y.; He, J.-P.; Arima, T.; Tokura, Y. *Physical Review Letters* **2006**, *96*.

(72) Lawes, G.; Melot, B.; Page, K.; Ederer, C.; Hayward, M. A.; Proffen, T.; Seshadri, R. *Physical Review B* **2006**, *74*, 024413.

(73) dela Cruz, C. R.; Yen, F.; Lorenz, B.; Park, S.; Cheong, S. W.; Gospodinov, M. M.; Ratcliff, W.; Lynn, J. W.; Chu, C. W. *J. Applied Physics* **2006**, *99*, 08R103.

(74) Inomata, A.; Kohn, K. *J. Phys.: Condens. Matter.* **1996**, *8*, 2673 - 2678.

(75) Golovenchits, E.; Sanina, V. *Journal of Physics: Condensed Matter* **2004**, *24*, 4325 - 4334.

(76) Goto, T.; Kimura, T.; Lawes, G.; Ramirez, A. P.; Tokura, Y. *Physical Review Letters* **2004**, *92*, 257201.

(77) Kimura, T.; Ishihara, S.; Shintani, H.; Arima, T.; Takahashi, K. T.; Ishizaka, K.; Tokura, Y. *Physical Review B* **2003**, *68*, 060403(R).

(78) Kimura, T.; Lawes, G.; Goto, T.; Tokura, Y.; Ramirez, A. P. *Physical Review B* **2005**, *71*, 224425.

(79) Kimura, T.; Lashley, J. C.; Ramirez, A. P. *Physical Review B* **2006**, *73*, 220401(R).

(80) Kamazawa, K.; Katano, S.; Tsunoda, Y. *Physica B* **2004**, *345*, 96 - 98.

(81) Joy, P. A.; Date, S. K. *Journal of Magnetism and Magnetic Materials* **2000**, *218*, 229-237.

Chapter 2: Experimental Techniques

2.1 Introduction

This chapter will deal with the synthetic methodologies, the equipment and characterization techniques used in this thesis. However specific synthetic procedures used to prepare the materials reported in this thesis will be given in detail in the later chapters.

2.2 Synthesis

Throughout this thesis the main synthetic procedure for the materials reported is the ceramic method, however a number of other techniques were attempted.

2.2.1 Ceramic Method

The solid state ceramic method[1] involves mixing solid reactants together in the correct molar ratios, and then heating at high temperatures. In general long reaction times are required as the whole reaction takes place in the solid state and so diffusion can be very slow. Sample homogeneity was crucial. Starting materials were thoroughly mixed using an agate pestle and mortar, or a ball mill for larger samples; samples were periodically removed from the furnace reground and then placed back into the furnace. This meant that synthesis procedures often involved a number of grinding and firing steps. Another important step was to press the

reactants into a pellet before heating forcing the particles to be closer to each other and therefore reducing the distance they have to diffuse.

A vital part of this process was the accurate weighing out of the starting materials. In some sections of this thesis hygroscopic starting materials were used. Great care was taken to ensure all of the water and CO_2 had been removed before weighing. They were stored in a furnace kept at 950°C from which they were removed and weighed out immediately for use in reactions.

Other considerations were reaction temperatures and conditions. Some starting materials could become volatile on heating and so could be lost from the reaction mixture; in these cases sealed tubes were required. Some starting materials could also react with the media the experiment was being carried out in, such as with the alumina crucibles; in this case platinum foil was placed between the sample and the reaction vessel to prevent loss of starting materials this way.

2.2.2 Sealed tube reactions

Many of the materials reported in this thesis used bismuth oxide, Bi_2O_3, as one of the starting materials; when heated to temperatures above 900°C this oxide becomes volatile. So for samples that required synthetic temperatures above 900°C and contained bismuth, sealed tubes were used. For this procedure the starting materials were accurately weighed out, thoroughly ground together, pressed into a pellet which was then wrapped with platinum foil and placed inside either a 12mm or

18mm diameter silica tube; the choice was made depending on sample size. The tube was attached to a vacuum line to seal the sample in a vacuum before heating.

The vacuum line consisted of two parts, a rough line that took the pressure down to ~10^{-2} torr and a high vacuum line that then took the pressure down to ~10^{-4} torr. After a vacuum had been generated the tube was sealed off by melting the silica using a blow torch.

2.2.3 Crystal growth from a flux

Although most of the synthesis reported in this thesis was the preparation of powder samples a number of crystal growth attempts were made. Crystal growth methods are advantageous because the starting materials do not have to be in the correct molar ratios for the materials to form, this method is often used as an exploratory technique to see what types of materials would form. It was not unusual for a number of crystals to form, each with a different composition that could be analyzed and the desired phase taken forward and made by the standard ceramic method.

Crystals are formed when the starting materials are heated up to above their melting point forming a melt and then cooled through the solidification temperature allowing crystallization to occur. Due to the solid state nature of the starting reagents, it is sometimes necessary to add an additional agent called a flux to act as a solvent, lowering the melting temperature of the reagents, promoting mixing between the reagents.

The main consideration that had to be taken into account when using this synthetic method was how to remove the crystals formed form the flux without damaging them. Often this was trial and error. The flux was left to soak in solutions of varying acids at varying concentrations, and the length of time left to soak was adjusted as was the temperature of the solution. The most effective crystal removal method was selected that yielded undamaged crystals in a reasonable time frame (one week).

2.2.4 High Pressure treatment

Some experiments reported in this thesis were carried out using high pressures (6GPa), for this a Multianvil press was used. All experiments reported in this thesis were carried out with the aid of Dr. Matthew Suchomel and Dr. Andrew Fogg. A ceramic octahedron was taken with hole bored through it into which the reaction vessel was placed. The reaction vessel consisted of a boron nitride crucible surrounded by a cylindrical graphite furnace. A platinum tube was placed inside containing the starting materials; this was capped at both ends with platinum foil. The fully assembled octahedron was then placed in the centre of eight tungsten carbide cubes and held in place using fiberglass squares. A copper electrode was placed on the surface of the two cubes that were in direct contact with the graphite furnace, allowing power to be supplied to the graphite furnace heating up the sample. This whole set-up was then placed inside the multianvil press wedges were placed around the cubes to hold it tightly in place. Pressures up to 6GPa were then applied to the sample. Once at pressure the sample was heated, the temperature of the reaction was controlled by the power applied. Calibration work carried out by Dr. Matthew Suchomel and Dr. Andrew Fogg was used to estimate the temperature

of the reaction. After the desired reaction time, the power was removed slowly followed by the pressure; the sample could then be removed from the octahedron in the form of a small pellet for characterization. Samples produced by this method were typically in the order of 50mg in mass; the cylindrical pellets produced were of the size ~3mm in diameter and ~5mm in length.

2.3 Diffraction Theory

Diffraction was the primary technique used to characterize the materials in this thesis; three types of radiation were used x-rays, neutrons and electrons. Numerous textbooks[1-3] explore in detail these techniques.

The periodic arrangements of atoms within a material act as point sources that scatter the radiation forming a diffraction pattern; Bragg's Law is used to explain this observation.

Bragg's law regards the structure as a series of layers each act as a semi-transparent plane. Some radiation is reflected off the plane, for this the angle of reflection equals the angle of incidence, the rest is transmitted through to subsequent planes where it may or may not be reflected and so on. This creates a number of reflections at different angles that when combined form a diffraction pattern.

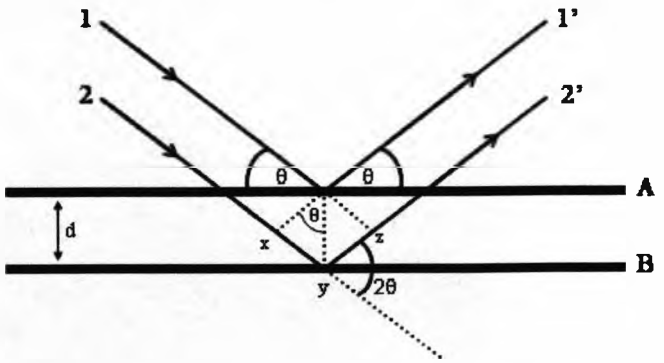

Figure 2.1: *Schematic of how Bragg's Law is derived for x-ray diffraction.*

For example consider two beams which are reflected by two adjacent planes A and B, within a crystal structure. The second beam (22') must have traveled extra distance, xyz, compared to the first beam (11'). For constructive interference to occur and hence a reflection peak, the two reflected beams must be in phase and so the extra distance, xyz, must be equal to a whole number of wavelengths. This gives rise to Bragg's Law:

$$xy = yz = d_{hkl} \sin \theta$$

Therefore: $$xyz = 2\, d_{hkl} \sin \theta$$

For both beams 1' & 2' to be in phase with 1 & 2: $$xyz = n\lambda$$

Thus giving rise to ***Bragg's Law:*** $$2\, d_{hkl} \sin \theta = n\lambda \qquad \textbf{Equation 2.1}$$

When Bragg's Law is satisfied the reflected beams are in phase and constructive interference occurs. However at other angles, not satisfying Bragg's Law, the reflected beams are out of phase causing destructive interference to occur. Therefore giving rise to a diffraction pattern consisting of reflections at specific angles. In

powder samples there are a large number of crystallites, all randomly orientated with respect to each other and so causing the radiation to be diffracted from the lattice planes within the crystals in all possible directions simultaneously. As a result each lattice plane reflection gives rise to a cone of diffraction being emitted from the sample; the intensity of the cones is measured as a function of the detector angle, 2θ.

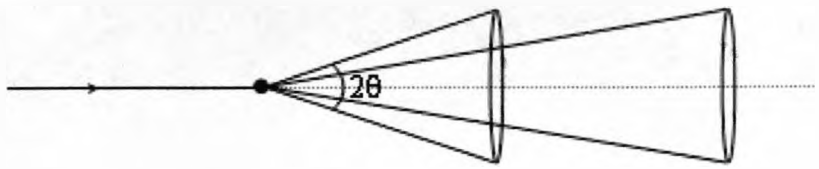

Figure 2.2: *Schematic of a beam of radiation being diffracted from a powder sample forming cones of diffraction*

In reality, things are not as simple as the material being an array of layers; they are built up of a regular arrangement of atoms in 3-D which is represented as the unit cell. The unit cell by definition is the smallest repeating unit which shows the full symmetry of the crystal structure. Each lattice plane that diffracts the radiation is unique and contains atoms; the planes are described using Miller indices, hkl. Using both the Miller indices of the plane and its d-spacing value, the unit cell parameters can be determined.

$$\frac{1}{d_{hkl}^2} = \frac{h^2}{a^2} + \frac{k^2}{b^2} + \frac{l^2}{c^2}$$ ***Equation 2.2***

For an orthogonal system where $\alpha = \beta = \gamma = 90^o$

Using this equation each of the reflections can be assigned Miller indices, and so the powder pattern is said to have been indexed.

2.3.1 Systematic Absences and Symmetry Considerations

Bragg's law only predicts the positions of the reflections; it does not take into consideration the reflections missing or the intensity of the reflections. Systematic reflection absences arise because of the symmetry of the unit cell.

The symmetry of a material is expressed by the space group of a material; this describes the symmetry of all atoms within the unit cell. Firstly we must consider the types of symmetry operations that can occur inside the unit cell that leaves the material unchanged. The following is list of possible symmetry operations:

Inversion ($\bar{1}$): An inversion point changes the co-ordinates (x,y,z) of an atom within the structure to (-x,-y,-z).

Reflections (m): This is when an atom(s) is reflected through a plane.

Proper Rotations (n): This describes an atom rotating about a point by an angle $2\pi/n$, the values of 'n' is used as the notation for this operation.

Improper Rotations ($\bar{n}$): This describes the combination of a rotation of the order n, followed by a reflection through a plane perpendicular to the rotation axis.

Screw Axis (n_p): This describes a helical movement, through the combination of a proper rotation of the order 'n' with a translation; the ratio p/n is the unit cell fractional distance that the translation occurs.

Glide Plane (*a, b, c, n or d*): This describes the combination of a reflection with a translation parallel to the plane; the different notations are given based on the distance of the translation with respect to the unit cell. 'a, b or c' notations are used when the translation is equal to half the unit cell edge along the corresponding direction. Notations 'n' and d' are given when the translation is equal to half-diagonal and quarter-diagonal respectively.

Another important consideration required when discussing the symmetry of a structure is the centering of the unit cell. Unit cells with no centering consist of eight of the same atoms are present on the corners of the cell. is known as a primitive (P) cell. A structure is described as body-centered (I) if the same atom that is present on the corners is present in the centre of the unit cell, whereas a face-centered (F) cell has the atom positioned in the centre of all six sides. When atoms are found in the centre of the top and bottom faces they are described by the axis that intersects the two faces, for example a C-centered unit cell has two atoms in the centre of the top and bottom face of the unit cell that is intersected by the c-axis.

Within a material a combination of the unit cell centering and a number of these symmetry elements are required to describe the positions of all of the atoms within the unit cell, therefore a term is required that explains this as a whole, the space group. The International tables for Crystallography[4] lists all of the 230 groups that can be formed in three-dimensions and describes each one fully. Systematic absences of the powder pattern are used to derive the space group of a material, they

arise due to the centering of the cell, and any glide planes and / or screw axes present within the structure.

2.3.2 Reflection Intensity

The intensity of the reflection is dependent on a number of factors, types of atoms within the unit cell and their distribution can all affect it; the structure factor[5] (F_{hkl}) can be used to model these effects and is given by:

$$F_{hkl} = \sum_j f_j N_j \left(\exp\left[2\pi i\left(hx_j + ky_j + lz_j\right)\right]\right)\exp\left(-M_j\right) \qquad \textit{Equation 2.3}$$

Where f_j = atomic scattering factor

N_j = occupancy factor of the atom on that particular site

x_j, y_j, z_j = fractional co-ordinate of the jth atom in the unit cell

$$M_j = 8\pi^2 \overline{U_{iso}^2} \sin^2 \frac{\vartheta}{\lambda^2} \qquad \textit{Equation 2.4}$$

U_{iso} = square root of the mean thermal parameter

Thermal vibrations of the atoms within the material cause a decrease in the intensity of the diffracted beam and an increase in the amount of background scattering.

The intensity of each reflection is directly proportional to the structure factor of the reflection,

$$I_{hkl} \propto \left|F_{hkl}\right|^2 \qquad \textit{Equation 2.5}$$

Therefore, powdered samples have unique diffraction patterns with both unique reflection positions and intensities. All of which have to be taken into consideration when analyzing the powder pattern.

2.3.3 Incommensurate Structures

Incommensurate structures like commensurate structures also have specific powder patterns, however the calculations required to explain them are much more complex. Incommensurate structures[6,7] have periodic distortions of the atomic positions and/or occupations from some fundamental structure, resulting in a number of satellite reflections. The fundamental structure is defined as the smallest unit that can be used to describe the structure; the full structure is made up of a number of these fundamental structures. The lattice parameters of the full incommensurate structure are not an integer number multiple of the fundamental structure along at least one direction, all Bragg reflections can however be indexed with integer values, hklmn.... Reflections *(hkl0)* are from the fundamental structure and reflections *(hklm)* where $m \neq 0$ are satellite reflections of the order $|m|$. A 'q' vector is used to describe the full incommensurate structure with respect to the fundamental structure, like in the case of the k-vector in magnetism *(Section 1.2.2.3)*. The q-vector is quoted using reciprocal space; this describes the directions the diffracted beams follow. It is inversely proportional to real space in which the structure exists. For example, a q-vector of $\frac{1}{2}$,0,0 means that the full structure is twice the size of the fundamental structure along the a-direction. What makes a structure incommensurate is that the full structure is not an integer number of fundamental units, the q-vector is often expressed to several decimal places.

The diffraction vector (H) of each spot in the diffraction pattern of a (3+n)-dimensional incommensurate structure can be written as:

$$H = h_1 a^* + h_2 b^* + h_3 c^* + \sum_{i=1...n}^{n} h_{3+i} q^i \qquad \textit{Equation 2.6}$$

Where: n = *number of modulation vectors*

q = *wave vector of the modulation wave*

a^*, b^* *and* c^* *reciprocal unit-cell vectors of the fundamental structure*

h_1, $h_2 \ldots h_{3+n}$ = *integer values used to assign the reflections*

The d-spacing of the peak can then be determined from:

$$d = \frac{1}{|H|} \qquad \textit{Equation 2.7}$$

The structure factor, as described in the section above, is used to calculate the intensity of the reflection, for an incommensurate structure this is given by the equation:

$$F_{hkl} = \sum_{\mu(R|\tau)} P^{\mu} \int_0^1 d\bar{x}_4^{\mu} \ldots \int_0^1 d\bar{x}_{3+n}^{\mu} f^{\mu}(n) P^{\mu}\left(\bar{x}_4^{\mu}, \ldots, \bar{x}_{3+n}^{\mu}\right) \times \exp\left(-\sum_{ij} h_i \left[RB^{\mu}\left(\bar{x}_4^{\mu}, \ldots, \bar{x}_{3+n}^{\mu}\right) \tilde{R} \right]_{ij} h_j + 2\pi i \sum_j \left\{ h_j \left[Rx^{\mu}\left(\bar{x}_4^{\mu}, \ldots, \bar{x}_{3+n}^{\mu}\right) \right]_j + h_j \tau_j \right\} \right)$$

Equation 2.8

This equation clearly demonstrates the complex nature of the calculations involved when refining the structure of an incommensurate structure; however similarities with the commensurate factor can be made. The average thermal parameter taken across the whole structure is given by the term $B^{\mu}\left(\bar{x}_4^{\mu}, \ldots, \bar{x}_{3+n}^{\mu}\right)$ in equation 2.8, and similarly the average occupation of the site is given by the term $P^{\mu}\left(\bar{x}_4^{\mu}, \ldots, \bar{x}_{3+n}^{\mu}\right)$. The

notation $\bar{x}_n^{\mu}$ donates the average atomic position of the uth atom in the fundamental structure in the nth direction.

The symmetry of an incommensurate structure is described like in the commensurate case (*section 2.3.1)* with a space group however extra terms must be added due to the increase in the number of dimensions being described. For example, Ibmm(q00, 0-p0)ss.gm. The first part (Ibmm) of the space group describes the symmetry of the fundamental structure, as this is only a three-dimensional structure it is one of the 230 space groups described in the international tables. The second part descibes the q-vector of the material, in the example case it shows that there are two modulation vectors (q,0,0 and 0,-p,0) along the x and y direction.

2.4 X-ray Powder Diffraction

X-ray powder diffraction[1-3] was the most important tool for characterizing materials presented in this thesis. It was used to identify what phases were forming, and the structure. Throughout this thesis the main source of powder X-ray diffraction was from the use of the two laboratory diffractometers, however we also had access to the Daresbury Synchrotron Radiation Source (SRS) for a limited number of experiments.

2.4.1 Generation of X-rays

X-rays are electromagnetic radiation with a wavelength in the region of 0.6 – 1.9Å, they can be generated by a number of different ways. Laboratory diffractometers produce monochromated X-ray beam, the choice of the metal target within the X-ray tube determines the wavelength of the resulting X-ray. Whereas at the SRS a beam of radiation is generated containing a range of wavelengths.

On the laboratory diffractometers a tungsten filament emits electrons. These electrons are then accelerated through a high voltage and into a collision with a metal target, in our case either copper or cobalt. The force of the collision is enough to eject one of the metals inner K shell (e.g. 1s) electrons creating a vacancy, an outer shell electron (either 2p, L shell or 3p, M shell) will then drop down to fill this vacancy. The energy the electron releases during this transition is given off as an X-ray. Due to the specific energy gap between the two electronic states, the resulting X-ray has a fixed energy and so a specific wavelength. Transitions involving the L shell electrons give rise to K_α radiation and K_β radiation arises from transitions involving the M shell electrons. Both K_α and K_β radiation consists of two components each, $K_{\alpha1}$, $K_{\alpha2}$ and $K_{\beta1}$, $K_{\beta2}$ respectively. The transition between the K and L shells are the most frequent, making the K_α radiation the most intense, and consequently used for the diffraction experiment. Filters are used to remove the K_β radiation, in the case of the copper target a nickel filter is used, whereas for a cobalt target an iron filter is used. The $K_{\alpha2}$ radiation is then removed using a monochromator, resulting in an intense single wavelength beam of X-rays.

Whereas in the SRS[8] intense beams covering a wide range of the electromagnetic spectrum are generated. At the SRS electrons are accelerated close to the speed of light in a 2GeV storage ring, which operates at high circulating currents (150 to 250 mA) with lifetimes up to 24hours. In the storage ring the electrons are kept in a circular path using a series of magnets, as the electrons are deflected by one of the magnets they emit an intense beam of radiation at a tangent from the ring. The flux of this radiation is very high, several orders of magnitude higher than the radiation produced in the lab diffractometers.

2.4.2 Fundamentals

X-rays are electromagnetic waves with an oscillating electric field, when these come into contact with the electron cloud surrounding an atom or ion they cause the electrons to vibrate. The vibrations cause the electron to emit radiation that is in phase with the incident X-ray beam, in effect each act as secondary X-ray point sources. This has a direct impact on which atoms can be located using X-ray powder diffraction. Light atoms with few electrons are difficult to find because their diffraction signal is so weak, whereas heavy atoms with a large number of electrons give off a strong diffraction single making them easy to find. This gives rise to the limitation of using X-ray diffraction as the powder pattern is dominated by the heavier elements. This is expressed as the form factor of an atom; the scattering of an X-ray can be affected by the atomic number along with the angle of the X-ray. Within a structure the distances between the atoms and so electrons are short; this has a direct impact on the amount interference between diffracted beams because only partial destructive and / or constructive interference can occur as the beams

originate close to each other. This results in the gradual decrease in intensity of the scattered beam as the 2θ angle (angle between the incident and diffracted beam) increases.

2.4.3 X-ray Diffraction Experiment Instruments

Three diffractometers were used to characterize the samples detailed in this thesis, the two lab diffractometers the STOE STADI P and the Panalytical X-pert pro and the Synchrotron Radiation Source (SRS) station 9.1 diffractometer.

2.4.3.1 Laboratory Diffractometers

Two lab diffractometers were used to carry out room temperature powder X-ray diffraction experiments for phase identification and structural characterization.

The STOE STADI P diffractometer has a copper metal target and as such gives out K_α radiation at a wavelength of 1.5406Å, the diffractometer was controlled using the Stoe WinXPow version 1.10 software package. The Panalytical X-pert pro diffractometer on the other hand has a cobalt metal target; therefore the K_α radiation is produced at a wavelength of 1.7890Å, controlled by X'Pert Data Collector version 2.0c software package. Both diffractometers operate at a voltage of 40kV and 40mA, and the pair was used in reflection mode using Bragg-Brentano geometry. Samples were placed on zero background plates and rotated to minimize the effect of preferred orientation in the recorded diffraction pattern.

The choice of diffractometer was made taking into account the elements present in the sample requiring characterization and then choosing the diffractometer based on which source would give the least fluorescence which leads to poor diffraction patterns. Fluorescence occurs when incident X-ray beams knock out inner shell electrons of atoms within the material being characterized, then as in the metal target within the X-ray tube, electrons from the outer shells drop down in energy to fill the vacancy and in doing so emit an X-ray. These are emitted in all directions, causing a large increase in the background of the observed pattern. This process also reduces the number of X-rays actually being diffracted and so causing the intensity of the reflections to be reduced. The amount of fluorescence radiation observed is dependent on the atomic number of the atoms present in the sample, relative to the metal target in the X-ray tube. Also the quality of the data required was taken into consideration when choosing the instrument and the efficiency of the detector (part of the instrument that collects the diffracted beams as a function of 2θ which is the angle between the incident and diffracted beam) plays a crucial part in this. The efficiency of the detector on the Panalytical is much greater than the detector on the Stoe this yields diffraction patterns of higher intensity from the Panalytical. The Panalytical can also collect data at much higher resolution in comparison to the Stoe, as on the Panalytical the angle between measurements can be adjusted whereas the Stoe can only make measurements every 0.05°.

In both cases, samples were prepared by first grinding the sample using an agate pestle and mortar in acetone to form a slurry. This was then placed onto a zero

background plate using a Pasteur pipette, the sample was then left to evaporate leaving an even sample layer on the holder. This was then placed into the diffractometer on the sample stage, adjusting the height to ensure that it was at the correct level.

2.4.3.2 Daresbury SRS Station 9.1 Diffractometer

Data was collected on station 9.1 of the Daresbury SRS[9] at room and variable temperature, and the diffractometer was in transmission mode using Debye-Scherrer geometry. Wavelengths in the range of 0.4 to 1.7Å were available, however in general wavelengths of 0.95Å or lower were selected based on the elements present in the sample, that produced the least fluorescence from the sample. The wavelength was set using a Si(111) channel cut crystal monochrometer to within 0.0001°.

Samples were prepared in capillaries, the sample were finally ground and then loaded into either a 0.5 or 0.3mm capillary. The choice of capillary size was based on the absorption of the sample, the higher the absorption the smaller capillary used; for samples with a large absorption the samples were diluted with boron or silica. Data was collected on this station at room temperature and higher temperatures. A furnace was attached to the diffractometer head and used to measure samples at temperatures between room temperature and 800°C.

2.5 Neutron Powder Diffraction

Neutrons have wavelengths that are comparable to interatomic spacings, and consequently can be used to carry out diffraction experiments in a similar way to X-rays. Neutron powder diffraction[1-3,10] is generally used as a complementary technique to X-ray diffraction, due to the fact that neutrons interact with atoms differently from X-rays. However the general principles are the same. In this thesis we had access to two neutron sources to carry out diffraction experiments, the main one being ISIS Pulsed Neutron and Muon Source in Oxford, UK however a few experiments were also carried out on the Institut Laue-Langevin (ILL) in Grenoble, France.

2.5.1 Generation of Neutrons

A neutron is a particle, with a neutral charge and a mass 1839 times greater than an electron; along with protons they make up the nuclei of an atom. There are two ways that neutrons can be generated, from a spallation (ISIS Pulsed Neutron and Muon Source) and reactor (ILL) source.

The ISIS Pulsed Neutron and Muon Source is a spallation neutron source. Here neutrons are generated when hydrogen gas is ionized into H^- ions and then accelerated in a ring stripping its electrons forming a proton beam. This beam is then pulsed towards a uranium target where fission occurs, producing high-energy, variable wavelength neutrons. The neutron beam is then moderated; this involves passing the beam through a solid or fluid causing elastic collisions to occur resulting

in the neutron beam losing some energy. The entire moderated beam, with a range of wavelengths is then used in the diffraction experiment; the diffraction pattern is therefore measured as a function of the Time of Flight (TOF) of the neutron from the initial neutron burst produced in the target. TOF is directly proportional to the neutron wavelength by combining the De-Broglie relationship with the fact that the distance traveled (D) is equal to the velocity (v) of the neutron multiplied by the time taken (t).

$$D = vxt \qquad \text{and} \qquad \lambda = \frac{h}{mv}$$

Therefore: $$\lambda = \frac{h}{Dm} xt \qquad \textbf{Equation 2.9}$$

h = *Planck's constant* (6.626×10^{-34} *Js*)

m = *mass of neutron* (1.675×10^{-27} *kg*)

This combined with the Bragg equation gives the interplanar distance as a function of TOF for a fixed angle.

$$d_{hkl} = \frac{h}{2Dm} x \frac{t}{\sin\theta} \qquad \textbf{Equation 2.10}$$

In contrast the ILL neutron source is a reactor source; the principles are the same as for the spallation source however here a beam of neutrons with a constant wavelength is generated. Nuclear fission on a uranium target produces a beam of high-energy variable-wavelength neutrons which is then moderated, as in the spallation source, to reduce the energy of the beam. This moderated beam is then

passed through a monochromator, consisting of two single crystals parallel to each other reflecting the beam at fixed angles to produce, according to Bragg's Law ($\lambda = 2d\sin\theta$), a beam of single wavelength neutrons.

The two sources are comparable to each other, however the pulsed spallation source allows much more rapid data collection as the whole pattern is collected at once as a function of TOF, therefore making it advantageous for variable temperature studies and the study of short time phenomena.

2.5.2 Fundamentals

The main difference between neutron and X-ray diffraction is how neutrons and X-rays are scattered by atoms. X-rays are scattered by the electron cloud surrounding the atom, therefore the more electrons the atom has the more the atom scatters X-rays. Consequently X-ray scattering is directly proportional to the atomic number. This has a number of impacts on the pattern. It makes it very difficult to distinguish elements with similar atomic numbers using X-rays and it also means that diffraction patterns are dominated by heavy atoms with a large number of electrons. Neutrons however are scattered by the nuclei of an atom. The size of the nuclei does not vary very much across the periodic table and so there is no simple relationship between neutron scattering and atomic number. The primary consideration with neutron scattering is the amount of resonance scattering; here neutrons are absorbed by the nuclei and released later. This is a completely random effect, and it means neighboring elements, even isotopes, can have different scattering lengths (i.e. how much they scatter), allowing elements that are impossible to discriminate in X-ray

patterns to be distinguished in the neutron pattern. The scattering lengths[11] of the elements presented in this thesis are given in *table 2.1*.

Element	Coherent Scattering Length / 10^{-15}m
Bi	8.532
La	8.24
Mn	-3.73
Ni	10.3
Co	2.49
Fe	9.45
Ti	-3.438

Table 2.1: *Comparison of the neutron scattering lengths of the elements presented in this thesis.*

Another advantage of using neutron powder diffraction over X-rays is because the neutrons are diffracted by the actual nuclei and not the electron cloud. Neutron diffraction measures the distance from one nuclei to another and not between electron clouds which can be distorted. Therefore the calculated atomic positions and bond lengths from the pattern are a true representation.

The most interesting result arising from neutron diffraction experiments is the ability to analyze the magnetic structure of a material. Magnetic properties, as discussed in Chapter One, depend on the presence of unpaired electrons within the material. Neutrons possess a magnetic moment, and so they are scattered by the magnetic moment of the unpaired electron(s). This gives rise to extra scattering in addition to

the scattering from the nuclear structure. Scattering of the neutron by the magnetic structure will only occur if the angle between the magnetic moment and the scattering axis is not equal to 0^{o}. Therefore when carrying out neutron diffraction on magnetically ordered materials consideration must be made as to the moment direction. If extra peaks are present when the material is magnetically ordered, this implies the presence of a magnetic superstructure and arises from anti-ferromagnetism where the unpaired electrons align anti-parallel. If extra intensity is observed when the sample is ordered it implies ferromagnetism, here the unpaired electrons are aligned parallel, their magnetic moments simply scatter in addition to the nuclear structure scattering.

However there are a few disadvantages to neutron diffraction, the main one being the cost, neutron sources are very expensive to run and so to be able to carry out experiments on these is a privilege. Also neutron sources are less intense in comparison to X-ray sources, this combined with the fact that they do not interact with matter to the same extent as X-rays do means that larger samples are required to carry out the experiment. Neutron diffraction experiments presented in this thesis were carried out on samples weighing typically 5g, whereas in contrast the X-ray powder diffraction experiments were carried on much smaller samples, typically 5mg.

2.5.3 Neutron Powder Diffraction Experiments

In this thesis four types of neutron diffractometers were used, the POLARIS, GEM and HRPD diffractometers at ISIS producing TOF diffraction patterns and D2b diffractometer at the ILL producing constant wavelength patterns.

2.5.3.1 POLARIS Diffractometer at ISIS, Oxford, UK

The POLARIS[12,13] diffractometer receives neutrons at high intensity, and collects data at medium resolution. The intense flux and high counting rate allow experiments to be carried out with short collection times or with a small amount of sample. The diffractometer has a total of 434 ^{3}He gas and ZnS scintillator detectors which are arranged into four banks, two low angle banks, one at 90° two-theta and another at backscattering angles. They are referred to as banks A, B, E and C respectively, details as shown in *table 2.2.*

	Low Angle (A)	**Low Angle (B)**	**Backscattering (C)**	**90 degrees (E)**
Detector Type	^{3}He	ZnS	^{3}He	ZnS
2θ Range /°	28 – 42	13 – 15	130 – 160	83 – 97
d-spacing range / Å	0.5 – 8.3	0.5 – 21.6	0.2 – 3.2	0.2 – 4.0

Table 2.2: *Details of the four detector banks on the POLARIS diffractometer*

Experiments were carried out with the samples placed inside thin walled vanadium cans, ranging in diameter from 5 to 11mm and 50 to 75mm in length, depending on the size of the sample ensuring the maximum amount of sample was in the beam.

The data presented in this thesis was collected on POLARIS at room temperature, at low temperatures in a cryostat and at high temperatures using a furnace.

2.5.3.2 GEM Diffractometer at ISIS, Oxford, UK

GEM[14] (GEneral Materials) diffractometer at ISIS receives high intensity neutrons and collects data at high resolution, this allows rapid data collection. The diffractometer has a large number of ZnS/^{6}Li scintillation detectors arranged into seven banks giving a good signal to noise ratio and covering a wide angular range of 5 to 170°. Details of each of these banks are shown in *table 2.3.*

Detector Bank	Mean Angle	2θ Range
1	9.39°	5.32–12.6°
2	17.98°	13.44–21.59°
3	34.96°	24.67–45.61°
4	63.62°	50.07–74.71°
5	91.30°	79.07–106.60°
6	154.40°	142.50–149.72°
7	159°	149.98–171.40°

Table 2.3: *Summary of the detector banks on the GEM diffractometer.*

Like in the POLARIS experiments, all samples were measured inside thin walled vanadium cans. Data presented in this thesis was collected at room temperature, at low temperatures when the sample can was placed inside a cryostat and at high temperatures inside a furnace. One experiment was carried out where powder

diffraction data was collected whilst the sample was in a magnetic field, for this a cryomagnet was used; this combined low temperatures with magnetic fields.

2.5.3.3 HRPD Diffractometer at ISIS, Oxford, UK

HRPD[15] (High Resolution Powder Diffractometer) is the highest resolution neutron powder diffractometer of its type in the world. It has been designed to achieve maximum practical resolution attainable with reasonable counting times. The high flux means that the neutrons have short wavelengths and so can look at very low d-spacing. There are three detectors on HRPD each collecting diffraction data simultaneously; the characteristics of each bank are given in *table 2.4*.

	Backscattering	**90°**	**Low Angle**
Detector Type	ZnS scintillator	ZnS scintillator	½" 10atm He^3 gas tubes
2θ range	160° - 176°	80° - 100°	28 – 32°
d-spacing range	~ 0.6 - 4.6Å	~ 0.9 - 6.6Å	~ 2.2 - 16.5Å

Table 2.4: *Summary of the detector details on HRPD*

Like with all of the ISIS diffractometers samples measured on HRPD were placed inside thin walled vanadium cans. Data presented in this thesis from HRPD was collected at room temperature, at high and low temperatures.

2.5.3.4 D2b Diffractometer at ILL, France

D2B[16] is a very high-resolution powder diffractometer collecting data at very high resolution. It receives constant wavelength neutrons that can be easily changed

through rotation of a Germanium crystal monochromator, and can collect complete diffraction patterns in as little as 15-60 minutes. Samples, like in ISIS, were placed in vanadium cans in order to carry out experiments; the data presented in this thesis was collected at room and lower temperatures using a cryostat.

2.6 Transmission electron microscope (TEM) and Electron Diffraction

Electron microscopy[1-3] is a useful technique as it requires only a very small amount of sample. It was used in this thesis to provide information on the structure of the materials and the elemental composition of the phases present.

Electrons are emitted from a tungsten filament and then accelerated through a high voltage, which relates directly to the wavelength of the resulting electron by:

$$\lambda = h(2meV)^{-1/2} \qquad \textit{Equation 2.11}$$

Where m = mass of an electron and e = charge of an electron, therefore the higher the voltage the smaller the wavelength. This beam of high energy electrons then passes through the sample a number of things can occur at his point, diffraction being the most useful. Electrons have much smaller wavelengths than X-rays and so their Bragg diffraction angles are much smaller, resulting in a narrow cone of diffraction centered round the electron beam. This gives rise to a diffraction pattern consisting of a pattern of spots. From this pattern the unit cell parameters and space group can be determined.

The pattern of spots is part of what is known as the reciprocal lattice of the true lattice; it is inversely related to the actual size and shape of the unit cell, the reciprocal lattice describes the distance and direction of the diffracted beam. The distance between the spots in the diffraction pattern can be used to determine the unit cell parameters and the systematic absence of spots in the pattern provides information on the space group of the material. To determine all this information in general a number of patterns must be taken showing diffraction pattern along different planes. It is normal to focus the beam on one crystallite and take diffraction patterns as the sample is rotated, thus building up the reciprocal space.

Another outcome of the electrons interacting with the sample is the generation of X-rays, by scanning the energy of the X-rays emitted the elements present in the sample can be identified. This allows the homogeneity of materials to be determined, each crystallite can be probed to establish which elements are present and in what ratio; it also allows small impurity phases to be identified.

When preparing samples for TEM care must be taken to make them as thin as possible, as electrons interact strongly with matter. A common side affect of electrons diffracting so efficiently is secondary diffraction a diffracted beam is then scattered for the second time by another lattice plane. This can give rise to extra spots in the diffraction pattern and makes the intensity of the diffraction spots unreliable, therefore electron diffraction patterns must be analyzed with care, and they can only give an indication as to the symmetry and cell parameters of the

material. For full structural analysis powder diffraction or single crystal diffraction is required.

2.6.1 TEM experiment

Experiments in this thesis were carried out on an electron microscope (make and model JOEL 2000FX) equipped with an EDAX analyser for energy dispersive spectroscopy (EDS) analysis. All electron diffraction experiments reported in this thesis were carried out by Dr. Mathieu Allix, the EDS experiments were carried out by both myself and Dr. Mathieu Allix. Samples for TEM were prepared by crushing the powder in *n*-butanol, the small crystallites in suspension were then deposited onto a holey carbon film, supported by a copper grid.

2.7 Structure Analysis

Throughout this thesis structural analysis of the phase synthesized has played a crucial part. The first step in structure analysis was to carry out profile matching (otherwise known as LeBail fitting) of the diffraction. This provides information on the cell parameters (and propagation vectors), peak shape and background function. Once these had been determined a full Rietveld refinement could be carried out. For this a good starting model is required as it is a structure refinement method not a structure solution method. The magnetic structure could be refined also by Rietveld analysis; however the symmetry of the magnetic spins first had to be determined.

In this thesis a number of programs were used to carry out these calculations. GSAS (General Structure Analysis System)[17] with the graphical user interface EXPGUI[18] was used to carry both LeBail fits and full Rietveld analysis; when combined with the program SARAh[19] the full magnetic structure could be determined. Incommensurate structures were fitted using FullProf.2k (Version 1.9c – May 2001-LLB JRC) and Jana2000[20] to carry out Rietveld structure refinements.

2.7.1 Profile Matching / LeBail fitting

LeBail fitting (or profile matching)[21,22] of the diffraction patterns requires no structural information, only the space group, cell parameters, peak shape and background function is fitted. In this thesis GSAS and FullProf were used to carry out LeBail fitting of the diffraction patterns collected.

2.7.2 Rietveld Refinement

The Rietveld Refinement[5,23-25] method is not a structure solution method therefore a good starting model must first be identified by other methods. The actual principles are simple using a least-square minimization technique, although to use it successfully a degree of expertise is required to avoid false minima. Numerous least squares refinements are carried out until the 'best-fit' between the entire observed powder pattern and the entire calculated pattern is obtained. The calculated pattern is based on the simultaneous refinement of the lattice parameters, crystal structure model, profile and instrument parameters. Only limited knowledge can be determined from the pattern care must be taken to examine the physical significance of the refined parameters during this process.

Diffraction patterns are recorded in intensity, y_i at each increment (i) in the pattern, depending on the method increments can be either scattering angle (2θ), energy parameter (Time-Of-Flight) or wavelength. The Rietveld method is the same whatever diffraction data is used; the quantity minimized in the least-squares refinement is:

$$s_y = \sum_i w_i \left(y_i(obs) - y_i(calc)\right)^2 \qquad \textbf{Equation 2.12}$$

Where: $w_i = [y_i(obs)]^{-1}$

$y_i(obs)$ *=observed intensity at the ith step*

$y_i(calc)$ *=calculated intensity at the ith step*

A diffraction pattern is typically a collection of many reflections each with an individual peak height, position and shape; the integrated area is proportional to the Bragg intensity, I_K, where K relates to the specific Miller indices of the reflection. The intensity of the reflection, as discussed in section 2.3, is proportional to the structure factor, therefore the calculated intensity is determined from the model summing together all contributions from the reflections plus the background.

$$y_i(calc) = y_{bi} + s\sum_K L_K |F_K|^2 \phi(2\theta_i - 2\theta_K) P_K A \qquad \textbf{Equation 2.13}$$

Where: y_{bi} *= Background intensity at the ith step*

s *= Scale factor*

K *= Represents the miller indices (hkl) for the reflection*

L_K *= Lorentz, polarization and multiplicity factors*

F_K *= Structure factor for the K reflection*

ϕ = *Peak shape function*

θ_i = *Position of the observed reflection*

θ_K = *Position of the calculated Bragg peak*

P_K = *Preferred orientation function*

A = *Absorption factor*

The parameters refined fall into two categories, profile and structural. The profile parameters are often refined first in a Le Bail fit of the data before proceeding to the Rietveld refinement, these include the lattice parameters, peak shape and zero point error. The structural parameters are required for the Rietveld method to calculate the intensity of the reflections; these include atomic positions, fractional occupancies and thermal parameters; all are included in the structure factor.

The background intensity (y_{bi}) can be obtained in various ways: a supplied table of background intensities, linear interpolation between operator-selected points in the pattern or using a specified background function. For the majority of refinements carried out in this thesis the method of linear interpolation between selected points was employed.

There are a number of parameters (R-values) which can be used to assess the agreement between the observed and calculated pattern. These goodness of fit parameters are updated with every refinement cycle.

$$R_p = 100 \frac{\sum_i |y_i(obs) - y_i(calc)|}{\sum_i y_i(calc)}$$ *R-pattern* ***(Equation 2.14)***

$$R_{wp} = 100 \left[\frac{\sum_i |y_i(obs) - y_i(calc)|^2}{\sum_i (y_i(calc))^2} \right]^{1/2}$$ *R-Weighted Pattern* ***(Equation 2.15)***

$$R_B = 100 \frac{\sum_I |I_K(obs) - I_K(calc)|}{\sum_I I_K(obs)}$$ *R-Bragg* ***(Equation 2.16)***

$$R_F = 100 \frac{\sum_i |F_K(obs) - F_K(calc)|}{\sum_i F_K(obs)}$$ *R-Structure* ***(Equation 2.17)***

$$\chi^2 = \left(\frac{R_{wp}}{R_e} \right)^2$$ *'Goodness of fit'* ***(Equation 2.18)***

$$R_e = \left[\frac{(N-P)}{\sum_i w_i (y_i(obs))} \right]^{1/2}$$ *R-Expected* ***(Equation 2.19)***

Where: N = *Number of observables*

P = *Number of parameters*

The R-factors *R-Bragg* and *R-Structure* are biased towards the model used as they are not based on the actual observed Bragg intensities but on those calculated using the model. Therefore they are insensitive to misfits in the pattern which are not from the phase(s) being modeled. The most reliable factor is the *R-Weighted Pattern* as it contains the residual which is actually being minimized in the least squares procedure; therefore it is a useful factor to assess the quality of the refinement. For a typical refinement R-values should be expected to be in the region of 10%.

The *'Goodness of Fit'* is also a meaningful parameter to determine the quality of the refinement, as the quality of the fit increases as the value of χ^2 decreases to an ideal value of 1. However χ^2 can be affected by poor quality data, resulting in artificially low values. A value less than 1 is consistent with this; typical χ^2 values for a refinement should be in the region of 2 and below.

Throughout the refinement these fit parameters should be constantly observed to assess the refinement. However as well as these values a visual check of the refinement plot is required. This allows problems with lattice parameters, peak shapes and background fitting to be identified. All structures detailed in this thesis were refined from powder diffraction patterns using GSAS.

2.7.3 Magnetic Structure Refinement

Magnetic structures were refined in this thesis using two programs which interacted with GSAS, called SARAh – *Representational Analysis* and SARAh – *Refine*[26-29]. SARAh – *Representational Analysis* was used to calculate the magnetic structures

possible from the space group of the nuclear structure using group theory. SARAh – *Refine* was then used to trial each of the possible structures and then finally insert the best one into the GSAS refinement.

The first step in any magnetic structure refinement was to identify the k-vector *(Chapter One, Section 1.2.2.3)* of the magnetic ordering. This along with the space group of the nuclear structure was inputted into SARAh – *Representational Analysis*. The program then runs group theory calculations to determine which symmetry operations (known as the Irreducible Representations, Γ) leave the k-vector invariant and so determining the basis vectors (ψ) that can be used to determine the orientation of the magnetic moments. Kovalev[30] tabulated a list of the Irreducible Representations for each space group; these form the basis for the calculations. In essence this program identifies the possible magnetic structures that are compatible with the space group and k-vector.

The next step is to take each of these possible structures and trial them, choosing the best structure based on the lowest χ^2 value to then be inserted into GSAS. A magnetic transition is a second-order phase transition as it does not involve the absorption or release of a specific amount of energy, therefore the Landau Theory can be applied to magnetic ordering transitions. The Landau theory states that for a second-order phase transition an ordered structure must be the result of only one Irreducible Representation. Therefore when trialing the possible magnetic structures, only basis vectors from the same Irreducible Representation can be mixed which

greatly reduces the number of trials. This trial and error method uses the reverse Monte-Carlo method this takes the starting model and allows all of the parameters to be refined in one go. In other words all degrees of freedom associated with the specific magnetic structure being investigated were explored. Once each of the possible magnetic structures (basis vector combinations) had been investigated, the best structure based on the lowest χ^2 value was inserted into the GSAS refinement.

The refinement of the magnetic structure could then be completed in GSAS. SARAh imports only the magnetic atoms into the magnetic phase. In GSAS the space group must be set to P1 and the lattice parameters of the phase constrained to that of the nuclear phase taking into account the k-vector. The orientation of the magnetic moments on each of the magnetic atoms was defined using SARAh, only the magnitude of the moment(s) is refined using GSAS.

2.7.4 Incommensurate Structure Refinement[5-7]

As in the refinement of commensurate structures the structure factor is used to calculate the intensity of the peaks in the diffraction pattern. However for incommensurate structures additional parameters are required to calculate the structure factor. Average values for atomic positions, occupancies and thermal parameters are used; these are calculated by summing the cosine and sine components of the q-vector wave. In this thesis LeBail fits of incommensurate structures were carried out using FullProf, whereas full structural refinements of incommensurate structures were carried out using the JANA2000 software.

2.8 Magnetization measurements

Magnetization measurements were carried out with a Quantum Design MPMS (Magnetic Property Measurement System) SQUID (Superconducting QUantum Interference Device) magnetometer[31]. The SQUID consists of a series of superconducting detection coils surrounding the sample environment, these coils are connected to the SQUID via superconducting wires forming a closed superconducting loop. The SQUID is simply a sensor that detects the current flowing through the wires; changes in the current as a sample is moved through the coil are used to determine the magnetic moment of the material. The samples measured were in the form of a pressed pellet and contained within a gelatin capsule fixed at the midpoint of a straw, the experiments carried out in the SQUID that are reported in this thesis fall into categories, DC and AC.

DC measurements were used to characterize magnetic transition temperatures and saturation moments. In a DC measurement a superconducting magnet is used to apply a static magnetic field to the sample. The sample was then moved through 4cm of the coil, the magnetic moment of the sample induces an electric current in the detection coil in doing so. The sample was stopped in discrete steps measuring the current which was then used to determine the overall change in current across the whole 4cm scan. This was repeated three times for each measurement and an average of the induced current was used to determine the magnetic moment of the sample. This was carried out at different temperatures, known as *Zero-Field-Cooled-Field-Cooled (ZFC-FC)* measurements and at different applied magnetic fields,

magnetizations runs. ZFC-FC magnetization data were collected from 2 to 400K using a 100 Oe field for the field cooled measurements; this was used to determine the ordering temperature of the samples. Magnetization hysteresis loops were recorded sweeping the field between ±5.5T; this was used to calculate the saturation moment of the material.

AC measurements were carried out in the same way as the DC measurements, the sample was moved through a 4cm scan in the detection coil and again the current was measured at discrete steps. The only difference was an oscillating magnetic field was used across the sample instead of a static one. Data was recorded using a 1Oe alternating field applied at different frequencies from 1 Hz to 1kHz and used to determine whether the sample was a spin glass. A discussion of the differences between a spin glass and an ordered magnet is given in *(Chapter One, Section 1.2.2.4).*

2.9 Electrical Properties

Impedance measurements were carried out within a capacitance range of 1pF – 0.1F using a Solatron 1255B Frequency Response Analyzer and a Solatron 1296 dielectric interface over a frequency range of 1-10^6Hz from room temperature to ~1000°C. Conducting samples, with a resistance lower than 100Ω could not be measured as they do not give reliable results.

Before the experiment can be made, electrodes must be attached to two faces of the sample separated by distance, d. To enable an accurate value for the area of the face and distance between them to be measured it is important to ensure the sample being measured is of uniform shape. Electrodes were attached to the sample using platinum paste; it was then baked at 800°C for 30 minutes to ensure connection between the sample and the electrodes. The electrodes were connected to both the Frequency Response Analyzer and the dielectric interface; the sample was then placed inside a tube furnace with a Eurotherm controller. SMART software was used to control the experiment, an AC voltage of 1.5V was selected and data was repeatedly collected stepwise over a frequency range of 1 to 10^6Hz. The real and imaginary impedance of the sample was collected as a function of frequency at different temperatures which was controlled manually using the Eurotherm controller on the furnace.

Impedance[2,32] is the ratio of the voltage over current flowing through the sample because an AC voltage is being applied it has a phase element to it, therefore both real (Z') and imaginary (Z'') components must be measured. The capacitance (C) of the sample was also measured during the experiment, this is a measure of the amount of electrical charged stored for a given voltage, again both the real (C') and imaginary (C'') capacitances were measured. Using these components the dielectric constant (ε_r) and dielectric loss (tan δ) could then be calculated.

Dielectric Constant (ε'):

$$\varepsilon' = \frac{C'}{C_o} \qquad \text{Where: } C_o = \frac{\varepsilon_o A}{d} \qquad \textbf{Equation 2.20}$$

C_o is the capacitance of free space (i.e as if there was a vacuum between the two electrode faces rather then sample)

ε_o = $8.854 \times 10^{-12} Fm^{-1}$ (Permittivity of free space)

A = Area of the face the electrode is attached to

d = Distance between the faces

Dielectric Loss:

Dielectric Loss = tan (δ) *Where:* $\delta = \left(\pi/2 + \vartheta\right)$ **Equation 2.21**

And: $\vartheta = \tan^{-1}\left(\frac{z''}{z'}\right)$

The dielectric constant is a measure of how much electrical charge is stored in the material relative to the dielectric constant of free space. For a ferroelectric, which is a polarized structure, this constant would be greater before the material undergoes a transition to an unpolarised form. A spike in this constant would be seen at the transition and so plotting the dielectric constant as a function of temperature is often used as a way to identify the transition temperature.

The dielectric loss is a measure of how well the sample holds charge. For a ferroelectric in the polarized form the material must be able to keep charge in order to remain polarized, a low dielectric loss (below 0.1) would be expected.

2.10 X-ray Absorption Spectroscopy

X-ray Absorption Spectroscopy (XAS) is reported in this thesis as a method for determining oxidation states of certain samples in the materials synthesized. The material under investigation was placed in the path of an X-ray beam, the intensity of the beam before and after the sample was recorded as a function of the energy of the beam. When an X-ray travels through a material it interacts with it causing some of the beams intensity to be absorbed by the sample. At certain energies the X-ray beam causes a core electron within atoms in the sample to be ejected. This is noted on the spectrum as a spike in the absorbance at a specific energy. From the energy of this absorbance the oxidation state of that particular atom can be determined.

All XAS data reported in this thesis were collected on station 7.1[33] of the Daresbury Synchrotron Radiation Source. This used a Si(111) crystal monochromator and allowed the energy range of 4 keV to 10 keV to be investigated. Samples under investigation were prepared by placing a small amount of the material in a thin strip on a piece of 'sticky-back'-plastic, the intensity of the X-ray beam was measured before and after this strip. The range of energy of the X-ray was selected carefully for each sample depending on what element was under investigation, for example Mn samples a range of 6 -7 keV was used, whereas for Ni samples a range of 8 – 9 keV was used. For this type of experiment the energy of the absorption edge was not absolute, as a result standards were always measured, these were materials with known oxidation states, the spectrum of the samples and standards were compared to determine the oxidation states. Because oxidation state results were obtained by

spectrum comparison a monitor spectrum was taken for each sample this was the metal of the element under investigation. The absorption edge of the metal is fixed, and so was used as a reference point between samples. As long as the monitor edge position of the samples under comparison were the same a true comparison between spectrum samples could be made.

2.11 References

(1) Dann, S. E. *Reactions and Characterization of Solids*; The Royal Society of Chemistry, 2000.

(2) West, A. R. *Solid State Chemistry and its Applications*; John Wiley & Sons, 1984.

(3) Smart, L. E.; Moore, E. A. *Solid State Chemistry: An introduction*; Third ed.; CRC Press, 2005.

(4) *International Tables for Crystallography, Volume A: Space-Group Symmetry*; Fifth ed.; Hahn, T., Ed., 2002.

(5) Young, R. A. *The Rietveld Method*; IUCr Oxford University Press, 1993.

(6) Yamamoto, A. *Acta Cryst. A* **1982**, *38*, 87-92.

(7) Dušek, M.; Petříček, V.; Wunschel, M.; Dinnebier, R. E.; Van-Smaalen, S. *J. Appl. Cryst.* **2001**, *34*, 398-404.

(8) http://www.srs.ac.uk/srs/index.html.

(9) http://www.srs.ac.uk/srs/stations/station9.1.html.

(10) G.E.Bacon *Neutron Diffraction*; Third ed. Oxford, 1975.

(11) NIST *Neutron News* **1992**, *3*, 29-37.

(12) Smith, R. I.; Hull, S. *Rutherford Appleton Laboratory Report* **1997**, *RAL-TR-97-038*.

(13) Hull, S.; Smith, R. I.; David, W. I. F.; Hannon, A. C.; Mayers, J.; Cywinski, R. *Physica B* **1992**, *180 & 181*, 1000-1002.

(14) Williams, W. G.; Ibberson, R. M.; Day, P.; Enderby, J. E. *Physica B* **1998**, *241-243*, 234-236.

(15) Ibberson, R. M.; David, W. I. F.; Knight, K. S. *Rutherford Appleton Laboratory Report* **1992**, *RAL-92-031*.

(16) www.ill.fr/YellowBook/D2B/.

(17) Larson, A. C.; Von-Dreele, R. B. In *Los Alamos National Laboratory Report* 2004; Vol. LAUR 86-748.

(18) Toby, B. H. *J. Appl. Cryst.* **2001**, *34*, 210 - 213.

(19) Wills, A. S. *Physica B* **2000**, *276*, 680.

(20) Petříček, V.; Dušek, M.; Palantinus, L. Institue of Physics, Praha, Czech Republic, 2000.

(21) Le-Bail, A.; Duroy, H.; Fourquet, J. L. *Mat. Res. Bull.* **1988**, *23*, 447-452.

(22) Rodriguez-Carvajal, J. *Physica B* **1993**, *192*, 55-69.

(23) Rietveld., H. M. *Acta Cryst.* **1967**, *22*, 151-152.

(24) Rietveld, H. M. *J. Appl. Cryst.* **1969**, *2*, 65.

(25) McCusker, L. B.; Von - Dreele, R. B.; Cox, D. E.; Louer, D.; Scardi, P. *J. Appl. Cryst.* **1999**, *32*, 36-50.

(26) Wills, A. S. *Physica B* **2000**, *276-278*, 680-681.

(27) Wills, A. S. *J. Phys. IV France* **2001**, *11*, Pr 9-133.

(28) A.S.Wills *Appl. Phys. A* **2002**, *Suppl.*, S856 - S858.

(29) Wills, A. S.; Lappas, A. *Journal of Physics and Chemistry of Solids* **2004**, *65*, 65-71.

(30) Kovalev, O. V. *Representations of crystallographic space groups*; 2nd ed.; Gordon & Breach: Amsterdam, 1993.

(31) McElfresh, M. *Fundamentals of magnetism and magnetic measurements. Featuring Quantum Design's Magnetic Property Measurement System*; Quantum Design, 1994.

(32) West, A. R.; Irvine, J. T. S.; Sinclair, D. C. *Adv. Mater.* **1990**, *2*, 132-138.

(33) http://www.srs.ac.uk/srs/stations/station7.1.htm.

Chapter 3: Synthesis and Characterisation of $Bi_2Mn_{4/3}Ni_{2/3}O_6$

3.1 Introduction

This chapter reports on the synthesis and characterisation of $Bi_2Mn_{4/3}Ni_{2/3}O_6$, which is a novel bismuth based perovskite material, synthesised under ambient conditions. Up to now only one other bismuth-based perovskite has been synthesised using these conditions, $BiFeO_3$[1] all other materials have required artificial methods such as high pressures or thin film substrates.

Structural investigations at variable temperatures using Powder X-ray Diffraction and Time of Flight Neutron Powder Diffraction are reported. Magnetic and dielectric measurements are also reported. This chapter combines a large amount of collaboration work carried out by members of the academic staff in both the University of Liverpool and other universities. Structural characterisations were carried out with the aid of Dr. John Claridge, Dr. Craig Bridges, Dr. Darren Bradshaw and Prof. Matthew Rosseinsky the electron microscopy study was carried out by Dr. Mathieu Allix and the dielectric study was performed with the assistance of Dr. Xioajun Kuang.

3.2 Synthesis

3.2.1 Ceramic Synthesis

Initially an attempt was made to prepare Bi_2MnNiO_6 by standard ceramic methods. During the course of the investigation it was shown that this phase could be prepared by high pressure synthesis[2]. Following the identification of the correct $Bi_2Mn_{4/3}Ni_{2/3}O_6$ composition by the energy dispersive spectroscopy (EDS) measurements, $Bi_2Mn_{4/3}Ni_{2/3}O_6$ samples were prepared by a standard ceramic method, on a scale between 0.5g and 5g. Stoichiometric quantities of Bi_2O_3 (Alfa 99.9995%), MnO_2 (Alfa Aesar 99.999%) and NiO (Alfa Aesar 99.998%) were ground together in a ball mill with Mg-stabilised zirconia milling media for 12 hours and pelletized. The pellet was placed on platinum foil in an alumina boat (reaction occurs with the boat if this precaution is not taken) and heated at 800 °C for 12 hours, 850 °C for 12 hours and then 875 °C for 12 hours. The pellet was ground in an agate mortar and pestle, repelletized and heated at 850 °C for 12 hours. This process was repeated twice. All steps used a heating rate of 5°C per minute and a cooling rate of 10°C per minute.

Oxygen content was determined by chemical analysis using redox titration. The sample was first dissolved in 6M HCl solution under an argon atmosphere: an excess of KI was then added to reduce the manganese and nickel species to Mn^{2+} and Ni^{2+}. The I_2 formed was then titrated using sodium thiosulfate in order to work out the quantity of reduced cations. This value then leads to the oxygen content assuming bismuth is in the +III oxidation state.

Following the method described above samples with the compositions $Bi_2Mn_{1.7}Ni_{0.3}O_6$ and $Bi_2Mn_{1.6}Ni_{0.4}O_6$ were attempted, however these were unsuccessful producing a range of oxides and a perovskite phase that was revealed by EDX as $Bi_2Mn_{4/3}Ni_{2/3}O_6$.

3.2.2 Crystal Growth

A number of attempts were made to grow crystals of $Bi_2Mn_{4/3}Ni_{2/3}O_6$, two different fluxes were attempted, Bi_2O_3 : NaCl[3] and Bi_2O_3 : B_2O_3[4]. These were selected as they had been previously used to grow crystals of $BiFeO_3$. However only the Bi_2O_3 : NaCl flux was found to form crystals of $Bi_2Mn_{4/3}Ni_{2/3}O_6$. A range of different temperatures, dwell times, heating and cooling rates were attempted along with a range of flux compositions and masses in order to maximise the yield of crystals formed. The most successful flux conditions are detailed below.

The starting composition consisted of Bi_2O_3 (64.12 mole %), MnO_2 (20.24 mole %), NiO (10.12 mole %) and NaCl (5.52 mole %) with a total mass of 30 grammes. The mixture was heated in a platinum crucible (14 mL volume) covered with a lid at 800 °C for 12 hours, then 850 °C for 12 hours, then 875 °C for 3 hours using a rate of 5°C/minute. The flux was then slow cooled to 820 °C at a rate of 0.5 °C/hour, and finally cooled to room temperature at a rate of 5 °C/minute. The crystals were extracted from the flux by boiling the mixture in 4M HNO_3 for approximately four days, followed by filtering. The crystals obtained were cubic in shape and approximately 1cm per edge in size.

3.3 Characterisation

3.3.1 Single Crystal X-Ray Diffraction

Single crystal x-ray diffraction data were collected at 150K on a 5 x 5 x 20 μm irregularly shaped fragment of one of the crystal samples on station 9.8 of the Daresbury Synchrotron Radiation Source. The structure was solved by Dr. Craig Bridges, Dr. Darren Bradshaw, Dr. John Claridge and Prof. Matthew Rosseinsky from Liverpool University to an orthorhombic perovskite–related cell, with Bi^{3+} ions on the A-site, and a random distribution of 33% Mn^{4+}, 33% Mn^{3+} and 33% Ni^{2+} ions on the B-site inside the oxygen octahedra. The structure was solved in the polar space group $Pn2_1m$ with the lattice parameters $a \approx \sqrt{2}a_p$, $b \approx 2\sqrt{2}a_p$ and $c \approx 4a_p$ (a_p is the parameter of the cubic perovskite subcell).

Lattice Parameters	
Space Group	$Pn2_1m$ (No. 31)
a / Å	5.4939(11)
b / Å	11.1150(2)
c / Å	15.5028(3)
Volume / $Å^3$	946.67(30)
Density / g cm^{-3}	9.616

Table 3.1: *Refined lattice parameters for the single crystal data collected at 150K on the* $Bi_2Mn_{4/3}Ni_{2/3}O_6$.

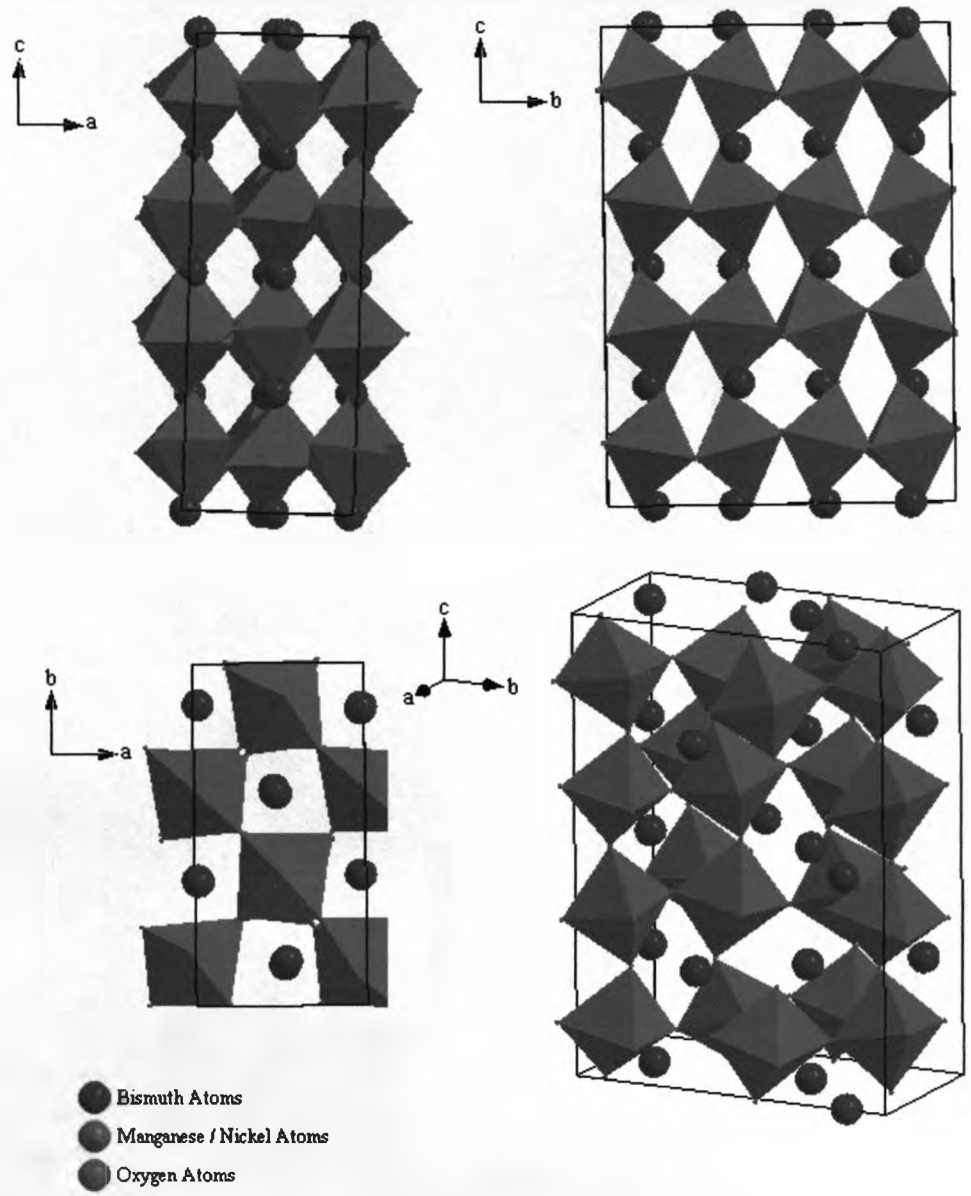

Figure 3.1: *Refined structure of $Bi_2Mn_{4/3}Ni_{2/3}O_6$ from the single crystal data.*

The structure as already discussed was refined in the polar space group $Pn2_1m$; to determine the level of polarization within the material, which according to the symmetry of the space group can only occur along the b-direction, a simple calculation was carried out using the refined positions and the average charge on

each site. A list of all atoms within the unit cell was generated, including all of the multiplicities for each site, then any atoms with fractional coordinates that were either less then zero or greater than one were discarded to ensure only atoms inside one unit cell were used in the calculation. The polarization along each direction for each atom was then calculated using the fractional co-ordinate along that specific direction combined with the site occupancy and the average atomic charge on the site, this was then summed along each direction.

	x - direction	y - direction	z - direction
Total charge per unit cell	1.776×10^{-15}	4.0008	7.105×10^{-15}

Table 3.2: *Polarization calculation results along each direction per unit cell.*

The polarization calculations show that the total charge per unit cell along the a and c directions are negligible compared with that along the b-direction. The charge along the b-direction was converted into a value that could be compared with other systems (coulombs per cm^2), rather than just the charge per unit cell for this system. This was done using the following formula:

$$Polarization = \frac{l_y \times P_y \times e}{v}$$

Where: l_y = *unit cell length (cm) along the y-direction (1Å = 1 x* 10^{-8} *cm)*

P_y = *Charge along the y-direction of the unit cell*

e = *Charge of an electron* $= 1.60219 \times 10^{-19}$ *Coulombs*

v = *volume of the unit cell* (cm^3)

By carrying out this calculation it was concluded that the $Bi_2Mn_{2/3}Ni_{2/3}O_6$ material had an overall polarization of 75.3μC/cm^2, which could be considered as high when compared to other materials. The high pressure analogue of this phase, Bi_2MnNiO_6 only has a polarization of 20μC/cm^2 and with the materials $BiInO_3$ (18μC/cm^2)[5], Bi_2FeCrO_6 (63μC/cm^2)[6] and Bi_2ZnTiO_6 (103 μC/cm^2)[7].

The fact that the sample has a calculated net polarization in the structure is a positive step towards a multiferroic material as it means that it has one of the two properties required.

3.3.2 Room temperature X-ray and neutron powder diffraction

Room temperature neutron powder diffraction data were collected on the D2B diffractometer at ILL, France on the ceramic sample. The structural model refined from the single crystal X-ray diffraction data was verified by Rietveld refinement using GSAS by Dr Craig Bridges, Dr. John Claridge and Prof. Matthew Rosseinsky. The refinement was found to be very temperamental due to the large number of atoms. In order to prevent it from diverging the nickel/manganese-oxygen bond lengths were constrained to be within ±0.01Å of the single crystal values. This resulted in a fit with parameters R_{wp} = 3.61%, $R(F^2)$ = 3.64%, the manganese : nickel ratio was refined to give an equal distribution of atoms on each site which confirmed the X-ray conclusion that the B – site is randomly occupied and that there is no ordering present within the material.

Atom	Occupancy	x	y	z	U_{iso}
Bi1	1	0.0177(3)	0.12849(11)	0.00000	0.0149(4)
Bi2	1	0.4702(3)	-0.13079(10)	0.0000	0.0075(3)
Bi3	1	0.5268(3)	-0.62489(9)	0.00000	0.0090(3)
Bi4	1	-0.0314(2)	0.11831(6)	-0.24536(4)	0.0040(2)
Bi5	1	0.4771(4)	-0.12071(7)	-0.25315(8)	0.0153(4)
Bi6	1	0.9774(3)	-0.36520(12)	0.00000	0.0140(4)
Mn7	0.66	0.4937(12)	-0.3733(12)	0.1234(2)	0.0043(6)
Mn8	0.66	0.0149(6)	-0.1226(12)	-0.1243(3)	0.0032(6)
Mn9	0.66	0.0097(6)	-0.1241(12)	-0.3734(3)	0.0049(7)
Mn10	0.66	-0.4926(13)	0.1279(12)	-0.1259(2)	0.0053(7)
Ni7	0.33	0.4937(12)	-0.3733(12)	0.1234(2)	0.0043(6)
Ni8	0.33	0.0149(6)	-0.1226(12)	-0.1243(3)	0.0032(6)
Ni9	0.33	0.0097(6)	-0.1241(12)	-0.3734(3)	0.0049(7)
Ni10	0.33	-0.4926(13)	0.1279(12)	-0.1259(2)	0.0053(7)
O1	1	0.720(3)	-0.5005(16)	0.1531(11)	0.015(3)
O2	1	0.554(5)	-0.404(3)	0.00000	0.012(4)
O3	1	0.441(4)	-0.334(2)	0.2467(8)	0.010(3)
O4	1	-0.311(3)	0.2708(16)	-0.1071(10)	0.019(3)
O5	1	0.268(3)	0.0009(17)	-0.1540(12)	0.016(4)
O6	1	-0.528(6)	0.107(3)	0.00000	0.029(7)
O7	1	-0.195(3)	0.0249(13)	-0.1332(8)	0.010(3)
O8	1	0.763(3)	-0.2408(16)	-0.0974(9)	0.013(3)
O9	1	0.270(4)	-0.243(2)	-0.0980(11)	0.025(4)
O10	1	0.062(4)	-0.157(2)	-0.2454(9)	0.013(4)
O11	1	0.041(5)	-0.075(2)	0.00000	0.015(5)
O12	1	0.708(4)	-0.236(2)	-0.3835(11)	0.034(5)
O13	1	-0.194(3)	0.0121(14)	-0.3564(9)	0.011(3)
O14	1	0.070(5)	-0.088(3)	-0.50000	0.020(5)

Table 3.3: *Refined fractional co-ordinates of* $Bi_2Mn_{4/3}Ni_{2/3}O_6$ *from the powder neutron diffraction data (D2b, ILL) collected at room temperature.*

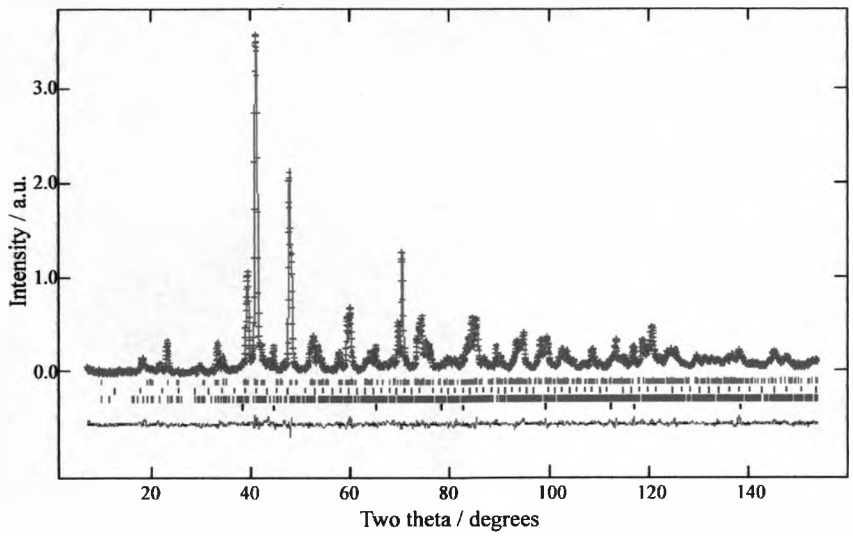

Figure 3.2: *Refinement of 300K powder neutron diffraction data (D2B, ILL) for a ceramic sample of* $Bi_2Mn_{4/3}Ni_{2/3}O_6$ *against the model refined from single crystal X-ray diffraction. Tick marks correspond to the* $Pn2_1m$ *phase (Red), NiO (Black),* $Bi_{12}MnO_{20}$ *(Blue), and a second perovskite BiMnNi phase modelled as monoclinic* $C2^8$ *(Green).*

As this is a ceramic sample the purity is not as high as that of the crystal sample, therefore a number of impurity phases had to be included in the refinement. Polarisation calculations were also carried out on this refined structure, a slightly smaller charge of 59.7μC/cm^2 was calculated along the b-direction. This is considered as the most reliable result for the polarisation of the material because, as already discussed in *Chapter Two*, neutron diffraction provides more accurate atomic positions as the powder pattern is not dominated by heavy atoms with lots of electrons.

Room temperature X-ray powder diffraction data were also collected on station 9.1 of the Daresbury Synchrotron Radiation source on the $Bi_2Mn_{4/3}Ni_{2/3}O_6$

ceramic sample. Rietveld refinement using the model refined from the single crystal X-ray diffraction data was also carried out. Again as with the neutron powder diffraction data the nickel/manganese-oxygen bond lengths were constrained to be within ±0.01Å of the single crystal values. The refinement revealed that the structure is actually slightly incommensurate by a misfit in the fit of the low angle peaks (*figure 3.3*).

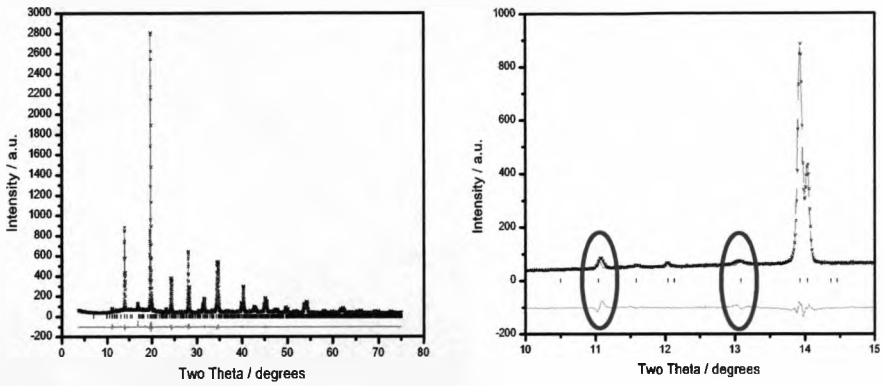

Figure 3.3: *X-ray powder diffraction patterns collected at room temperature on station 9.1, the full pattern is shown with a zoom of the low angle region highlighting the modulated peaks which are circled. The red crosses are the observed data, black line is the calculated profile, the green line is the difference plot and the black markers are the Bragg positions.*

The modulation was refined by Dr. John Claridge with two-dimensional modulation vectors, q_1 = (0.4911(2), 0 ,0) and q_2 = (0, -0.5015(3), 0) in the superspace group Ibmm(q00,0-p0)ss.gm. The modulated unit cell is described with the lattice parameters $a \approx 55\sqrt{2}a_p$, $b \approx 4a_p$ and $c \approx \sqrt{2}a_p$ (a_p is the parameter of the cubic perovskite subcell), indicating that the modulation occurs along the

a-direction resulting in the unit cell being 55 times longer in that direction than the commensurate structure. It is the movement of the bismuth atoms off position within the structure that causes the modulation through the structure *(figure 3.5)*, this shift of position also causes the polarisation in the material to be cancelled, resulting in a non-polar structure forming.

Lattice Parameters		Fit Parameters	
a / Å	5.573980(5)	R_{wp} / %	5.62
b / Å	7.776452(9)	R_p / %	4.39
c / Å	5.507555(8)		
(q_1 , 0 , 0)	0.491132(2)		
(0 , q_2 , 0)	-0.501449(3)		

Table 3.4: *Refined lattice parameters and goodness of fit parameters from the incommensurate Rietveld refinement carried out on the room temperature powder X-ray diffraction data of* $Bi_2Mn_{4/3}Ni_{2/3}O_6$.

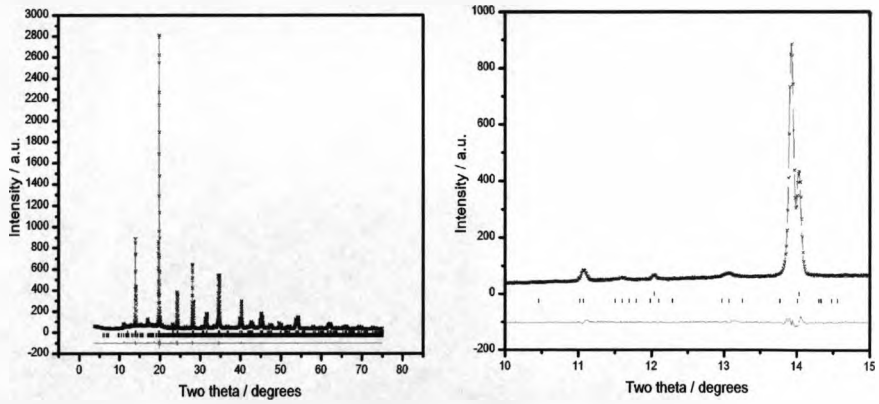

Figure 3.4: *X-ray powder diffraction patterns collected at room temperature on station 9.1, the full pattern is shown with a zoom of the low angle region highlighting the improved fit on the modulated peaks. The red crosses are the observed data, black line is the calculated profile, the green line is the difference plot and the black markers are the Bragg positions.*

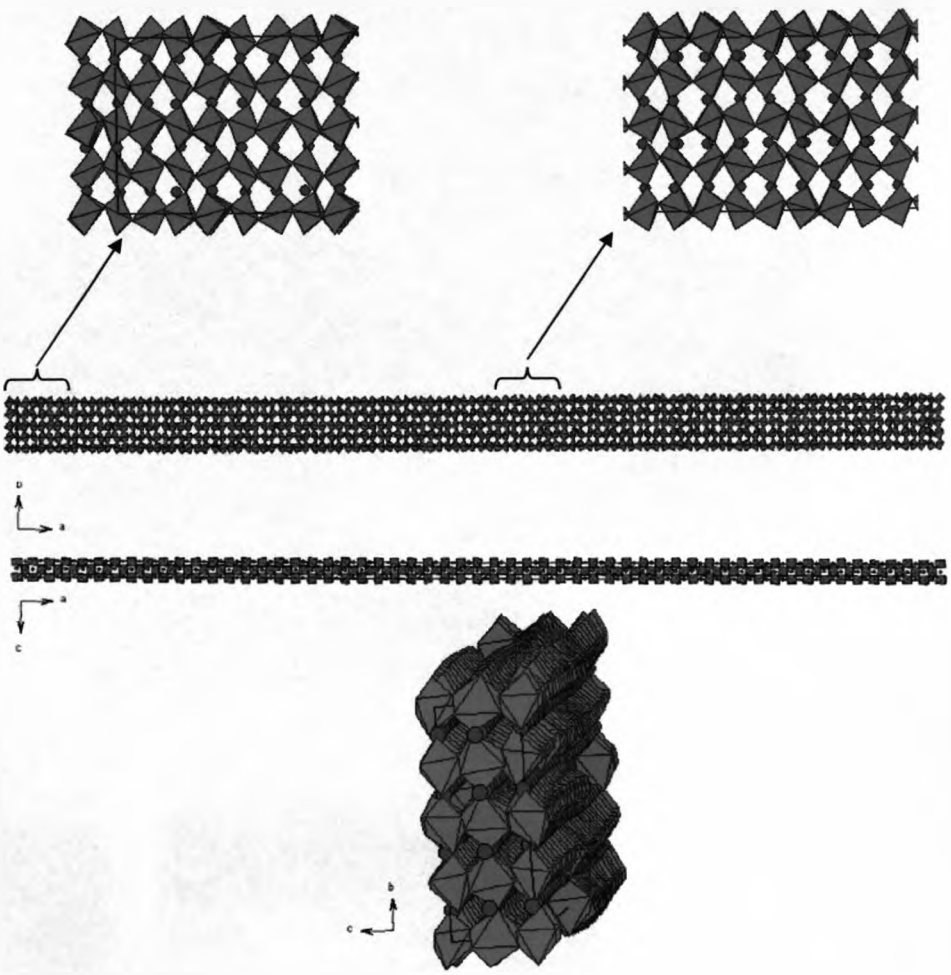

Figure 3.5: *Incommensurate structure viewed along the different projections, the modulation can clearly be seen in the bismuth atoms. Blue spheres are the* Bi^{3+} *ions (A-site); the purple octahedra contain a random distribution of 33%* Mn^{4+}*, 33%* Mn^{3+} *and 33%* Ni^{2+} *ions (B-site) in the centre with oxygen atoms on the corners.*

3.3.3 Variable Temperature X-ray Powder Diffraction

X-ray powder diffraction data were collected on station 9.1 of the Daresbury Synchrotron Radiation Source between room temperature and 450°C on both the $Bi_2Mn_{4/3}Ni_{2/3}O_6$ ceramic sample and crystal sample. On heating, both samples appeared to undergo a structural change from the incommensurate room temperature structure to a commensurate Pnma structure in the region of 280°C. During heating data were collected over a small 2θ range, an extra peak due to the Pnma structure could clearly be seen to grow in as the temperature was increased *(figure 3.6)*.

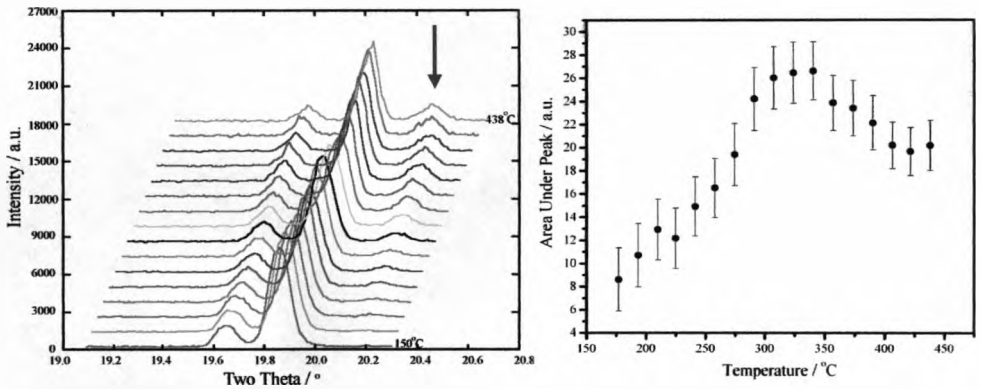

Figure 3.6: *X-ray diffraction patterns collected with increasing temperature are shown on the left. The extra peak that grew in as the material changed is marked with an arrow, the area under this peak changed between 177°C and 291°C was tracked as a function of temperature.*

The cell parameters of the sample were calculated *(figure 3.7)* from the small angular range collected, by carrying out a LeBail fit using GSAS in the space group $Pn2_1m$ (which was originally thought of as the room temperature space group).

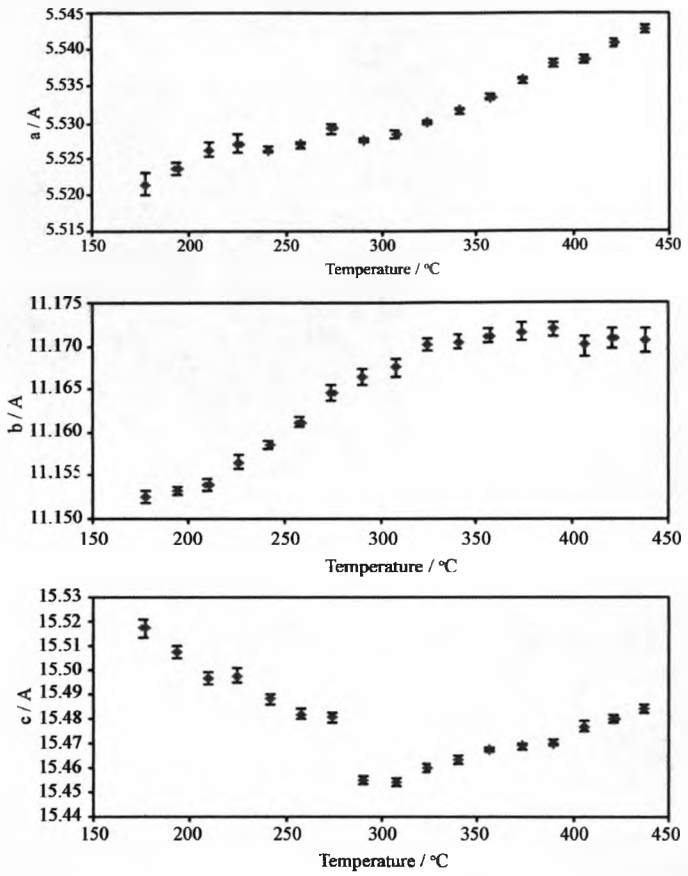

Figure 3.7: *Variable temperature X-ray powder diffraction data was collected on station 9.1 of the Daresbury Synchrotron Radiation Source between room temperature and 450°C. The cell parameters of the material were tracked as a function of temperature.*

The calculated cell parameters were then converted into their corresponding perovskite unit cell (a_p) values (i.e. $a \sim \sqrt{2}a_p$, $b \sim 2\sqrt{2}a_p$ and $c \sim 4a_p$). The ratio between these values was calculated and plotted as a function of temperature *(figure 3.8)*. The temperature of the structural change can clearly be seen in both the a:b and c:b ratios. What is probably the most significant is the variation in the

perovskite unit cell volume with temperature. Below the transition temperature when the material is in the incommensurate structure the volume does not appear to vary with temperature, the modulation must absorb the expansion of the cell without increasing the volume. Above the transition temperature, when the material is in the commensurate structure the volume increases with temperature.

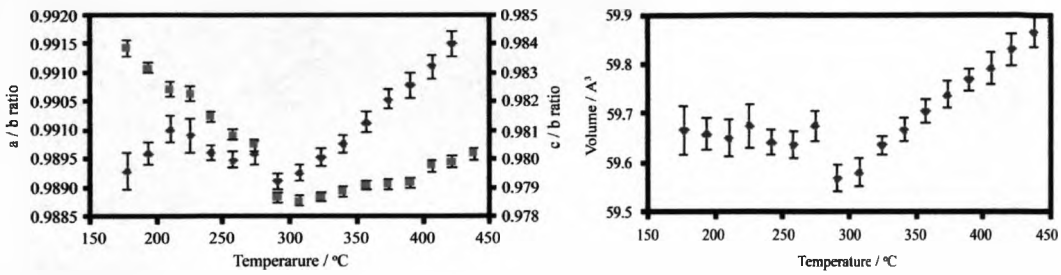

Figure 3.8: *Variation in the perovskite unit cell (a_p) values with temperature, left plot is the variation in the a / b and c / b ratios, and right plot is the variation in the unit cell volume*

In all unit cell parameters values *(Figures 3.7 and 3.8)* the trend with increasing temperature changes in the temperature region of 280°C. This suggests that the $Bi_2Mn_{4/3}Ni_{2/3}O_6$ material undergoes a structural transition at this temperature.

Powder X-ray data was collected above the transition on station 9.1 of the Daresbury Synchrotron Radiation Source on both the ceramic sample and a ground up crystal sample, Rietveld refinement was carried out on the data sets using the centrosymmetric, non-polar Pnma structural model. Fit parameters and Bond Valence Sums confirm that the material transforms into the Pnma structure above ~280°C. This is a distorted form of the perovskite, with Bi^{3+} on the A-site in an 8 co-ordinate environment, and a random distribution of Mn^{3+}, Mn^{4+} and Ni^{2+} on the B-site in a six co-ordinate environment. Distortion from the parent

perovskite structure occurs due to tilting of the BO_6 octahedra. This is in contrast to the high pressure analogous phase, Bi_2MnNiO_6[9], which undergoes a monoclinic to monoclinic ferroelectric structural transition at ~200°C. The lanthanum analogue, La_2MnNiO_6[10], undergoes a structural transition from monoclinic to rhombohedral at ~375°C. $BiMnO_3$[11] also exhibits a ferroelectric structural transition at ~25°C from monoclinic to monoclinic and $BiNiO_3$[12] is reported to be triclinic at room temperature.

Ground Up Crystal Sample:

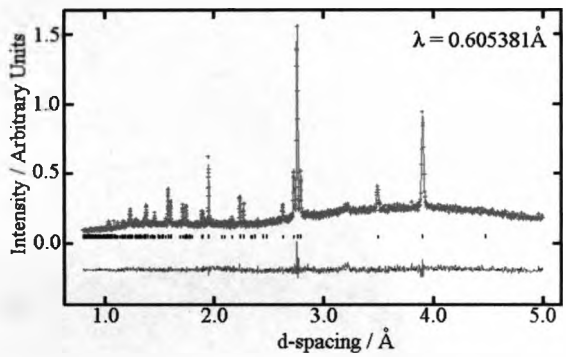

Figure 3.9: *Rietveld Refinement of 350°C powder X-ray diffraction data collected on a ground up crystal sample of $Bi_2Mn_{4/3}Ni_{2/3}O_6$ against the Pnma model. The red crosses are observed data, the solid green line is the calculated pattern and the pink line is the difference.*

Lattice Parameters		Fit Parameters	
Space Group	Pnma	R_{wp} / %	4.67
a / Å	5.5817(2)	R_p / %	4.25
b / Å	7.8095(3)	Rf^2 / %	20.06
c / Å	5.4581(2)	χ^2	1.368
Volume / Å^3	237.92(1)		
Density / g cm^{-3}	8.743		

Table 3.5: *Refined lattice parameters and goodness of fit parameters from the Rietveld refinement of 350°C powder X-ray diffraction data collected on a ground up crystal sample of $Bi_2Mn_{4/3}Ni_{2/3}O_6$.*

Atom	Occupancy	x	y	z	Uiso
Bi1	1	-0.0466(4)	0.25	0.00375(18)	0.0313(7)
Mn1	0.667	0	0	0.5	0.0137(15)
Ni1	0.333	0	0	0.5	0.0137(15)
O1	1	0.518(8)	0.25	-0.072(10)	0.097(22)
O2	1	0.304(6)	-0.035(4)	0.708(6)	0.033(10)

Table 3.6: *Refined positional parameters from the Rietveld refinement of 350°C powder X-ray diffraction data for the ground up crystal sample of* $Bi_2Mn_{4/3}Ni_{2/3}O_6$.

	Atom Bonds	Bond Length (l_i) / Å	Bond Valence Sum, v_i (expected oxidation state)
Bi	Bi – O1	2.46405 (5)	**2.573 (3+)**
	Bi – O1	3.17615 (4)	
	Bi – O1	3.13436 (6)	
	Bi – O1	2.37193 (5)	
	Bi – O2 (x2)	2.43689 (5)	
	Bi – O2 (x2)	2.73552 (24)	
	Bi – O2 (x2)	2.62607 (4)	
$Mn_{2/3}$	Mn1 – O2 (x2)	1.99405 (11)	**3.104 (3.5+)**
	Mn1 – O2 (x2)	2.06035 (34)	
	Mn1 – O2 (x2)	1.95436 (34)	
$Ni_{1/3}$	Ni1 – O2 (x2)	1.99405 (11)	**2.353 (2+)**
	Ni1 – O2 (x2)	2.06035 (34)	
	Ni1 – O2 (x2)	1.95436 (34)	

Table 3.7: *Selected bond lengths and Bond Valence Sums[13] obtained from the powder X-ray diffraction data collected at 350°C for the crystal sample of* $Bi_2Mn_{4/3}Ni_{2/3}O_6$.

$$BVS = \Sigma^{N}_{i=1} v_i \qquad v_i = exp[(R_o - l_i)/B]$$

$$B = 0.37$$

$$R_o(Bi^{3+}) = 2.094^{14}$$

$$R_o(Ni^{2+}) = 1.654^{14}$$

$$R_o(0.5Mn^{4+} + 0.5Mn^{3+}) = 1.7565^{14}$$

Ceramic Sample:

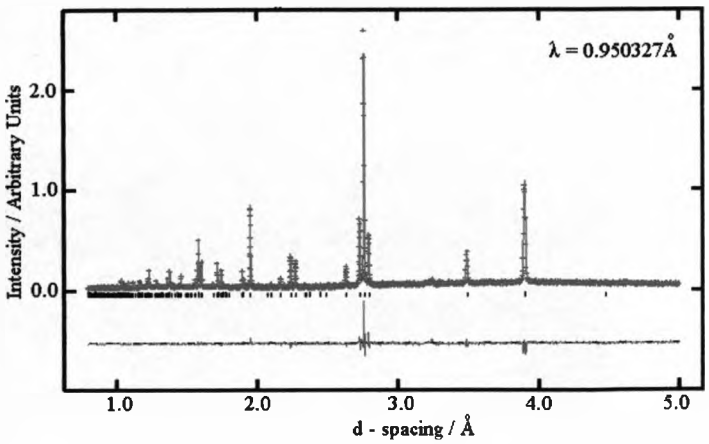

Figure 3.10: *Rietveld Refinement of 350°C powder X-ray diffraction data for the ceramic sample of* $Bi_2Mn_{4/3}Ni_{2/3}O_6$ *against the Pnma model. The red crosses are observed data, the solid green line is the calculated pattern and the pink line is the difference.*

Lattice Parameters		Fit Parameters	
Space Group	Pnma	R_{wp} / %	8.09
a / Å	5.5862(1)	R_p / %	7.26
b / Å	7.8084(1)	Rf^2 / %	10.97
c / Å	5.4558(1)	χ^2	1.471
Volume / $Å^3$	237.93(1)		
Density / g cm^{-3}	8.741		

Table 3.8: *Refined lattice parameters and goodness of fit parameters from the Rietveld refinement of 350°C powder X-ray diffraction data for the ceramic sample of* $Bi_2Mn_{4/3}Ni_{2/3}O_6$.

Atom	Occupancy	x	y	z	Uiso
Bi1	1	-0.04712(18)	0.25	0.0038(6)	0.0396(3)
Mn1	0.667	0	0	0.5	0.0082(6)
Ni1	0.333	0	0	0.5	0.0082(6)
O1	1	0.5198(26)	0.25	0.0827(25)	0.025(5)
O2	1	0.2935(24)	-0.0284(17)	0.6934(22)	0.0253(34)

Table 3.9: *Refined positional parameters from the Rietveld refinement of 350°C powder X-ray diffraction data for the ceramic sample of* $Bi_2Mn_{4/3}Ni_{2/3}O_6$.

	Atom Bonds	Bond Length (l_i) / Å	Bond Valence Sum, v_i (expected oxidation state)
Bi	Bi – O1	2.466 (14)	**2.569 (3+)**
	Bi – O1	3.201 (14)	
	Bi – O1	3.18 (14)	
	Bi – O1	2.328 (11)	
	Bi – O2 (x2)	2.481 (11)	
	Bi – O2 (x2)	2.784 (14)	
	Bi – O2 (x2)	2.568 (15)	
$Mn_{2/3}$	Mn1 – O2 (x2)	2.0066 (32)	**3.081 (3.5+)**
	Mn1 – O2 (x2)	2.043 (14)	
	Mn1 – O2 (x2)	1.964 (13)	
$Ni_{1/3}$	Ni1 – O2 (x2)	2.0066 (32)	**2.335 (2+)**
	Ni1 – O2 (x2)	2.043 (14)	
	Ni1 – O2 (x2)	1.964 (13)	

Table 3.10: *Selected bond lengths and Bond Valence Sums*[13] *obtained from the powder X-ray diffraction data collected at 350°C for the ceramic sample of* $Bi_2Mn_{4/3}Ni_{2/3}O_6$.

3.3.4 Variable Temperature Neutron Powder Diffraction

Powder diffraction data was collected on the D2b diffractometers at the ILL at 5K and 300K, and on the GEM diffractometers at ISIS. All measurements were carried out on the ceramic (5g scale) sample.

The low temperature data revealed no extra Bragg scattering suggesting that the sample does not contain any long range magnetic ordering as the temperature is decreased. This conclusion was made after careful comparison between the two data sets, particularly in the high d-space (low 2θ) region where magnetic scattering is generally observed.

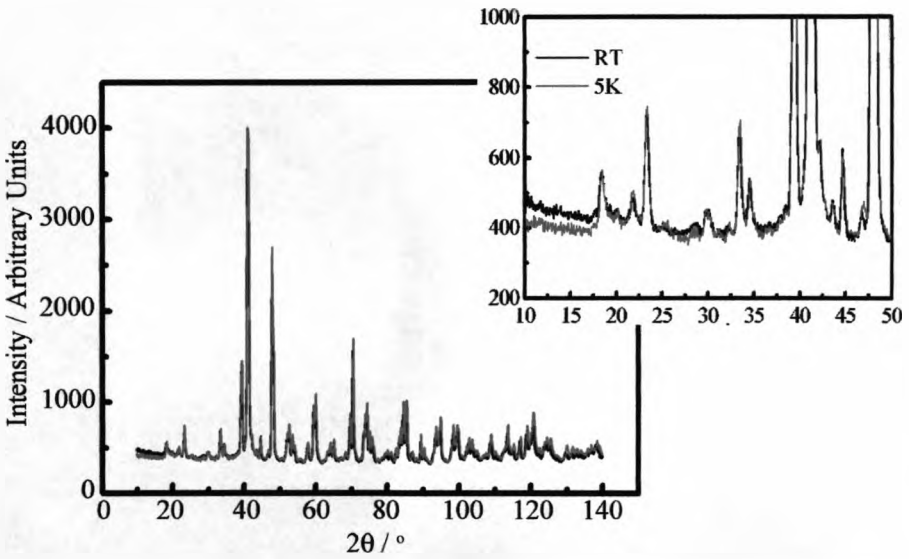

Figure 3.11: *Neutron powder diffraction data collected on the D2b diffractometer at the ILL at 5K and room temperature. A close up of the high d-space region is given to highlight the absence of magnetic scattering in this sample.*

Data was collected on the material in 1K intervals between 50K and 25K on GEM, the variation in the cell parameters and q-vectors with temperature was calculated by carrying out a Profile Matching fit using FullProf. The data was fitted with five separate phases, one being the basic structure in the space group Ibmm, and four phases containing each combination of the two q-vectors used to describe the incommensurate structure, $(q_1,0,0)$, $(0,q_2,0)$, $(q_1,q_2,0)$ and $(q_1,-q_2,0)$. The cell parameters and absolute values of the q-vectors were constrained to be the same in each phase. The fits *(figure 3.12)* showed a clear change in trend in the cell parameters in the region of the magnetic transition temperature (35K) see later section 3.3.6.

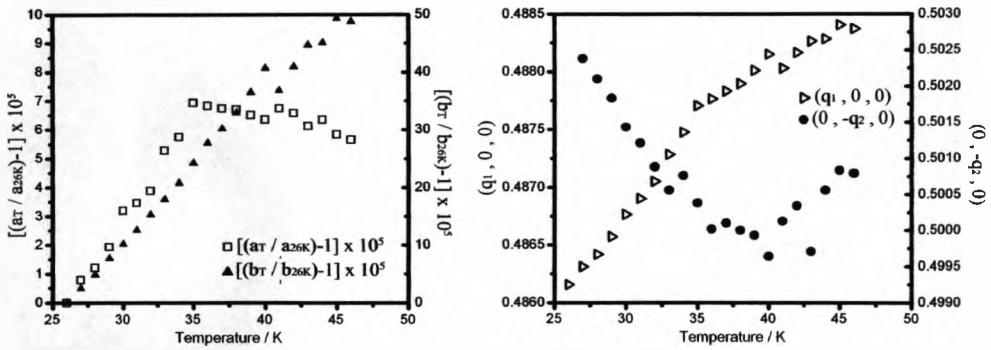

Figure 3.12: *Variation in the cell parameters and q-vectors of the incommensurate phase with temperature close to the magnetic transition temperature, 35K.*

High temperature data collected at 250°C on the GEM diffractometer supported the structural transition observed in the variable temperature synchrotron data. Rietveld refinements were carried out on the high temperature data using the Pnma structural model. Fit parameters and Bond Valence Sums confirm that the material transforms into the Pnma structure.

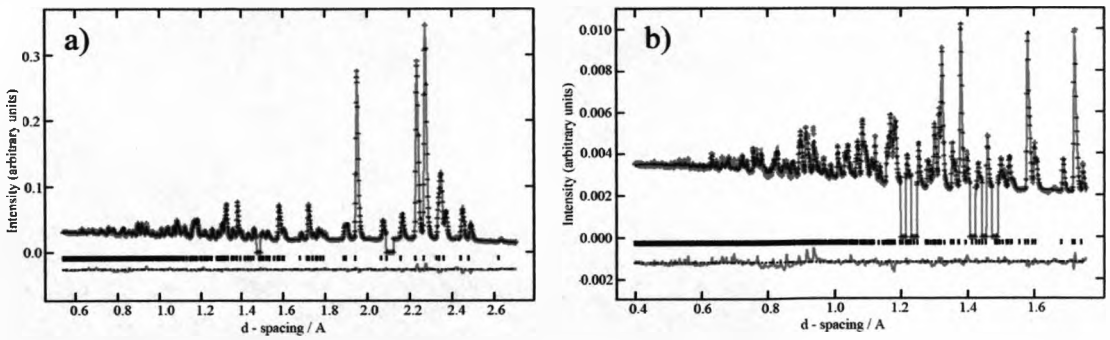

Figure 3.13: *Rietveld Refinement of powder neutron diffraction data for the ceramic sample of* $Bi_2Mn_{4/3}Ni_{2/3}O_6$ *collected at 250°C on GEM against the Pnma model. The red crosses are observed data, the solid green line is the calculated pattern and the pink line is the difference, figure a) is the 90° bank and figure b) is the back scattering 154° bank.*

(χ^2 *= 21.14, wRp = 3.33%, Rp =2.46%)*

Vanadium peaks (from the sample container) in the region of ~2.10, ~1.48, and ~1.23 Å have been excluded. Peaks due to the sample environment (furnace) in the region of ~1.45, ~ 1.42 and ~1.2 Å have also been excluded in bank 6.

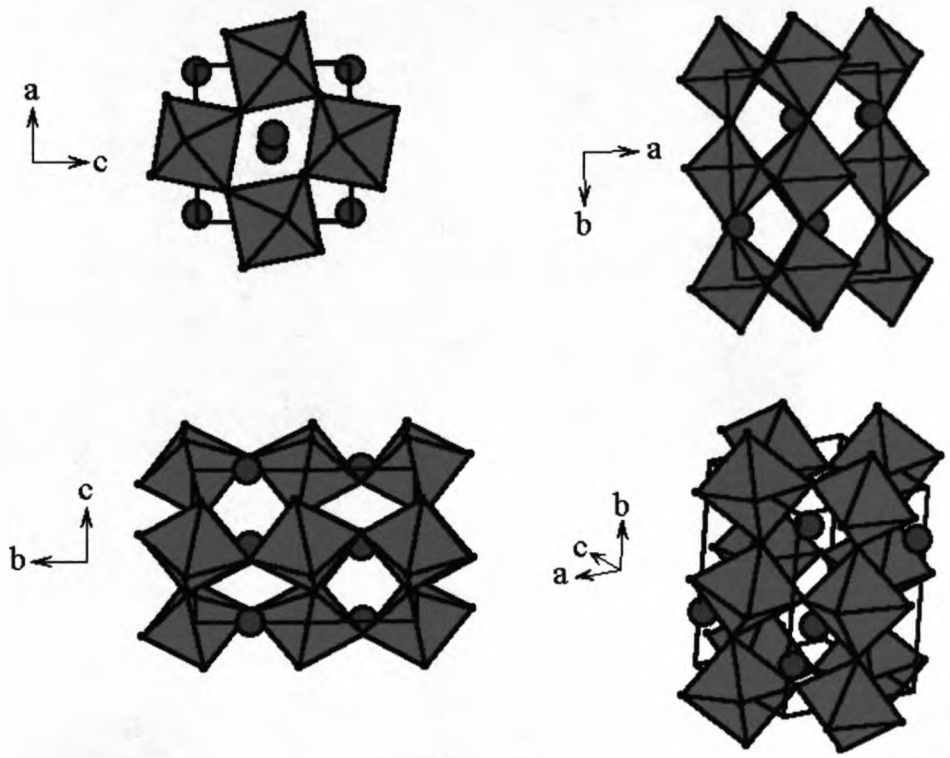

Figure 3.14: *Refined structure of $Bi_2Mn_{4/3}Ni_{2/3}O_6$ obtained from the GEM data collected at 250°C viewed along the different planes. Blue spheres are Bi, purple octahedra containing randomly 33% Mn^{4+}, 33% Mn^{3+}, 33% Ni^{2+} surrounded by oxygen.*

Atom	Occupancy	x	y	z	Uiso
Bi1	1	-0.04709(14)	0.25	0.00375(18)	0.0196(3)
Mn1	0.667	0	0	0.5	0.0645(23)
Ni1	0.333	0	0	0.5	0.0645(23)
O1	1	0.52561(19)	0.25	-0.08342(21)	0.0172(4)
O2	1	0.29762(15)	-0.03810(11)	0.70011(16)	0.0230(5)

Table 3.11: *Refined atomic co-ordinates obtained from the Rietveld refinement of the GEM data collected at 250°C for the ceramic sample of $Bi_2Mn_{4/3}Ni_{2/3}O_6$*

	Atom Bonds	Bond Length (l_i) / Å	Bond Valence Sum, v_i (expected oxidation state)
Bi	Bi – O1	2.4353 (11)	**2.707 (3+)**
	Bi – O1	3.2363 (11)	
	Bi – O1	2.3249 (15)	
	Bi – O1	3.1828 (11)	
	Bi – O2 (x2)	2.4125 (11)	
	Bi – O2 (x2)	2.7008 (11)	
	Bi – O2 (x2)	2.6527 (10)	
$Mn_{2/3}$	Mn1 – O2 (x2)	2.00743 (27)	**3.032 (3.5+)**
	Mn1 – O2 (x2)	2.0109 (8)	
	Mn1 – O2 (x2)	2.0088 (8)	
$Ni_{1/3}$	Ni1 – O2 (x2)	2.00743 (27)	**2.298 (2+)**
	Ni1 – O2 (x2)	2.0109 (8)	
	Ni1 – O2 (x2)	2.0088 (8)	

Table 3.12: *Selected bond lengths and Bond Valence Sums[13] obtained from the GEM data collected at 250°C.*

3.3.5 Transmission Electron Microscopy

Samples for transmission electron microscopy (TEM) were prepared by crushing the powder in n-butanol and the small crystallites in suspension were deposited onto a holey carbon film, supported by a copper grid. The electron diffraction (ED) study was carried out by Dr. Mathieu Allix using a JEOL 2000FX electron microscope equipped with an EDAX analyser. Energy dispersive spectroscopy (EDS) analyses were systematically carried out during the ED study.

The electron diffraction study at room temperature was not of high enough resolution to observe the modulation, but supported the original conclusion of the

polar space group $Pn2_1m$ and the cell parameters $a \approx \sqrt{2}a_p$, $b \approx 2\sqrt{2}a_p$ and $c \approx 4a_p$. High temperature electron diffraction was also carried out on this material, this also confirmed the Pnma space group and lattice parameters concluded from the powder diffraction refinement.

3.3.6 Magnetic Measurements

Magnetic susceptibility data were collected using a Quatum Design MPMS SQUID magnetometer. Each sample was loaded at room temperature and cooled in the absence of an applied field to 2K. A field of 100Oe was then applied and measurements were recorded between 2 and 300K, this system was then cooled again to 2K in the applied field and the measurements between 2 and 300K were repeated.

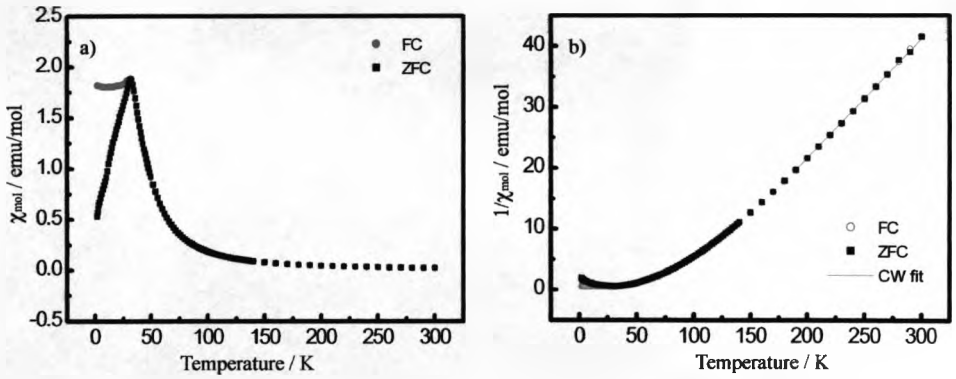

Figure 3.15: *ZFC-FC data collected on $Bi_2Mn_{4/3}Ni_{2/3}O_6$ (crystal sample) at 100Oe. The plots show that the magnetic ordering temperature is ~ 35K. Curie-Weiss fitting (150 – 300K) of the inverse chi reveals a Curie constant of 5.1emu/mol and a positive Weiss constant (θ = 89.7K) implying ferromagnetic exchange.*

The magnetic susceptibility *(figure 3.15)* showed a divergence between the zero-field-cooled and the field-cooled data at 35K. This was taken as the magnetic freezing temperature of the sample, above this value (between 200 and 300K) the data was fitted by the simple Curie-Weiss equation:

$$\chi(T) = C / (T - \theta)$$

The Curie constant (C) was fitted to 5.1 emu/mol and the corresponding effective magnetic moment was calculated ($\mu_{eff} = (8C)^{1/2}$) as 6.39μ_B/mol. The expected effective magnetic moment was calculated from the electronic configuration of the magnetic ions present $\frac{2}{3}Ni^{2+}$, $\frac{2}{3}Mn^{3+}$ and $\frac{2}{3}Mn^{4+}$ ($\mu_{eff} = [n(n+2)]^{1/2}$, *where* n = *number of unpaired electrons*) as 5.60μ_B/mol. This is lower than the actual observed moment and could be due to a number of factors, either the oxidation states of the magnetic ions present in the material are incorrect or the material simply was not in the Curie Weiss region between 150 and 300K. If the oxidation states within the sample were incorrect, such as only Mn^{3+} was present then the effective magnetic based on $\frac{4}{3}Mn^{3+}$ and $\frac{2}{3}Ni^{2+}$ is expected to be 6.11μ_B/mol, again this is lower than the observed value for the $Bi_2Mn_{4/3}Ni_{2/3}O_6$ material. Also when comparing the observed effective moment with that of similar materials such as $Bi_2(Mn^{4+})(Ni^{2+})O_6$ μ_{eff} = 4.1μ_B/mol[2], $Bi(Mn^{3+})O_3$ μ_{eff} = 4.79μ_B/mol[15], $Bi(Ni^{2+})O_3$ μ_{eff} = 2.90μ_B/mol[16] and $La_2(Mn^{4+})(Ni^{2+})O_6$[17] μ_{eff} = 5μ_B/mol, all have lower values than that observed for the $Bi_2Mn_{4/3}Ni_{2/3}O_6$ material. This leads to the conclusion that this material is simply not in the Curie Weiss region between 150 and 300K, explaining the inconsistencies between the observed and expected values.

DC magnetization hysteresis loops were recorded *(figure 3.16)* with a field sweep between 0 and 5.5T at 2, 25, 60 and 300K. The 300K data revealed that the material was paramagnetic at room temperature. A maximum magnetic moment of 3.55 μ_B/mol was observed in the 2K data, however saturation of the sample was not achieved by a field of ±5.5T.

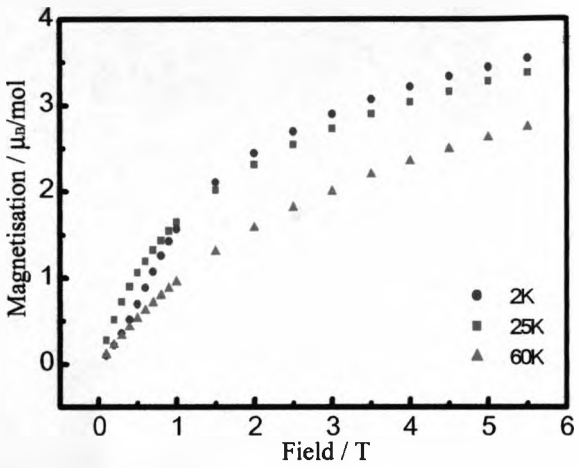

Figure 3.16: *Magnetization of $Bi_2Mn_{4/3}Ni_{2/3}O_6$ collected at 2K, 25K, and 60K. Shows that as the temperature is increased the ordering within the sample decreases.*

Although the zero-field-cooled-field-cooled data implied that the material was becoming ferromagnetically ordered below 35K, no extra Bragg scattering was observed in the neutron diffraction data below this temperature *(section 3.3.3)*, which means that there is no long range ferromagnetic ordering present within the sample. To investigate what was occurring at the transition temperature AC susceptibility data was recorded over a 1 to 1000Hz frequency range with an AC driving field of 1Oe *(figure 3.17)*. The frequency dependency of the maxima in the susceptibility data indicated that the transition at 35K was due to spin glass

freezing[18,19] rather than long range magnetic ordering. Spin glass freezing, as discussed in *Chapter One*, means magnetic ordering occurs only over a very small range (within a few atoms).

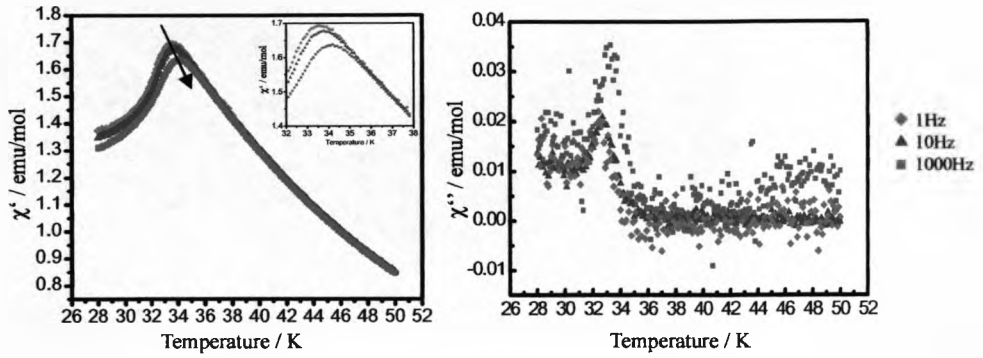

Figure 3.17: *Frequency dependence of the ac susceptibility of $Bi_2Mn_{4/3}Ni_{2/3}O_6$ shows that the transition at 35K is due to spin glass freezing. Plots of the real (left) and imaginary (right) components are given.*

The spin glass nature of the material was confirmed by the displaced nature of a DC magnetization hysteresis loop (field sweep between ±1T) that was recorded on the crystal sample at 2K after cooling from 300K in a field of 1T.

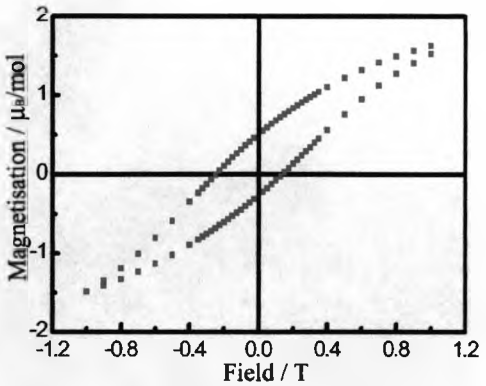

Figure 3.18: *Field dependence of the dc magnetization at 2K collected on the crystals after cooling in a 1T field.*

All measurements were carried out on both the ceramic and crystal $Bi_2Mn_{4/3}Ni_{2/3}O_6$ samples. However the data obtained from the crystal sample were regarded as the most accurate as the crystal sample contained the least amount of trace impurities. As a result all figures quoted have been calculated from the crystal data set. All samples were measured inside a gelatine capsule that was fixed to the midpoint of a straw. Ceramic samples were measured in the form of pressed pellets that were fixed into place by inverting the capsule, crystals were measured in the same way however they were held in place using vacuum grease to prevent them spinning in the applied field. The diamagnetic correction for this sample was calculated as 1.427×10^{-4} emu/mol and was subtracted from all data recorded.

3.3.7 Muon Spin Relaxation

Prof. Stephen Blundell at the University of Oxford carried out zero-field muon spin relaxation (ZF-μ^+SR) measurements on the ceramic sample of $Bi_2Mn_{4/3}Ni_{2/3}O_6$ using the MuSR instrument at the ISIS Pulsed Muon facility, Rutherford Appleton Laboratory, U.K., using a closed-cycle refrigerator. The samples were wrapped in silver foil and mounted on a silver sample holder.

In a μ^+SR experiment[20] a beam of spin-polarized positive muons are targeted at the sample, the muons become implanted within the sample and occupy interstitial positions within the crystal structure with their spins all pointing in the forward direction. Whilst sat here the muon relaxes and precesses, the rate at which it does this is known as the relaxation rate. This can be tracked by measuring the direction of its polarization and can provide information on the

magnetic field of sample. What is actually measured is the direction in which the muon decays; a muon has a lifetime of 2.2 μs, when it decays into two neutrinos and a positron. The positron is emitted instantaneously along the direction of the muon spin. Recording the time dependence of the direction of positron emissions allows determination of the muon polarization, and so the relaxation and precession of the muon spin.

Positrons are detected by detectors forward (F) and backward (B) of the initial muon polarization direction, the number of positrons detected in the two detectors as a function of time following the muon implantation (NF(t) and NB(t)) are recorded. These values are then used to calculate the decay positron asymmetry (A(t)), which is directly proportional to the average spin polarization of the muons stopping within the sample.

$$A(t) = \frac{N_F(t) - \alpha_{exp} N_B(t)}{N_F(t) + \alpha_{exp} N_B(t)}$$

(α_{exp} is an experimental calibration constant and A(t) is the asymmetry of the muon decay at time)

Muon data was collected on $Bi_2Mn_{4/3}Ni_{2/3}O_6$ at six temperatures. The initial asymmetry (measured at t=0) corresponds to ~27%, which is the theoretical maximum value expected for the geometry of detectors in this spectrometer. At high temperature (300K) the relaxation of the muon spin can be seen to follow simple exponential behavior *(figure 3.19(a))* this is indicative of paramagnetism. However as the sample was cooled, the paramagnetic spin fluctuations slow down providing less resistance to the muon relaxing, so causes an increase in the

muon-spin relaxation rate and so a decrease in the muon polarization within the sample. This can be seen on *figure 3.19(a)* by the asymmetry decreasing with temperature. Below ~40 K, the initial asymmetry falls sharply and the relaxation rate decreases. This can be explained by magnetic order developing in the sample and leading to an internal field at the muon site which causes muon precession faster than $1/t_{pulse}$, where t_{pulse}~70 ns and is not directly observable at ISIS. The temperature dependency of the initial muon polarization (*figure 3.19(b)*) shows a transition from an ordered phase where the initial polarization is 0% to a paramagnetic phase at 37K when the initial polarization is 100%.

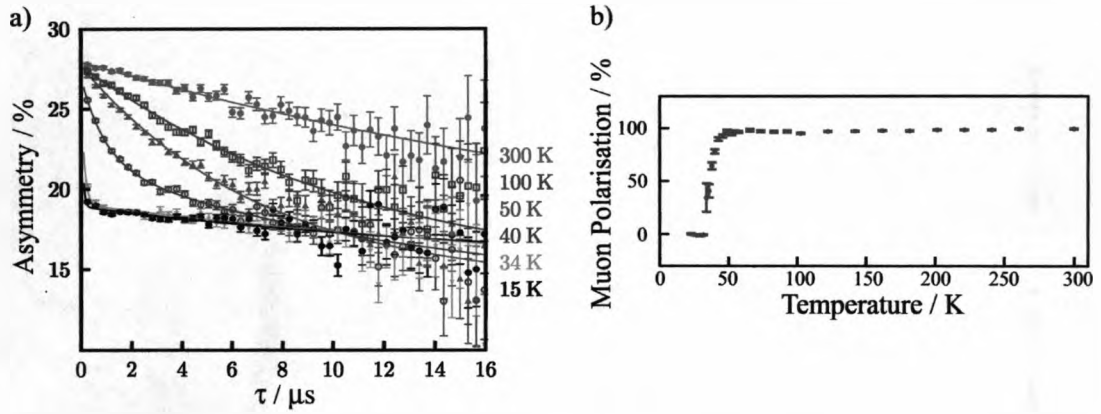

Figure 3.19 a): *Muon asymmetry data for a polycrystalline sample of $Bi_2Mn_{4/3}Ni_{2/3}O_6$ as a function of time for six selected temperatures. The data do not relax to 0% asymmetry due to a substantial contribution from muons stopping in the sample holder and cryostat tails*

Figure 3.19 b): *The initial normalised muon polarization of $Bi_2Mn_{4/3}Ni_{2/3}O_6$ as a function of temperature. (normalization has been carried out to display the percentage of muons not coupled to a static, ordered local field, therefore 0% in the ordered phase and 100% in the paramagnetic phase)*

3.3.8 X-ray absorption spectroscopy (XAS)

XAS was carried out on station 7.1 at the SRS. Data was recorded on samples at room temperature across the Mn and Ni K edge in ~ 0.5eV steps, Mn and Ni metal K edges were collected simultaneously as a form of energy calibration. All samples were recorded in transmission mode, $BiMnO_3$, La_2MnNiO_6, La_2NiO_4 and $LaSrNiO_4$ were all run as Mn^{3+}, Mn^{4+}, Ni^{2+} and Ni^{3+} standards respectively.

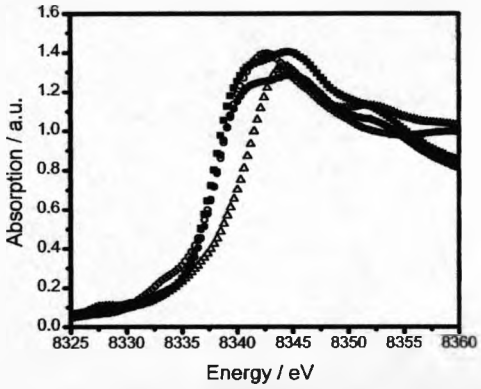

Sample	*Edge Position / eV*
La_2NiO_4 (Ni^{2+} Standard)	*8338.65*
$LaSrNiO_4$ (Ni^{3+} Standard)	*8340.51*
Ceramic $Bi_2Mn_{4/3}Ni_{2/3}O_6$ sample	*8338.65*
Crystal $Bi_2Mn_{4/3}Ni_{2/3}O_6$ sample	*8338.65*

***Figure 3.20**: X-ray absorption spectroscopy collected across the Ni K edge in ~ 0.5eV steps. The edge positions calculated for each of the samples are given in the table.*

(Closed squares: Ceramic $Bi_2Mn_{4/3}Ni_{2/3}O_6$ sample; Closed circles: Crystal $Bi_2Mn_{4/3}Ni_{2/3}O_6$ sample; Open circles: Ni^{2+} standard (La_2NiO_4); Open triangles: Ni^{3+} standard ($LaSrNiO_4$))

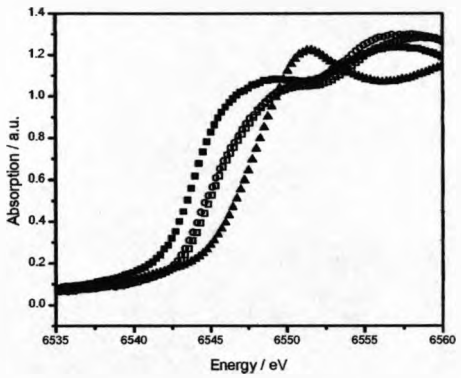

Sample	*Edge Position / eV*
$BiMnO_3$ (Mn^{3+} Standard)	*6543.99*
La_2MnNiO_6 (Mn^{4+} Standard)	*6548.62*
Ceramic $Bi_2Mn_{4/3}Ni_{2/3}O_6$ sample	*6545.35*
Crystal $Bi_2Mn_{4/3}Ni_{2/3}O_6$ sample	*6545.95*

***Figure 3.21**: X-ray absorption spectroscopy collected across the Mn K edge in ~ 0.5eV steps. The edge positions calculated for each of the samples are given in the table.*

(Open squares: Ceramic $Bi_2Mn_{4/3}Ni_{2/3}O_6$ sample; Open circles: Crystal $Bi_2Mn_{4/3}Ni_{2/3}O_6$ sample; Closed squares: Mn^{3+} standard ($BiMnO_3$); Closed Triangles: Mn^{4+} standard (La_2MnNiO_6))

The XAS results show that the absorption edge of the nickel in both the ceramic and crystal samples and the 2+ standard are at the same energy. This suggests that the nickel in the $Bi_2Mn_{4/3}Ni_{2/3}O_6$ sample is in the 2+ oxidation state. The manganese edge XAS shows that the absorption edges of the ceramic and crystal samples occurs half way between the edges of the 4+ and 3+ standards, this would imply that there are two manganese sites present within the material giving an average oxidation state of 3.5+. This results in an overall charge balanced composition of $(Bi^{3+})_2(Mn^{4+})_{2/3}(Mn^{3+})_{2/3}(Ni^{2+})_{2/3}(O^{2-})_6$.

3.3.9 Dielectric Measurements

A.C. impedance data were collected with the assistance of Dr. Xiaojun Kuang using a Solatron 1255B Frequency Response Analyzer and a Solatron 1296 dielectric interface over the frequency range of 1-10^6Hz from room temperature to 400°C (*Figure 3.22*). Silver paste electrodes were thermally treated at 400°C for ~30 minutes before the measurement began. The conductivity at room temperature was measured at ~1 x $10^{-3}\Omega^{-1}cm^{-1}$, this is considered too high to carry out any conclusive ferroelectric tests.

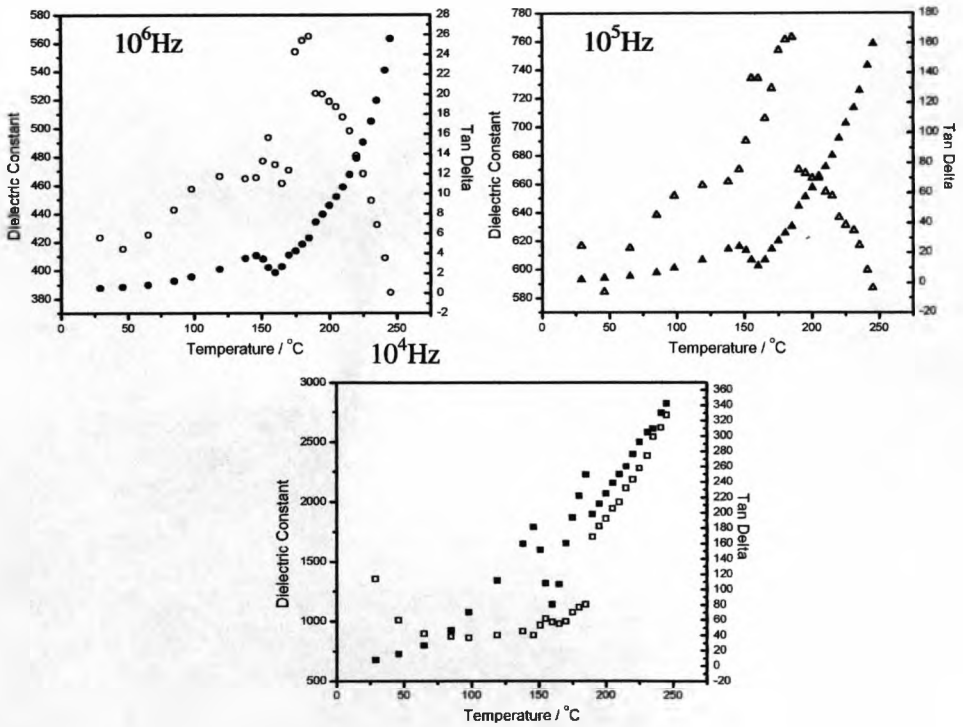

Figure 3.22: *Temperature dependencies of the dielectric constant and Tan Delta at selected frequencies. Open data points are the dielectric constants and closed data points are the tan delta data points*

The temperature dependence of the dielectric constant shows a maximum in the temperature region of ~200°C, this suggests that the sample is undergoing a ferroelectric-like transition. This transition is supported by the fact that the sample undergoes a structural transition from the room temperature modulated structure to one refined in a non-polar space group.

The material was also sent off to Professor P. Shiv Halasyamani at the University of Houston, Texas, USA for Second Harmonic Generation (SHG)[21] testing. The appearance of the phenomena SHG can be used to determine whether the material is non-centrosymmetric and so whether it is likely to be a ferroelectric. SHG is defined as the conversion of a specific wavelength of light into half its original, this occurs as a direct result of the polarisation in the material. A beam of light from a Nd-YAG laser (1064nm) is applied to the sample, if SHG occurs a green light (~500nm) will be emitted from the sample. Unfortunately the result came back negative for SHG suggesting that the material is not polarised at room temperature. Although many factors could have caused this negative result, the most likely explanation is that the modulation in the material cancels out any polarity as already discussed in *section 3.3.2.*

3.3.10 High Pressure Treatment of Ceramic Sample

A small amount of the ceramic sample was taken and placed inside a Pt lined Al_2O_3 crucible encased in a cylindrical graphite furnace. This assembly was then set in a magnesia based cast octahedra and loaded into a Walker-type multianvil press. The pressure was then increased to 6GPa and held for an hour. The sample

was then heated to 700°C for 30minutes. X-ray powder diffraction data confirmed that the sample had not changed structure. However magnetization measurements did reveal an increase in the magnetization of the sample.

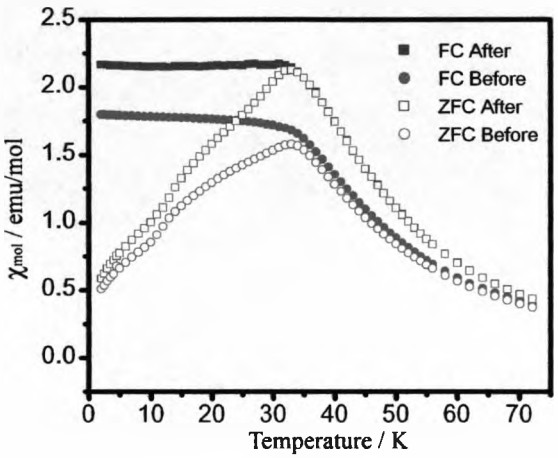

Figure 3.23: *ZFC-FC data collected at 100Oe on $Bi_2Mn_{4/3}Ni_{2/3}O_6$ before and after treatment at 700°C for 30 minutes at 6GPa. An increase in the magnetization can be seen after the high pressure treatment.*

AC susceptibility data was collected on the material before and after the high pressure treatment to investigate the effect this had on the nature of the magnetic ordering and determine whether the pressure had increased the level of long range ordering within the material. As many of the bismuth based perovskites formed under high pressure are ordered, it was thought that by putting the $Bi_2Mn_{4/3}Ni_{2/3}O_6$ material under pressure may induce ordering within the sample. However both the before and after samples exhibited the same frequency dependent maxima at the ordering temperature, suggesting that both only have short range magnetic ordering and are spin glass materials. Therefore, the

pressure treatment appears to have not induced any further ordering within the sample, only increasing the magnetization of the material.

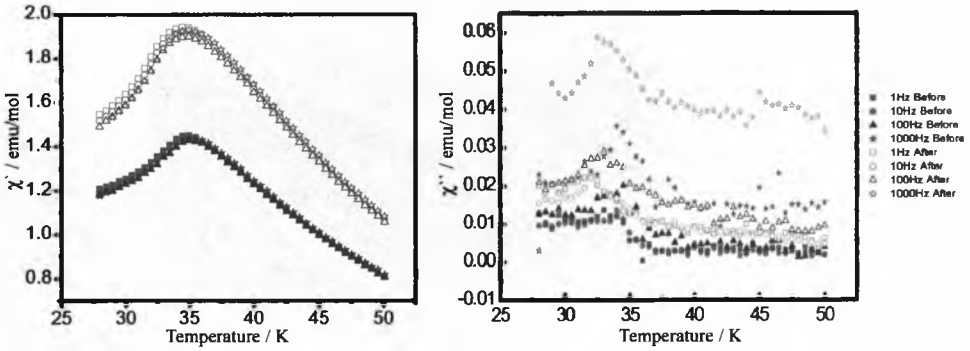

Figure 3.24: *AC susceptibility of $Bi_2Mn_{4/3}Ni_{2/3}O_6$ before and after treatment at 700°C for 30 minutes at 6GPa, plots of the real (left) and imaginary (right) components are given.*

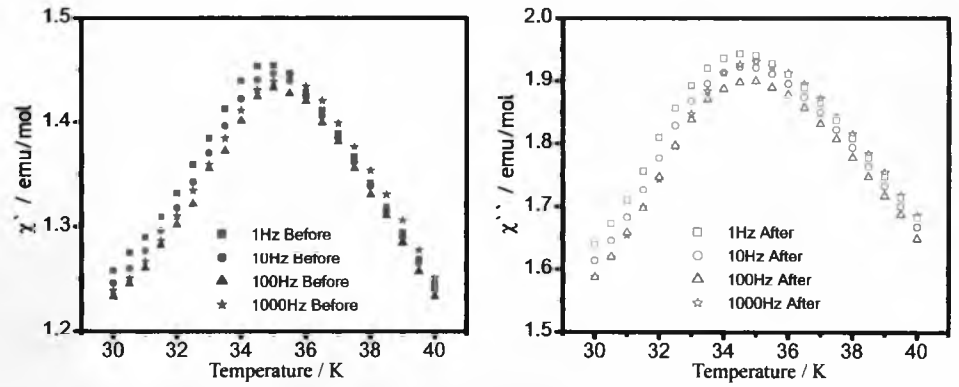

Figure 3.25: *Plots of the AC susceptibility of $Bi_2Mn_{4/3}Ni_{2/3}O_6$ before (left) and after (right) treatment at 700°C for 30 minutes at 6GPa.*

3.3.11 Slow Cooling Treatment of Ceramic Sample

A ceramic sample was prepared as detailed in *section 3.2.1.* However for the final step of heating at 850°C for 12 hours a cooling rate of 1°C per minute was

used instead of 10°C per minute. This was with the aim to see if slow cooling increased the magnetic ordering within the sample. ZFC-FC measurements using a field of 100Oe were carried out on a standard cooled sample and a slow cooled sample.

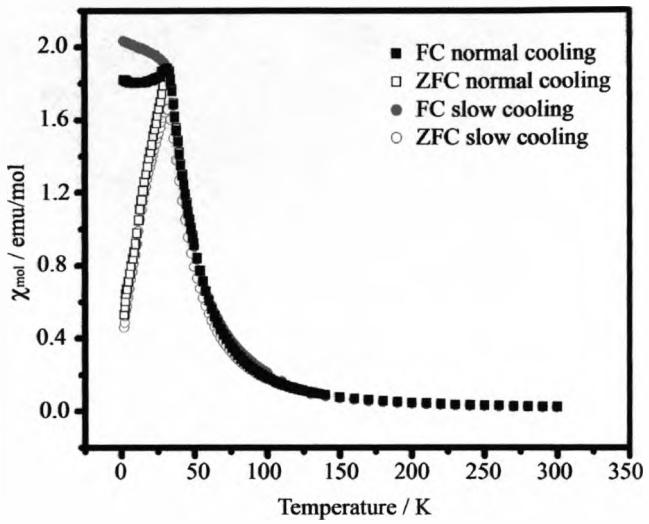

Figure 3.26: *ZFC-FC data collected at 100Oe on $Bi_2Mn_{4/3}Ni_{2/3}O_6$ after normal cooling from 850°C at 10°C per minute and after slow cooling from 850°C at 1°C per minute.*

The results clearly indicate that slow cooling during the synthetic procedure has no effect on the magnetism. This is in contrast to the effect of pressure on the material which causes an increase in the magnetisation of the material *(section 3.3.8).*

3.4 Discussion

3.4.1 Room Temperature Structure

Refinement of single crystal X-ray diffraction data led to the conclusion that the $Bi_2Mn_{4/3}Ni_{2/3}O_6$ material exhibited a unit cell $\sqrt{2}a_p$ x $2\sqrt{2}a_p$ x $4a_p$ structure described in the polar space group $Pn2_1m$. The structure is perovskite based with bismuth on the A-site and a random distribution of Mn^{4+}, Mn^{3+} and Ni^{2+} on the B-site inside the oxygen octahedra. Powder neutron diffraction data was also collected and the refinement supported the single crystal structural model, with a polarisation of 59.7μC/cm^2.

When the refinement was carried out on the high resolution x-ray powder diffraction data collected, a misfit was observed on the low angle region suggesting that the material may be modulated. The incommensurate structure was refined using a Ibmm fundamental cell $\sqrt{2}a_p$ x $2a_p$ x $\sqrt{2}a_p$ with the modulation vectors q_1 = (0.4911(2), 0 ,0) and q_2 = (0, -0.5015(3), 0). This produced a structure which was similar to the commensurate structure, the modulation occurred mainly along the a-direction. Polarisation calculations were carried out on the refined modulated structure. This was because the incommensurate structure does not, by definition, have a single classical unit cell the calculation requires generation of the supercell, as the size of this cell increases, the calculated polarisation decreases. This indicates that the incommensurate modulation cancels out the polarisation caused by the distortion around Bi, producing a non-polar material. The absence of polarisation in the refined structure is consistent with dielectric measurements which were

inconclusive for ferroelectricity and an inactive Second Harmonic Generation (SHG) result. The oxidation state of Ni in $Bi_2Mn_{4/3}Ni_{2/3}O_6$ was confirmed by XAS to be +2, this was indicated by the fact that $Bi_2Mn_{4/3}Ni_{2/3}O_6$ and La_2NiO_4 showed an absorption edge at the same energy position. The Mn edge XAS indicated that the oxidation state of Mn in $Bi_2Mn_{4/3}Ni_{2/3}O_6$ was neither 3+ or 4+, supporting the 33% Mn^{3+}, 33% Mn^{4+}, 33% Ni^{2+} conclusion.

3.4.2 High Temperature Structure

As the material was heated it underwent a structural phase transition from the modulated form to a commensurate structure refined in the non-polar Pnma cell, as indicated by synchrotron powder diffraction. This transition was consistent with the dielectric response which indicated a phase transition in this temperature region.

3.4.3 Magnetic Properties

Magnetic susceptibility measurements recorded in low field indicate a divergence between the Zero-Field-Cooled and Field-Cooled magnetisation below 35K. Variable temperature neutron diffraction data recorded above and below this transition revealed no extra scattering, suggesting the transition was not due to a magnetically ordered state but rather to a spin glass-like state. This is consistent both with the frequency dependence of the AC susceptibility data and the displaced nature of the M(H) loop measured after field cooling in 1T through the transition. The high field M(H) data do not saturate but approach a value of 1.77μ_B per site, which is considerably less than the 2.80μ_B per site expected value for fully ferromagnetic coupling.

The raw muon data collected on $Bi_2Mn_{4/3}Ni_{2/3}O_6$ at six temperatures showed that as the temperature decreased the relaxation rate of the sample increases rapidly due to the slowing-down of paramagnetic spin fluctuations. However below ~40 K, the initial asymmetry falls sharply and the relaxation rate decreases, this can be related to the magnetic order which develops in the sample. The temperature dependence of the initial muon polarization also confirms the magnetic transition of 35K.

The high temperature magnetisation data (150 to 300K) was fitted to the Curie-Weiss, a curie constant of 5.1 emu/mol and the corresponding effective magnetic moment of $6.39\mu_B$/mol were calculated. These are considerably higher than the expected values of C = 3.92 emu/mol and μ_{eff} = 5.60 μ_B/mol which are based on $Mn^{4+}/Mn^{3+}/Ni^{2+}$ in the ratio 33%, 33%,33% suggested by the composition. This would suggest that the sample is not in the true Curie-Weiss region between 200 and 300K.

Slow cooling of the material from the synthesis temperature does not change the magnetic response. However treatment of the material under 6 GPa produced a small increase in the magnetisation below ordering temperature.

3.4.4. Summary

In summary this chapter has detailed the synthesis and characterisation of a novel bismuth-base perovskite material under ambient condition, to date only one other type of these materials has been known to be synthesised under these conditions,

$BiFeO_3$[1]. All other materials, such as $BiCoO_3$[22], $BiCrO_3$[23,24], $BiScO_3$[21] and many more have all required high pressure or thin film synthesis. A particularly remarkable observation is the fact that the two end members $BiMnO_3$[15] and $BiNiO_3$[16], and the initial target phase Bi_2MnNiO_6[2] all require high pressure synthesis. The stability of this $Bi_2Mn_{4/3}Ni_{2/3}O_6$ phase is probably due to the presence of the three oxidation states on the b-site of the perovskite.

Initial structural characterisation on this material did suggest that it was polar with a calculated polarisation of $60\mu C/cm^2$, and a ferroelectric like phase transition occurring at ~200°C from a polar to non – polar structure. However negative SHG results and inconclusive dielectric testing put in doubt the polarity at room temperature. Closer inspection of the diffraction data revealed a modulation in the structure that cancelled out the polarisation, therefore ruling out the possibility of this material being a ferroelectric. The structure of this material is based on the perovskite unit cell with Bi^{3+} on the A-site and a random distribution of Mn^{4+}, Mn^{3+}, Ni^{2+} on the B-site inside the oxygen octahedra. It is the tilting of these octahedra that causes the distortion from the parent perovskite unit. The modulation occurs due to the movement of the bismuth ions off position creating a wave in the structure along the a and b direction.

The magnetism of this material was also not as straight forward as first thought. The material was shown to have a magnetic ordering temperature of 35K, well below the structural 'ferroelectric' transition at 200°C (473K) unfortunately preventing any coupling between the two. However, neutron diffraction experiments above and below this transition revealed no extra Bragg scattering,

this indicated that below the transition temperature no long range magnetic ordering was present. Further experiments, AC susceptibility and magnetisation runs at 2K after cooling in an applied field, led to the conclusion that the material was a spin glass[18,19] rather than a ferromagnet. This means that there are small pockets (in the range of a few atoms) of ferromagnetic ordering, all arranged randomly throughout the material. This has probably arisen due to the random distribution of Mn^{4+}, Mn^{3+}, Ni^{2+} on the B-site which leads to competing antiferromagnetic couplings which dilutes the ferromagnetic Mn^{4+}- Ni^{2+} interactions.

Despite initial favourable results this material was found not to be polar due to the modulation in the structure and not to be a ferromagnet, but a spin glass, therefore ruling out the possibility of this material being multiferroic. However this is a unique material and did open the door for further exploration of potential multiferroics through substitution on the B-site, which I go on to discuss in later chapters.

3.5 References

(1) Kumar, M. M.; Palkar, V. R.; Srinivas, K.; Suryanarayana, S. V. *Applied Physics Letters* **2000**, *76*, 2764-2766.

(2) Azuma, M.; Takata, K.; Saito, T.; Ishiwata, S.; Shimakawa, Y.; Takano, M. *J. Amer. Chem. Soc.* **2005**, *127*, 8889-8892.

(3) Gabbasova, Z. V.; Kuz'min, M. D.; Zvezdin, A. K.; Dubenko, I. S.; Murashov, V. A.; Rakov, D. N.; Krynetsky, I. B. *Physics Letters A* **1991**, *158*, 491-498.

(4) Kubel, F.; Schmid, H. *Acta Cryst. B* **1990**, *46*, 698-702.

(5) Belik, A. A.; Stefanovich, S. Y.; Lazoryak, B. I.; Takayama-Muromachi, E. *Chem. Mater.* **2006**, *18*, 1964-1968.

(6) Suchomel, M. R.; et.al. *Applied Physics Letters* **2007**, *90*, 112909-112911.

(7) Suchomel, M. R.; et.al. *Chem. Mater.* **2006**, *18*, 4987-4989.

(8) Montanari, E.; Righi, L.; Calestani, G.; Migliori, A.; Giloli, E.; Bolzoni, F. *Chem. Mater.* **2005**, *17*, 1765.

(9) Azuma, M.; Takata, K.; Saito, T.; Ishiwata, S.; Shimakawa, Y.; Takano, M. *J. Amer. Chem. Soc.* **2005**, *127*, 8889-8892.

(10) Bull, C. L.; Gleeson, D.; Knight, K. S. *J. Physics: Condensed Matter* **2003**, *15*, 4927-4936.

(11) Belik, A. A.; Yokosawa, T.; Kimoto, K.; Matsui, Y.; Takayama-Muromachi, E. *Chemistry of materials* **2007**, *19*, 1679-1689.

(12) Ishiwata, S.; Azuma, M.; Takano, M.; Nishibori, E.; Takata, M.; Sakata, M.; Kato, K. *J. Mater. Chem.* **2002**, *12*, 3733-3737.

(13) Brown, I. D. *Chemical Society* **1978**, *7*, 359-376.

(14) Brown, I. D. *Acta Cryst. B* **1985**, *41*, 244-247.

(15) Belik, A. A.; et.al. *J. Amer. Chem. Soc.* **2007**, *129*, 971-977.

(16) Ishiwata, S.; Azuma, M.; Takano, M.; Nishibori, E.; Takata, K.; Sakata, M.; Kato, K. *J. Mater. Chem.* **2002**, *12*, 3733-3737.

(17) Matar, S. F.; Subramanian, M. A.; Villesuzanne, A.; Eyert, V.; Whangbo, M. H. *Journal of Magnetism and Magnetic Materials* **2007**, *308*, 116-119.

(18) Blundell, S. J. *Magnetism in condensed matter*; Oxford University Press: Oxford, 2001.

(19) Mydosh, J. A. *Spin Glasses: an experimental introduction* London, Washington and DC, 1993.

(20) Blundell, S. J. *Contemporary Physics* **1999**, *40*, 175.

(21) Ok, K. M.; Chi, E. O.; Halasyamani, P. S. *Chemical Society Reviews* **2006**, *35*, 710-717.

(22) Belik, A. A.; et.al. *Chem. Mater.* **2006**, *18*, 798-803.

(23) Niitak, S.; et.al. *Solid State Ionics* **2004**, *172*, 557-559.

(24) Belik, A. A.; et.al. *J. Amer. Chem. Soc.* **2006**, *128*, 706-707.

Chapter 4: Synthesis and characterisation of the $Bi_{2-x}La_xMn_{4/3}Ni_{2/3}O_6$ series

4.1 Introduction

This chapter reports on the lanthanum doping study carried out on $Bi_2Mn_{4/3}Ni_{2/3}O_6$ synthesis and characterisations are reported for each of the materials over the full range. This chapter details the effect of lanthanum doping on the structure at variable temperatures through the use of X-ray and neutron powder diffraction data for each of the materials synthesised. The effect of lanthanum doping on the magnetism is also investigated.

The aim of this chapter was to increase the magnetic ordering temperature of the $Bi_2Mn_{4/3}Ni_{2/3}O_6$ material in the attempt to couple the magnetic transition with the structural one. This was with the aim of synthesising a multiferroic material, however as already discussed in *Chapter Three* the structural transition is not ferroelectric as the material is not polar due to a modulation observed with the bismuth ions. Lanthanum was chosen as the dopant on the bismuth site as it is of similar size and electronic configuration. Also it is known to form materials which have high magnetic ordering temperatures. $LaMnO_3$, $LaCrO_3$ and $LaFeO_3$ have antiferromagnetic ordering temperatures of 100, 320 and 750K respectively[1]. The double perovskites $LaFe_{0.5}Cr_{0.5}O_3$[2], $LaMn_{0.5}Rh_{0.5}O_3$[3], La_2MnNiO_6[4] and La_2MnCoO_6[4] have ordering temperatures of T_N = 265K, T_c = 120K, T_c = 280K and T_c = 145K respectively.

4.2 Synthesis

Samples of $Bi_{2-x}La_xMn_{4/3}Ni_{2/3}O_6$ where x = 0, 0.1, 0.3, 0.5, 0.7, 0.8, 0.9, 1, 1.1, 1.2, 1.4, 1.6, 1.9 and 2 were prepared by a standard solid state reaction method on a 0.5g and 5g scale. Stoichiometric quantities of Bi_2O_3 (Alfa 99.9995%), La_2O_3 (Alfa Aesar 99.998%, dried at 1000°C for 24hours), MnO_2 (Alfa Aesar 99.999%) and NiO (Alfa Aesar 99.998%) were ground together in an agate mortar and pestle, and then pelletized. The pellet was placed on platinum foil in an alumina boat (reaction occurs with the boat if this precaution is not taken) and heated stepwise at various temperatures and conditions depending on the La content. *Table 4.1* gives the synthetic conditions of each sample. Heating and cooling rates of 5 and 10°C/minute were used respectively. The material was heated at the stated temperatures for 12 intervals (unless otherwise stated) with grinding and re-pelletizing in-between.

X	Temperatures (°C) of the 12hour (unless otherwise stated) heating intervals
0.1	800, 850, 875, 850, 850
0.3	800, 850, 875, 850, 875, 875
0.5	800, 850, 900, 900, 900
0.7	800, 850, 900, 925, 950
0.8	800, 850, 900, 950, 950, 950
0.9	800, 850, 900, 950, 950, 950
1	800, 850, 900, 950, 950, 950
1.1	800, 850, 900, 950, 950, 950
1.2	800, 850, 900, 950, 950, 1000 (sealed tube, 48hours)
1.5	800, 850, 900, 950, 950, 1000 (sealed tube, 48hours)
1.7	800, 850, 900, 1000 (sealed tube, 48hours)
1.9	800, 850, 900, 950, 950, 1000 (sealed tube, 48hours)
2	800, 850, 900, 1000 (48hours), 1100 (24hours), 1200 (24hours), 1300 (4 days)

Table 4.1: *Synthetic procedures used for each of the samples made in the* $Bi_{2-x}La_xMn_{4/3}Ni_{2/3}O_6$ *series.*

As can be seen from *table 4.1*, samples containing bismuth were only heated to a maximum of 950°C in air; above this the samples were sealed in silica tubes to prevent bismuth loss from the sample. The synthetic procedure for the pure lanthanum material is based on the literature procedure for La_2MnNiO_6[5].

4.3 Characterisation

4.3.1 X-ray and neutron powder diffraction

4.3.1.1 Room temperature X-ray powder diffraction on $Bi_{1.9}La_{0.1}Mn_{4/3}Ni_{2/3}O_6$

X-ray powder diffraction data were collected on station 9.1 of the Daresbury Synchrotron Radiation Source at room temperature. At first the powder pattern appeared to index to the unit cell consistent with $Pn2_1m$, an orthorhombic cell with the parameters $\sqrt{2}a_p$ x $2\sqrt{2}a_p$ x $4a_p$, which was originally thought to be the space group $Bi_2Mn_{4/3}Ni_{2/3}O_6$. However when a Le-Bail fit was carried in GSAS *(figure 4.1 and table 4.2)* using this space group it revealed a misfit on the low angle peaks like in the parent material, which suggested that this substituted material was also modulated.

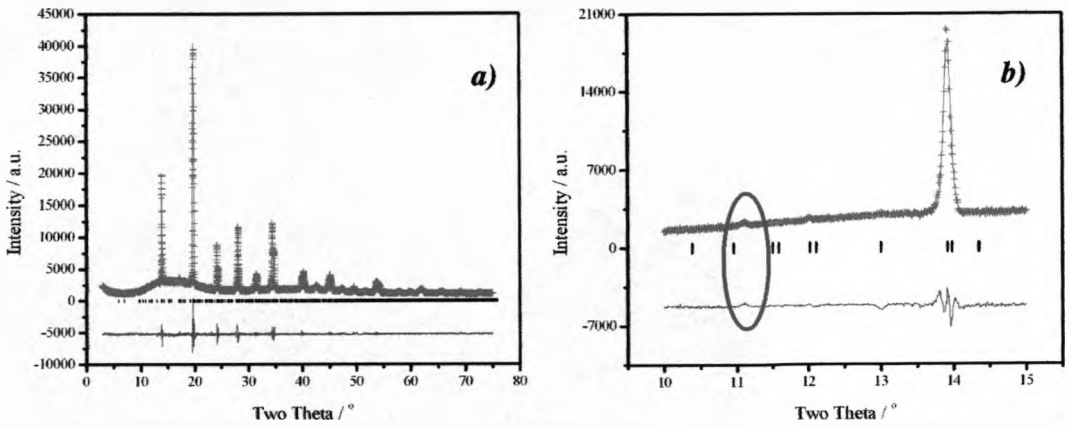

Figure 4.1: *Le Bail fit in the space group $Pn2_1m$ of the XRD data collected at room temperature on Station 9.1 of the Daresbury SRS. The pink crosses are the observed data, green line is the calculated profile, the purple line is the difference plot and the black markers are the Bragg positions. Plot a) is the full diffraction pattern; plot b) is an expanded area of the pattern which highlights the misfit on the low angle peaks due to the modulation.*

Lattice Parameters		Fit Parameters	
Space Group	$Pn2_1m$	R_{wp} / %	5.32
a / Å	5.5746(1)	R_p / %	4.32
b / Å	11.0242(4)	χ^2	3.078
c / Å	15.6043(5)		
Volume / Å^3	958.97(3)		

Table 4.2: *Refined lattice parameters and goodness of fit parameters from the commensurate Le Bail fit carried out on the room temperature powder X-ray diffraction data of $Bi_{1.9}La_{0.1}Mn_{4/3}Ni_{2/3}O_6$.*

The data was then fitted in the same superspace group as for the parent material, Ibmm(q00,0-p0)ss.gm with similar modulation vectors. A LeBail fit was carried out using the program Jana2000, the lattice parameters and modulation vectors obtained

are given in *table 4.3*. A full Rietveld refinement of the modulated structure could not be carried out on this data due to the quality for reliable structural parameters single crystal data would be required. Therefore it must be assumed that the modulated structure of this material is the same as $Bi_2Mn_{4/3}Ni_{2/3}O_6$ as discussed in chapter three, with 5% of the bismuth on the A-site substituted for lanthanum.

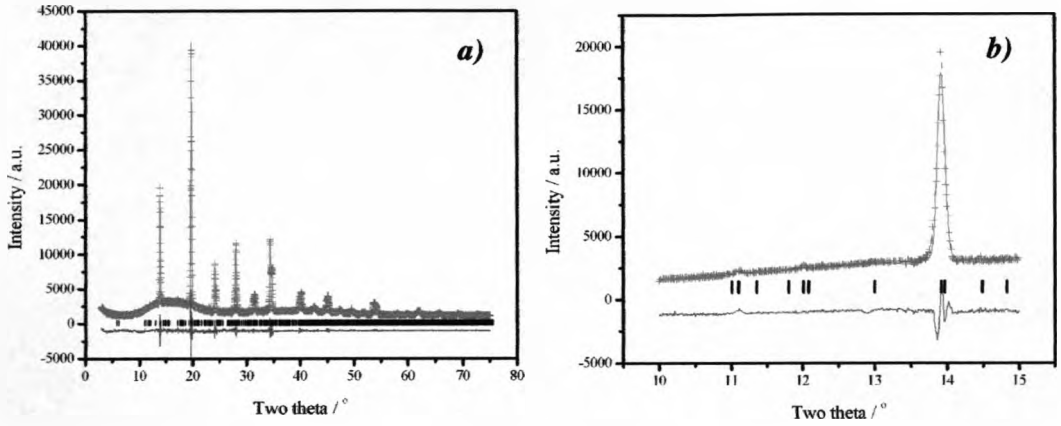

Figure 4.2: *Le Bail fit in the incommensurate model to the XRD data collected at room temperature on Station 9.1 of the Daresbury SRS. The pink crosses are the observed data, green line is the calculated profile, the purple line is the difference plot and the black markers are the Bragg positions. Plot a) is the full diffraction pattern, plot b) is an expanded area of the pattern which highlights the improved fit on the low angle peaks when compared to the commensurate fit.*

	Lattice Parameters			Fit Parameters	
Space Group	Ibmm				
a / Å	5.5740(1)	(q_1, 0, 0)	0.483574	R_{wp} / %	4.62
b / Å	7.8137(2)	(0, q_2 , 0)	-0.574135	R_p / %	3.40
c/ Å	5.5119				

Table 4.3: *Refined lattice parameters and goodness of fit parameters from the incommensurate Le Bail fit carried out on the room temperature powder X-ray diffraction data of* $Bi_{1.9}La_{0.1}Mn_{4/3}Ni_{2/3}O_6$.

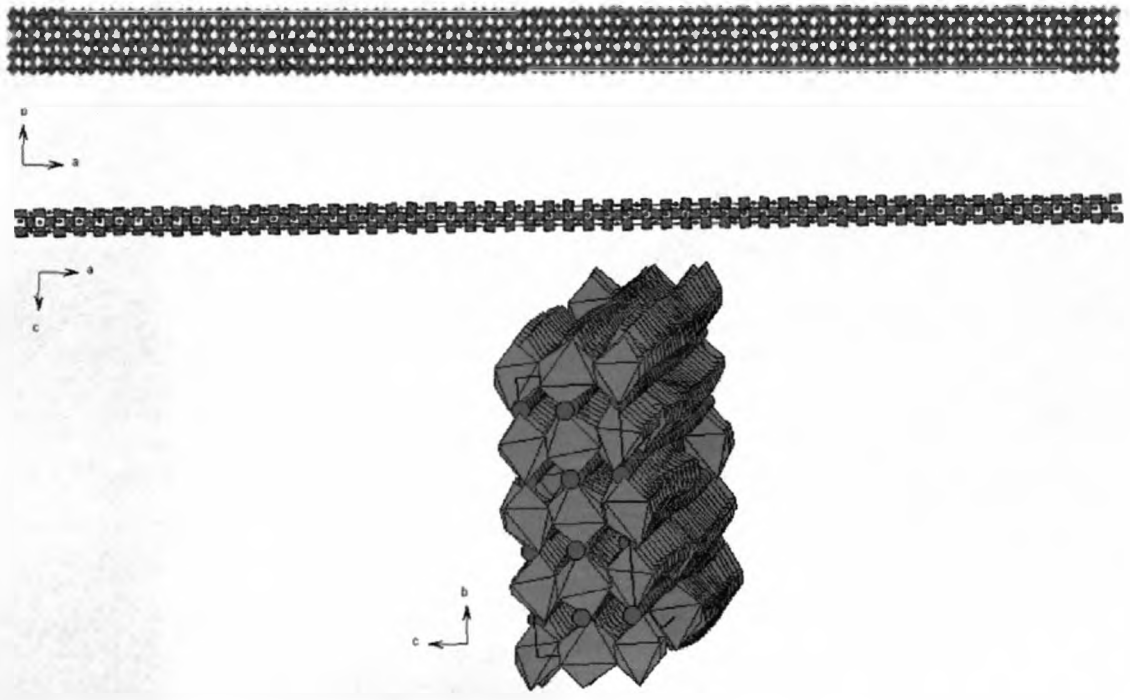

Figure 4.3: *Incommensurate structure of the parent* $Bi_2Mn_{4/3}Ni_{2/3}O_6$ *viewed along the different projections, the modulation can clearly be seen in the blue spheres. It is assumed that the lanthanum doped materials adopted this same structure; blue spheres are the* Bi^{3+} *and* La^{3+} *ions; the purple octahedra contain a random distribution of 33%* Mn^{4+}, *33%* Mn^{3+} *and 33%* Ni^{2+} *ions in the centre with oxygen atoms on the corners.*

4.3.1.2 Variable temperature X-ray and neutron powder diffraction on $Bi_{1.7}La_{0.3}Mn_{4/3}Ni_{2/3}O_6$ and $Bi_{1.5}La_{0.5}Mn_{4/3}Ni_{2/3}O_6$

X-ray powder diffraction data were collected on station 9.1 of the Daresbury Synchrotron Radiation Source between room temperature and 400°C on both the x = 0.3 and 0.5 samples. The room temperature diffraction data for both samples exhibited the same misfit on the low angle peaks when fitted in the commensurate $Pn2_1m$ space group as the x = 0.1 and 0 materials did, therefore profile matching was also carried out in the same superspace group as for the parent material, Ibmm(q00,0-p0)ss.gm. The refined parameters are given in *table 4.4*.

x =	Lattice Parameters				Fit Parameters	
0.3	Space Group	Ibmm				
	a / Å	5.5672(1)	(q_1, 0, 0)	0.486736(8)	R_{wp} / %	4.83
	b / Å	7.7983(1)	(0, q_2 , 0)	-0.570204(2)	R_p / %	3.53
	c/ Å	5.5091(1)				
0.5	Space Group	Ibmm				
	a / Å	5.5634(2)	(q_1, 0, 0)	0.501425(12)	R_{wp} / %	7.28
	b / Å	7.7960(1)	(0, q_2 , 0)	-0.584783(14)	R_p / %	4.79
	c/ Å	5.5151(1)				

Table 4.4: *Refined lattice parameters and goodness of fit parameters from the incommensurate Le Bail fit carried out on the room temperature powder X-ray diffraction data for both* $Bi_{1.7}La_{0.3}Mn_{4/3}Ni_{2/3}O_6$ *and* $Bi_{1.5}La_{0.5}Mn_{4/3}Ni_{2/3}O_6$.

The profile matching refinement carried out on the x = 0.5 material proved slightly unstable and yielded high fit parameters. This could be explained by considering the structure of this material as a mixture of two phases at room temperature, the $Bi_2Mn_{4/3}Ni_{2/3}O_6$ room temperature structure and the commensurate Pnma structure

(high temperature $Bi_2Mn_{4/3}Ni_{2/3}O_6$ structure). In other words, the x = 0.5 sample is in the middle of a structural transition at room temperature. Joint refinement of the two structures proved impossible due to the number of reflections generated from the incommensurate structure. However the x = 0.3 material yielded reasonable fit parameters from the incommensurate fit, suggesting that this sample has the same modulated structure as the $Bi_2Mn_{4/3}Ni_{2/3}O_6$ material at room temperature, with 15% of the bismuth on the A-site substituted for lanthanum.

On heating both samples appeared to undergo the same structural transition as the parent material just at a slightly lower temperature, ~100°C and ~50°C for x = 0.3 and 0.5 respectively, compared to ~ 280°C for the parent material. During heating data were collected over a small angular range in both cases *(figure 4.4)*. In the data for the x = 0.3 sample an extra peak due to the Pnma structure could clearly be seen to grow in as the temperature was increased. However in the x = 0.5 case the extra peak in the Pnma structure is already present and broad, appearing only to sharpen as the temperature is increased and making it difficult to determine the actual transition temperature. This supports the conclusion made from the instability of the room temperature incommensurate refinement that at room temperature the material is a mixture of the two structures.

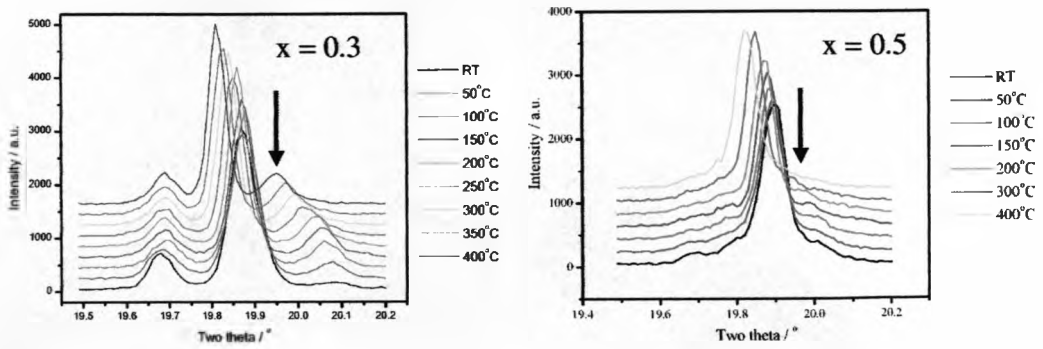

Figure 4.4: *X-ray diffraction patterns collected with increasing temperature. The extra peaks that grew in (or sharpen) as the materials change structure are marked with arrows.*

In both cases powder X-ray data were collected above the transition, Rietveld refinement was carried out on the data using the same centrosymmetric, non-polar space group Pnma model that the high temperature $Bi_2Mn_{4/3}Ni_{2/3}O_6$ phase was fitted in. Fit parameters and bond valence sums confirm that both materials transform into the Pnma structure above 100°C.

$Bi_{1.7}La_{0.3}Mn_{4/3}Ni_{2/3}O_6$ Material at 150°C:

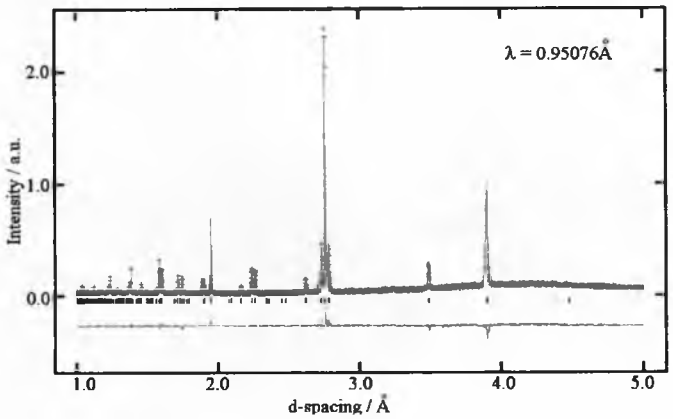

Figure 4.5: *Rietveld refinement of X-ray data against the Pnma model. Red crosses are the observed data, green line is the calculated pattern and the pink line is the difference.*

Lattice Parameters		Fit Parameters	
Space Group	Pnma	R_{wp} / %	8.43
a / Å	5.5625(8)	R_p / %	7.55
b / Å	7.7959(3)	R_f^2 / %	7.53
c / Å	5.4613(9)	χ^2	1.371
Volume / Å^3	236.83(5)		
Density / g cm^{-3}	8.488		

Table 4.5: *Refined lattice parameters and goodness of fit parameters from the Rietveld refinement of the 150°C powder diffraction data for the $Bi_{1.7}La_{0.3}Mn_{4/3}Ni_{2/3}O_6$ material.*

Atom	Occupancy	x	y	z	Uiso
Bi1	0.85	0.04407(18)	0.25	-0.0024(8)	0.0249(14)
La1	0.15	0.04407(18)	0.25	-0.0024(8)	0.0249(14)
Mn1	0.667	0.0	0.0	0.5	-0.0057(15)
Ni1	0.333	0.0	0.0	0.5	-0.0057(15)
O1	1	0.4796(26)	0.25	0.0656(31)	0.0176(29)
O2	1	0.1964(25)	-0.0305(17)	0.7984(24)	0.0176(29)

Table 4.6: *Refined fractional positions from the Rietveld refinement of powder X-ray data collected at 150°C on* $Bi_{1.7}La_{0.3}Mn_{4/3}Ni_{2/3}O_6$.

	Atom Bonds	Bond Length (l_i) / Å	Bond Valence Sum, v_i (expected oxidation state)
$Bi_{0.85}$	Bi – O1	3.160 (14)	2.557 (3+)
	Bi – O1	2.451 (14)	
	Bi – O1	3.093 (18)	
	Bi – O1	2.415 (18)	
	Bi – O2 (x2)	2.586 (15)	
	Bi – O2 (x2)	2.776 (15)	
	Bi – O2 (x2)	2.439 (11)	
$La_{0.15}$	La – O1	3.160 (14)	3.157 (3+)
	La – O1	2.451 (14)	
	La – O1	3.093 (18)	
	La – O1	2.415 (18)	
	La – O2 (x2)	2.586 (15)	
	La – O2 (x2)	2.776 (15)	
	La – O2 (x2)	2.439 (11)	
$Mn_{2/3}$	Mn1 – O2 (x2)	1.984 (32)	3.138 (3.5+)
	Mn1 – O2 (x2)	1.978 (14)	
	Mn1 – O2 (x2)	2.029 (14)	
$Ni_{1/3}$	Ni1 – O2 (x2)	1.984 (32)	2.379 (2+)
	Ni1 – O2 (x2)	1.978 (14)	
	Ni1 – O2 (x2)	2.029 (14)	

Table 4.7: *Selected bond lengths and Bond Valence Sums*[6] *obtained from the Rietveld refinement of powder X-ray data collected at 150°C on* $Bi_{1.7}La_{0.3}Mn_{4/3}Ni_{2/3}O_6$. *(*$BVS = \Sigma^{N}_{i=1}\, v_i$; $v_i = exp[(R_o - l_i)/B]$; $B = 0.37$; $R_o(Bi^{3+}) = 2.094$[7]; $R_o(La^{3+}) = 2.172$[7]; $R_o(Ni^{2+}) = 1.654$[7]; $R_o(0.5Mn^{4+} + 0.5Mn^{3+}) = 1.7565$[7]*)*

$Bi_{1.5}La_{0.5}Mn_{4/3}Ni_{2/3}O_6$ Material at 150°C:

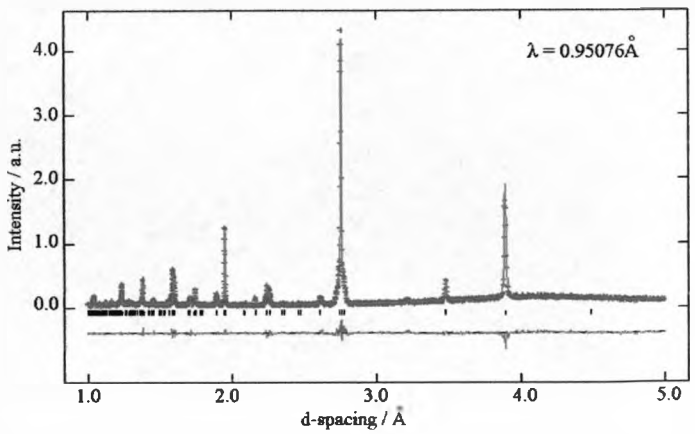

Figure 4.6: *Rietveld refinement of X-ray data against the Pnma model. Red crosses are the observed data, green line is the calculated pattern and the pink line is the difference.*

Lattice Parameters		Fit Parameters	
Space Group	Pnma	R_{wp} / %	8.01
a / Å	5.5424(1)	R_p / %	7.11
b / Å	7.7918(2)	R_f^2 / %	7.27
c / Å	5.4783(2)	χ^2	2.104
Volume / $Å^3$	236.59(7)		
Density / g cm^{-3}	8.300		

Table 4.8: *Refined lattice parameters and goodness of fit parameters from the Rietveld refinement of the 150°C powder diffraction data for the $Bi_{1.5}La_{0.5}Mn_{4/3}Ni_{2/3}O_6$ material.*

Atom	Occupancy	x	y	z	Uiso
Bi1	0.75	0.04078(17)	0.25	-0.0042(7)	0.0243(13)
La1	0.25	0.04078(17)	0.25	-0.0042(7)	0.0243(13)
Mn1	0.667	0.0	0.0	0.5	0.0048(14)
Ni1	0.333	0.0	0.0	0.5	0.0048(14)
O1	1	0.4976(23)	0.25	0.050(5)	0.0215(31)
O2	1	0.2113(30)	-0.0322(20)	0.8035(28)	0.0215(31)

Table 4.9: *Refined fractional positions from the Rietveld refinement of powder X-ray data collected at 150°C on* $Bi_{1.5}La_{0.5}Mn_{4/3}Ni_{2/3}O_6$.

	Atom Bonds	Bond Length (l_i) / Å	Bond Valence Sum, v_i (expected oxidation state)
$Bi_{0.75}$	Bi – O1	3.025 (13)	**2.362 (3+)**
	Bi – O1	2.549 (13)	
	Bi – O1	3.001 (26)	
	Bi – O1	2.499 (26)	
	Bi – O2 (x2)	2.615 (19)	
	Bi – O2 (x2)	2.759 (19)	
	Bi – O2 (x2)	2.458 (12)	
$La_{0.25}$	La – O1	3.025 (13)	**2.917 (3+)**
	La – O1	2.549 (13)	
	La – O1	3.001 (26)	
	La – O1	2.499 (26)	
	La – O2 (x2)	2.615 (19)	
	La – O2 (x2)	2.759 (19)	
	La – O2 (x2)	2.458 (12)	
$Mn_{2/3}$	Mn1 – O2 (x2)	1.9673 (35)	**3.240 (3.5+)**
	Mn1 – O2 (x2)	2.049 (16)	
	Mn1 – O2 (x2)	1.945 (16)	
$Ni_{1/3}$	Ni1 – O2 (x2)	1.9673 (35)	**2.456 (2+)**
	Ni1 – O2 (x2)	2.049 (16)	
	Ni1 – O2 (x2)	1.945 (16)	

Table 4.10: *Selected bond lengths and Bond Valence Sums*[6] *obtained from the Rietveld refinement of powder X-ray data collected at 150°C on* $Bi_{1.5}La_{0.5}Mn_{4/3}Ni_{2/3}O_6$.

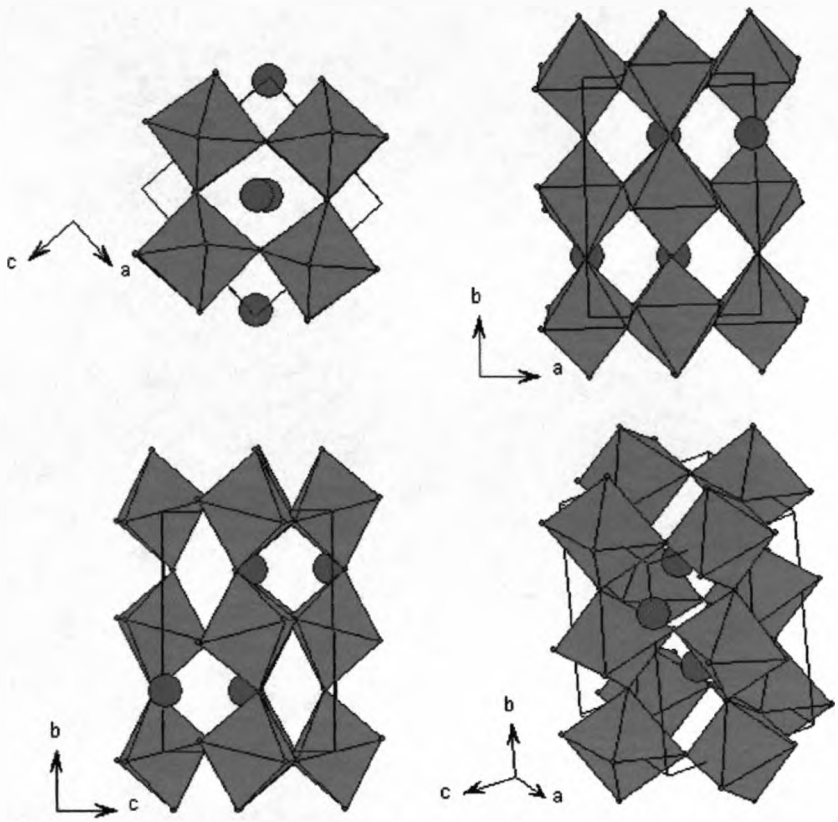

Figure 4.7: *Commensurate Pnma structure of x = 0.3 and 0.5 at 150°C. Blue spheres are the Bi^{3+} and La^{3+} ions; the purple octahedra contain a random distribution of 33% Mn^{4+}, 33% Mn^{3+} and 33% Ni^{2+} ions in the centre with oxygen atoms on the corners.*

Powder neutron diffraction data were also collected on this material at room temperature and 2K on the POLARIS diffractometer at ISIS. The powder patterns of both materials measured at 2K were exactly the same as that recorded at room temperature, suggesting that the materials where in the same structure at 2K as at room temperature. This revealed, that like in the parent case there was no extra Bragg scattering at low temperatures and so like the x = 0 material these substituted materials also contain no long range magnetic ordering.

4.3.1.3 Room temperature X-ray powder diffraction on $Bi_{1.3}La_{0.7}Mn_{4/3}Ni_{2/3}O_6$

X-ray powder diffraction data were collected on station 9.1 of the Daresbury Synchrotron Radiation Source between room temperature on the x = 0.7 sample. The room temperature diffraction data exhibited the same misfit on the low angle peaks when fitted in the $Pn2_1m$ space group as the x = 0.5, 0.3, 0.1 and 0 materials did, therefore profile matching was also carried out in the superspace group as for the parent material, Ibmm(q00,0-p0)ss.gm. The refined parameters are given in *table 4.11.*

	Lattice Parameters			Fit Parameters	
Space Group	Ibmm				
a / Å	5.5696(1)	(q_1, 0, 0)	0.487645(2)	R_{wp} / %	5.20
b / Å	7.7939(2)	(0, q_2 , 0)	-0.600957(1)	R_p / %	3.76
c/ Å	5.5113(1)				

Table 4.11: *Refined lattice parameters and goodness of fit parameters from the profile matching fit carried out using Jana2000 on the room temperature diffraction data on* $Bi_{1.3}La_{0.7}Mn_{4/3}Ni_{2/3}O_6$.

As in the case of the x = 0.5 material this refinement was slightly unstable and produced fit parameters that reflected this. Therefore it can be concluded that this material is also a mixture of the incommensurate and commensurate structures at room temperature. However no variable temperature data were collected on this material as a result only an assumption can be made that on cooling the material goes fully incommensurate and on heating the structure goes fully commensurate.

4.3.1.4 Variable temperature neutron powder diffraction on $Bi_{1.2}La_{0.8}Mn_{4/3}Ni_{2/3}O_6$

Room temperature neutron powder diffraction data were collected on the x = 0.8 material using the POLARIS diffractometer at ISIS. The data was refined using the Pnma model, bond valence sums and fit parameters supported this model, which was also supported by the electron diffraction that was obtained on this sample (*section 4.3.2*).

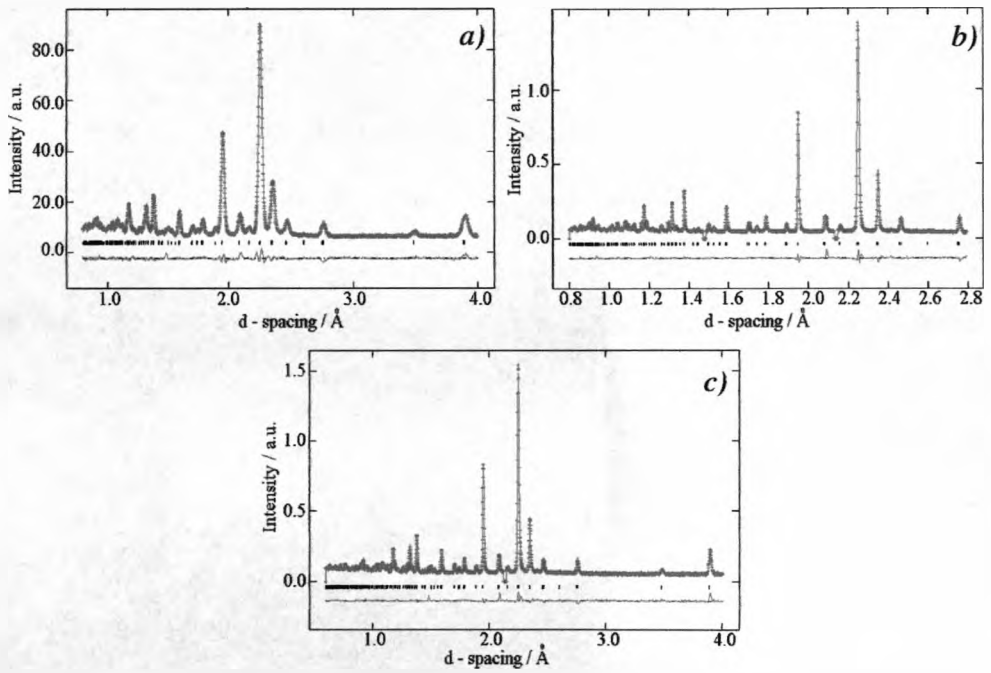

Figure 4.8: *Rietveld Refinement of powder neutron diffraction data collected at room temperature using the POLARIS diffractometer on the x=0.8 material against the Pnma model. The red crosses are observed data, the solid green line is the calculated pattern and the pink line is the difference, figure a) is the low angle bank A, figure b) is the back scattering bank C and figure c) is the 90° bank E.*

Lattice Parameters		Fit Parameters	
Space Group	Pnma		
a / Å	5.5182(8)	R_{wp} / %	3.87
b / Å	7.7889(12)	R_p / %	3.79
c / Å	5.5004(8)	χ^2	5.962
Volume / Å^3	236.41(10)		
Density / g cm^{-3}	8.011		

Table 4.12: *Refined lattice parameters and goodness of fit parameters from the Rietveld refinement of the room temperature neutron powder diffraction data for the* $Bi_{1.2}La_{0.8}Mn_{4/3}Ni_{2/3}O_6$ *material.*

Atom	Occupancy	x	y	z	Uiso
Bi1	0.6	0.02785(18)	0.25	0.0083(4)	0.0145(3)
La1	0.4	0.02785(18)	0.25	0.0083(4)	0.0145(3)
Mn1	0.667	0	0	0.5	0.0459(15)
Ni1	0.333	0	0	0.5	0.0459(15)
O1	1	0.48542(33)	0.25	-0.0696(5)	0.0177(3)
O2	1	0.21368(24)	-0.03943(21)	0.78438(23)	0.0177(3)

Table 4.13: *Refined fractional positions from the Rietveld refinement of the room temperature neutron powder diffraction data collected on the* $Bi_{1.2}La_{0.8}Mn_{4/3}Ni_{2/3}O_6$ *material.*

	Atom Bonds	Bond Length (l_i) / Å	Bond Valence Sum, v_i (expected oxidation state)
$Bi_{0.6}$	Bi – O1	3.0237 (19)	2.564 (3+)
	Bi – O1	2.561 (19)	
	Bi – O1	2.4243 (32)	
	Bi – O1	3.0963 (32)	
	Bi – O2 (x2)	2.7659 (16)	
	Bi – O2 (x2)	2.6516 (15)	
	Bi – O2 (x2)	2.4015 (19)	
$La_{0.4}$	La – O1	3.0237 (19)	3.165 (3+)
	La – O1	2.561 (19)	
	La – O1	2.4243 (32)	
	La – O1	3.0963 (32)	
	La – O2 (x2)	2.7659 (16)	
	La – O2 (x2)	2.6516 (15)	
	La – O2 (x2)	2.4015 (19)	
$Mn_{2/3}$	Mn1 – O2 (x2)	1.9861 (6)	3.198 (3.5+)
	Mn1 – O2 (x2)	1.9828 (14)	
	Mn1 – O2 (x2)	1.9993 (16)	
$Ni_{1/3}$	Ni1 – O2 (x2)	1.9861 (6)	2.424 (2+)
	Ni1 – O2 (x2)	1.9828 (14)	
	Ni1 – O2 (x2)	1.9993 (16)	

Table 4.14: *Selected bond lengths and Bond Valence Sums[6] obtained from the Rietveld refinement of powder neutron data collected at room temperature on* $Bi_{1.2}La_{0.8}Mn_{4/3}Ni_{2/3}O_6$.

As this material was already in the Pnma structure at room temperature, it would suggest that the transition from the incommensurate structure to the Pnma form which has occurred in all previous samples must in this case occur below room temperature. Therefore variable temperature neutron powder diffraction data were collected on the $Bi_{1.2}La_{0.8}Mn_{4/3}Ni_{2/3}O_6$ material between room temperature and 2K on the HRPD diffractometer at ISIS *(figure 4.9)*. However visual inspection of the

data shows only a slight broadening of the main peak in the diffraction pattern with increasing temperature, no extra peaks are seen, this broadening occurs between 200K and 250K suggesting that the material may be undergoing a structural change at this temperature.

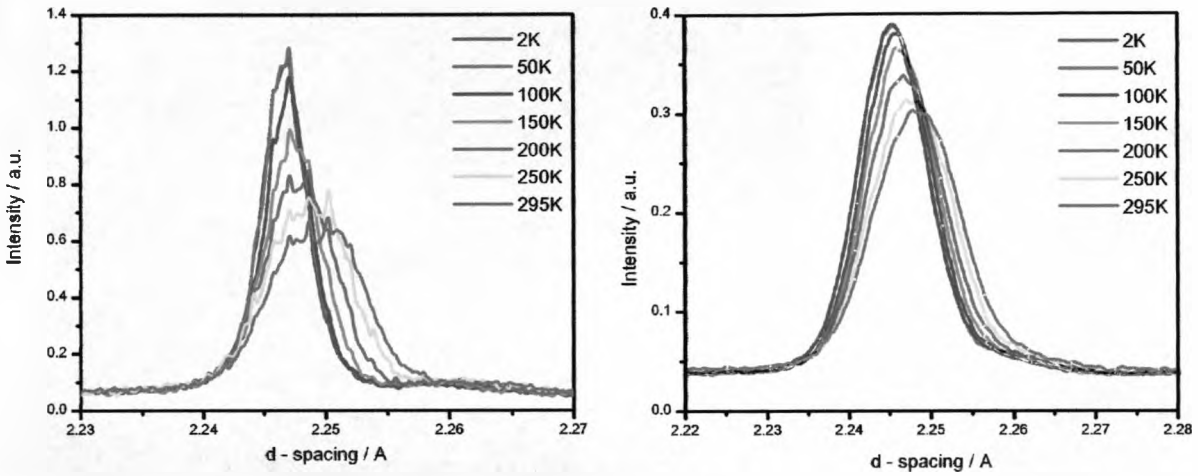

Figure 4.9: *Variable temperature neutron powder diffraction patterns, focused on the main peak of the patterns. a) Pattern collected on the 168.33° detector (bank 1); b) Pattern collected on the 90° detector (bank 2).*

A Le-Bail fit was carried out on the full diffraction pattern at each temperature in the Pnma model. The calculated cell parameters were then converted into their corresponding perovskite unit cell (a_p) values (i.e. $a \sim \sqrt{2}a_p$, $b \sim 2\sqrt{2}a_p$ and $c \sim \sqrt{2}a_p$). The ratio between these values was calculated and plotted as a function of temperature *(figure 4.10)*, the temperature of the structural change can clearly be seen in both the c:a and b:a ratios.

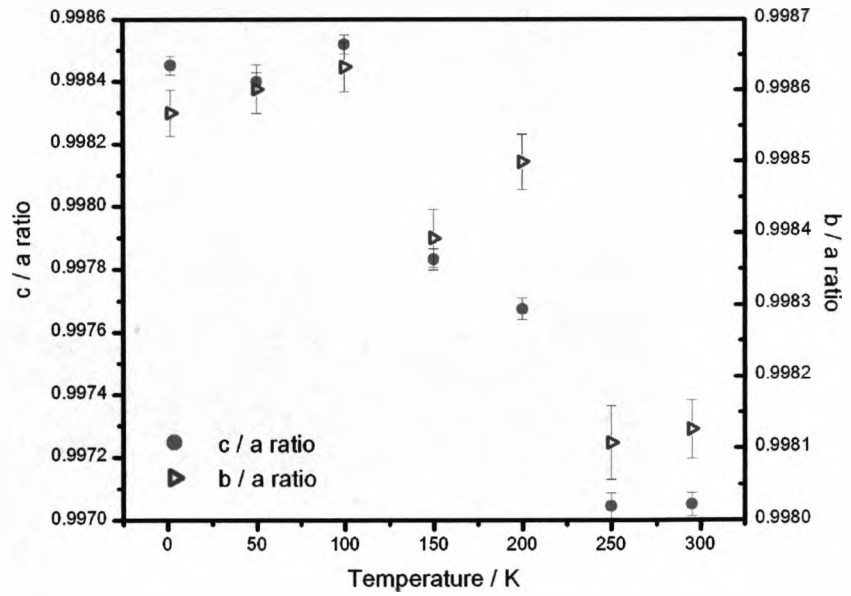

Figure 4.10: *Variation of the perovskite unit cell values with temperature of the* $Bi_{1.2}La_{0.8}Mn_{4/3}Ni_{2/3}O_6$ *material.*

The variation in the cell parameters with temperature suggest that the structure is undergoing a phase transition between 150 and 200K when a mixed structure phase is present, below this (≤100K) the material is in the incommensurate structure and above (≥250K) the material is in the commensurate Pnma form.

The neutron powder diffraction data collected at 2K on the HRPD diffractometer were fitted to the incommensurate pure bismuth room temperature structure using FullProf. The Jana2000 program that had been used to fit all previous samples to the incommensurate structure could not be used as it was not compatible with neutron TOF data. A profile matching fit was carried out to determine the cell parameters and modulation vectors. As in the x = 0 case, the data was fitted with five separate phases, one being the basic structure in the space group Ibmm, and four phases

containing each combination of the two q-vectors used to describe the incommensurate structure, $(q_1,0,0)$, $(0,q_2,0)$, $(q_1,q_2,0)$ and $(q_1,-q_2,0)$. The cell parameters and absolute values of the q-vectors were constrained to be the same in each phase.

	Lattice Parameters			Fit Parameters	
Space Group	Ibmm				
a / Å	5.5047(2)	$(q_1, 0, 0)$	0.51603(5)	χ^2	13.3
b / Å	7.7935(3)	$(0, q_2, 0)$	-0.46584(3)		
c/ Å	5.4785(2)				

Table 4.15: *Refined cell parameters and modulation vectors from the profile matching fit carried out on neutron diffraction data collected at 2K on* $Bi_{1.2}La_{0.8}Mn_{4/3}Ni_{2/3}O_6$.

So, in conclusion this phase is thought to be fully incommensurate at 2K and commensurate at 300K.

4.3.1.5 Variable temperature neutron powder diffraction on $Bi_{1.1}La_{0.9}Mn_{4/3}Ni_{2/3}O_6$

Neutron powder diffraction data were collected on this material at room temperature and 2K on the POLARIS diffractometer at ISIS. The room temperature data was refined in the Pnma model, fit parameters and bond valence sums confirm this structure.

Lattice Parameters		Fit Parameters	
Space Group	Pnma		
a / Å	5.5105(1)	R_{wp} / %	3.97
b / Å	7.7816(2)	R_p / %	3.81
c / Å	5.4994(2)	χ^2	3.626
Volume / Å^3	235.82(3)		
Density / g cm^{-3}	7.933		

Table 4.16: *Refined parameters from the Rietveld refinement of the room temperature neutron powder diffraction data for the* $Bi_{1.1}La_{0.9}Mn_{4/3}Ni_{2/3}O_6$ *material.*

Atom	Occupancy	x	y	z	Uiso
Bi1	0.55	0.02658(19)	0.25	0.0087(4)	0.0193(5)
La1	0.45	0.02658(19)	0.25	0.0087(4)	0.0193(5)
Mn1	0.667	0	0	0.5	0.0449(16)
Ni1	0.333	0	0	0.5	0.0449(16)
O1	1	0.48444(33)	0.25	-0.0694(5)	0.0187(5)
O2	1	0.21391(25)	-0.04013(24)	0.78130(24)	0.0187(5)

Table 4.17: *Refined fractional positions from the Rietveld refinement of the room temperature neutron powder diffraction data collected on the* $Bi_{1.1}La_{0.9}Mn_{4/3}Ni_{2/3}O_6$ *material.*

	Atom Bonds	Bond Length (l_i) / Å	Bond Valence Sum, v_i (expected oxidation state)
$Bi_{0.55}$	Bi – O1	3.0182 (18)	**2.490 (3+)**
	Bi – O1	2.5593 (18)	
	Bi – O1	2.4266 (34)	
	Bi – O1	3.093 (4)	
	Bi – O2 (x2)	2.7795 (17)	
	Bi – O2 (x2)	2.6383 (14)	
	Bi – O2 (x2)	2.3995 (21)	
$La_{0.45}$	La – O1	3.0182 (18)	**3.074 (3+)**
	La – O1	2.5593 (18)	
	La – O1	2.4266 (34)	
	La – O1	3.093 (4)	
	La – O2 (x2)	2.7795 (17)	
	La – O2 (x2)	2.6383 (14)	
	La – O2 (x2)	2.3995 (21)	
$Mn_{2/3}$	Mn1 – O2 (x2)	1.9844 (6)	**3.219 (3.5+)**
	Mn1 – O2 (x2)	1.9698 (16)	
	Mn1 – O2 (x2)	2.0073 (18)	
$Ni_{1/3}$	Ni1 – O2 (x2)	1.9844 (6)	**2.440 (2+)**
	Ni1 – O2 (x2)	1.9698 (16)	
	Ni1 – O2 (x2)	2.0073 (18)	

Table 4.18: *Selected bond lengths and Bond Valence Sums[6] obtained from the Rietveld refinement of powder neutron data collected at room temperature on* $Bi_{1.1}La_{0.9}Mn_{4/3}Ni_{2/3}O_6$.

On cooling the sample did not appear to undergo a structural transition, however extra scattering was observed on two of the peaks, suggesting that the material was becoming magnetically ordered at 2K. The absence of any extra reflections at 2K only the appearance of extra scattering indicates that the material becomes ferromagnetically ordered.

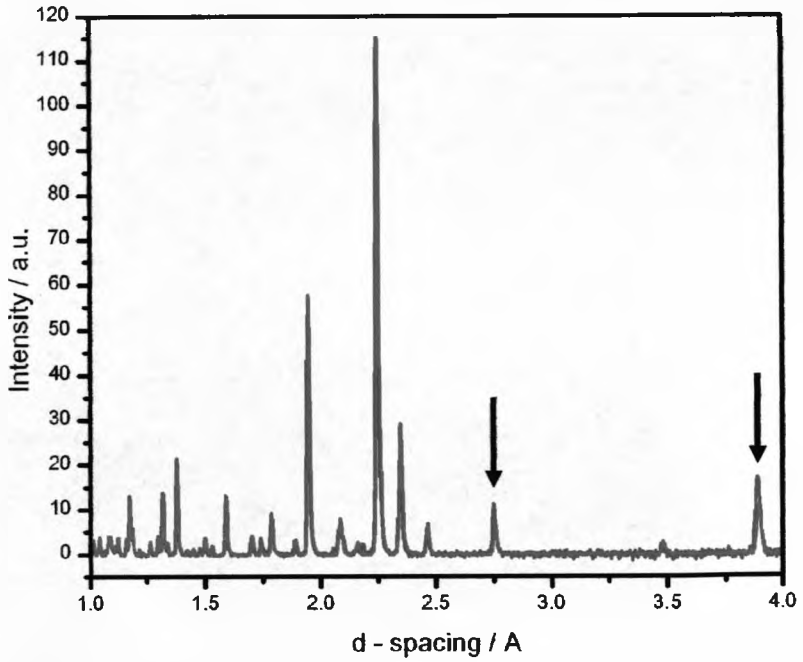

Figure 4.11: *Neutron powder diffraction patterns of $Bi_{1.1}La_{0.9}Mn_{4/3}Ni_{2/3}O_6$ collected at room temperature (red line) and 2K (blue line). The arrows indicate the positions were extra scattering was observed due to magnetic ordering.*

The low temperature structure was refined, and confirmed to be the same as that at room temperature, in the Pnma perovskite model; the bond-valence sums and fit parameters also support this model.

Lattice Parameters		**Fit Parameters**	
Space Group	Pnma		
a / Å	5.4973(2)	R_{wp} / %	1.65
b / Å	7.7676(3)	R_p / %	1.80
c / Å	5.4979(3)	χ^2	3.298
Volume / $Å^3$	234.76(1)		
Density / g cm^{-3}	7.968		

Table 4.19: *Refined lattice parameters from the Rietveld refinement of $Bi_{1.1}La_{0.9}Mn_{4/3}Ni_{2/3}O_6$ on the neutron diffraction data collected at 2K on POLARIS.*

Atom	Occupancy	x	y	z	U_{iso}
Bi1	0.45	0.02510(23)	0.25	0.0140(4)	0.0101(4)
La1	0.55	0.02510(23)	0.25	0.0140(4)	0.0101(4)
Mn1	0.667	0	0	0.5	0.0264(13)
Ni1	0.333	0	0	0.5	0.0264(13)
O1	1	0.4885(4)	0.25	-0.0700(6)	0.0095(5)
O2	1	0.2164(4)	-0.03976(30)	0.7824(4)	0.0196(5)

Table 4.20: *Refined positional parameters from the Rietveld refinement of* $Bi_{1.1}La_{0.9}Mn_{4/3}Ni_{2/3}O_6$ *on the neutron diffraction data collected at 2K on POLARIS.*

	Atom Bonds	Bond Length (l_i) / Å	Bond Valence Sum, v_i (expected oxidation state)
$Bi_{0.55}$	Bi – O1	2.9856 (23)	**2.509 (3+)**
	Bi – O1	2.5892 (25)	
	Bi – O1	2.449 (4)	
	Bi – O1	3.063 (4)	
	Bi – O2 (x2)	2.7918 (23)	
	Bi – O2 (x2)	2.6197 (18)	
	Bi – O2 (x2)	2.3837 (26)	
$La_{0.45}$	La – O1	2.9856 (23)	**3.097 (3+)**
	La – O1	2.5892 (25)	
	La – O1	2.449 (4)	
	La – O1	3.063 (4)	
	La – O2 (x2)	2.7918 (23)	
	La – O2 (x2)	2.6197 (18)	
	La – O2 (x2)	2.3837 (26)	
$Mn_{2/3}$	Mn1 – O2 (x2)	1.9807 (7)	**3.250 (3.5+)**
	Mn1 – O2 (x2)	1.9799 (25)	
	Mn1 – O2 (x2)	1.9895 (28)	
$Ni_{1/3}$	Ni1 – O2 (x2)	1.9807 (7)	**2.464 (2+)**
	Ni1 – O2 (x2)	1.9799 (25)	
	Ni1 – O2 (x2)	1.9895 (28)	

Table 4.21: *Selected bond lengths and Bond Valence Sums[6] obtained from Rietveld refinement of powder neutron data collected on* $Bi_{1.1}La_{0.9}Mn_{4/3}Ni_{2/3}O_6$ *at 2K.*

The magnetic structure of this compound was refined simultaneously to the fundamental structure using the group of SARAh programs with GSAS, using a magnetic k-vector of 0,0,0 consistent with a ferromagnetically ordered material. The magnetic moment of the material was refined to 1.55(3)μ_B per magnetic atom, or 3.10μ_B/mol with the spins aligned along the b-direction. The expected value if the material was fully ferromagnetically arranged is 3μ_B/mol consistent with the observed magnetic moment.

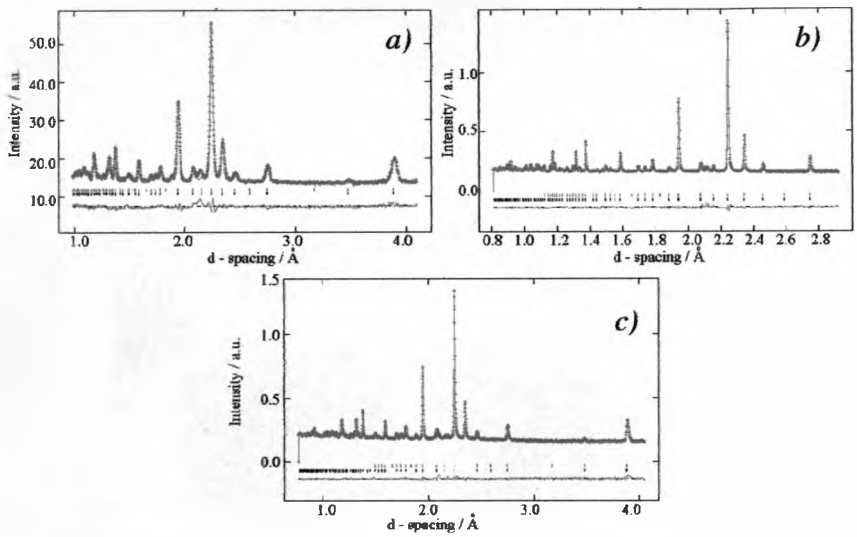

Figure 4.12: *Rietveld Refinement of powder neutron diffraction data collected at 2K using the POLARIS diffractometer on the x=0.9 material against the Pnma model (red ticks) and a magnetic structure with a (0,0,0,) k-vector (black ticks). The red crosses are observed data, the solid green line is the calculated pattern and the pink line is the difference, figure a) is the low angle bank A, figure b) is the back scattering bank C and figure c) is the 90° bank E.*

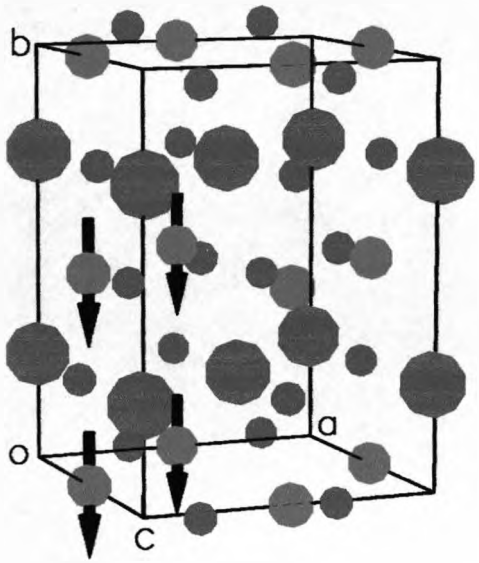

Figure 4.13: *Picture of the refined magnetic structure. Purple circles are the bismuth atoms; green circles are the manganese and nickel atoms; red circles are the oxygen atoms; arrows indicate the direction of the magnetic spin within the sample.*

4.3.1.6 Variable temperature neutron powder diffraction on $Bi_{0.8}La_{1.2}Mn_{4/3}Ni_{2/3}O_6$

Variable temperature neutron powder diffraction data was collected on $Bi_{0.8}La_{1.2}Mn_{4/3}Ni_{2/3}O_6$ between room temperature and 2K. The room temperature data was refined in the Pnma model.

Lattice Parameters		Fit Parameters	
Space Group	Pnma		
a / Å	5.5042(3)	R_{wp} / %	5.79
b / Å	7.7968(4)	R_p / %	5.82
c / Å	5.5026(3)	χ^2	5.864
Volume / Å^3	236.14(2)		
Density / g cm^{-3}	7.626		

Table 4.22: *Refined lattice parameters and goodness of fit parameters from the Rietveld refinement of the room temperature neutron powder diffraction data for the* $Bi_{0.8}La_{1.2}Mn_{4/3}Ni_{2/3}O_6$ *material.*

Atom	Occupancy	x	y	z	Uiso
Bi1	0.4	0.01831(27)	0.25	0.02210(28)	0.0081(5)
La1	0.6	0.01831(27)	0.25	0.02210(28)	0.0081(5)
Mn1	0.667	0	0	0.5	0.0213(17)
Ni1	0.333	0	0	0.5	0.0213(17)
O1	1	0.4943(6)	0.25	-0.0612(5)	0.0114(5)
O2	1	0.2269(4)	-0.04704(21)	0.7778(4)	0.0114(5)

Table 4.23: *Refined fractional positions from the Rietveld refinement of the room temperature neutron powder diffraction data collected on the* $Bi_{0.8}La_{1.2}Mn_{4/3}Ni_{2/3}O_6$ *material.*

	Atom Bonds	Bond Length (l_i) / Å	Bond Valence Sum, v_i (expected oxidation state)
$Bi_{0.4}$	Bi – O1	2.9205 (34)	2.612 (3+)
	Bi – O1	2.6597 (34)	
	Bi – O1	2.5396 (33)	
	Bi – O1	2.9694 (33)	
	Bi – O2 (x2)	2.9134 (16)	
	Bi – O2 (x2)	2.5400 (17)	
	Bi – O2 (x2)	2.3532 (22)	
	Bi – O2 (x2)	3.2650 (34)	
$La_{0.6}$	La – O1	2.9205 (34)	3.225 (3+)
	La – O1	2.6597 (34)	
	La – O1	2.5396 (33)	
	La – O1	2.9694 (33)	
	La – O2 (x2)	2.9134 (16)	
	La – O2 (x2)	2.5400 (17)	
	La – O2 (x2)	2.3532 (22)	
	La – O2 (x2)	3.2650 (34)	
$Mn_{2/3}$	Mn1 – O2 (x2)	1.9783 (5)	3.229 (3.5+)
	Mn1 – O2 (x2)	2.0077 (25)	
	Mn1 – O2 (x2)	1.9722 (26)	
$Ni_{1/3}$	Ni1 – O2 (x2)	1.9783 (5)	2.448 (2+)
	Ni1 – O2 (x2)	2.0077 (25)	
	Ni1 – O2 (x2)	1.9722 (26)	

Table 4.24: *Selected bond lengths and Bond Valence Sums[6] obtained from the Rietveld refinement of powder neutron data collected at room temperature on* $Bi_{0.8}La_{1.2}Mn_{4/3}Ni_{2/3}O_6$.

The low temperature data revealed extra Bragg scattering on a number reflections, *figure 4.14*, suggesting that, like in the x = 0.9 case, at 2K the material is magnetically ordered. Again the absence of any extra reflections in the 2K data, and the appearance of extra scattering is consistent with the material being ferromagnetically ordered.

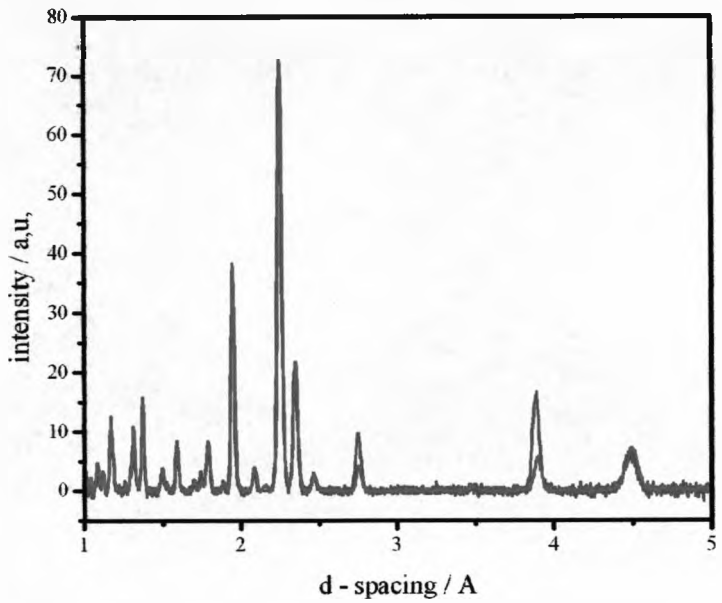

Figure 4.14: *Neutron powder diffraction pattern (bank A) of* $Bi_{0.8}La_{1.2}Mn_{4/3}Ni_{2/3}O_6$ *collected at room temperature (red line) and at 2K (blue line) on the POLARIS diffractometer.*

The low temperature structure was refined, and confirmed to be the same as that at room temperature, in the Pnma perovskite model.

Lattice Parameters		**Fit Parameters**	
Space Group	Pnma		
a / Å	5.4942(2)	R_{wp} / %	2.39
b / Å	7.7695(2)	R_p / %	2.61
c / Å	5.4772(3)	χ^2	2.433
Volume / Å^3	233.80(5)		
Density / g cm^{-3}	7.703		

Table 4.25: *Refined lattice parameters from the Rietveld refinement of* $Bi_{0.8}La_{1.2}Mn_{4/3}Ni_{2/3}O_6$ *on the neutron diffraction data collected at 2K on POLARIS.*

Atom	Occupancy	x	y	z	U_{iso}
Bi1	0.4	0.0075(5)	0.25	-0.03426(21)	0.0112(6)
La1	0.6	0.0075(5)	0.25	-0.03426(21)	0.0112(6)
Mn1	0.667	0	0	0.5	0.0245(24)
Ni1	0.333	0	0	0.5	0.0245(24)
O1	1	0.4782(6)	0.25	0.0236(6)	0.0112(5)
O2	1	0.2796(4)	-0.05367(16)	0.7737(5)	0.0112(5)

Table 4.26: *Refined positional parameters from the Rietveld refinement of* $Bi_{0.8}La_{1.2}Mn_{4/3}Ni_{2/3}O_6$ *on the neutron diffraction data collected at 2K on POLARIS.*

	Atom Bonds	Bond Length (l_i) / Å	Bond Valence Sum, v_i (expected oxidation state)
$Bi_{0.4}$	Bi – O1	2.9250 (13)	**2.130 (3+)**
	Bi – O1	2.6050 (12)	
	Bi – O1	2.6850 (15)	
	Bi – O1	2.8010 (15)	
	Bi – O2 (x2)	2.9847 (9)	
	Bi – O2 (x2)	2.5575 (8)	
	Bi – O2 (x2)	2.6170 (7)	
	Bi – O2 (x2)	2.9755 (9)	
$La_{0.6}$	La – O1	2.9250 (13)	**2.630 (3+)**
	La – O1	2.6050 (12)	
	La – O1	2.6850 (15)	
	La – O1	2.8010 (15)	
	La – O2 (x2)	2.9847 (9)	
	La – O2 (x2)	2.5575 (8)	
	La – O2 (x2)	2.6170 (7)	
	La – O2 (x2)	2.9755 (9)	
$Mn_{2/3}$	Mn1 – O2 (x2)	1.95038 (9)	**3.675 (3.5+)**
	Mn1 – O2 (x2)	2.1865 (8)	
	Mn1 – O2 (x2)	1.7824 (6)	
$Ni_{1/3}$	Ni1 – O2 (x2)	1.95038 (9)	**2.786 (2+)**
	Ni1 – O2 (x2)	2.1865 (8)	
	Ni1 – O2 (x2)	1.7824 (6)	

Table 4.27: *Selected bond lengths and Bond Valence Sums[6] obtained from Rietveld refinement of powder neutron data collected at 2K on* $Bi_{0.8}La_{1.2}Mn_{4/3}Ni_{2/3}O_6$.

The magnetic structure of this compound was refined simultaneously to the fundamental structure using the group of SARAh programs with GSAS, using a magnetic k-vector of 0,0,0 consistent with a ferromagnetically ordered material. The magnetic moment of the material was refined to 2.06(3)μ_B per magnetic atom, or 4.12μ_B/mol again with the spins aligned along the b-direction. The expected value if this material was fully ferromagnetically ordered material is 3μ_B/mol which again os consistent with the calculated value. The magnetic structure is the same as that refined for the x = 0.9 material given in *figure 4.13*.

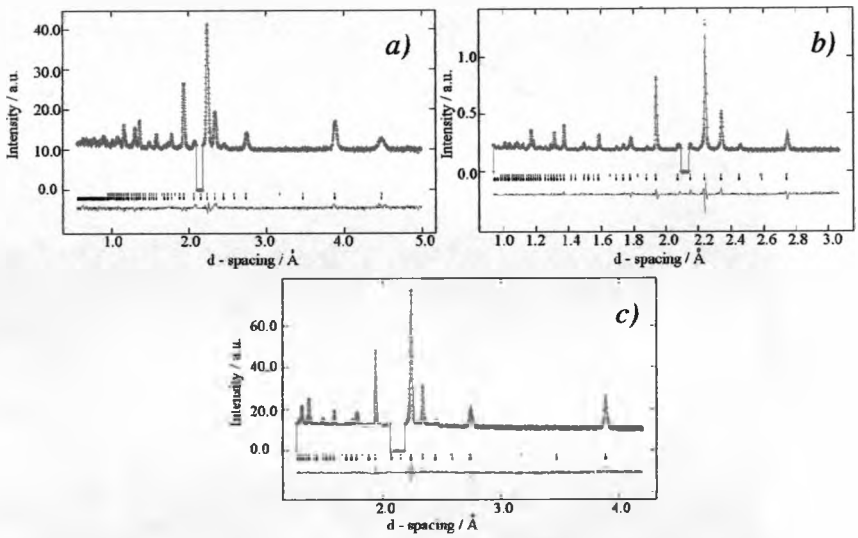

Figure 4.15: *Rietveld refinement of neutron data collected on the POLARIS diffractometer at 2K against the Pnma model (red ticks) and a magnetic structure with a (0,0,0,) k-vector (black ticks). Red crosses are observed data, the solid green line is the calculated pattern and the pink line is the difference, figure a) is the low angle bank A, figure b) is the back scattering bank C and figure c) is the 90° bank E.*

4.3.1.7 Variable temperature neutron powder diffraction on $La_2Mn_{4/3}Ni_{2/3}O_6$

Neutron powder diffraction data were collected on $La_2Mn_{4/3}Ni_{2/3}O_6$ at room temperature and 2K on this POLARIS diffractometer in ISIS. The room temperature data was refined in the Pnma model.

Lattice Parameters		Fit Parameters	
Space Group	Pnma		
a / Å	5.4895(1)	R_{wp} / %	2.51
b / Å	7.7747(1)	R_p / %	3.75
c / Å	5.5257(1)	χ^2	5.435
Volume / Å^3	235.83(2)		
Density / g cm^{-3}	6.847		

Table 4.28: *Refined parameters from the Rietveld refinement of the room temperature neutron powder diffraction data for the $La_2Mn_{4/3}Ni_{2/3}O_6$ material.*

Atom	Occupancy	x	y	z	Uiso
La1	1	0.02218(7)	0.25	-0.00521(10)	0.0065(1)
Mn1	0.667	0	0	0.5	0.0056(2)
Ni1	0.333	0	0	0.5	0.0056(2)
O1	1	0.49254(12)	0.25	0.06631(11)	0.0091(1)
O2	1	0.27538(7)	0.03579(5)	0.72563(8)	0.0099(1)

Table 4.29: *Refined fractional positions from the Rietveld refinement of the room temperature neutron powder diffraction data collected on the $La_2Mn_{4/3}Ni_{2/3}O_6$ material.*

	Atom Bonds	Bond Length (l_i) / Å	Bond Valence Sum, v_i (expected oxidation state)
$La_{1.0}$	La – O1	2.9342 (7)	2.999 (3+)
	La – O1	2.6121 (7)	
	La – O1	3.1047 (9)	
	La – O1	2.4307 (9)	
	La – O2 (x2)	2.6302 (5)	
	La – O2 (x2)	2.7926 (5)	
	La – O2 (x2)	3.161 (5)	
	La – O2 (x2)	2.4683 (6)	
$Mn_{2/3}$	Mn1 – O2 (x2)	1.97835 (12)	3.305 (3.5+)
	Mn1 – O2 (x2)	1.9792 (4)	
	Mn1 – O2 (x2)	1.9739 (4)	
$Ni_{1/3}$	Ni1 – O2 (x2)	1.97835 (12)	2.505 (2+)
	Ni1 – O2 (x2)	1.9792 (4)	
	Ni1 – O2 (x2)	1.9739 (4)	

Table 4.30: *Selected bond lengths and Bond Valence Sums[b] obtained from the Rietveld refinement of powder neutron diffraction data collected at room temperature on* $La_2Mn_{4/3}Ni_{2/3}O_6$.

Again, the low temperature data revealed extra Bragg scattering on two reflections suggesting that at 2K the material is magnetically ordered. The absence of any extra reflections in the 2K data, and the appearance of extra scattering is consistent with the material being ferromagnetically ordered.

Lattice Parameters		Fit Parameters	
Space Group	Pnma		
a / Å	5.4891(1)	R_{wp} / %	1.55
b / Å	7.7710(1)	R_p / %	2.62
c / Å	5.5213(1)	χ^2	3.137
Volume / Å^3	235.51(1)		
Density / g cm^{-3}	6.856		

Table 4.31: *Refined lattice parameters from the Rietveld refinement of $La_2Mn_{4/3}Ni_{2/3}O_6$ on the neutron diffraction data collected at 2K on POLARIS.*

Atom	Occupancy	x	y	z	U_{iso}
La1	1	0.02531(7)	0.25	-0.00556(11)	0.0027(1)
Mn1	0.667	0	0	0.5	0.0022(2)
Ni1	0.333	0	0	0.5	0.0022(2)
O1	1	0.49233(13)	0.25	0.06751(12)	0.0060(1)
O2	1	0.27649(8)	0.03589(6)	0.72426(8)	0.0063(1)

Table 4.32: *Refined positional parameters from the Rietveld refinement of $La_2Mn_{4/3}Ni_{2/3}O_6$ on the neutron diffraction data collected at 2K on POLARIS.*

	Atom Bonds	Bond Length (l_i) / Å	Bond Valence Sum, v_i (expected oxidation state)
$La_{1.0}$	La – O1	2.9532 (7)	**2.895 (3+)**
	La – O1	2.5951 (7)	
	La – O1	3.1079 (10)	
	La – O1	2.4254 (9)	
	La – O2 (x2)	2.6258 (6)	
	La – O2 (x2)	2.7802 (5)	
	La – O2 (x2)	2.4682 (6)	
$Mn_{2/3}$	Mn1 – O2 (x2)	1.97863 (13)	**3.303 (3.5+)**
	Mn1 – O2 (x2)	1.9785 (5)	
	Mn1 – O2 (x2)	1.9750 (5)	
$Ni_{1/3}$	Ni1 – O2 (x2)	1.97863 (13)	**2.504 (2+)**
	Ni1 – O2 (x2)	1.9785 (5)	
	Ni1 – O2 (x2)	1.9750 (5)	

Table 4.33: *Selected bond lengths and Bond Valence Sums[6] obtained from the Rietveld refinement of powder neutron data collected at 2K on $La_2Mn_{4/3}Ni_{2/3}O_6$.*

The magnetic structure of this compound was refined simultaneously to the fundamental structure *(tables 4.31 – 1.33)* using the SARAh programs with GSAS, using a magnetic k-vector of 0,0,0 consistent with a ferromagnetically ordered material. The magnetic moment was refined to 2.17(1)μ_B per magnetic atom, or 4.34μ_B/mol and the structure is the same as that refined for the x = 0.9 material given in *figure 4.13* with the spins aligned parallel along the b-direction. The expected value if this material was fully ferromagnetically ordered material is 3μ_B/mol

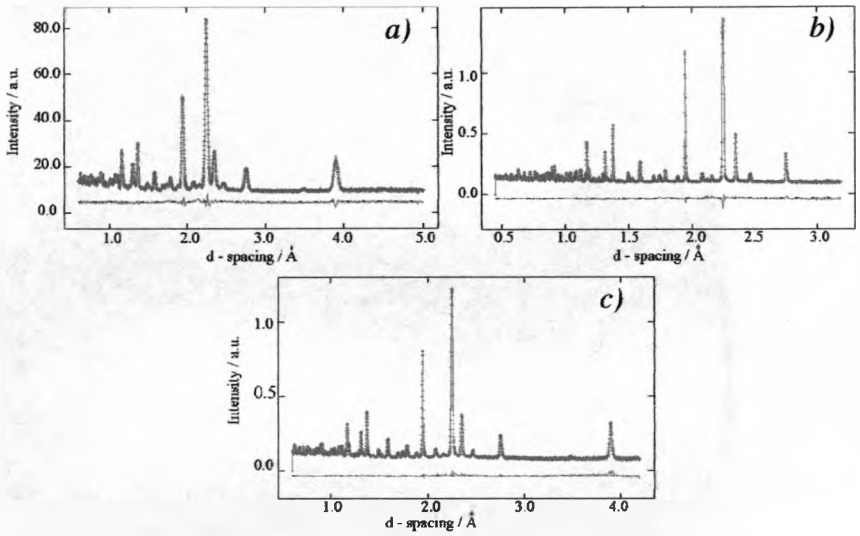

Figure 4.16: *Rietveld Refinement of powder neutron data collected at 2K using the POLARIS diffractometer on the x=2 material against the Pnma model and a magnetic structure with a (0,0,0,) k-vector. The red crosses are observed data, the solid green line is the calculated pattern and the pink line is the difference, figure a) is the low angle bank A, figure b) is the back scattering bank C and figure c) is the 90° bank E.*

4.3.1.8 Summary of diffraction data obtained

The structural study carried out on the $Bi_{2-x}La_xMn_{4/3}Ni_{2/3}O_6$ series revealed that two main structure types were forming, like in the parent x = 0 case, an incommensurate low temperature and commensurate high temperature form. Both are based on the perovskite unit *(figure 4.17)*, with Bi^{3+} and La^{3+} ions on the A-site and a random distribution of 33% Mn^{4+}, 33% Mn^{3+} and 33% Ni^{2+} ions on the B-site inside the oxygen octahedra. No evidence of any ordering on the B-site was seen for any of the materials. It is the tilting of these octahedra that causes the distortion of the structure of these materials from the perovskite unit. In the incommensurate structure, the A-site cation distorts off position causing a modulation in the structure.

As the amount of lanthanum doping was varied, the structure that formed also varied. High bismuth content samples favoured the incommensurate structure *(figure 4.18(a))* whereas high lanthanum content materials favoured the commensurate Pnma form *(figure 4.18(b))*. The temperature at which these materials underwent the transition between these two forms was decreased from ~200°C for x = 0, with increasing lanthanum doping until x = 0.9 when the material was in the commensurate Pnma structure at all temperatures. *Figure 4.19* summarises the effect of lanthanum doping and temperature on the structure of the material.

An added observation, was that once enough lanthanum was doped into the material so that it was commensurate at all temperatures ($x \geq 0.9$), the materials exhibited extra Bragg scattering in the low temperature neutron diffraction data, which would suggest that the incommensurate structure is not magnetically ordered whereas the

commensurate one is. The absence of any extra reflections, only extra intensity suggested that ferromagnetic ordering was occurring and as such each pattern was refined with a magnetic structure using the k-vector 0,0,0 with the spins aligned parallel along the b-direction. As the lanthanum content increased so did the refined magnetic moment.

$Bi_{2-x}La_xMn_{4/3}Ni_{2/3}O_6$ (x =)	Calculated magnetic Moment / μ_B mol^{-1}
0.9	3.10
1.2	4.12
2	4.34

Table 4.34: *Variation of the refined magnetic moment with lanthanum content*

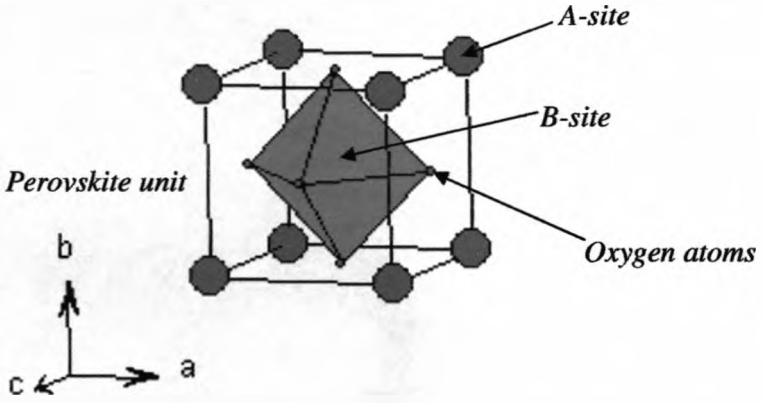

Figure 4.17: *Perovskite unit*

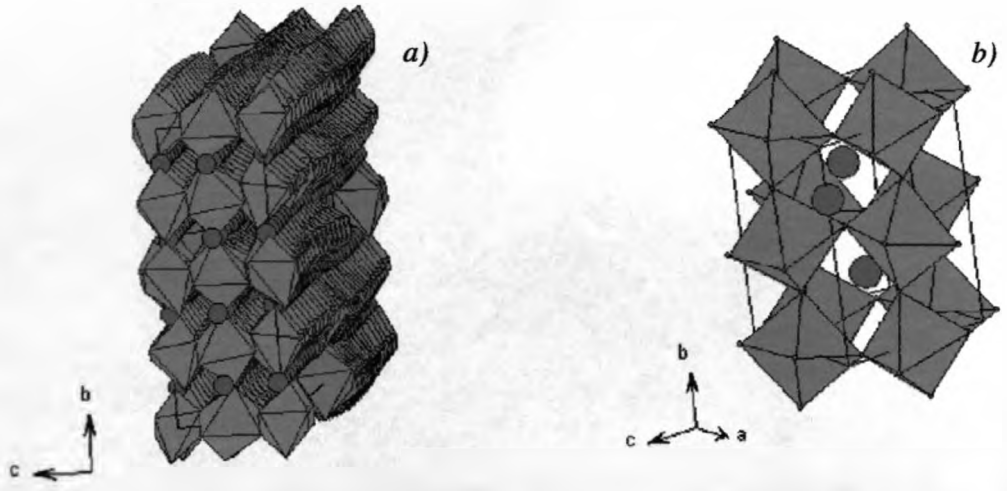

Figure 4.18: *Structures adopted by the $Bi_{2-x}La_xMn_{4/3}Ni_{2/3}O_6$ series; a) Incommensurate structure; b) Commensurate Pnma structure*

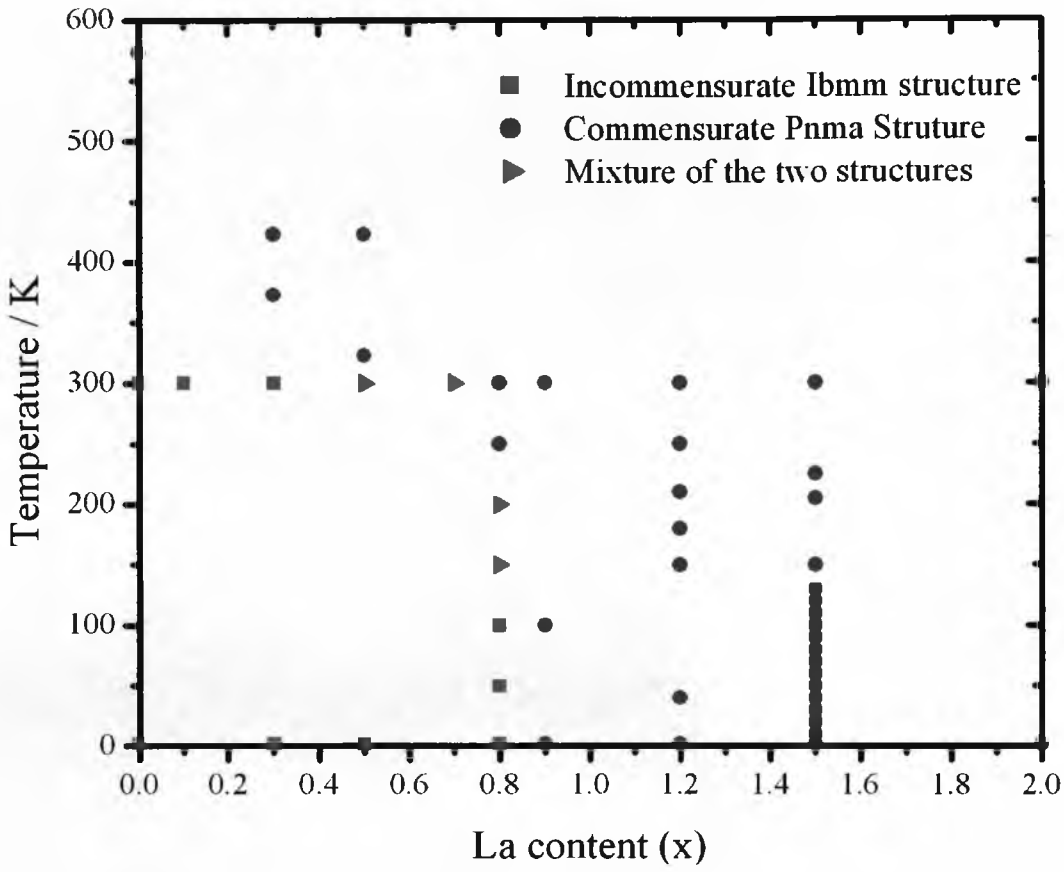

Figure 4.19: *Variation in structure of materials in the* $Bi_{2-x}La_xMn_{4/3}Ni_{2/3}O_6$ *series with lanthanum content (x) and temperature.*

4.3.2 Transmission Electron Microscopy

Samples for transmission electron microscopy (TEM) were prepared by crushing the powder in n-butanol and the small crystallites in suspension were deposited onto a holey carbon film, supported by a copper grid. Energy dispersive spectroscopy (EDS) analyses was carried out by myself on each of the samples in the $Bi_{2-x}La_xMn_{4/3}Ni_{2/3}O_6$ series to check the homogeneity of the sample and to ensure that the bismuth to lanthanum ratio was as expected. This is something which is very difficult to determine from the powder diffraction, as discussed in *Chapter Two*.

An electron diffraction (ED) study was carried out at room temperature on the $Bi_{1.2}La_{0.8}Mn_{4/3}Ni_{2/3}O_6$ sample by Dr. Mathieu Allix using a JEOL 2000FX electron microscope equipped with an EDAX analyser. Energy dispersive spectroscopy (EDS) analyses were systematically carried out during the ED study. The electron diffraction was also carried out on this material, confirming the Pnma space group and lattice parameters concluded from the powder neutron diffraction refinement *(section 4.3.1.4)*.

4.3.3 X-ray Absorption Spectroscopy (XAS)

XAS was carried out on station 7.1 at the Daresbury SRS. Data was recorded on the samples at room temperature across the Mn K edge in ~ 0.5eV steps, Mn metal K edges were run simultaneously as a form of energy calibration. All samples were recorded in transmission mode, $BiMnO_3$ and La_2MnNiO_6 were run as Mn^{3+} and Mn^{4+} standards respectively.

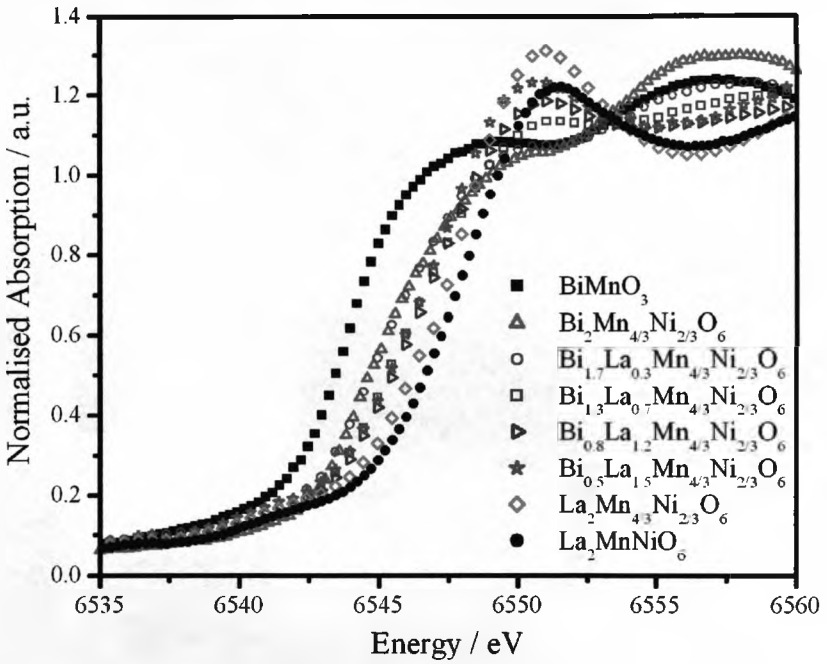

Figure 4.20: *X-ray absorption spectroscopy collected across the manganese K edge in ~ 0.5eV steps for a selection of the samples in the* $Bi_{2-x}La_xMn_{4/3}Ni_{2/3}O_6$ *series.*

The edge positions for each of these samples were calculated and are given in *table 4.35*, they support the conclusion made in the parent case of the charge balanced formula, $(Bi^{3+})_{2-x}(La^{3+})_x(Mn^{4+})_{2/3}(Mn^{3+})_{2/3}(Ni^{2+})_{2/3}(O^{2-})_6$. However there is a clear trend seen in these values with lanthanum content, as this increases the edge position

also increases tending towards the Mn^{4+} standard edge position, with three clear areas.

Sample	Edge Position / eV
$BiMnO_3$ (Mn^{3+} standard)	6543.98779
$Bi_2Mn_{4/3}NiO_6$	6543.94727
$Bi_{1.7}La_{0.3}Mn_{4/3}Ni_{2/3}O_6$	6545.62647
$Bi_{1.3}La_{0.7}Mn_{4/3}Ni_{2/3}O_6$	6545.62647
$Bi_{0.8}La_{1.2}Mn_{4/3}Ni_{2/3}O_6$	6547.34912
$Bi_{0.5}La_{1.5}Mn_{4/3}Ni_{2/3}O_6$	6547.34912
$La_2Mn_{4/3}Ni_{2/3}O_6$	6547.34912
La_2MnNiO_6 (Mn^{4+} standard)	6548.61914

Table 4.35: *Edge positions calculated from the XAS data collected on the manganese edge on selected samples in the $Bi_{2-x}La_xMn_{4/3}Ni_{2/3}O_6$ series.*

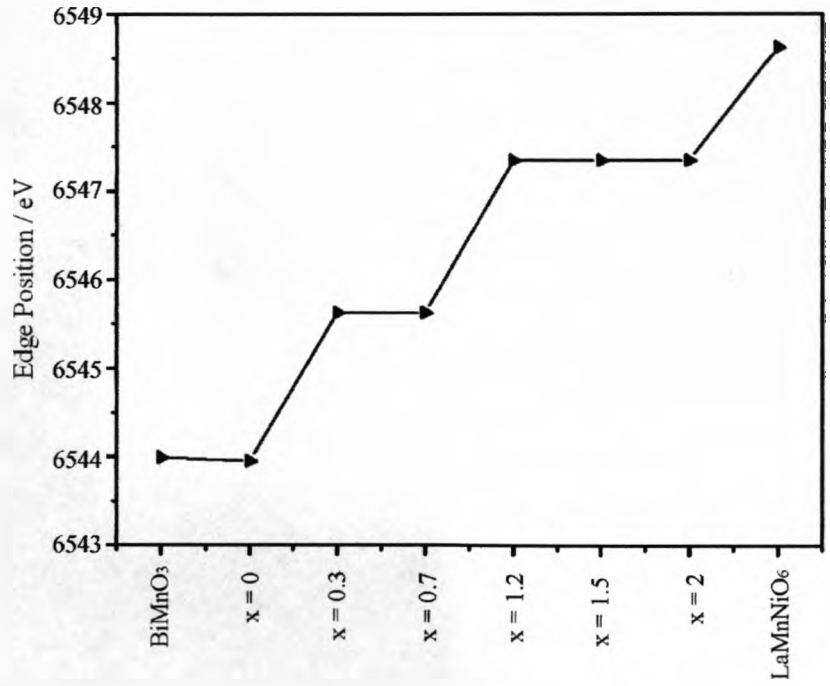

Figure 4.21: *Variation in the edge position of the manganese edge with lanthanum content in the $Bi_{2-x}La_xMn_{4/3}Ni_{2/3}O_6$ series with respect to the two standards $BiMnO_3$ (Mn^{3+} standard) and La_2MnNiO_6 (Mn^{4+} standard).*

Taking forward the conclusions made from the structural study the three groups of data seen on *figure 4.21* could simply reflect the variation of structure with lanthanum content. The x = 0 material is in the incommensurate structure at room temperature; materials with x = 0.3 and 0.7 are either in the incommensurate structure but have a transition temperature close to room temperature or are a mixture of the two forms at room temperature. Whereas the x = 1.2, 1.5 and 2 materials are in the commensurate structure at room temperature. Therefore the three groups of data observed in the XAS is indicative of the three structure types, incommensurate, mixture and commensurate the lanthanum content increases.

4.3.4 Magnetic Measurements

Magnetic susceptibility data were collected using a Quatum Design MPMS SQUID magnetometer on each of the samples synthesised. Each sample was loaded at room temperature and cooled in the absence of an applied field to 2K. A field of 100Oe was then applied and measurements were recorded between 2 and 300K (400K for samples with a lanthanum content greater than x = 0.7), this system was then cooled again to 2K in the applied field and the measurements between 2 and 300K (or 400K) were repeated.

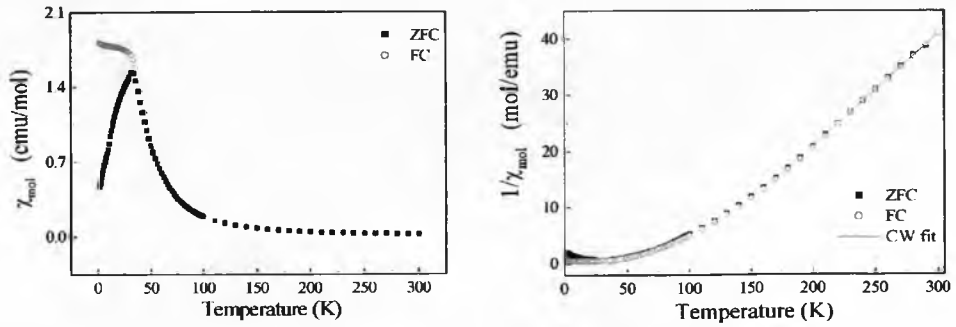

Figure 4.22: *ZFC-FC data collected at 100Oe collected on x=0.1, the ordering temperature is ~ 35K. Curie-Weiss fitting (200 – 300K) of the inverse chi reveals a Curie constant of 4.97 emu/mol and a positive Weiss constant (θ = 96.27K).*

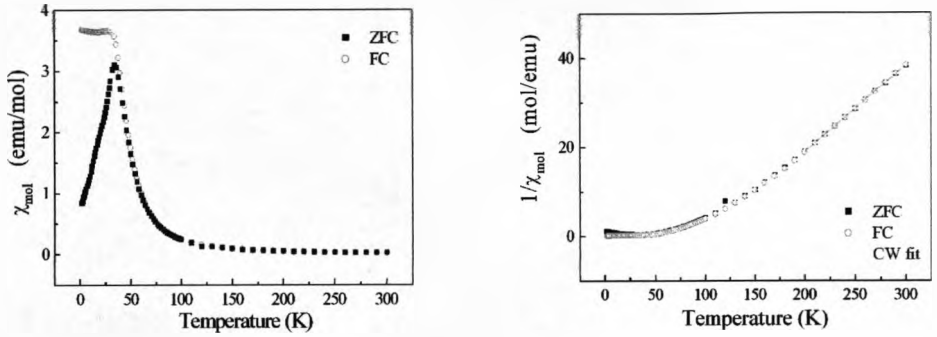

Figure 4.23: *ZFC-FC data collected at 100Oe collected on x=0.3, the ordering temperature is ~ 40K. Curie-Weiss fitting (200 – 300K) of the inverse chi reveals a Curie constant of 5.17 emu/mol and a positive Weiss constant (θ = 102.6K).*

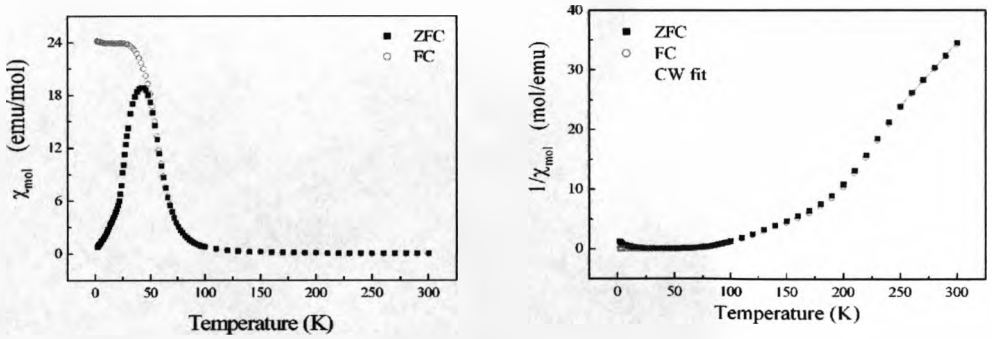

Figure 4.24: *ZFC-FC data collected at 100Oe collected on x=0.5, the ordering temperature is ~ 50K. Curie-Weiss fitting (250 – 300K) of the inverse chi reveals a Curie constant of 4.72 emu/mol and a positive Weiss constant (θ = 137.1K).*

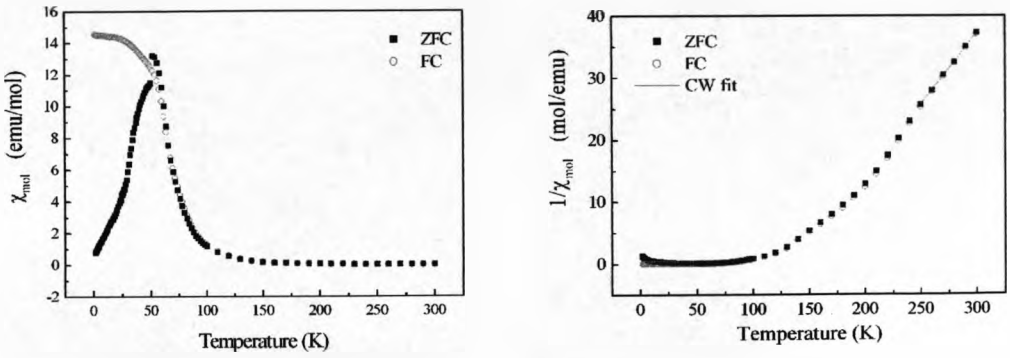

Figure 4.25: *ZFC-FC data collected at 100Oe collected on x=0.7, the ordering temperature is ~ 60K. Curie-Weiss fitting (250 – 300K) of the inverse chi reveals a Curie constant of 4.30 emu/mol and a positive Weiss constant (θ = 139.8K).*

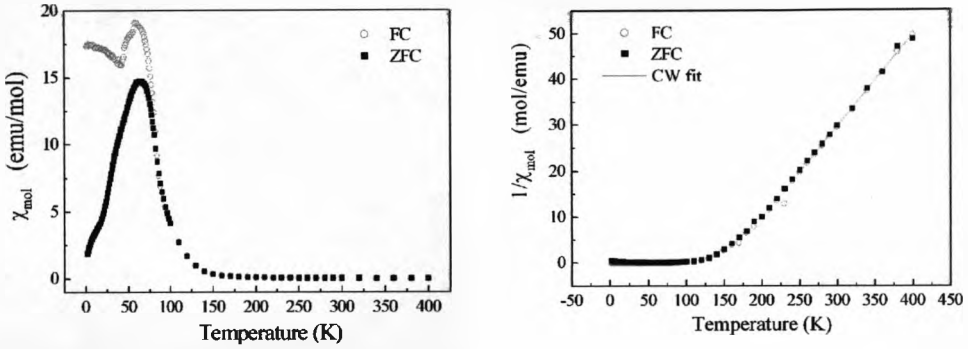

Figure 4.26: *ZFC-FC data collected at 100Oe collected on x=0.8, the ordering temperature is ~ 85K. Curie-Weiss fitting (250 – 400K) of the inverse chi reveals a Curie constant of 5.00 emu/mol and a positive Weiss constant (θ = 152.0K).*

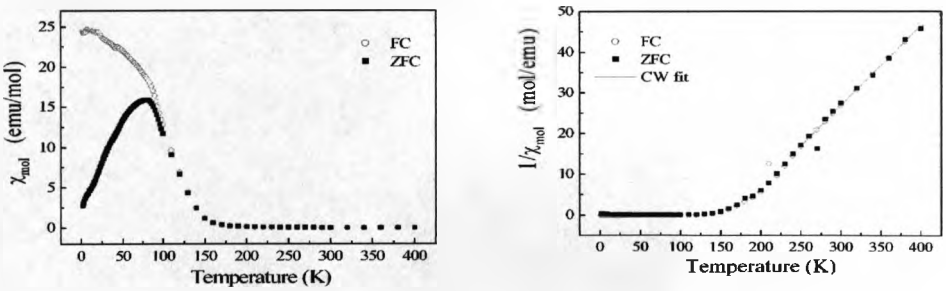

Figure 4.27: *ZFC-FC data collected at 100Oe collected on x=0.9, the ordering temperature is ~ 120K. Curie-Weiss fitting (250 – 400K) of the inverse chi reveals a Curie constant of 5.06 emu/mol and a positive Weiss constant (θ = 164.4K).*

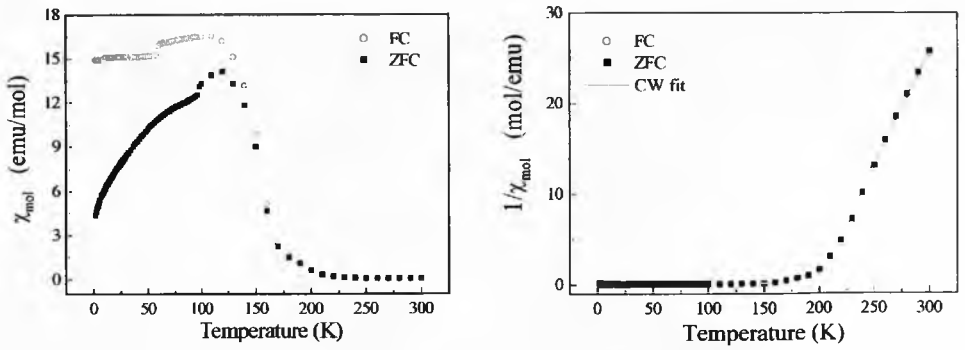

Figure 4.28: *ZFC-FC data collected at 100Oe collected on x=1.0, the ordering temperature is ~ 160K. Curie-Weiss fitting (250 – 300K) of the inverse chi reveals a Curie constant of 3.94 emu/mol and a positive Weiss constant (θ = 198.7K).*

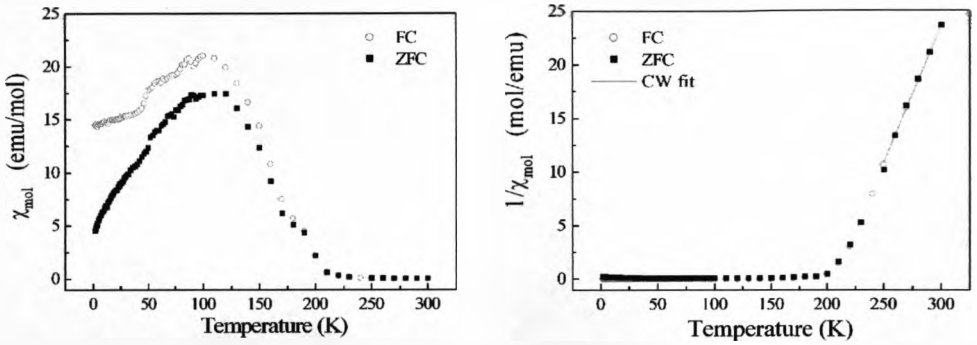

Figure 4.29: *ZFC-FC data collected at 100Oe collected on x=1.1, the ordering temperature is ~ 180K. Curie-Weiss fitting (250 – 300K) of the inverse chi reveals a Curie constant of 3.93 emu/mol and a positive Weiss constant (θ = 207.7K).*

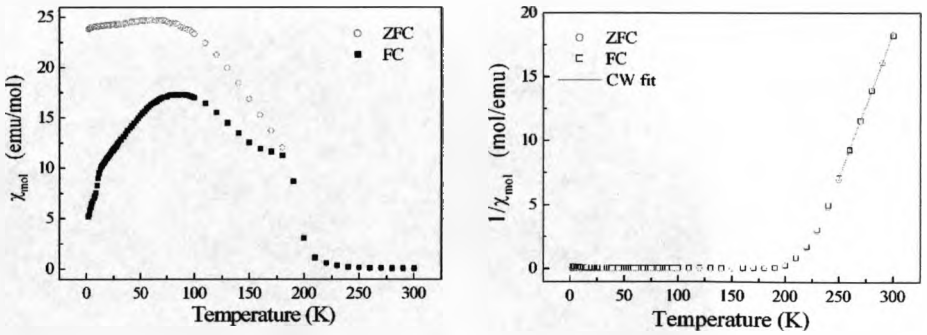

Figure 4.30: *ZFC-FC data collected at 100Oe collected on x=1.2, the ordering temperature is ~ 160K. Curie-Weiss fitting (250 – 300K) of the inverse chi reveals a Curie constant of 4.39 emu/mol and a positive Weiss constant (θ = 219.6K).*

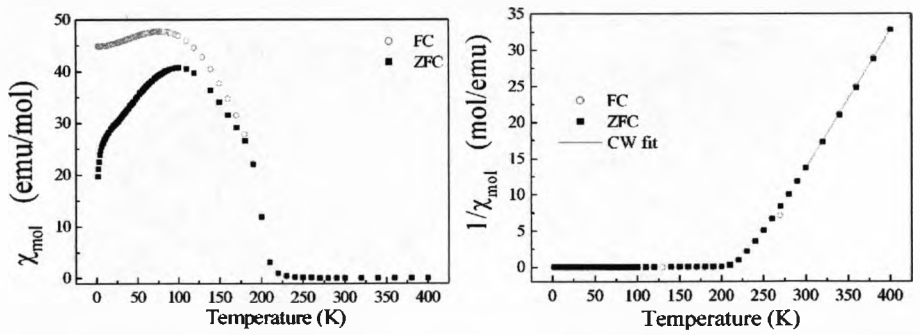

Figure 4.31: *ZFC-FC data collected at 100Oe collected on x=1.5, the ordering temperature is ~ 190K. Curie-Weiss fitting (300 – 400K) of the inverse chi reveals a Curie constant of 5.19 emu/mol and a positive Weiss constant (θ = 230.1K).*

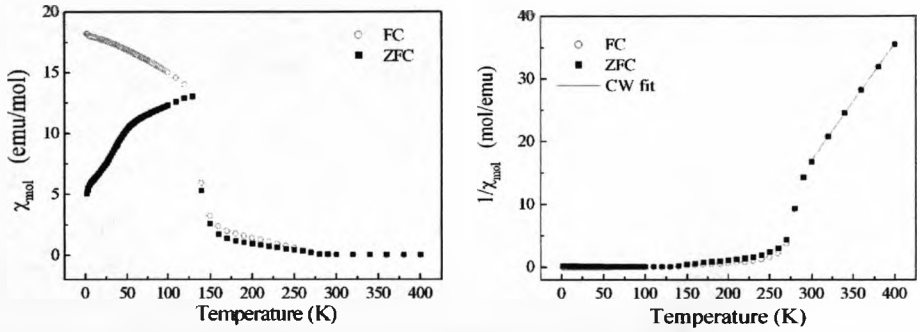

Figure 4.32: *ZFC-FC data collected at 100Oe collected on x=1.7, the ordering temperature is ~ 260K. Curie-Weiss fitting (300 – 400K) of the inverse chi reveals a Curie constant of 5.34 emu/mol and a positive Weiss constant (θ = 209.8K).*

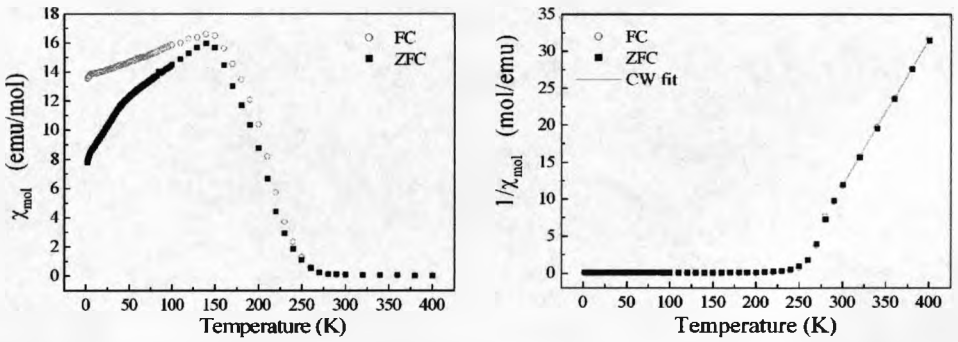

Figure 4.33: *ZFC-FC data collected at 100Oe collected on x=1.9, the ordering temperature is ~ 260K. Curie-Weiss fitting (300 – 400K) of the inverse chi reveals a Curie constant of 5.04 emu/mol and a positive Weiss constant (θ = 240.7K).*

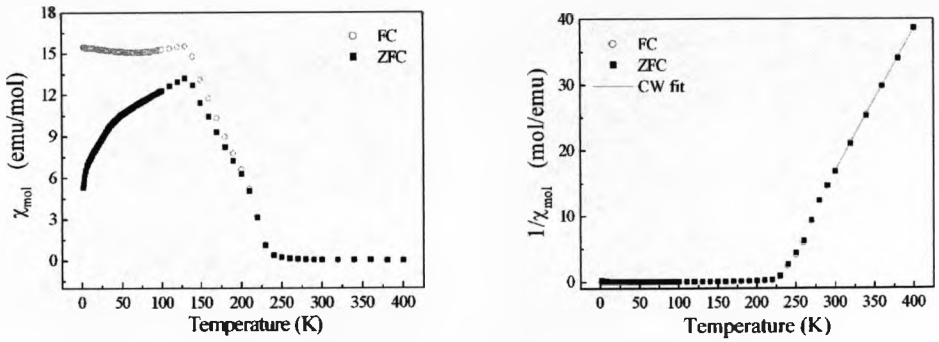

Figure 4.34: *ZFC-FC data collected at 100Oe collected on x=2.0, the ordering temperature is ~ 230K. Curie-Weiss fitting (300 – 400K) of the inverse chi reveals a Curie constant of 4.59 emu/mol and a positive Weiss constant (θ = 223.1K).*

Each sample *(figures 4.22 – 4.34)* displayed magnetic susceptibility that exhibited a divergence between the zero-field-cooled and the field-cooled data, this was taken as the magnetic ordering temperature of the material. As the lanthanum content increases in the material so does the magnetic ordering temperature. A summary of the variation in transition temperature with lanthanum content is given in *Table 4.36.*

$Bi_{2-x}La_xMn_{4/3}Ni_{2/3}O_6$ (x =)	Magnetic Ordering Temperature / K
0	35
0.1	35
0.3	40
0.5	50
0.7	60
0.8	85
0.9	120
1	160
1.1	180
1.2	180
1.5	190
1.7	260
1.9	260
2	230

Table 4.36*: Variation of the magnetic ordering temperature with lanthanum content.*

Above these temperatures the data was fitted by the simple Curie-Weiss equation:

$$\chi(T) = C / (T - \theta)$$

The curie constant as already discussed in *Chapter One*, can then be used to calculated the corresponding effective moment of the material using $\mu_{eff} = (8C)^{1/2}$.

$Bi_{2-x}La_xMn_{4/3}Ni_{2/3}O_6$ x =	Curie Constant / emu mol^{-1}	Effective Moment (μ_{eff}) / μ_B mol^{-1}	Weiss Constant (θ)
0	5.01	6.39	89.7
0.1	4.97	6.31	96.2
0.3	5.17	6.43	102.6
0.5	4.72	6.15	137.1
0.7	4.30	5.87	139.8
0.8	5.00	6.33	152.0
0.9	5.06	6.36	164.4
1	3.94	5.61	198.7
1.1	3.93	5.61	207.7
1.2	4.39	5.93	219.6
1.5	5.19	6.44	230.1
1.7	5.34	6.53	209.8
1.9	5.04	6.35	240.7
2	4.59	6.06	223.1

Table 4.37: *Variation of Curie constant, effective moment and Weiss constant of the material with lanthanum content.*

For each sample a positive Weiss constant was fitted to the data above the magnetic transition temperature, suggesting that in each case the material was becoming ferromagnetically ordered. The expected effective magnetic moment for each of these samples was calculated from the electronic configuration of the magnetic ions present $\frac{2}{3}Ni^{2+}$, $\frac{2}{3}Mn^{3+}$ and $\frac{2}{3}Mn^{4+}$ ($\mu_{eff} = [n(n+2)]^{1/2}$, *where* n = *number of*

unpaired electrons) as $5.60\mu_B$/mol. As can be seen from *table 4.35* a range of Curie constants and effective moments were calculated as the lanthanum content was varied, all higher than the expected value. As discussed in *Chapter Three* with the pure bismuth sample, this could be due to a number of factors, either the oxidation states of the magnetic ions present in the materials are incorrect or the materials were simply was not in the Curie Weiss region. If the oxidation states within the sample were incorrect, such as only Mn^{3+} was present then the effective magnetic based on $\frac{4}{3}Mn^{3+}$ and $\frac{2}{3}Ni^{2+}$ is expected to be $6.11\mu_B$/mol. Also when comparing the observed effective moments with that for similar materials such as $La_2(Mn^{4+})(Ni^{2+})O_6$ $\mu_{eff} = 5\mu_B$/mol[8], $Bi_2(Mn^{4+})(Ni^{2+})O_6$ $\mu_{eff} = 4.1\mu_B$/mol[9], $Bi(Mn^{3+})O_3$ $\mu_{eff} = 4.79\mu_B$/mol[10] and $Bi(Ni^{2+})O_3$ $\mu_{eff} = 2.90\mu_B$/mol[11]. This leads to the conclusion that these materials were simply not in the Curie Weiss region, and so explains the inconsistencies between the observed and expected values.

DC magnetization data was recorded on selected materials (*figures 4.35 – 4.46*) at 300 and 2K between ±5T. The 300K data revealed that all materials were paramagnetic at room temperature. The 2K data in each case displayed a saturation in the magnetic moment, suggesting that the materials were ferromagnetically ordered at this temperature.

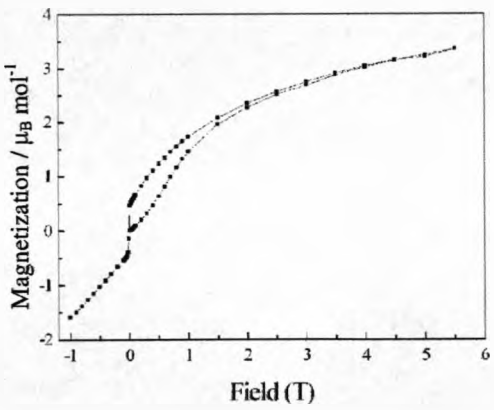

Figure 4.35: *Magnetization data collected at 2K on x = 0.1, the magnetic moment at 5T was calculated to be 3.25μ_B/mol however the material had clearly not saturated.*

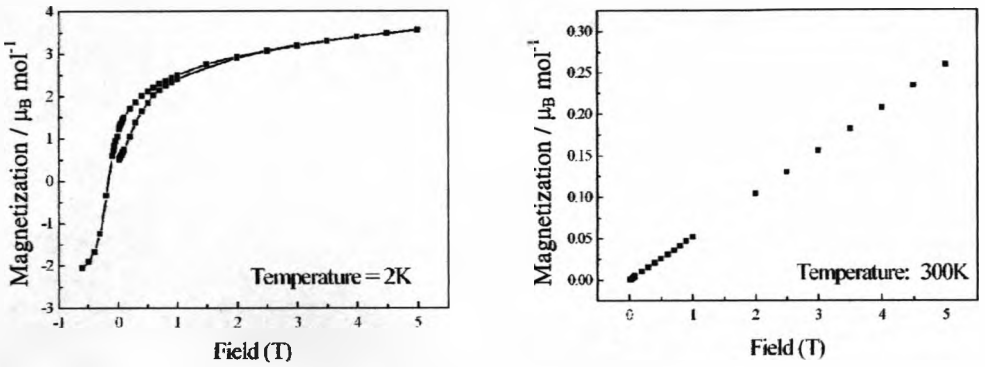

Figure 4.36: *Magnetization data collected at 2K and 300K on x = 0.5, the magnetic moment at 2K, 5T was calculated to be 3.25μ_B/mol however the material had clearly not saturated.*

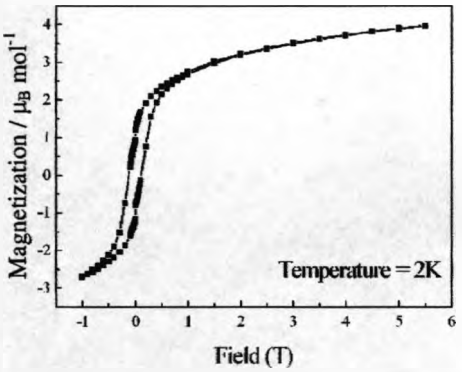

Figure 4.37: *Magnetization data collected at 2K on x = 0.7, the magnetic moment at 5T was calculated to be 3.90μ_B/mol however the material had clearly not saturated.*

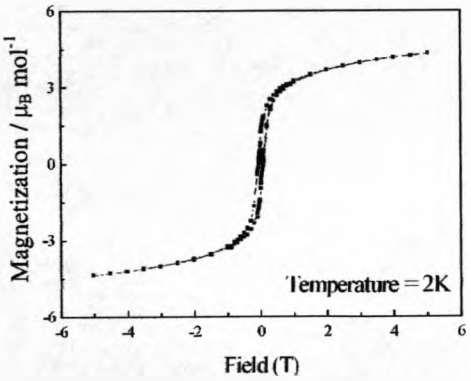

Figure 4.38: *Magnetization data collected at 2K on x = 0.8, the magnetic moment at 5T was calculated to be 4.34μ_B/mol however the material had clearly not saturated.*

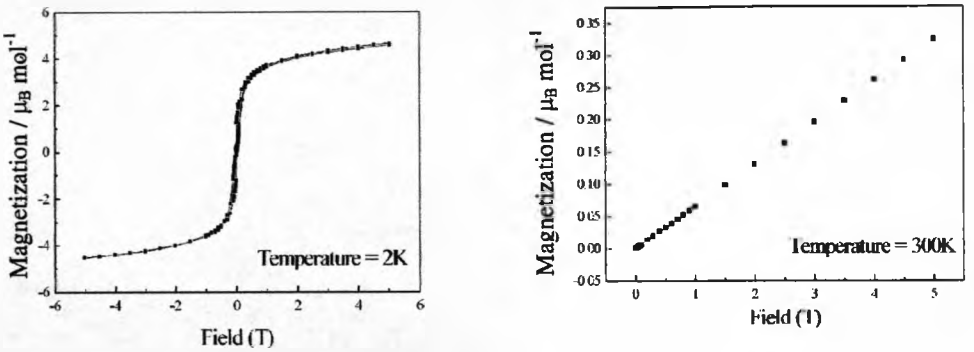

Figure 4.39: *Magnetization data collected at 2K and 300K on x = 0.9, the magnetic moment at 2K, 5T was calculated as 4.65μ_B/mol however the material had clearly not saturated.*

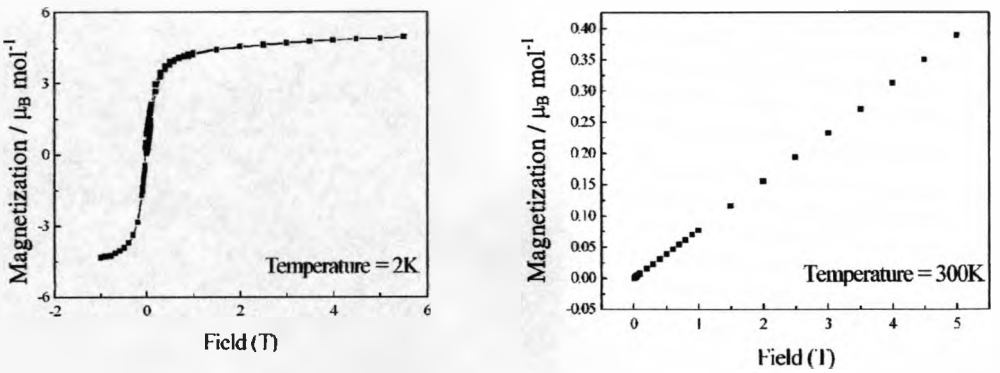

Figure 4.40: *Magnetization data collected at 2K and 300K on x = 1.0, the magnetic moment at 2K, 5T was calculated to be 4.91μ_B/mol however the material had clearly not saturated.*

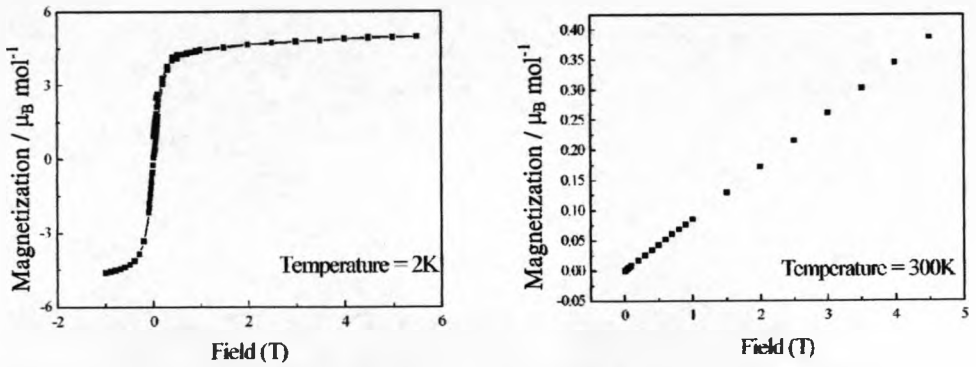

Figure 4.41: *Magnetization data collected at 2K and 300K on x = 1.1, the magnetic moment at 2K, 5T was calculated to be 4.96μ_B/mol however the material had clearly not saturated.*

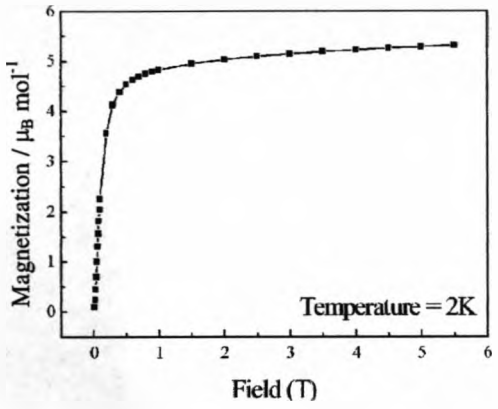

Figure 4.42: *Magnetization data collected at 2K on x = 1.2, the magnetic moment at 5T was calculated to be 5.29μ_B/mol however the material had clearly not saturated.*

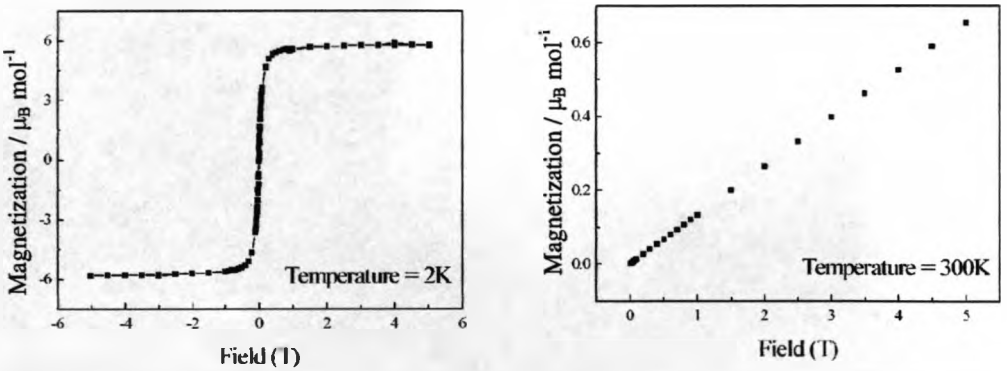

Figure 4.43: *Magnetization data collected at 2K and 300K on x = 1.5, the magnetic moment at 2K, 5T was calculated to be 5.82μ_B/mol however the material had clearly not saturated.*

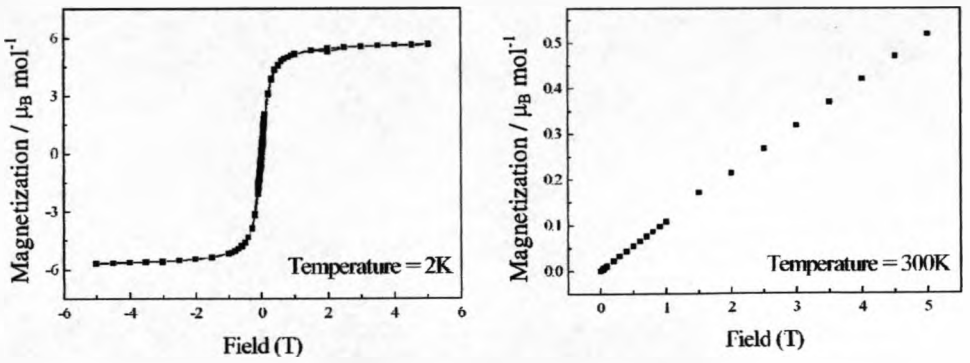

Figure 4.44: *Magnetization data collected at 2K and 300K on x = 1.7, the magnetic moment at 2K, 5T was calculated to be 5.67μ_B/mol.*

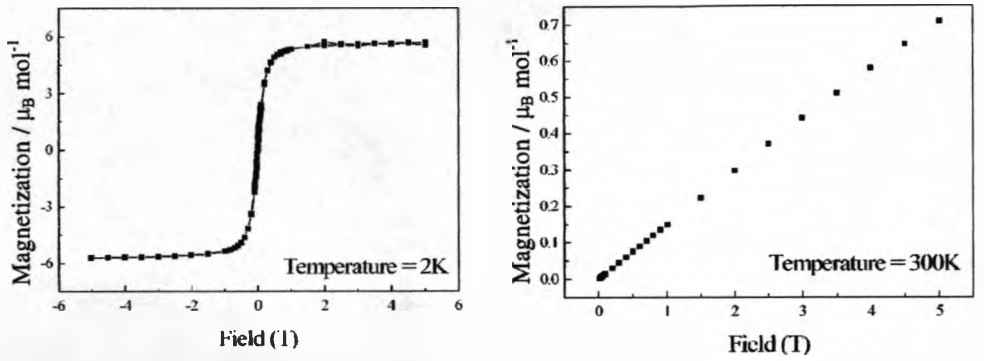

Figure 4.45: *Magnetization data collected at 2K and 300K on x = 1.9, the magnetic moment at 2K, 5T was calculated to be 5.67μ_B/mol.*

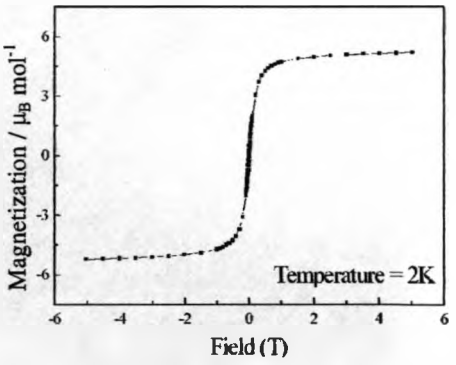

Figure 4.46: *Magnetization data collected at 2K on x = 2.0, the magnetic moment at 5T was calculated to be 5.22μ_B/mol.*

The following table lists the maximum magnetic moments observed in each material, only materials with greater lanthanum content than 1.2 achieved saturation, therefore the magnetic moments are quoted at a field 5T.

$Bi_{2-x}La_xMn_{4/3}Ni_{2/3}O_6$ (x =)	Magnetic Moment at 5T / μ_B mol^{-1}
0	3.55
0.1	3.25
0.5	3.56
0.7	3.90
0.8	4.34
0.9	4.65
1	4.91
1.1	4.96
1.2	5.29
1.5	5.82
1.7	5.67
1.9	5.67
2	5.22

Table 4.38: *Variation of the magnetic moment of each material measured at 5T with lanthanum content.*

Although the zero-field-cooled-field-cooled (ZFC-FC) data implied that the all of these materials were becoming ferromagnetically ordered, no extra Bragg scattering was observed in the neutron diffraction data measured at 2K for materials with a lanthanum content of x = 0.8 and less *(sections 4.3.1.1 to 4.3.1.5)*. This implies that, as in the case of the parent material *(Chapter Three)*, there is no long range ferromagnetic ordering present within the material for these samples. This is probably due to the fact that, as in the parent case, the transition seen in the ZFC-FC data of materials exhibited no extra scattering in the neutron diffraction data at 2K was due to spin glass freezing[12,13] rather than long range magnetic ordering. Spin

glass freezing, as discussed in *Chapter One*, means magnetic ordering occurs only over a very small range (within a few atoms). To investigate this AC susceptibility data was recorded over a 1 to 1000Hz frequency range with an AC driving field of 1Oe for a material exhibiting no extra scattering in the 2K neutron data (x = 0.8) and one that does (x = 0.9).

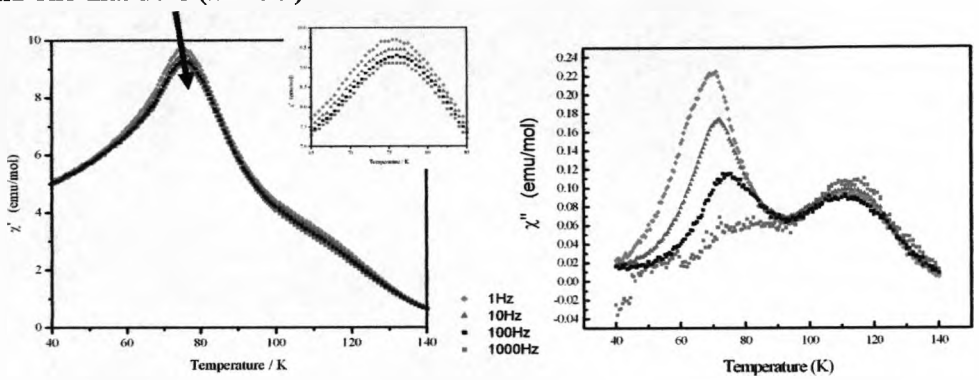

Figure 4.47: *Frequency dependence of the AC susceptibility of $Bi_{1.2}La_{0.8}Mn_{4/3}Ni_{2/3}O_6$ shows that the transition at 85K has a frequency dependency and so is due to spin glass freezing. Plots of the real (left) and imaginary (right)*

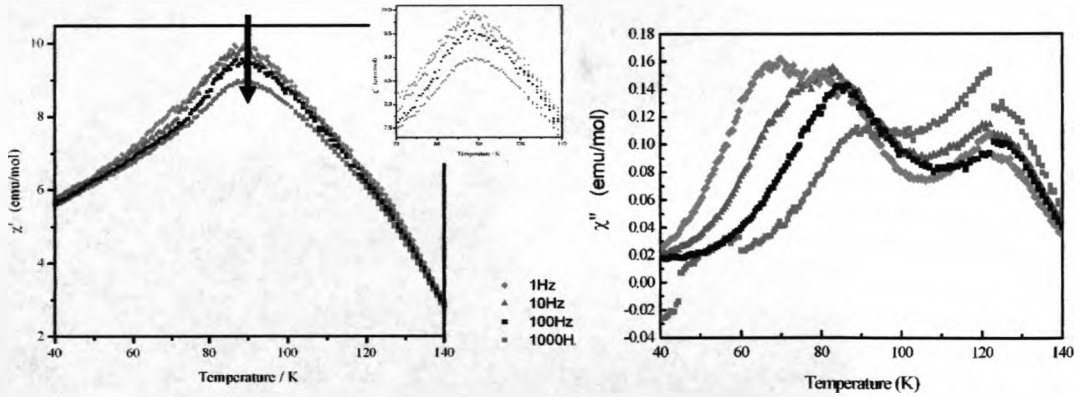

Figure 4.48: *Frequency dependence of the AC susceptibility of $Bi_{1.1}La_{0.9}Mn_{4/3}Ni_{2/3}O_6$ shows that the transition at 120K has no frequency dependency and so is due to long range ferromagnetic ordering. Plots of the real (left) and imaginary (right) components are given.*

Figures 4.47 and *4.48* show that the material which exhibited no extra scattering in the neutron diffraction data at 2K (x = 0.8, *figure 4.47*) displayed a frequency dependent maxima in the AC susceptibility data, whereas the material that did exhibit extra Bragg scattering at 2K (x = 0.9, *figure 4.48*) did not have a frequency dependent maxima. This implies that the magnetic transition observed in the $Bi_{1.2}La_{0.8}Mn_{4/3}Ni_{2/3}O_6$ material is due to spin glass ordering, whereas the magnetic transition in the $Bi_{1.1}La_{0.9}Mn_{4/3}Ni_{2/3}O_6$ material was due to long range magnetic ordering.

Taking this conclusion forward and applying it to all of the samples in the $Bi_{2-x}La_xMn_{4/3}Ni_{2/3}O_6$ series leads to the conclusion that all materials with a lanthanum content less than x = 0.9 display no long range ordering at low temperatures, but transform to spin glass states. Whereas for materials with a lanthanum content of x = 0.9 and greater, these display long range magnetic ordering and can therefore be considered as ferromagnets below their ordering temperatures. In this series of materials, the ferromagnetism arises from the coupling between Mn^{4+} and Ni^{2+} ions. Ferromagnetic ordering occurs due to the super exchange interaction between the empty e_g-orbital of Mn^{4+} (d^3 configuration) and the occupied e_g-orbital of Ni^{2+} (d^8 configuration). The spin glass state arises due to the presence of Mn^{3+} in the material, this has a d^4 electronic configuration and so has an occupied e_g-orbital. This means that antiferromagnetic coupling can occur through the interaction of two occupied e_g-orbitals.

For each of these materials the magnetic structure has been refined from the low temperature neutron diffraction data. Reasonable agreement was seen (*table 4.39*) between the SQUID observed magnetic moments and those calculated form the diffraction pattern using the magnetic k-vector of 0,0,0. The slight inconsistency between the observed and calculated moments can be explained by the fact the calculated moment was refined only from the extra scattering on two peaks in the diffraction pattern.

$Bi_{2-x}La_xMn_{4/3}Ni_{2/3}O_6$ x =	SQUID observed magnetic moment / μ_B mol^{-1}	Calculated magnetic Moment / μ_B mol^{-1}
0.9	4.65	3.10
1.2	5.29	4.12
2	5.22	4.34

Table 4.39: *Comparison between the SQUID observed magnetic moments and those calculated from the 2K neutron diffraction data for the ferromagnetic materials.*

All measurements were carried out inside a gelatine capsule fixed to the midpoint of a straw; the samples were measured in the form of pressed pellets which were fixed into place by inverting the capsule. The diamagnetic correction for each sample was calculated, ((2-x(25)+x(20)+92) x 10^{-6} emu/mol) and subtracted from all data recorded.

4.3.5 Muon Spin Relaxation

Prof. Stephen Blundell at the University of Oxford carried out zero-field muon spin relaxation (ZF-μ^+SR) measurements on three samples in the $Bi_{2-x}La_xMn_{4/3}Ni_{2/3}O_6$ series (x = 0.5, 0.9 and 1.2) using the MuSR instrument at the ISIS Pulsed Muon facility, Rutherford Appleton Laboratory, U.K, using a closed-cycle refrigerator. The samples were wrapped in silver foil and mounted on a silver sample holder. Measurements were also obtained on the pure bismuth sample and are detailed in *Chapter 3, section 3.3.6.*

Muon data were collected on each of the samples at six temperatures. The initial asymmetry (measured at t=0) corresponded to ~27% in each case, which is the theoretical maximum value expected for the geometry of detectors in this spectrometer. At high temperatures the relaxation of the muon spin can be seen to follow simple exponential behavior in each of the samples, this is indicative of paramagnetism. However as the samples were cooled, the paramagnetic spin fluctuations slow down providing less of resistance to the muon relaxing, so causes an increase in the muon-spin relaxation rate and so a decrease of the muon polarization within the sample.

In each case as the material was cooled below a certain temperature the initial asymmetry fell sharply and the relaxation rate decreased (*figure 4.49*). This can be explained by magnetic order developing in the sample and leading to an internal field at the muon site which causes muon precession faster than $1/t_{pulse}$, where

t_{pulse}~70 ns and is not directly observable at ISIS. As the doping level of lanthanum in the sample increases the temperature at which this is observed increases, which is consistent with the SQUID data *(section 4.3.4)* increasing transition temperatures with increasing lanthanum level. The data suggests that the magnetic ordering occurs below 85K in the x = 0.5 sample, whereas for the x = 0.9 and 1.2 samples ordering occurs below 150 and 200K respectively.

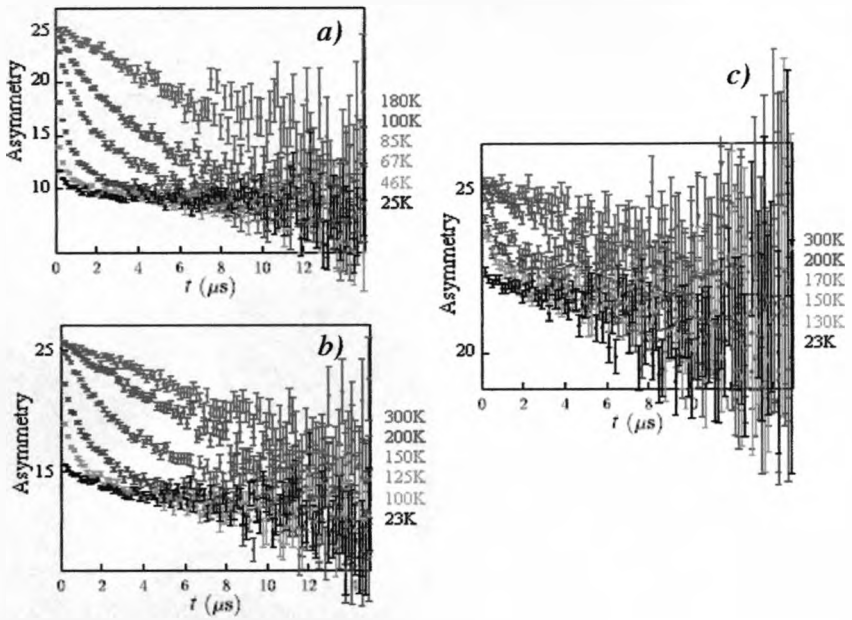

Figure 4.49: *Muon asymmetry data collected on three samples in the $Bi_{2-x}La_xMn_{4/3}Ni_{2/3}O_6$ series (x = 0.5(a) , 0.9(b) and 1.2(c)) as a function of time for six selected temperatures. The data do not relax to 0% asymmetry due to a substantial contribution from muons stopping in the sample holder and cryostat tails.*

The temperature dependency of the initial muon polarization for each of the samples measured shows clearly the temperature of the transitions from ordered phases

where the initial polarization is 0% to paramagnetic phases when the initial polarization is 100% increases with lanthanum content. The ordering temperatures seen in the muon data are consistent with the SQUID observed ordering temperatures *(section 4.3.4)* of 50, 120 and 180K for samples with x = 0.5, 0.9 and 1.2 respectively.

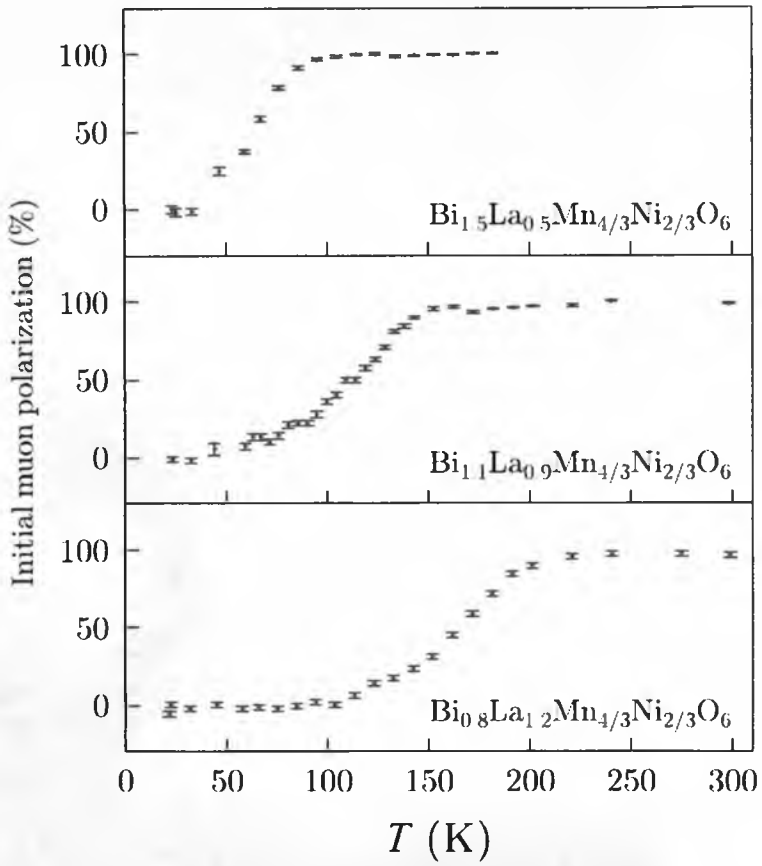

Figure 4.50: *The initial normalized muon polarization of three samples in the $Bi_{2-x}La_xMn_{4/3}Ni_{2/3}O_6$ series (normalization has been carried out to display the percentage of muons not coupled to a static, ordered local field, therefore 0% in the ordered phase and 100% in the paramagnetic phase)*

4.3.6 Dielectric Properties

A.C. impedance data were collected on one of the materials in the $Bi_{2-x}La_xMn_{4/3}Ni_{2/3}O_6$ series, x = 0.1 to investigate the effect of lanthanum doping on the dielectric properties. Measurements were carried out with the assistance of Dr. Xiaojun Kuang using a Solatron 1255B Frequency Response Analyzer and a Solatron 1296 dielectric interface over the frequency range of 1-10^6Hz from room temperature to 200°C. Silver paste electrodes were thermally treated at 400°C for ~30 minutes before the measurement began. The conductivity at room temperature was measured at ~3 x $10^{-3}\Omega^{-1}cm^{-1}$, this is considered too high to carry out any conclusive ferroelectric tests.

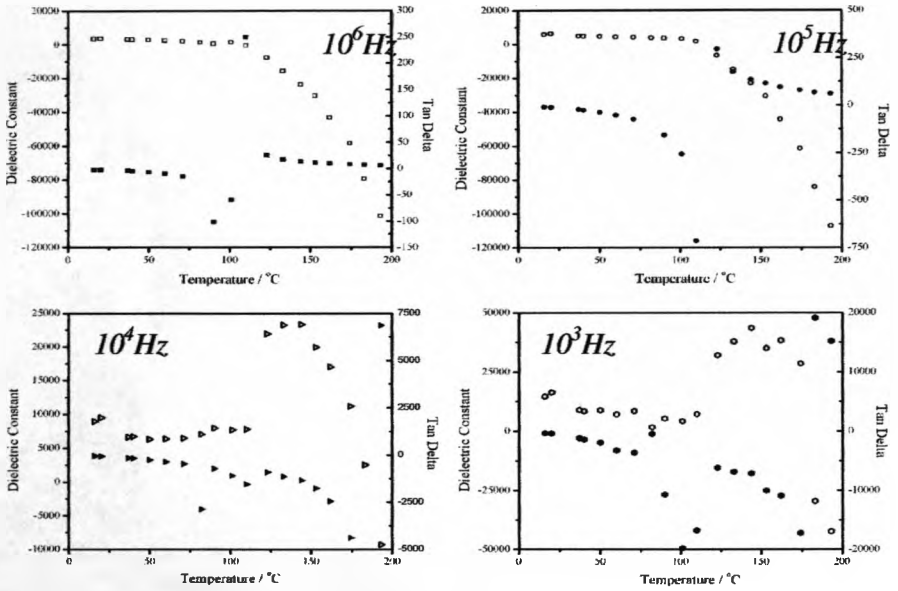

Figure 4.51: *Temperature dependencies of the dielectric constant and Tan Delta at selected frequencies collected on $Bi_{1.9}La_{0.1}Mn_{4/3}Ni_{2/3}O_6$. Open data points are the dielectric constants and closed data points are the tan delta data points.*

The temperature dependency of the dielectric constant *(figure 4.51)* shows a maximum in the temperature region of ~150°C suggesting that the sample is undergoing a ferroelectric-like transition. However no variable temperature diffraction data was collected on this material to support this, although materials with a lower and higher lanthanum content than this sample exhibit structural transitions close to this temperature, ~200°C for x = 0 and ~100°C for x = 0.3.

4.4 Discussion

4.4.1 Structural Study

The structural study carried out revealed two perovskite based structures as in the x = 0 material. The structure the material adopted varied with varying lanthanum doping. High bismuth content materials favoured the incommensurate structure, whereas high lanthanum content materials favoured the commensurate Pnma form. The temperature at which the material underwent the transition between these forms decreased from ~200°C for the x = 0 sample as the lanthanum doping increased until by x = 0.9 and onwards, when all materials were in the Pnma structure at all temperatures. Both the incommensurate and commensurate forms are perovskite based, with Bi^{3+} and La^{3+} ions on the A-site with a random distribution of 33% Mn^{4+}, 33% Mn^{3+} and 33% Ni^{2+} ions on the B-site in site the oxygen octahedra. It is the tilting of these octahedra that causes the distortion of the structure from the perovskite unit in the two forms. The modulation in the incommensurate structure was caused by the movement of the A-site cations (Bi^{3+} and La^{3+}) off position.

In summary, a full doping study of $Bi_2Mn_{4/3}Ni_{2/3}O_6$ with lanthanum was carried out. The structure the materials adopted could be varied with lanthanum content. Unfortunately, as in the parent material, the high bismuth content incommensurate structure was not polar as the modulation had cancelled out any polarisation and so ruled out any possibility for ferroelectricity. However, this study could be applied to future materials which are polar and under went a transition to a non-polar form, as this study did show that it was possible to tune the temperature of this transition with lanthanum content.

4.4.2 Magnetic Properties

The magnetic properties of the materials were studied as the lanthanum content was varied. The magnetic ordering temperature was shown to increase with increasing lanthanum content. Curie-Weiss fitting of the data above the transitions suggested that each of the materials was becoming ferromagnetic. However, low temperature neutron diffraction data revealed that only samples with a lanthanum content of $x = 0.9$ and more exhibited extra Bragg scattering at 2K, therefore only these materials displayed long range magnetic ordering. Tests carried out on materials with a lanthanum content less than $x = 0.9$ revealed that, like in the $x = 0$ case, the magnetic transition was due to spin glass freezing rather than ordering. This arises due to the random distribution of Mn^{4+}, Mn^{3+} and Ni^{2+} ions on the B-site, meaning that other antiferromagnetic couplings can occur and not just the ferromagnetic Mn^{4+} - Ni^{2+} coupling.

Materials that were true ferromagnets ($x \geq 0.9$) as already stated displayed extra Bragg scattering in the low temperature neutron diffraction data. The magnetic structure was refined from this using a k-vector of 0,0,0 which was consistent with ferromagnetism. This revealed that the spins on the B-site align parallel along the B-direction, the refined magnetic moments were slightly lower than that observed. This can be explained by the fact that the structure was calculated from the extra scattering on only two peaks.

4.4.3 Summary

To summarise, a full doping study was carried out on $Bi_2Mn_{4/3}Ni_{2/3}O_6$ with lanthanum. It was shown that it is possible to vary both the structural transition and magnetic ordering temperatures with lanthanum content. The initial aim was to prepare a polar material that would undergo a transition to a non-polar form, i.e. a ferroelectric and attempt to couple this with a magnetic transition, i.e. form a multiferroic material. Unfortunately, the polar structure in this series was incommensurate and the modulation cancelled out the polarity. Only transitions from the incommensurate structure to commensurate form were seen, however by varying the lanthanum content the temperature at which this occurred was also varied. Also, the magnetic transition temperature was found to vary with lanthanum content, increasing from 35K with $x = 0$ to 230K with $x = 2$. Therefore had the material been polar, doping lanthanum into the material would have lowered the structural transition and increased the magnetic ordering temperatures enough so that the material was ferromagnetically ordered and polar simultaneously, and so producing a multiferroic material. *Figure 4.52* estimates at what doping level this

would have occurred by plotting both transition temperatures on the same plot, It is estimated that a multiferroic material would have been formed at x ~ 0.85.

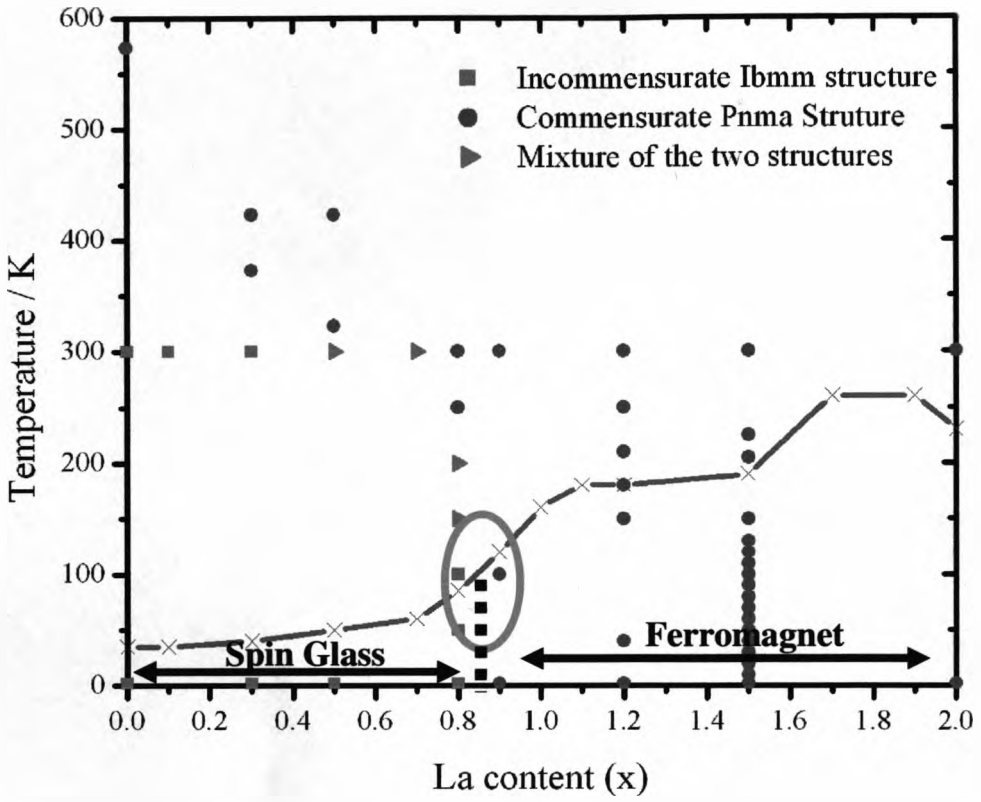

Figure 4.52: *Phase diagram showing the effect of lanthanum content on both the structure of the material and the magnetic transition temperature. The circle represents the area estimated that the structural and magnetic transition would be higher and low enough so the couple.*

Although this investigation proved unsuccessful in producing multiferroic material, it did show how through the use of lanthanum doping that it is possible to tune the transition temperatures of a material. This work could be taken forward and used in

a material that exhibited a high ferroelectric transition and low magnetic transition temperature to bring the two to meet and form a multiferroic material.

4.5 References

(1) Koehler, W. C.; Wollan, E. O. *Journal of Physics and Chemistry of Solids* **1957**, *2*, 100-106.

(2) Azad, A. K.; Mellergard, A.; Eriksson, S. G.; Ivanov, S. A.; Yunus, S. M.; Lindberg, F.; Svensson, G.; Mathieu, R. *Materials Research Bulletin* **2005**, *40*, 1633-1644.

(3) Schinzer, C. *Journal of Physics and Chemistry of Solids* **2000**, *61*, 1543-1551.

(4) Joly, V. L. J.; Date, S. K.; Joy, P. A. *Solid State Communications* **2004**, *130*, 547-550.

(5) Bull, C. L.; Gleeson, D.; Knight, K. S. *J. Physics: Condensed Matter* **2003**, *15*, 4927-4936.

(6) Brown, I. D. *Chemical Society* **1978**, *7*, 359-376.

(7) Brown, I. D. *Acta Cryst. B* **1985**, *41*, 244-247.

(8) Matar, S. F.; Subramanian, M. A.; Villesuzanne, A.; Eyert, V.; Whangbo, M. H. *Journal of Magnetism and Magnetic Materials* **2007**, *308*, 116-119.

(9) Azuma, M.; Takata, K.; Saito, T.; Ishiwata, S.; Shimakawa, Y.; Takano, M. *J. Amer. Chem. Soc.* **2005**, *127*, 8889-8892.

(10) Belik, A. A.; et.al. *J. Amer. Chem. Soc.* **2007**, *129*, 971-977.

(11) Ishiwata, S.; Azuma, M.; Takano, M.; Nishibori, E.; Takata, M.; Sakata, M.; Kato, K. *J. Mater. Chem.* **2002**, *12*, 3733-3737.

(12) Blundell, S. J. *Magnetism in condensed matter*; Oxford University Press: Oxford, 2001.

(13) Mydosh, J. A. *Spin Glasses: an experimental introduction* London, Washington and DC, 1993.

(14) Blundell, S. J. *Contemporary Physics* **1999**, *40*, 175.

Chapter 5: Synthesis and Characterization of other perovskite systems

5.1 Introduction

This chapter will deal with the exploration of other perovskites following on from the work carried out on the $Bi_{2-x}La_xMn_{4/3}Ni_{2/3}O_6$ system. Key principles found during the work on the $Bi_{2-x}La_xMn_{4/3}Ni_{2/3}O_6$ system were taken and applied to other perovskite systems. This included precautions to prevent bismuth loss from the material through use of platinum foil, step-wise reaction temperatures starting at temperatures below the melting point of Bi_2O_3 and heating samples to no greater than 950°C above which bismuth loss is known to occur. It also included taking the novel composition, $Bi_2(M1^{4+})_{2/3}(M2^{3+})_{2/3}(M3^{2+})_{2/3}O_6$ and exploring substitutions that could be carried out on the three metal sites.

A number of trials were made exploring other possible perovskite phases that could be made at ambient pressure. However as this chapter will demonstrate this proved very difficult, and provided an insight as to how unique the $Bi_{2-x}La_xMn_{4/3}Ni_{2/3}O_6$ system is.

5.2 $Bi_2Ti_{2/3}Mn_{2/3}Ni_{2/3}O_6$

5.2.1 Synthesis

The sample $Bi_2Mn_{4/3}Ni_{2/3}O_6$ was taken and an attempt to substitute the Mn^{4+} with Ti^{4+} was made. Samples were prepared by a standard ceramic method, on a scale between 0.5g and 5g. Stoichiometric quantities of Bi_2O_3 (Alfa 99.9995%), TiO_2 (Alfa Aesar 99.995%), MnO_2 (Alfa Aesar 99.999%) and NiO (Alfa Aesar 99.998%) were ground and pelletized. The pellet was placed on platinum foil in an alumina boat (reaction occurs with the boat if this precaution is not taken) and heated at 800°C for 12 hours, 850°C for 12 hours, 900°C for 12 hours and then 950 °C for 12 hours. In between each firing stage the pellet was ground in an agate mortar and pestle, and then repelletized. All steps used a heating rate of 5°C per minute and a cooling rate of 10°C per minute.

5.2.2 Characterization

5.2.2.1 Room temperature X-ray Powder Diffraction

X-ray powder diffraction data were collected on station 9.1 of the Daresbury Synchrotron Radiation Source at room temperature. At first the powder pattern appeared to index to the unit cell based on the originally thought $Bi_2Mn_{4/3}Ni_{2/3}O_6$ non-centrosymmetric space group, $Pn2_1m$ an orthorhombic cell with the parameters $\sqrt{2}a_p$ x $2\sqrt{2}a_p$ x $4a_p$. This would have meant that the material was polarised at room temperature. However when a LeBail fit was carried out in GSAS using this space

group it revealed a misfit on the low angle peaks like in the parent material, which suggested that this substituted material was also modulated.

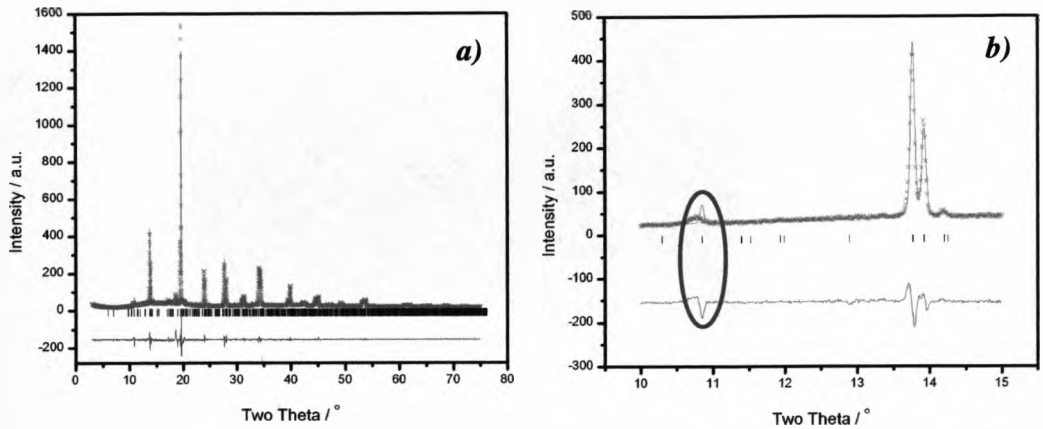

Figure 5.1: *Le Bail fit in the space group $Pn2_1m$ of the X-ray Powder Diffraction data collected at room temperature on Station 9.1 of the Daresbury Synchrotron Radiation Source. The pink crosses are the observed data, green line is the calculated profile, the purple line is the difference plot and the black markers are the Bragg positions. Plot a) is the full diffraction pattern; plot b) is an expanded area of the pattern which highlights the misfit on the low angle peaks due to the modulation.*

Lattice Parameters		**Fit Parameters**	
Space Group	$Pn2_1m$	R_{wp} / %	6.02
a / A	5.6232(1)	R_p / %	5.19
b / Å	11.1661(3)	χ^2	4.632
c / Å	15.6696(3)		
Volume / $Å^3$	983.88(2)		

Table 5.1: *Refined lattice parameters and goodness of fit parameters from the commensurate Le Bail fit carried out on the room temperature powder X-ray diffraction data of $Bi_2Mn_{2/3}Ti_{2/3}Ni_{2/3}O_6$.*

The data were then fitted in the same superspace group as for the parent material, Ibmm(q00,0-p0)ss.gm. A LeBail fit was carried out using the program Jana2000, the lattice parameters and modulation vectors obtained are given in *table 5.2*. A full Rietveld refinement of the modulated structure could not be carried out on this data due to the quality, for reliable structural parameters single crystal data would be required. Therefore it must be assumed that the modulated structure of $Bi_2Mn_{2/3}Ti_{2/3}Ni_{2/3}O_6$ is the same as $Bi_2Mn_{4/3}Ni_{2/3}O_6$ as discussed in chapter three, with a random distribution of Ti^{4+}, Mn^{3+} and Ni^{2+} on the B-site inside the oxygen octahedra.

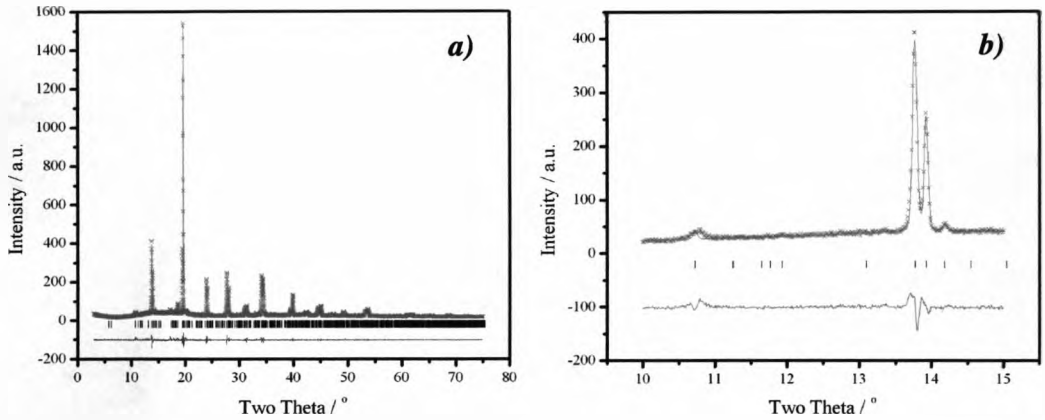

Figure 5.2: *Le Bail fit in the incommensurate model to the X-ray Powder Diffraction data collected at room temperature on Station 9.1 of the Daresbury Synchrotron Radiation Source. The pink crosses are the observed data, green line is the calculated profile, the purple line is the difference plot and the black markers are the Bragg positions. Plot a) is the full diffraction pattern, plot b) is an expanded area of the pattern which highlights the improved fit on the low angle peaks when compared to the commensurate fit.*

Lattice Parameters		Fit Parameters	
Space Group	Ibmm	R_{wp} / %	5.32
a / Å	5.62478(6)	R_p / %	3.69
b / Å	7.83558(10)		
c / Å	5.58292(2)		
(q_1 , 0 , 0)	0.54199(8)		
(0 , q_2 , 0)	-0.48700(13)		

Table 5.2: *Refined lattice parameters and goodness of fit parameters from the incommensurate Le Bail fit carried out on the room temperature powder X-ray diffraction data of* $Bi_2Mn_{2/3}Ti_{2/3}Ni_{2/3}O_6$.

5.2.2.2 Variable temperature X-Ray Powder Diffraction

X-ray powder diffraction data were collected on station 9.1 of the Daresbury Synchrotron Radiation Source between room temperature and 400°C. Analysis of this revealed that the material was undergoing a structural transition from the room temperature incommensurate structure to a commensurate Pnma structure over the region of 200 to 270°C. During heating data were collected over a small 2θ range (*figure 5.3*), an extra peak due to the Pnma structure could clearly be seen to grow in as the temperature was increased.

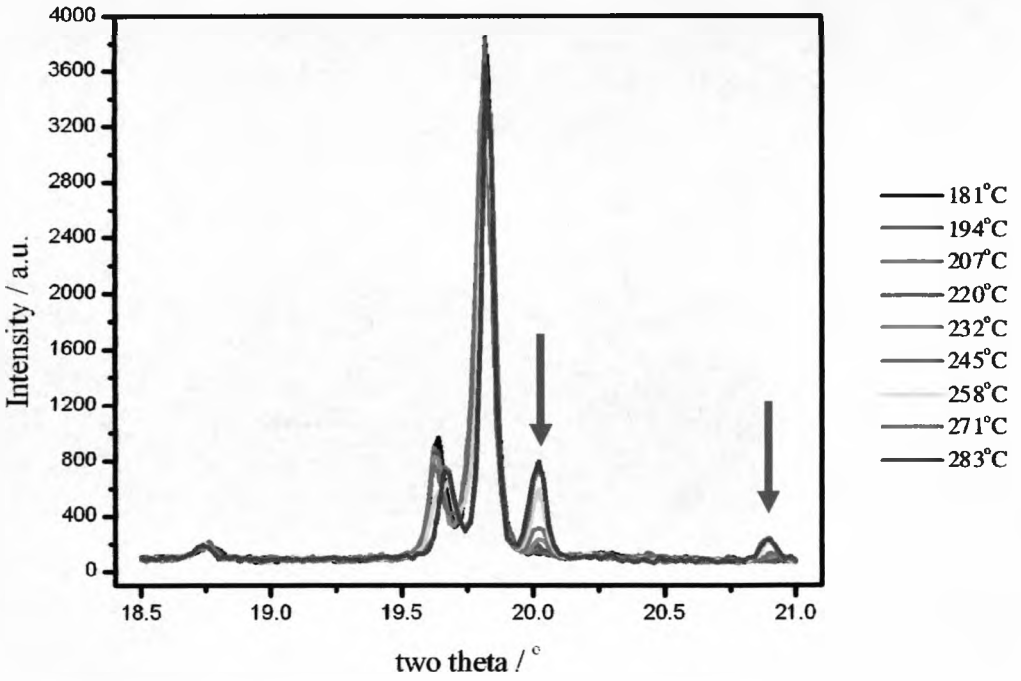

Figure 5.3: *X-ray powder diffraction patterns collected as $Bi_2Mn_{2/3}Ti_{2/3}Ni_{2/3}O_6$ was heated up on station 9.1 of the Daresbury radiation source. The blue arrows indicate the extra peaks that grew in on heating.*

The cell parameters of the sample were calculated from the small angular range collected, by carrying out a LeBail fit using GSAS in the space group $Pn2_1m$ using the cell $\sqrt{2}a_p$ x $2\sqrt{2}a_p$ x $4a_p$.

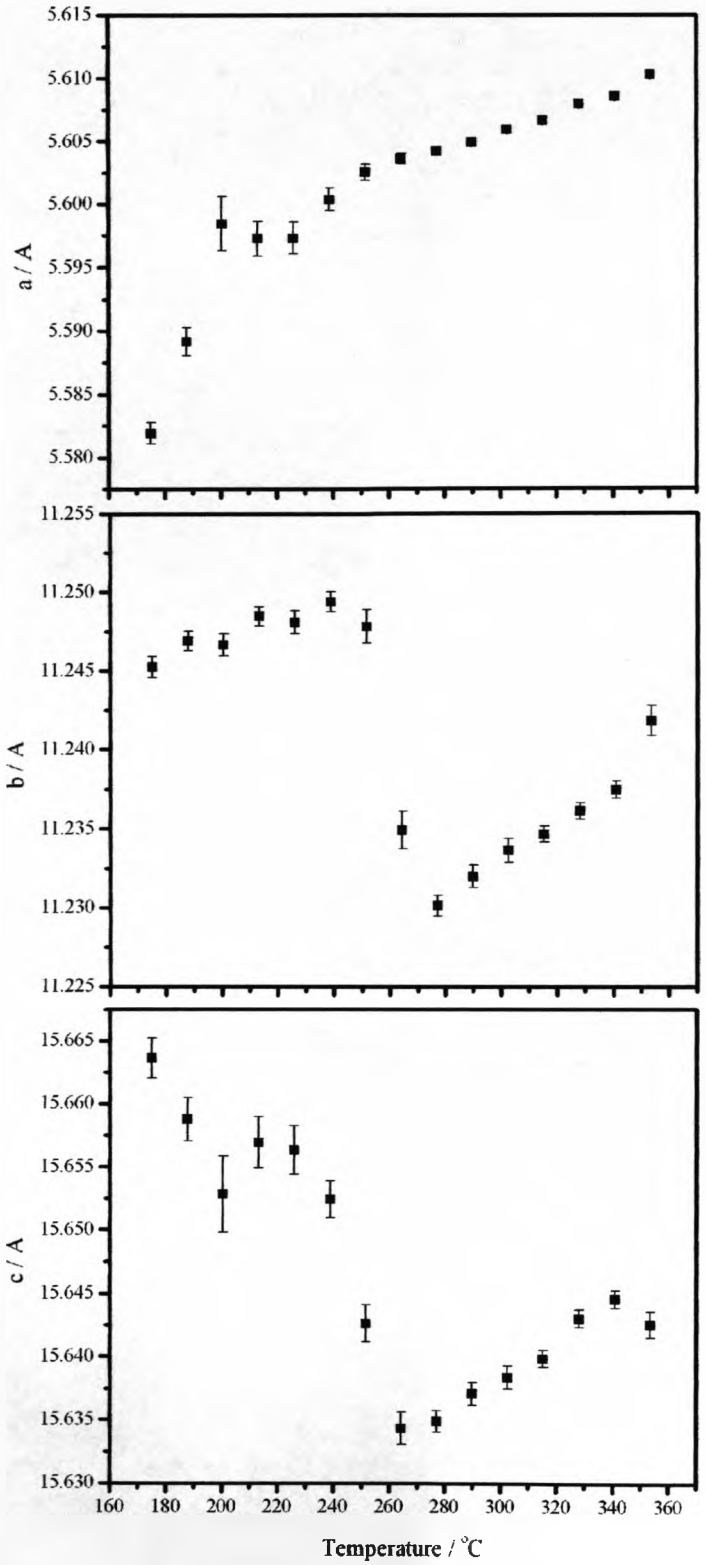

Figure 5.4: *Variation in cell parameters with temperature calculated from Le-Bail fits of the X-ray powder diffraction data collected on Daresbury SRS station 9.1*

The calculated cell parameters were then converted into their corresponding perovskite unit cell (a_p) values (i.e. a ~ $\sqrt{2}a_p$, b ~ $2\sqrt{2}a_p$ and c ~ $4a_p$). The ratio between these values was calculated and plotted as a function of temperature. The temperature of the structural change (200 to 270°C) can clearly be seen in both the a:b and c:b ratios *(figure 5.5)*. What is probably the most significant is the variation in the perovskite unit cell volume with temperature (a('a_p') x b('a_p') x c('a_p')). Before and after the material transforms it exhibits what can be considered as normal thermal expansion. However during the temperature region whilst the structure is changing the volume does not appear to vary significantly.

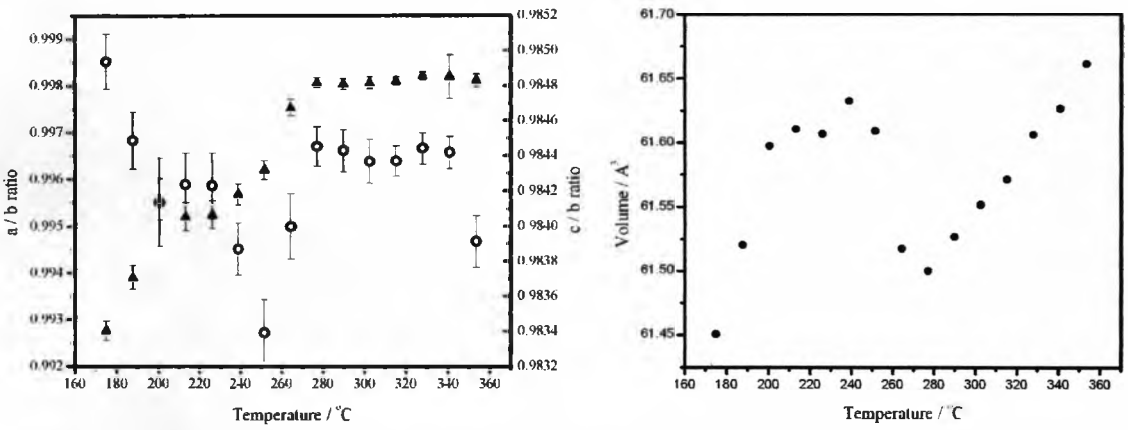

Figure 5.5: *Variation in the perovskite unit cell (a_p) values with temperature, left plot is the variation in the a / b (triangles) and c / b (circles) ratios, and right plot is the variation in the unit cell volume.*

Powder X-ray data were collected above the transition (at 400°C) on station 9.1 of the Daresbury Synchrotron Radiation Source. Rietveld refinement was carried out on the data using the non-polar Pnma structural model. Fit parameters and Bond Valence Sums confirm that the material adopts the Pnma structure above ~280°C.

This is a distorted form of the perovskite, with Bi^{3+} on the A-site in an 8 co-ordinate environment, and a random distribution of Ti^{4+}, Mn^{3+} and Ni^{2+} on the B-site in a six co-ordinate environment. Distortion from the parent perovskite structure occurs due to tilting of the BO_6 octahedra.

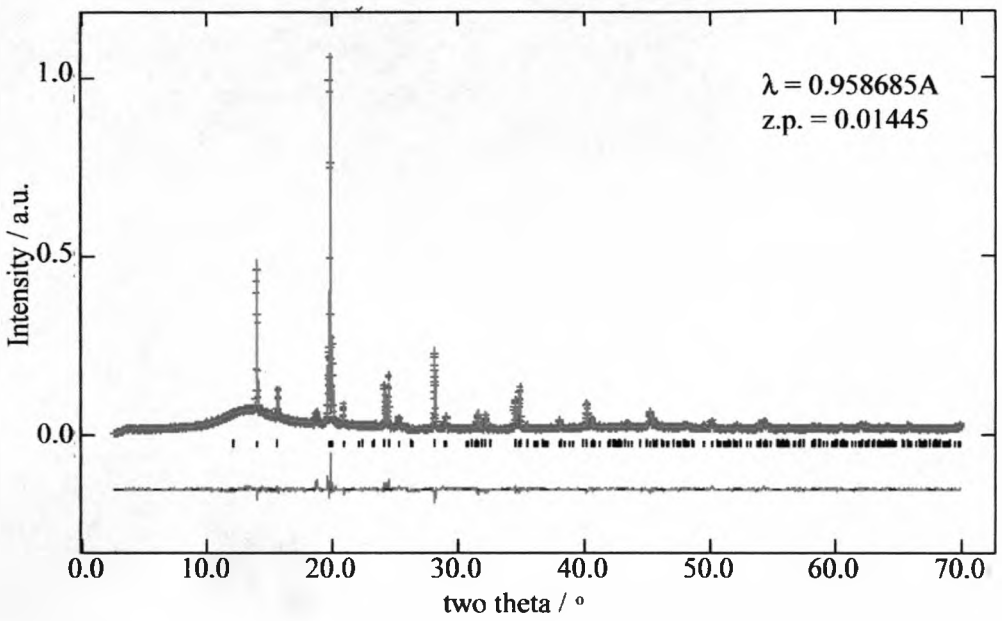

Figure 5.6: *Rietveld Refinement of 400°C powder X-ray diffraction data of $Bi_2Mn_{2/3}Ti_{2/3}Ni_{2/3}O_6$ against the Pnma model. The red crosses are observed data, the solid green line is the calculated pattern and the pink line is the difference.*

Lattice Parameters		Fit Parameters	
Space Group	Pnma	R_{wp} / %	8.27
a / Å	5.6192(1)	R_p / %	6.36
b / Å	7.8929(2)	Rf^2 / %	16.91
c / Å	5.5269(1)	χ^2	1.902
Volume / $Å^3$	245.13(1)		
Density / g cm^{-3}	8.422		

Table 5.3: *Refined lattice parameters and goodness of fit parameters from the Rietveld refinement of 400°C powder X-ray diffraction data of $Bi_2Mn_{2/3}Ti_{2/3}Ni_{2/3}O_6$.*

Atom	Occupancy	x	y	z	Uiso
Bi1	1	-0.03994(24)	0.25	-0.0071(9)	0.0528(8)
Mn1	0.333	0	0	0.5	0.0004(11)
Ti1	0.333	0	0	0.5	0.0004(11)
Ni1	0.333	0	0	0.5	0.0004(11)
O1	1	0.5111(34)	0.25	0.03(1)	0.064(11)
O2	1	0.2078(35)	-0.0169(34)	0.6968(30)	0.038(6)

Table 5.4: *Refined positional parameters from the Rietveld refinement of 400°C powder X-ray diffraction data of* $Bi_2Mn_{2/3}Ti_{2/3}Ni_{2/3}O_6$.

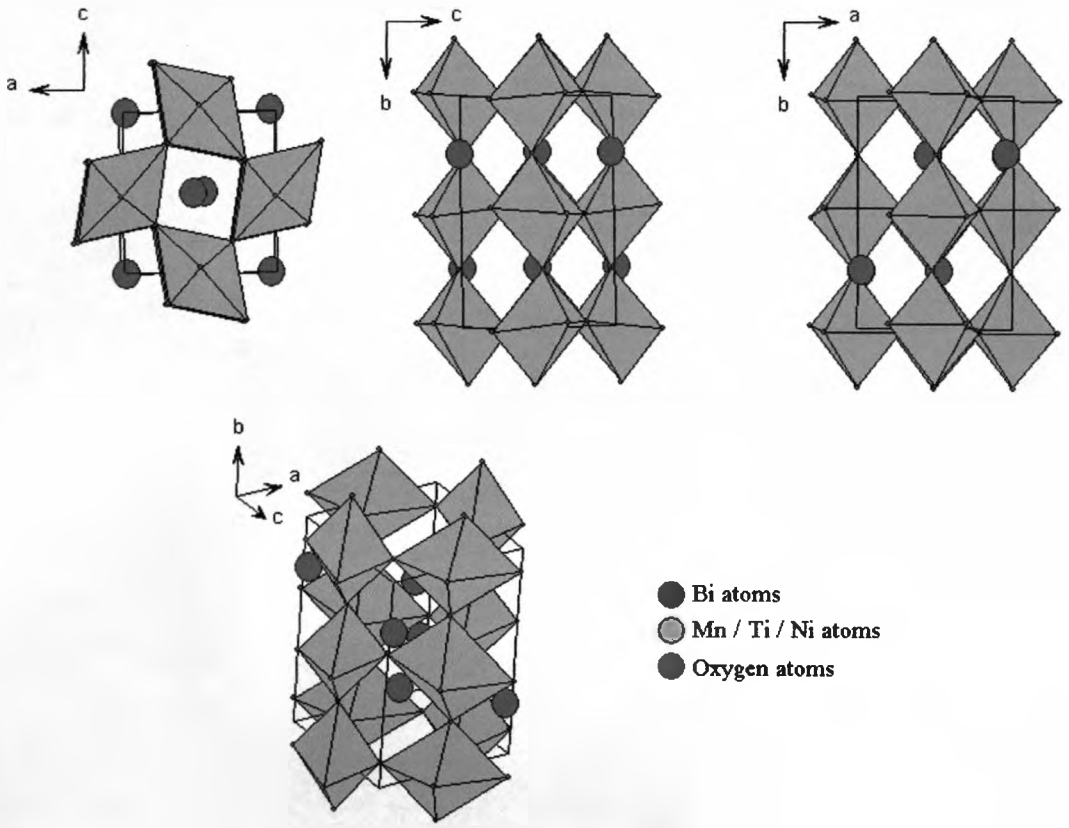

Figure 5.7: *Refined structure of* $Bi_2Mn_{2/3}Ti_{2/3}Ni_{2/3}O_6$ *obtained from the 9.1 data collected at 400°C viewed along the different planes. Blue spheres are Bi, pink octahedra containing randomly 33%* Ti^{4+}, *33%* Mn^{3+}, *33%* Ni^{2+} *surrounded by oxygen.*

The refined structure shown in *figure 5.7* shows a slightly distorted B-site oxygen octahedron, this is due to the structure being refined from powder X-ray diffraction data. It is very difficult to accurately determine the position of oxygens in a material when a heavy atom such as bismuth is also present. As discussed in *Chapter Two*, x-rays are scattered by the electron cloud surrounding the atoms and so if fewer electrons are present, the less the atom scatters the electron and so the harder it is to accurately locate that atom. In this case the pattern is dominated by the scattering of the bismuth and so makes it difficult to locate the oxygens. This also explains the inconsistency seen in the bond valence sums between the expected oxidation state of the B-site cations and that calculated (υ_i) from the refinement which are based on the bond distances between the metals and the oxygen. This could have been improved by collecting neutron diffraction data on this material.

	Atom Bonds	Bond Length (l_i) / Å	Bond Valence Sum, v_i (expected oxidation state)
Bi	Bi – O1	2.534 (19)	**1.880 (3+)**
	Bi – O1	3.104 (19)	
	Bi – O1	2.93 (5)	
	Bi – O1	2.63 (5)	
	Bi – O2 (x2)	3.016 (22)	
	Bi – O2 (x2)	2.847 (22)	
	Bi – O2 (x2)	2.688 (24)	
	Bi – O2 (x2)	2.747 (25)	
$Mn_{1/3}$	Mn1 – O2 (x2)	1.983 (5)	**4.602 (3+)**
	Mn1 – O2 (x2)	1.597 (17)	
	Mn1 – O2 (x2)	2.355 (17)	
$Ti_{1/3}$	Ti1 – O2 (x2)	1.983 (5)	**4.858 (4+)**
	Ti1 – O2 (x2)	1.597 (17)	
	Ti1 – O2 (x2)	2.355 (17)	
$Ni_{1/3}$	Ni1 – O2 (x2)	1.983 (5)	**3.456 (2+)**
	Ni1 – O2 (x2)	1.597 (17)	
	Ni1 – O2 (x2)	2.355 (17)	

Table 5.5: *Selected bond lengths and Bond Valence Sums[1] obtained from the powder x-ray diffraction data collected at 400°C of $Bi_2Mn_{2/3}Ti_{2/3}Ni_{2/3}O_6$.*

$BVS = \Sigma^{N}_{i=1} v_i$ $\quad R_o(Bi^{3+}) = 2.09^2$ $\quad R_o(Ni^{2+}) = 1.654^2$

$v_i = exp[(R_o - l_i)/B]$ $\quad R_o(Ti^{4+}) = 1.78^3$

$B = 0.37$ $\quad R_o(Mn^{3+}) = 1.76^2$

5.2.2.3 X-Ray Absorption Spectroscopy

XAS was carried out on station 7.1 at the SRS. Data were recorded at room temperature across the Ni K edge in ~ 0.5eV steps in transmission mode, a Ni metal K edge was run simultaneously as a form of energy calibration. La_2NiO_4 and $LaSrNiO_4$ were run as Ni^{2+} and Ni^{3+} standards respectively.

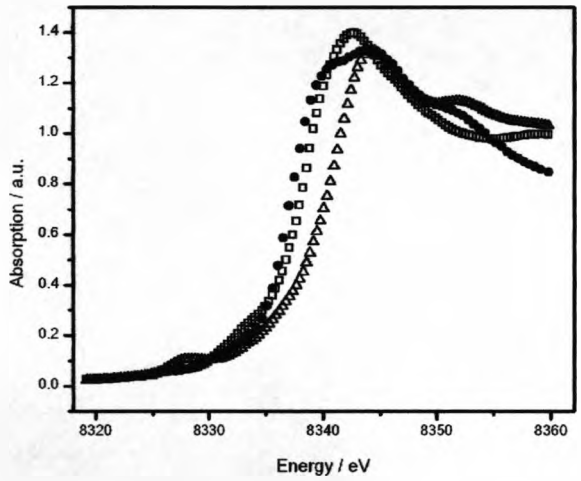

Sample	Edge Position / eV
La_2NiO_4 (Ni^{2+} Standard)	8338.54
$LaSrNiO_4$ (Ni^{3+} Standard)	8341.22
$Bi_2Mn_{2/3}Ti_{2/3}Ni_{2/3}O_6$ sample	8337.96

Figure 5.8: *X-ray absorption spectroscopy collected across the Ni K edge in ~ 0.5eV steps. The edge positions calculated for each of the samples are given in the table.*

Open squares: La_2NiO_4 (Ni^{2+} Standard), Open triangle: $LaSrNiO_4$ (Ni^{3+} Standard), and Closed circles: $Bi_2Mn_{2/3}Ti_{2/3}Ni_{2/3}O_6$ sample.

The XAS results show that the absorption edge of the nickel in both the sample and the 2+ standard are at the same energy, this suggests that the nickel in the $Bi_2Ti_{2/3}Mn_{2/3}Ni_{2/3}O_6$ sample is in the 2+ oxidation state. This suggests that the Ti has substituted the Mn^{4+} in the $Bi_2Mn_{4/3}Ni_{2/3}O_6$ material and gives an overall charge

balanced composition of $(Bi^{3+})_2(Ti^{4+})_{2/3}(Mn^{3+})_{2/3}(Ni^{2+})_{2/3}(O^{2-})_6$. However manganese edge XAS would be required to confirm this.

5.2.2.4 Dielectric Measurements

A.C. impedance data was collected with the assistance of Dr. Xiaojun Kuang using a Solatron 1255B Frequency Response Analyzer and a Solatron 1296 dielectric interface over the frequency range of 1-10^6Hz from room temperature to 400°C (*Figure 5.9*). Silver paste electrodes were thermally treated at 400°C for ~30 minutes before the measurement began. The conductivity at room temperature was measured at 5 x $10^{-5}\Omega^{-1}cm^{-1}$, this is considered too high to carry out any conclusive ferroelectric tests.

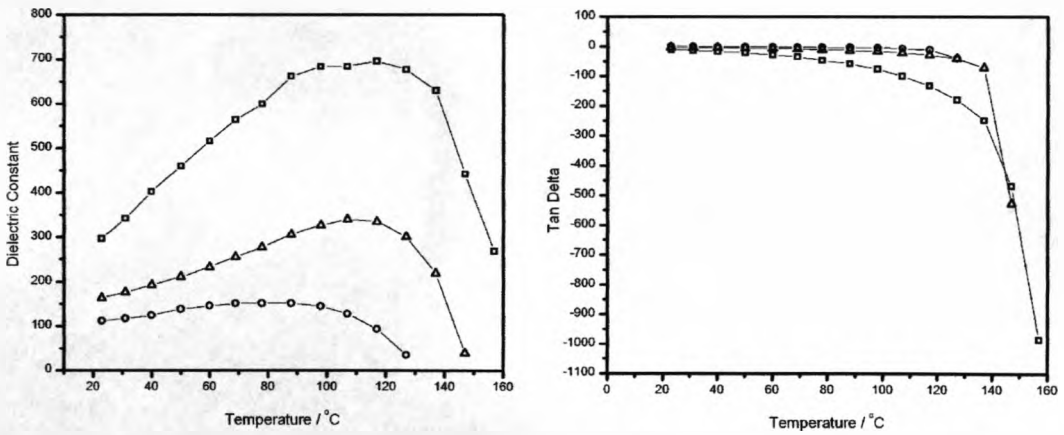

Figure 5.9: *Temperature dependencies of the dielectric constant (left plot) and Tan Delta (right plot) at selected frequencies. Open circle: 10^6Hz; Open triangle: 10^5Hz; Open Square: 10^4Hz*

The temperature dependency of the dielectric constant shows a maximum in the temperature region of 90 – 120°C, which suggests the sample is undergoing a

ferroelectric-like transition. This transition is supported by the fact that the sample undergoes a structural transition from the room temperature modulated structure to one refined in a non-polar space group. The material was also sent off to Professor P. Shiv Halasyamani at the University of Houston, Texas, USA for Second Harmonic Generation[4] (SHG) testing. As already discussed in *Chapter Three* the appearance of the phenomena SHG can be used to determine whether the material is non-centrosymmetric and so whether it is likely to be a ferroelectric. SHG is defined as the conversion of a specific wavelength of light into half its original, this occurs as a direct result of the polarisation in the material. A beam of light from a Nd-YAG laser (1064nm) is applied to the sample, if SHG occurs a green light will be emitted from the sample. Unfortunately the result came back negative for SHG, this suggests that the material is not polarised at room temperature. Although many factors could have caused this negative result, the most likely explanation is that the modulation in the material cancels out any polarity.

5.2.2.5 Magnetic Measurements

Magnetic susceptibility data were collected using a Quantum Design MPMS SQUID magnetometer. The diamagnetic correction for this sample was calculated as 1.40 x 10^4 emu/mol and was subtracted from all data recorded. The sample was loaded at room temperature and cooled in the absence of an applied field to 2K. A field of 100Oe was then applied and measurements were recorded between 2 and 300K, this system was then cooled again to 2K in the applied field and the measurements between 2 and 300K were repeated.

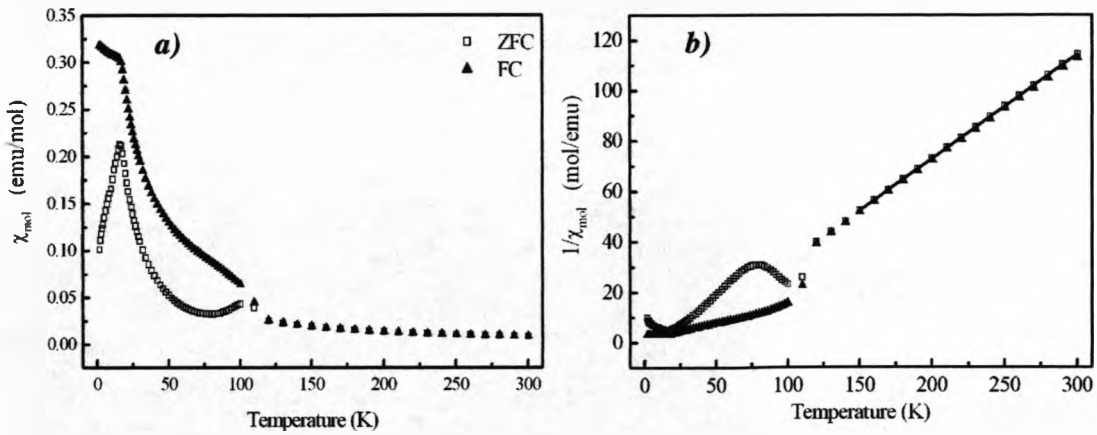

Figure 5.10: *a) ZFC-FC data collected at 100Oe and b) Inverse plot of the ZFC-FC data collected. Curie-Weiss fitting of the inverse chi of the zero-field-cooled reveals a Curie constant of 2.42emu/mol and a positive Weiss constant (θ = 24K) implying ferromagnetic ordering*

The magnetic susceptibility showed a divergence between the zero-field-cooled and the field-cooled data at 100K, this was taken as the magnetic ordering temperature of the sample, above this value (between 150 and 300K) the data was fitted by the simple Curie-Weiss equation for paramagnetism:

$$X(T) = C / (T - \theta)$$

The Curie constant (C) was fitted to 2.42 emu/mol and the corresponding effective magnetic moment was calculated from this Curie constant ($\mu_{eff} = (8C)^{1/2}$) as 4.4 μ_B/mol. The expected effective magnetic moment was calculated from the electronic configuration of the magnetic ions present $\frac{2}{3}Ni^{2+}$, $\frac{2}{3}Mn^{3+}$ and $\frac{2}{3}Ti^{4+}$ (μ_{eff} = $[n(n+2)]^{1/2}$, *where n = number of unpaired electrons*) as 4.62μ_B/mol. Good consistency is observed between the collected and expected effective moments.

DC magnetization data was recorded with a field sweep between -1T and 5.5T at 2K. A maximum magnetic moment of 1.25 μ_B/mol was observed in the 2K data, however saturation of the sample was not achieved by a field of ±5.5T.

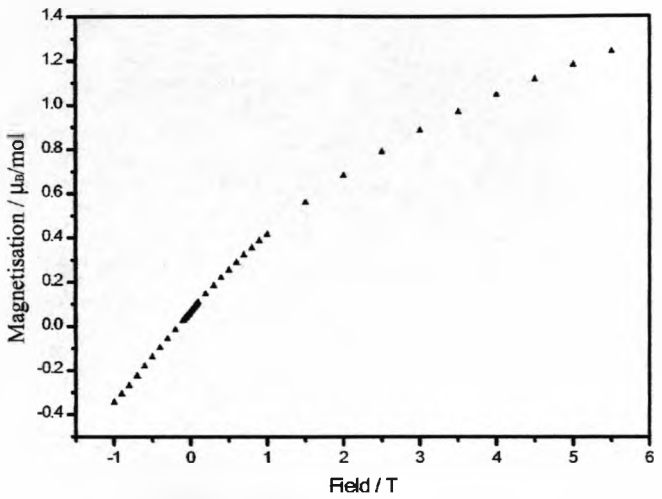

Figure 5.11: *Magnetization of $Bi_2Ti_{2/3}Mn_{2/3}Ni_{2/3}O_6$ collected at 2K.*

5.2.3 Discussion

This section has shown that it is possible to substitute the Mn^{4+} ions within the $Bi_2Mn_{4/3}Ni_{2/3}O_6$ material for Ti^{4+} to form another novel bismuth based perovskite at ambient pressure. The material was found to have a perovskite based structure that was modulated at room temperature and commensurate above 280°C. This transition was consistent with a maximum in the dielectric constant, however due to the high conductivity of the sample no conclusive ferroelectric tests were carried out. However a negative SHG result at room temperature would imply that the sample is not polarised at room temperature. Magnetisation data revealed a possible ferromagnetic transition at ~100°C, however no neutron diffraction studies were carried out on this material to confirm this.

No evidence was found to suggest any coupling between the structural transition from the modulated to non-polar structure and the magnetic transition.

5.3 $Bi_{2-x}La_xMn_{4/3}Co_{2/3}O_6$

5.3.1 Synthesis

Initially an attempt was made to prepare Bi_2MnCoO_6 by standard ceramic methods, during the course of my investigations it was reported that this phase can be prepared by high pressure synthesis[5]. However energy dispersive spectroscopy (EDS) measurements showed that the perovskite phase forming with the highest bismuth content was $BiLaMn_{4/3}Co_{2/3}O_6$. Samples with this correct composition were prepared by a standard ceramic method, on a scale between 0.5g and 5g. Stoichiometric quantities of Bi_2O_3 (Alfa 99.9995%), La_2O_3 (Alfa Aesar 99.998%), MnO_2 (Alfa Aesar 99.999%) and Co_3O_4 (Alfa Aesar 99.998%) were ground and pelletized. The pellet was placed on platinum foil in an alumina boat (reaction occurs with the boat if this precaution is not taken) and heated at 800°C for 12 hours, 850°C for 12 hours, 900°C for 12 hours and then 950°C for 12 hours. In between each firing stage the pellet was ground in an agate mortar and pestle, and then repelletized. All steps used a heating rate of 5°C per minute and a cooling rate of 10°C per minute. All characterisation techniques discussed in the following sections were performed on the highest bismuth content sample $BiLaMn_{4/3}Co_{2/3}O_6$.

5.3.2 Characterization

5.3.2.1 Room Temperature Powder X-ray Diffraction

X-ray powder diffraction data were collected on station 9.1 of the Daresbury Synchrotron Radiation Source at room temperature. Rietveld refinement of the data was carried out in the orthorhombic space group Pnma, fit parameters and bond valence sums confirmed this refinement.

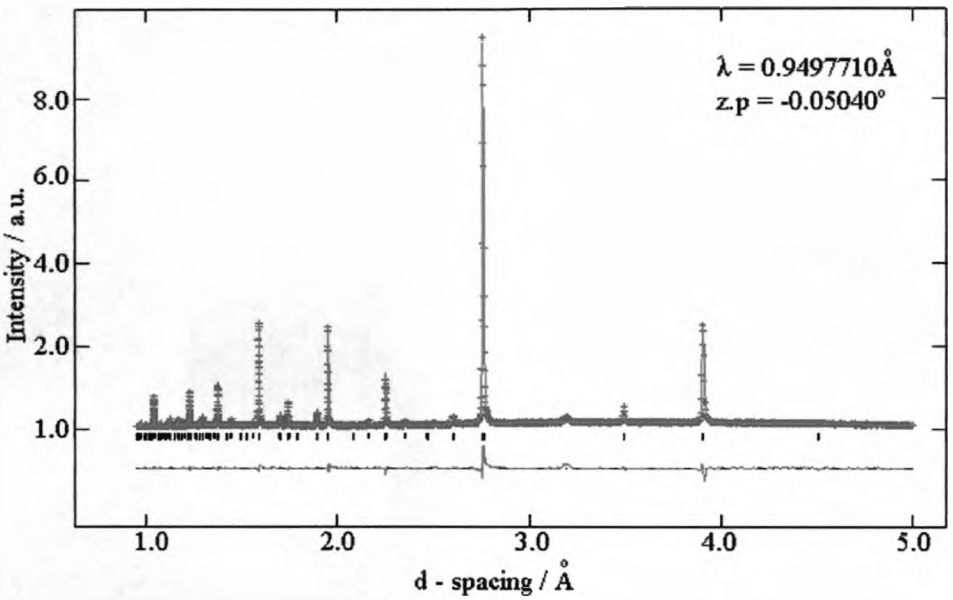

Figure 5.12: *Rietveld refinement of X-ray powder diffraction data collected at room temperature on station 9.1 of the SRS on* $BiLaMn_{4/3}Co_{2/3}O_6$.

Lattice Parameters		Fit Parameters	
Space Group	Pnma (No. 62)		
a / Å	5.5301(6)	R_{wp} / %	6.94
b / Å	7.8015(10)	R_p / %	5.14
c / Å	5.5127(5)	Rf^2	6.63
volume / Å^3	237.83(3)	χ^2	4.595
density / g cm^{-3}	7.770		

Table 5.6: *Refined lattice parameters and fit parameters from the Rietveld refinement of the X-ray powder diffraction data collected at room temperature on* $BiLaMn_{4/3}Co_{2/3}O_6$

Atom	Occupancy	x	y	z	U_{iso}
Bi1	0.5	-0.03121(14)	0.25	-0.00560(29)	0.02017(28)
La1	0.5	-0.03121(14)	0.25	-0.00560(29)	0.02017(28)
Mn1	0.667	0.0	0.0	0.5	-0.0069(4)
Co1	0.333	0.0	0.0	0.5	-0.0069(4)
O1	1	0.5100(20)	0.25	0.0820(33)	0.0155(23)
O2	1	0.2885(24)	-0.0212(19)	0.7086(24)	0.0155(23)

Table 5.7: *Refined positional parameters from the Rietveld refinement of the X-ray powder diffraction data collected at room temperature on* $BiLaMn_{4/3}Co_{2/3}O_6$

	Atom 1	Bond Length / Å	Bond Valence Sum, v_i (expected oxidation state)
$Bi_{0.5}$	Bi – O1	2.583 (11)	2.443 (3+)
	Bi – O1	3.031 (11)	
	Bi – O1	3.186 (18)	
	Bi – O1	2.346 (18)	
	Bi – O2 (x2)	3.176 (11)	
	Bi – O2 (x2)	2.526 (11)	
	Bi – O2 (x2)	2.809 (15)	
	Bi – O2 (x2)	2.593 (16)	
$La_{0.5}$	La – O1	2.583 (11)	3.016 (3+)
	La – O1	3.031 (11)	
	La – O1	3.186 (18)	
	La – O1	2.346 (18)	
	La – O2 (x2)	3.176 (11)	
	La – O2 (x2)	2.526 (11)	
	La – O2 (x2)	2.809 (15)	
	La – O2 (x2)	2.593 (16)	
$Mn_{2/3}$	Mn1 – O2 (x2)	2.003 (4)	3.032 (3.5+)
	Mn1 – O2 (x2)	1.974 (14)	
	Mn1 – O2 (x2)	1.994 (15)	
$Co_{1/3}$	Co1 – O2 (x2)	2.003 (4)	2.298 (2+)
	Co1 – O2 (x2)	1.974 (14)	
	Co1 – O2 (x2)	1.994 (15)	

Table 5.8: *Selected bond lengths and Bond Valence Sums[1] obtained from the Daresbury 9.1 data collected at room temperature.*

$BVS = \Sigma^{N}_{i=1} v_i$ $\quad v_i = exp[(R_o - l_i)/B]$

$B = 0.37$

$R_o(Bi^{3+}) = 2.094^{2}$

$R_o(La^{3+}) = 2.172^{2}$

$R_o(Co^{2+}) = 1.685^{6}$

$R_o(0.5Mn^{4+} + 0.5Mn^{3+}) = 1.7565^{2}$

The BVS (*table 5.8)* gives an average oxidation state of 3+ on the metal site, this suggest that Co^{3+} may only be present and therefore only Mn^{3+} would be present to give a charge balanced formula. However more experiments would be required to confirm this.

The Pnma structure as already discussed in *section 5.2.2.2* is a distorted form of perovskite, with Bi^{3+} on the A-site in an 8 co-ordinate environment, and a random distribution of Mn^{4+}, Mn^{3+} and Co^{2+} on the B-site in a six co-ordinate environment. Distortion from the parent perovskite structure occurs due to tilting of the BO_6 octahedra. On looking at the refined structure *(similar to figure 5.7)* it becomes clear that the refined position of the oxygens from this data are unreliable, it can be clearly seen that the oxygen octahedra surrounding the metal ions are not in the right place and as a result the octahedra appear as an unusual shape. This, as already discussed in *Chapter 2*, is due to the fact that oxygen atoms are light atoms containing only a few electrons and because of the presence of the two much heavier atoms, bismuth and lanthanum, which over power the diffraction pattern making the oxygens difficult to locate. Neutron diffraction will provide a much more reliable structure as the diffraction pattern is not influenced by size of the atom but on the form factor which does not vary proportional with the number of electrons within the atom

5.3.2.2 Variable Temperature Powder Neutron Diffraction

Powder neutron diffraction data were collected at room temperature and 2K on the POLARIS diffractometer at the ISIS Neutron and Muon Source. The room temperature data confirmed the Pnma space group and model from the X-ray data,

however from the neutron data the oxygen refined positions were much more reliable and realistic. The fit parameters and refined model are given in *tables 5.10 – 5.12*. Again the BVS (*table 5.12)* suggest the possibility of Co^{3+}, however the results from the neutron refinement are not as conclusive to the presence Co^{3+} as the X-ray data were.

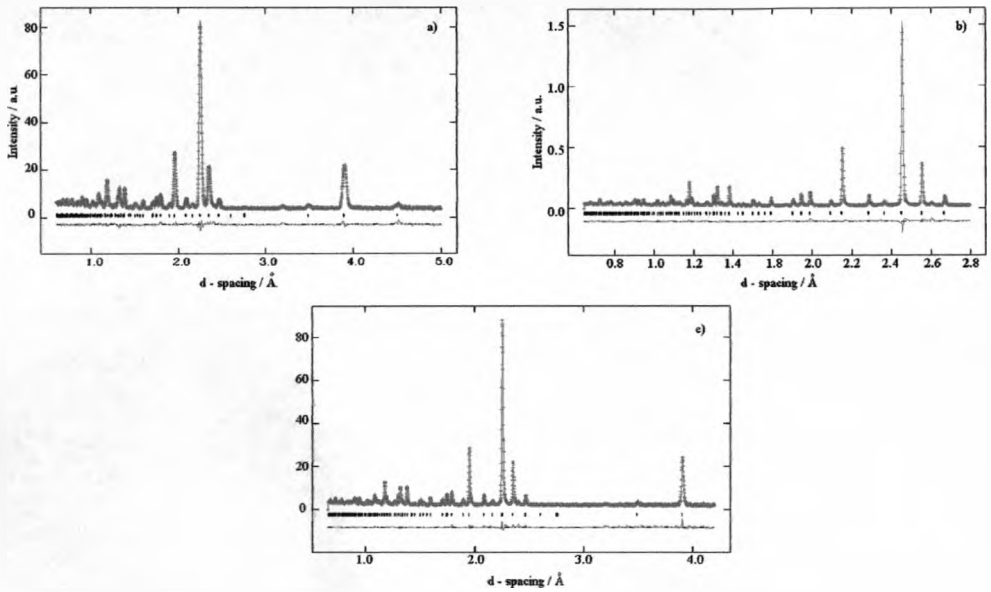

Figure 5.13: *Rietveld Refinement of powder neutron diffraction data collected at room temperature on the POLARIS diffractometers against the Pnma model. The red crosses are observed data, the solid green line is the calculated pattern and the pink line is the difference, figure a) is the low angle bank A, figure b) is the back scattering bank C and figure b) is the 90° bank E.*

Lattice Parameters	
Space Group	Pnma (No. 62)
a / Å	5.5269(1)
b / Å	7.8009 (2)
c / Å	5.5140(1)
volume / $Å^3$	237.74(8)
density / g cm^{-3}	7.773

Table 5.9: *Refined lattice parameters from the Rietveld refinement of* $BiLaMn_{4/3}Co_{2/3}O_6$ *on the neutron diffraction data collected at room temperature on POLARIS.*

Fit Parameters – Bank A		Fit Parameters – Bank C		Fit Parameters – Bank E	
R_{wp} / %	4.74	R_{wp} / %	3.19	R_{wp} / %	3.69
R_p / %	4.00	R_p / %	4.12	R_p / %	5.20
R_f^2	6.68	R_f^2	5.20	R_f^2	6.36
				Overall χ^2	**2.614**

Table 5.10: *Refined fit parameters from the Rietveld refinement of* $BiLaMn_{4/3}Co_{2/3}O_6$ *on the neutron diffraction data collected at room temperature on POLARIS.*

Atom	Occupancy	x	y	z	U_{iso}
Bi1	0.5	-0.02945(13)	0.25	0.00970(25)	0.0135(2)
La1	0.5	-0.02945(13)	0.25	0.00970(25)	0.0135(2)
Mn1	0.667	0	0	0.5	0.0029(3)
Co1	0.333	0	0	0.5	0.0029(3)
O1	1	0.51331(23)	0.25	-0.07212(32)	0.0121(2)
O2	1	0.28344(20)	-0.04046(15)	0.71762(19)	0.0178(2)

Table 5.11: *Refined positional parameters from the Rietveld refinement of* $BiLaMn_{4/3}Co_{2/3}O_6$ *on the neutron diffraction data collected at room temperature on POLARIS.*

	Atom 1	Bond Length / Å	Bond Valence Sum, v_i (expected oxidation state)
$Bi_{0.5}$	Bi – O1	2.567 (13)	2.449 (3+)
	Bi – O1	3.033 (12)	
	Bi – O1	2.424 (22)	
	Bi – O1	3.110 (22)	
	Bi – O2 (x2)	2.416 (14)	
	Bi – O2 (x2)	2.627 (11)	
	Bi – O2 (x2)	2.788 (12)	
$La_{0.5}$	La – O1	2.567 (13)	3.024 (3+)
	La – O1	3.033 (12)	
	La – O1	2.424 (22)	
	La – O1	3.110 (22)	
	La – O2 (x2)	2.416 (14)	
	La – O2 (x2)	2.627 (11)	
	La – O2 (x2)	2.788 (12)	
$Mn_{2/3}$	Mn1 – O2 (x2)	1.992 (35)	3.166 (3.5+)
	Mn1 – O2 (x2)	1.998 (13)	
	Mn1 – O2 (x2)	1.989 (12)	
$Co_{1/3}$	Co1 – O2 (x2)	1.992 (35)	2.610 (2+)
	Co1 – O2 (x2)	1.998 (13)	
	Co1 – O2 (x2)	1.989 (12)	

Table 5.12: *Selected bond lengths and Bond Valence Sums[1] obtained from Rietveld refinement on the neutron diffraction data collected at room temperature on POLARIS.*

$$BVS = \Sigma^{N}_{i=1} v_i \qquad v_i = exp[(R_o - l_i)/B]$$

$$B = 0.37$$

$$R_o(Bi^{3+}) = 2.094^{2}$$

$$R_o(La^{3+}) = 2.172^{2}$$

$$R_o(Co^{2+}) = 1.685^{6}$$

$$R_o(0.5Mn^{4+} + 0.5Mn^{3+}) = 1.7565^{2}$$

The low temperature data revealed extra Bragg scattering on a number of reflections, *figure 5.14*, suggesting that at 2K the material is magnetically ordered. The absence of any extra reflections in the 2K data, and the appearance of extra scattering is consistent with the material being ferromagnetically ordered.

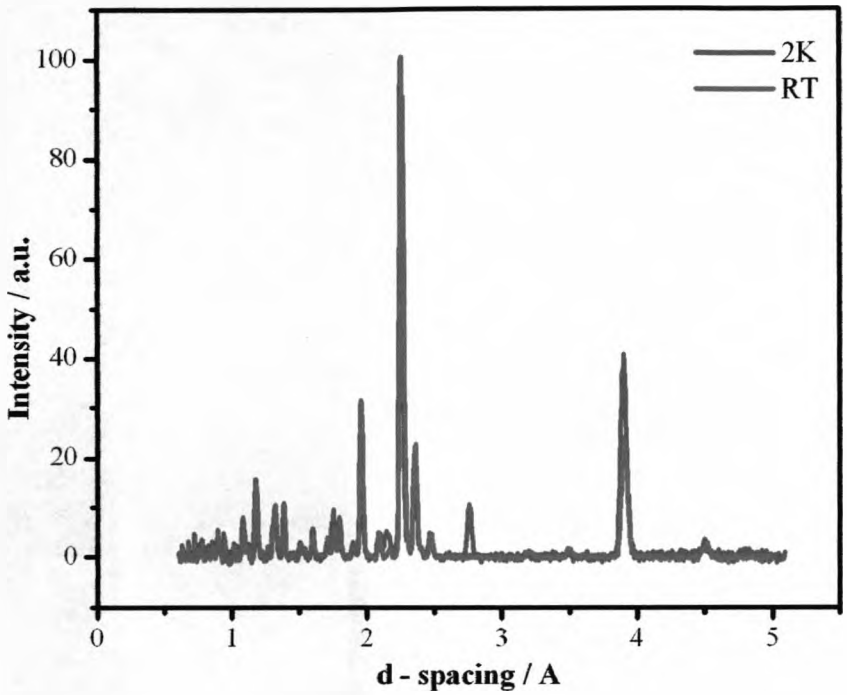

Figure 5.14: *Neutron powder diffraction pattern (bank A) of* $BiLaMn_{4/3}Co_{2/3}O_6$ *collected at room temperature and at 2K on the POLARIS diffractometer.*

The low temperature structure was refined, and confirmed to be the same as that at room temperature, in the Pnma pervoskite model; the bond-valence sums also support this model. Again the BVS are inconclusive as to distinguish between Co^{2+} / Co^{3+}.

Lattice Parameters	
Space Group	Pnma (No. 62)
a / Å	5.5129(2)
b / Å	7.7842 (3)
c / Å	5.5084(25)
volume / $Å^3$	237.74(8)
density / g cm^{-3}	7.773

Table 5.17: *Refined lattice parameters from the Rietveld refinement of* $BiLaMn_{4/3}Co_{2/3}O_6$ *on the neutron diffraction data collected at 2K on POLARIS.*

Fit Parameters – Bank A		Fit Parameters – Bank C		Fit Parameters – Bank E	
R_{wp} / %	2.40	R_{wp} / %	1.17	R_{wp} / %	1.51
R_p / %	1.76	R_p / %	1.82	R_p / %	2.45
R_f^2	6.91	R_f^2	9.81	R_f^2	7.39
				Overall χ^2	**2.417**

Table 5.18: *Refined fit parameters from the Rietveld refinement of* $BiLaMn_{4/3}Co_{2/3}O_6$ *on the neutron diffraction data collected at 2K on POLARIS.*

Atom	Occupancy	x	y	z	U_{iso}
Bi1	0.5	-0.02785(17)	0.25	0.01102(31)	0.0095(2)
La1	0.5	-0.02785(17)	0.25	0.01102(31)	0.0095(2)
Mn1	0.667	0	0	0.5	0.0024(3)
Co1	0.333	0	0	0.5	0.0024(3)
O1	1	0.51122(33)	0.25	-0.0721(4)	0.0093(3)
O2	1	0.28261(29)	-0.04096(20)	0.71871(28)	0.0177(3)

Table 5.19: *Refined positional parameters from the Rietveld refinement of* $BiLaMn_{4/3}Co_{2/3}O_6$ *on the neutron diffraction data collected at 2K on POLARIS.*

	Atom 1	Bond Length / Å	Bond Valence Sum
$Bi_{0.5}$	Bi – O1	2.581 (20)	2.479 (3+)
	Bi – O1	3.006 (19)	
	Bi – O1	2.427 (30)	
	Bi – O1	3.098 (30)	
	Bi – O2 (x2)	2.405 (20)	
	Bi – O2 (x2)	2.614 (15)	
	Bi – O2 (x2)	2.797 (17)	
$La_{0.5}$	La – O1	2.581 (20)	3.061 (3+)
	La – O1	3.006 (19)	
	La – O1	2.427 (30)	
	La – O1	3.098 (30)	
	La – O2 (x2)	2.405 (20)	
	La – O2 (x2)	2.614 (15)	
	La – O2 (x2)	2.797 (17)	
$Mn_{2/3}$	Mn1 – O2 (x2)	1.987 (5)	3.204 (3.5+)
	Mn1 – O2 (x2)	1.995 (21)	
	Mn1 – O2 (x2)	1.984 (19)	
$Co_{1/3}$	Co1 – O2 (x2)	1.987 (5)	2.641 (2+)
	Co1 – O2 (x2)	1.995 (21)	
	Co1 – O2 (x2)	1.984 (19)	

Table 5.20: *Selected bond lengths and Bond Valence Sums[1] obtained from Rietveld refinement on the neutron diffraction data collected at 2K on POLARIS.*

$$BVS = \Sigma^{N}_{i=1} v_i \qquad v_i = exp[(R_o - l_i)/B]$$

$$B = 0.37$$

$$R_o(Bi^{3+}) = 2.094\text{Å}^2$$

$$R_o(La^{3+}) = 2.172\text{Å}^2$$

$$R_o(Co^{2+}) = 1.685\text{Å}^6$$

$$R_o(0.5Mn^{4+} + 0.5Mn^{3+}) = 1.7565\text{Å}^2$$

The magnetic structure of this compound was refined simultaneously to the fundamental structure using the group of SARAh programs with GSAS, using a magnetic k-vector of 0,0,0 consistent with a ferromagnetically ordered material. The magnetic moment of the material was refined to 2.98(2)μ_B per magnetic atom, or 5.95μ_B/mol with the spins aligned parallel in the b-direction. This supports the expected value of 3.66.

5.3.2.3 Magnetic Measurements

Magnetic susceptibility data were collected using a Quantum Design MPMS SQUID magnetometer. The diamagnetic correction for this sample was calculated as 1.37 x 10^4 emu/mol and was subtracted from all data recorded. The sample was loaded at room temperature and cooled in the absence of an applied field to 2K. A field of 100Oe was then applied and measurements were recorded (zero-field-cooled(ZFC)) between 2 and 300K. This system was then cooled again to 2K in the applied field and the measurements between 2 and 300K were repeated (field-cooled(FC)).

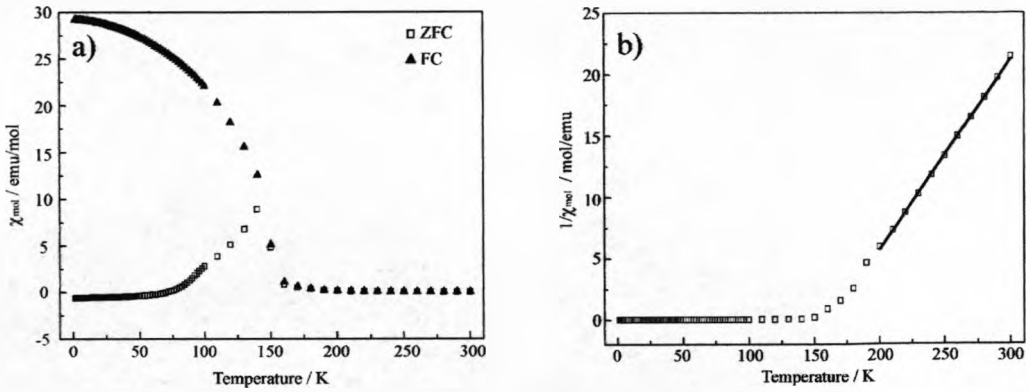

Figure 5.15: *a) ZFC-FC data collected at 100Oe and b) Inverse plot of the ZFC data collected. The plots show that the magnetic ordering temperature is ~ 150K. Curie-Weiss fitting of the inverse chi of the zero-field-cooled reveals a Curie constant of 6.4emu/mol and a positive Weiss constant (θ = 163K) implying ferromagnetic ordering*

The magnetic susceptibility showed a divergence between the zero-field-cooled and the field-cooled data at 150K, this was taken as the magnetic ordering temperature of the sample, above this value (between 200 and 300K) the data was fitted by the simple Curie-Weiss equation for paramagnetism:

$$X(T) = C / (T - \theta)$$

The Curie constant (C) was fitted to 6.4 emu/mol and the corresponding effective magnetic moment calculated from this Curie constant ($\mu_{eff} = (8C)^{1/2}$) 7.1 μ_B/mol. The expected effective magnetic moment was calculated from the electronic configuration of the magnetic ions present $\frac{2}{3}Co^{2+}$, $\frac{2}{3}Mn^{3+}$ and $\frac{2}{3}Mn^{4+}$ (μ_{eff} = $[n(n+2)]^{1/2}$, *where n = number of unpaired electrons*) as 6μ_B/mol. The inconsistency may be due to the presence of Co^{3+} which was suggested by the BVS in previous

sections. If this was the case the charge balanced formula would be $(Bi^{3+})(La^{3+})(Co^{3+})(Mn^{3+})(O^{2-})_6$ and the expected effective moment would be 6.9 μ_B/mol. This provides more evidence to the possibility of Co^{3+} presence rather than Co^{2+}.

A DC magnetization hysteresis loop was recorded with a field sweep between -1T and 5.5T at 2K (*figure 5.16 – jumps in the data is due to the sample moving during data collection).* A maximum magnetic moment of 5.85 μ_B/mol was observed in the 2K data, however saturation of the sample was not achieved by a field of ±5.5T. From the refinement of the neutron diffraction data at 2K (*section 5.2.2.2)* the magnetic moment was refined as 5.96 μ_B/mol (2.98 μ_B/magnetic ion). This is slightly higher than the SQUID observed magnetic moment, supporting the conclusion that the material was not fully saturated by 5.5T.

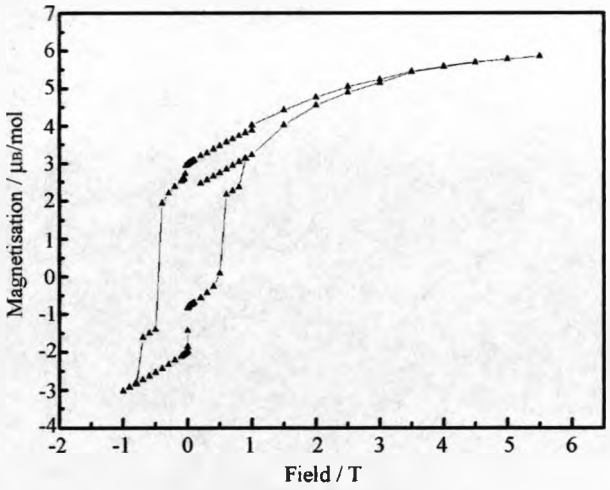

Figure 5.16: *Magnetization of $BiLaMn_{4/3}Co_{2/3}O_6$ collected at 2K.*

5.3.2.4 X-ray absorption spectroscopy (XAS)

XAS was carried out on station 7.1 at the SRS. Data was recorded at room temperature across the Co K edge in ~ 0.5eV steps in transmission mode, a Co metal K edge was run simultaneously as a form of energy calibration. $NdSrCoO_4$ and $NdSrCoO_{3.48}$ were run as Co^{3+} and Co^{2+} standards respectively.

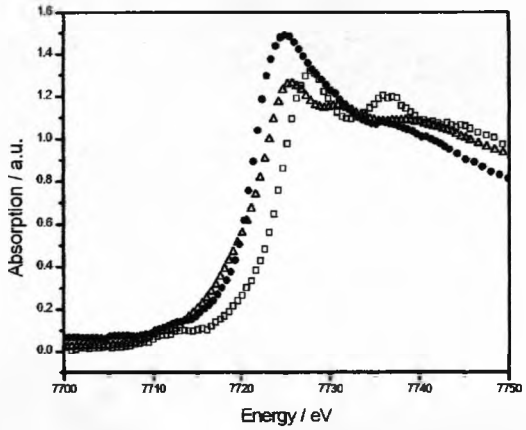

Sample	Edge Position / eV
$NdSrCoO_{3.48}$ (Co^{2+} Standard)	7721.62
$NdSrCoO_4$ (Co^{3+} Standard)	7725.33
$BiLaMn_{4/3}Co_{2/3}O_6$ sample	7721.62

***Figure 5.17**: X-ray absorption spectroscopy collected across the Co K edge in ~ 0.5eV steps. The edge positions calculated for each are given in the table.*
Closed circle: $BiLaMn_{4/3}Co_{2/3}O_6$ sample, Open triangle: $NdSrCoO_{3.48}$ (Co^{2+} Standard), and Open square: $NdSrCoO_4$ (Co^{3+} Standard).

The XAS results show that the oxidation state of the cobalt in the sample is 2+, as both the sample and $NdSrCoO_{3.48}$ have the same edge position. This suggests that the overall charge balanced formula is $(Bi^{3+})_2(Mn^{4+})_{2/3}(Mn^{3+})_{2/3}(Co^{2+})_{2/3}(O^{2-})_6$ and rules out the possibility of the presence of Co^{3+} that was speculated from the BVS results (*sections 5.3.2.1 / 2)* and from the magnetic measurements (*section 5.3.2.3).*

5.3.3 Discussion

Attempts to replace the Ni^{2+} in the $Bi_2Mn_{4/3}Ni_{2/3}O_6$ material with another divalent cation proved successful in the case of Co^{2+}, however the material could only be prepared if 50% or more doping of lanthanum was present, the pure bismuth phase proved impossible to form. Variable temperature diffraction data was used to determine the structure of $BiLaMn_{4/3}Co_{2/3}O_6$ at room temperature and below. Data at both room temperature and 2K were refined in the non-polar space group Pnma. This is a perovskite model with a random mixture of Bi^{3+} and La^{3+} on the A-site and a random distribution of $\frac{1}{3}Co^{2+}$, $\frac{1}{3}Mn^{3+}$ and $\frac{1}{3}Mn^{4+}$ on the B-site inside an oxygen octrahra. The bond-valence sums calculated from the refinements raised the question of the metal oxidation state in the material, suggesting that Co^{3+} and Mn^{3+} may only be present. However XAS data collected confirmed the oxidation state of Co as 2+.

Extra Bragg scattering was observed in the low temperature neutron diffraction data, this along with SQUID magnetrometry data suggested that the sample was ferromagnetically ordered (along the b-direction) with a k vector of (0,0,0). Both the refined magnetic moment from the diffraction data and that observed from the SQUID were consistent giving a moment in the region of ~6 μ_B/mol. The effective magnetic moment calculated from the ZFC-FC measurements supported the Co^{3+} presence, however as already discussed XAS had already ruled this out.

Although this sample exhibited true ferromagnetism with a favourably high ordering temperature, the material unfortunately adopted a non-polar structure. This is

probably due to the presence of the 50% lanthanum on the bismuth site, and the fact that bismuth is not present in a high enough concentration to stabilise a polar structure through its lone pair.

5.4 $BiMn_{0.6}Fe_{0.4}O_3$

5.4.1 Synthesis

Initially an attempt was made to prepare $BiMn_{0.5}Fe_{0.5}O_3$ by standard ceramic methods. However energy dispersive spectroscopy (EDS) measurements showed that the perovskite phase forming had a different composition, $BiMn_{0.6}Fe_{0.4}O_3$. However during the course of my work it was reported[7] that it was possible to synthesis a number of compositions in the solid solution $BiFeO_3$ and $BiMnO_3$ under ambient conditions.

Samples with this correct composition were prepared by a standard ceramic method, on a scale between 0.5g and 5g. Stoichiometric quantities of Bi_2O_3 (Alfa 99.9995%), MnO_2 (Alfa Aesar 99.999%) and Fe_2O_3 (Alfa Aesar 99.998%) were ground together and pelletized. The pellet was placed on platinum foil in an alumina boat (reaction occurs with the boat if this precaution is not taken) and heated at 800°C for 12 hours, 850°C for 12 hours, 875°C for 12 hours and then 900°C for 12 hours. In between each firing stage the pellet was ground in an agate mortar and pestle, and then repelletized, all steps used a heating rate of 5°C per minute and a cooling rate of 10°C per minute.

5.4.2 Characterization

5.4.2.1 Room Temperature Powder X-ray Diffraction

X-ray powder diffraction data were collected on station 9.1 of the Daresbury Synchrotron Radiation Source at room temperature. At first the powder pattern appeared to index to a unit cell based on the original commensurate $Bi_2Mn_{4/3}Ni_{2/3}O_6$ orthorhombic cell ($\sqrt{2}a_p$ x $2\sqrt{2}a_p$ x $4a_p$). A recent report on the solid solution $BiFe_{1-x}Mn_xO_3$[7] also reported that all room temperature diffraction patterns of x = 0 to 0.7 were fitted to this cell. In the absence of electron diffraction the pattern was fitted in the orthorhombic pattern with no systematic absences, Pmmm. However the LeBail fit carried out in GSAS revealed a misfit on the low angle peaks like in the $Bi_2Mn_{4/3}Ni_{2/3}O_6$ material, which suggested that this material may also be modulated.

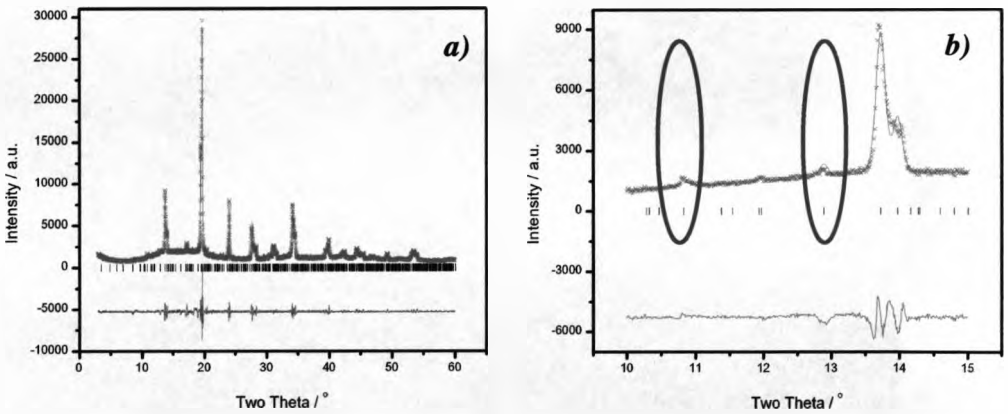

Figure 5.18: *LeBail fit in the space group Pmmm of the X-ray Powder Diffraction data collected at room temperature on Station 9.1 of the Daresbury Synchrotron Radiation Source. The pink crosses are the observed data, green line is the calculated profile, the purple line is the difference plot and the black markers are the Bragg positions. Plot a) is the full diffraction pattern, plot b) is an expanded area of the pattern which highlights the misfit on the low angle peaks due to the incommensurate structure.*

Lattice Parameters		Fit Parameters	
Space Group	Pmmm	R_{wp} / %	7.50
a / Å	5.6329(2)	R_p / %	5.89
b / Å	11.2160(5)	χ^2	4.449
c / Å	15.6160(7)		
Volume / Å^3	986.60(4)		

Table 5.21: *Refined lattice parameters and goodness of fit parameters from the commensurate LeBail fit carried out on the room temperature powder X-ray diffraction data of* $BiMn_{0.6}Fe_{0.4}O_3$.

The data were then fitted in the same superspace group as $Bi_2Mn_{4/3}Ni_{2/3}O_6$, Ibmm(q00,0-p0)ss.gm. A LeBail fit was carried out using the program Jana2000, the lattice parameters and modulation vectors obtained are given in *table 5.22*. The quality of the data is poor, making refining accurate cell parameters diificult and so the refined parameters are not as reliable. A full Rietveld refinement of the modulated structure could not be carried out on this data due to the quality, therefore it must be assumed that the modulated structure is the same as $Bi_2Mn_{4/3}Ni_{2/3}O_6$ as discussed in chapter three, with a random distribution of Mn^{3+} and Fe^{3+} on the b-site inside the oxygen octahedra.

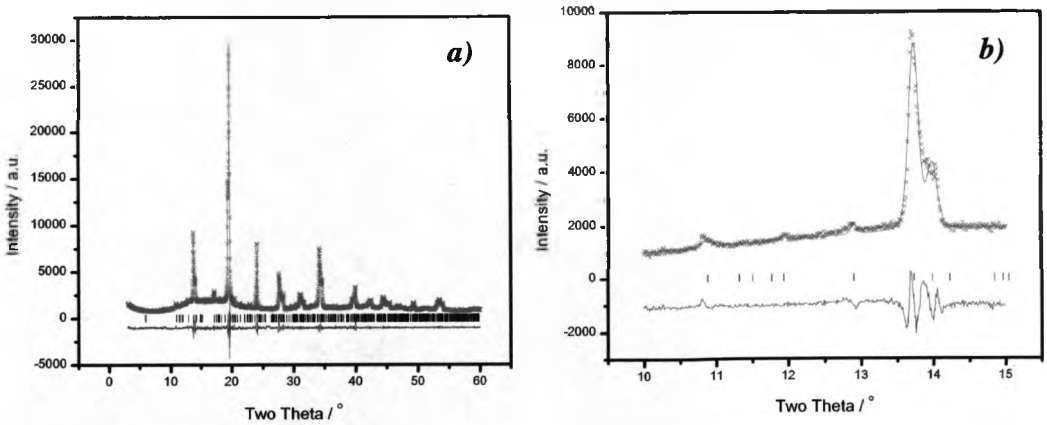

Figure 5.19: *LeBail fit in the incommensurate model to the X-ray Powder Diffraction data collected at room temperature on Station 9.1 of the Daresbury Synchrotron Radiation Source. The pink crosses are the observed data, green line is the calculated profile, the purple line is the difference plot and the black markers are the Bragg positions. Plot a) is the full diffraction pattern, plot b) is an expanded area of the pattern which highlights the improved fit on the low angle peaks when compared to the commensurate fit.*

Lattice Parameters		**Fit Parameters**	
Space Group	Ibmm	R_{wp} / %	6.25
a / Å	5.6336(2)	R_p / %	4.72
b / Å	7.8039(3)		
c / Å	5.6054(2)		
(q_1 , 0 , 0)	0.495298(13)		
(0 , q_2 , 0)	-0.532605(30)		

Table 5.22: *Refined lattice parameters and goodness of fit parameters from the incommensurate LeBail fit carried out on the room temperature powder x-ray diffraction data of* $BiMn_{0.6}Fe_{0.4}O_3$.

5.4.2.2 X-ray absorption spectroscopy (XAS)

XAS was carried out on station 7.1 at the SRS. Data was recorded at room temperature across the Fe K edge in ~ 0.5eV steps in transmission mode, a Fe metal K edge was ran simultaneously as a form of energy calibration. $LaFeO_3$ and $FeSO_4.xH_2O$ were run as Fe^{3+} and Fe^{2+} standards respectively.

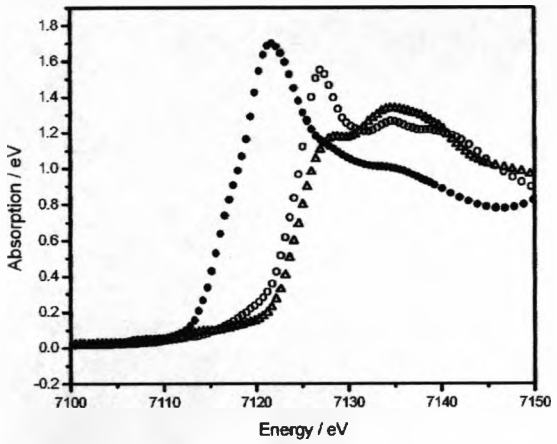

Sample	Edge Position / eV
$FeSO_4.xH_2O$ (Fe^{2+} Standard)	7119.27
$LaFeO_3$ (Fe^{3+} Standard)	7124.05
$BiMn_{0.6}Fe_{0.4}O_3$ sample	7124.93

Figure 5.20: *X-ray absorption spectroscopy collected across the Fe K edge in ~ 0.5eV steps. The edge positions calculated for each of the samples are given in the table.*

Closed circle: $FeSO_4.xH_2O$ (Fe^{2+} Standard), Open circle: $LaFeO_3$ (Fe^{3+} Standard), and Open triangle: $BiMn_{0.6}Fe_{0.4}O_3$ sample.

The XAS results show that the absorption edge of the iron in both the sample and the 3+ standard are at the same energy, this suggests that the iron in the $BiMn_{0.6}Fe_{0.4}O_3$ sample is in the 3+ oxidation state. This gives an overall charge balanced composition of $(Bi^{3+})(Mn^{3+})_{0.6}(Fe^{3+})_{0.4}(O^{2-})_3$.

5.4.3 Discussion

Attempts to make a bismuth based perovskite containing both manganese and iron have proved successful, although only one composition was synthesised. A recent report[7] shows however that a solid solution exists between $BiMnO_3$ and $BiFeO_3$. The material exhibits a modulated perovskite structure at room temperature, consisting of Bi^{3+} ions on the a-site, with a random distribution of Fe^{3+} and Mn^{3+} on the b-site. The material is modulated along both the 'a' and 'b' directions in the unit cell. However the sample was poorly crystalline and so gave rise to a poorly resolved diffraction pattern. Therefore the poor quality of the fit could simply have been due to this, rather than modulation within the sample.

No electrical or magnetic property measurements were carried out on this material. Further experiments would be required to determine whether any coupling occurs between any magnetism or electrical properties. However reports suggest that this is not the case for this system.

5.5 Synthesis and characterisation of other attempted perovskites

This section discusses all the attempts made to synthesise bismuth based perovskites that were abandoned due to negative results. Details of the attempts made and the phases that were formed instead are given. The Stoe WinXPow software and database were used to identify phases formed.

5.5.1 $Bi_{2-x}La_xFe_{1-y}Cr_yO_3$

Initially $BiFeO_3$ was made by taking stoichiometric quantities of Bi_2O_3 (Alfa 99.9995%) and Fe_2O_3 (Alfa Aesar 99.998%), thoroughly ground together and then pelletized. The sample was then heated a 850°C for 24 hours using a heating rate of 5°C per minute and a cooling rate of 10°C per minute.

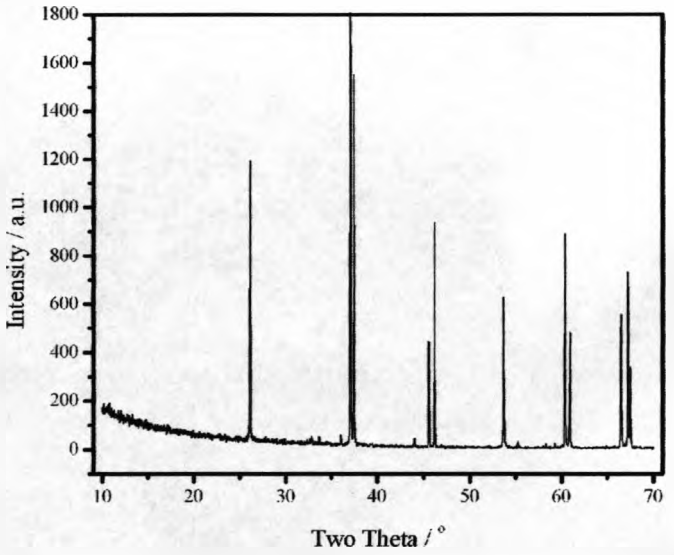

Figure 5.21: *X-ray powder diffraction pattern of $BiFeO_3$, λ = 1.788965Å (Co source)*

The powder pattern was indexed to a trigonal hexagonal unit cell, a = 5.5747Å and c = 13.8582Å in the space group R3c (no. 161) which is comparable to literature data on this compound[8].

An attempt was made to introduce chromium directly into the $BiFeO_3$ material, 10% and 50% substitution were both attempted, samples were heated to 850°C for varying lengths of time.

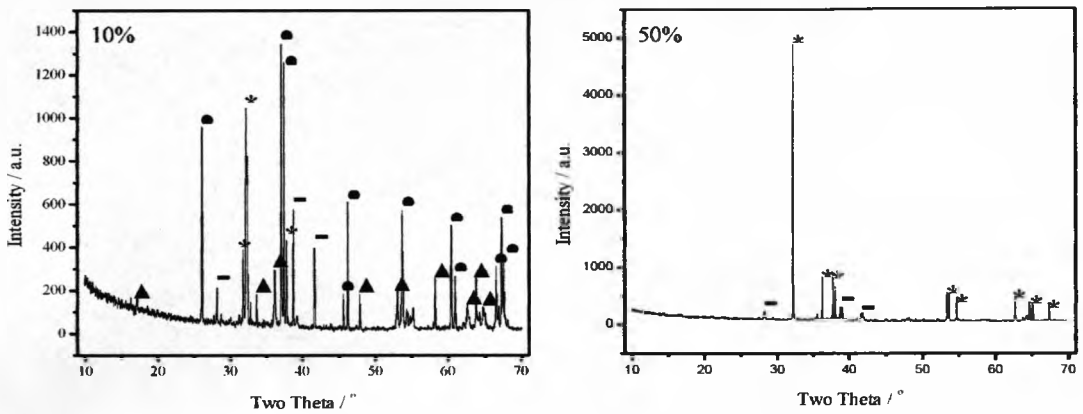

Figure 5.22: *X-ray diffraction patterns of the 10% and 50% chromium substituted $BiFeO_3$ attempts. Closed circles: $BiFeO_3$; Closed squares: $Cr_{2-x}Fe_xO_3$[9]; Stars: $Bi_7CrO_{12.5}$[10]; Closed triangles: $Bi_2Fe_4O_9$[11] (λ = 1.788965Å (Co source))*

Both synthetic trials proved unsuccessful, the 10% substitution as shown in *figure 5.22* formed a variety of products, whilst the 50% substitution formed mainly one phase, $Bi_7CrO_{12.5}$[10].

A second synthetic strategy was then attempted using 10, 25, 50 and 50% Lanthanum substitution on the Bismuth site and 10, 25, 50 and 75% substitution of

chromium on the iron site. The following table gives a summary of the synthetic attempts temperatures in the region of 850 to 1100°C were used depending on the lanthanum content.

Bi Site Substitution / %	Fe Site Substitution / %	Phase(s) formed
10	10	$BiFeO_3$ phase, starting materials and $Bi_7CrO_{12.5}$[10]
10	50	$Bi_7CrO_{12.5}$[10] and starting materials
25	25	$BiFeO_3$, $Bi_7CrO_{12.5}$[10] and starting materials
50	10	$LaFeO_3$[12], $BiFeO_3$ and starting materials
50	50	$Bi_7CrO_{12.5}$[10], $LaCrO_3$[13] and starting materials
75	75	$LaFeO_3$[12] and $LaCrO_3$[13]

Table 5.23: *Summary of synthetic results from trials on both lanthanum and chromium substitution into* $BiFeO_3$

All phases formed could be indexed to existing materials, no evidence was found of chromium substitution on the iron site.

In summary, this thesis has shown that all attempts to form chromium substituted $BiFeO_3$ materials using solid state methods have failed. A number of synthetic trials have been attempted including the use of lanthanum as a stabiliser; a recent report supported this conclusion[14]. The report states that $BiFe_{1-x}Cr_xO_3$ materials can only be synthesised using a combustible method from the nitrate starting materials.

5.5.2 $Bi_2Mn_{2-x}Ru_xO_6$

Initially an attempt to make Bi_2MnRuO_6 was made, however during the course of the synthesis it became apparent that another non-perovskite phase was forming with another composition. This was confirmed using Electron Dispersive Spectroscopy in the TEM as $Bi_2Mn_{2/3}Ru_{4/3}O_7$. Using this new composition, stoichiometric quantities of Bi_2O_3 (Alfa 99.9995%), MnO_2 (Alfa Aesar 99.999%) and RuO_2 (Engelhard 99.95%) were ground together, pelletized and heated between 800 and 925°C in 25°C intervals in 12hour steps using a heating rate of 5°C per minute and cooling rate of 10°C per minute.

The $Bi_2Ru_2O_7$ type-phase forming could be indexed to a cubic unit cell with a cell parameter of 10.242(3)Å in the space group Fd-3m , this supports the TEM results that manganese was being introduced onto the ruthenium site as the un-doped material has a unit cell parameter of 10.293Å[15] and so the decrease in the size of the unit cell supports the introduction of the smaller manganese ion onto the ruthenium site. The remaining peaks were matched to the phase $Bi_{12}MnO_{20}$[16].

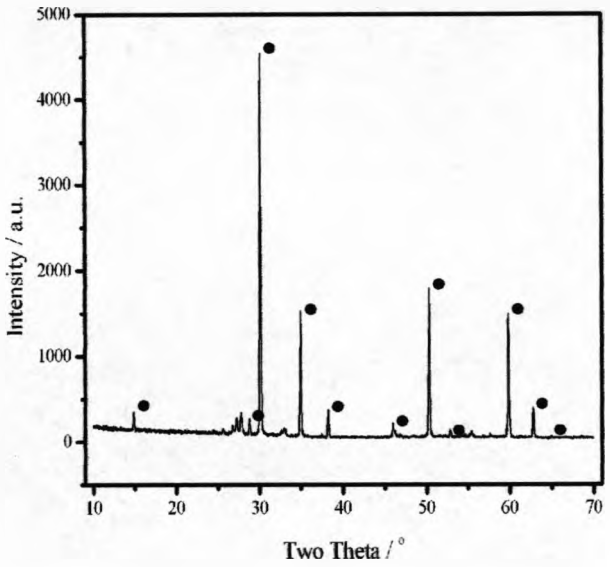

Figure5.23: *X-ray powder diffraction pattern of $Bi_2Mn_{2/3}Ru_{4/3}O_7$ sample (λ = 1.54060Å (Cu source)), marked peaks belong to the cubic phase, any remaining peaks can be matched to a $Bi_{12}MnO_{20}$ impurity phase.*

5.5.3 $Bi_2Mn_{1-x}(Zn / Cu / Mg)_xO_6$

Synthetic trials of this system focused on attempts for 50% substitution on the manganese site. Stoichiometric quantities of Bi_2O_3 (Alfa Aesar 99.9995%), MnO_2 (Alfa Aesar 99.999%) and then the relevant ZnO (Alfa Aasar 99.99%), CuO (Alfa Aesar 99.995%) and MgO (Aldrich 99.99%) were taken thoroughly ground together and pelletized. The samples were heated up to 800°C for 12 hours followed by 850°C for a further 12 hours, heating and cooling rates of 5 and 10°C per minutes were used respectively.

The Bi_2MnCuO_6 sample melted, flowed over the platinum foil and reacted with the alumina crucible analysis of this proved impossible. On reflection this material

would have been a good candidate for a crystal growth attempt, although this was never attempted during my project.

Both the Bi_2MnZnO_6 and Bi_2MnMgO_6 samples yielded no perovskite phase, the main phase that formed was based on $Bi_{12}MnO_{20}$[16] any remaining peaks in the X-ray pattern were matched to starting materials. In both cases the main phase was indexed to a cubic phase in the space group I23 (No. 197), the zinc and magnesium samples were indexed to unit cells with cubic parameters of 10.1939(6)Å and 10.2218(5)Å respectively. These did not match with any of the reference data for $Bi_{12}ZnO_{20}$ (a = 10.205Å)[17], $Bi_{12}MnO_{20}$ (a = 10.206Å)[16], or $Bi_{12}MgO_{20}$ (a = 10.255Å)[18] and so implied that a mixture of the two metals was being incorporated into these structure types.

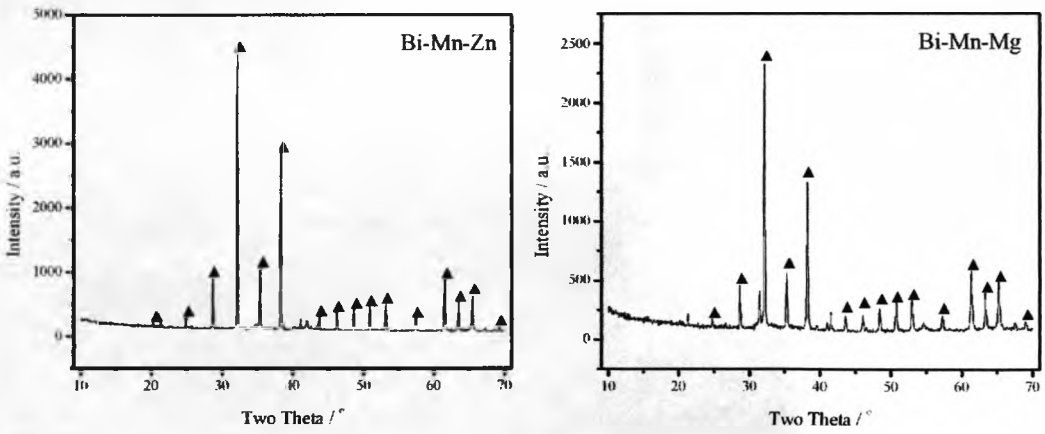

Figure 5.24: *X-ray powder diffraction patterns of Bi-Mn-Zn and B-Mn-Mg system, λ = 1.788965Å (Co source). Marked peaks belong to the cubic $Bi_{12}MnO_{20}$ type phase all remaining peaks belong to starting materials.*

5.5.4 $Bi_2Ti_{2/3}X_{2/3}Y_{2/3}O_6$ (X = Mn, Ga and Lu; Y = Zn, Mg and Ni)

Synthetic trials to substitute on both the Mn^{3+} and Ni^{2+} site in the $Bi_2(Ti^{4+})_{2/3}(Mn^{3+})_{2/3}(Ni^{2+})_{2/3}O_6$ material were attempted. The stoichiometric quantities of the relevant starting materials were taken, the supplier and purity details of which are given in table 5.24, ground together and pelletized.

Starting Material	Supplier	Purity
Bi_2O_3	Alfa Aesar	99.9995%
TiO_2	Alfa Aesar	99.995%
MnO_2	Alfa Aesar	99.999%
Ga_2O_3	Alfa Aesar	99.99%
Lu_2O_3	Alfa Aesar	99.99%
ZnO	Alfa Aesar	99.99%
MgO	Aldrich	99.99%
NiO	Alfa Aesar	99.998%

Table 5.24: *Details of the starting material suppliers and purity used in the* $Bi_2Ti_{2/3}X_{2/3}Y_{2/3}O_6$ *(X = Mn, Ga, Lu; Y = Zn, Mg, Ni) system trials.*

The samples were then heated at 800°C for 12hours, 850°C for 12hours and finally 900°C for 12hours, using heating and cooling rates of 5 and 10°C per minute respectively. None of the samples formed any perovskite phases, in each case the powder X-ray diffraction patterns were matched to known oxides using the Stoe WinX-Pow software and database. A summary of the range of oxides formed in each system is given in table 5.25.

X	Y	Phase(s) formed
Ga	Zn	Predominantly $Bi_4Ti_3O_{12}$[19] with Bi_2O_3
Ga	Mg	Mainly a $Bi_{12}(Ga/Ti/Mg)O_{20}$[18,20] type phase plus $Bi_4Ti_3O_{12}$[19]
Ga	Ni	Predominantly $Bi_4Ti_3O_{12}$[19] with Bi_2O_3
Lu	Zn	Mainly $Bi_{12}TiO_{20}$[20] type phase, plus a small amount of $(BiLa)Ti_2O_7$[21]
Lu	Mg	Mainly $Bi_{12}TiO_{20}$[20] type phase, plus a small amount of $(BiLa)Ti_2O_7$[21]
Lu	Ni	Mainly $Bi_{12}TiO_{20}$[20] type phase, plus a small amount of $(BiLa)Ti_2O_7$[21]
Mn	Zn	Equal amounts of $Bi_{12}TiO_{20}$[20] and $Bi_4Ti_3O_{12}$[19] type phases
Mn	Mg	Equal amounts of $Bi_{12}TiO_{20}$[20] and $Bi_4Ti_3O_{12}$[19] type phases

Table 5.25: *Summary of the phases formed in the synthetic attempts of the systems* $Bi_2Ti_{2/3}X_{2/3}Y_{2/3}O_6$ *(X = Mn, Ga, Lu; Y = Zn, Mg, Ni) system trials.*

5.5.5 $Bi_2Sn_{2/3}Fe_{2/3}X_{2/3}O_6$ (X = Zn, Mg, Ni and Co)

Synthetic trials to substitute on all B-sites in $Bi_2(Mn^{4+})_{2/3}(Mn^{3+})_{2/3}(Ni^{2+})_{2/3}O_6$ was attempted, Sn^{4+} was placed on the Mn^{4+} site, Fe^{3+} was placed on the Mn^{3+} site and a range of metals were placed on the Ni^{3+}site. The stoichiometric quantities of the relevant starting materials were taken, Bi_2O_3 (Alfa 99.9995%) SnO (Alfa Aesar 99.998%) $_2$, Fe_2O_3 (Alfa Aesar 99.998%), NiO (Alfa Aesar 99.998%), ZnO (Alfa Aesar 99.99%), MgO (Aldrich 99.99%) and Co_3O_4 (Alfa Aesar 99.998%) ground together and pelletized. The samples were then heated at 800°C for 12hours, 850°C for 12hours and finally 900°C for 12hours, using heating and cooling rates of 5 and 10°C per minute respectively.

No perovskite phases were formed in any of the samples, in each case the powder X-ray diffraction patterns were matched to known oxides using the Stoe WinX-Pow

software and database. A summary of the range of oxides formed in each system is given in table 5.26.

X	Phase(s) formed
Ni	Predominantly $Bi_{12}(Fe/Ni)O_{20}$[11,22] type phase with $Bi_2Sn_2O_7$[23]
Zn	Predominantly $Bi_{12}(Fe/Zn)O_{20}$[11,17] type phase with $Bi_2Sn_2O_7$[23]
Mg	Predominantly $Bi_{12}(Fe/Mg)O_{20}$[11,18] type phase with $Bi_2Sn_2O_7$[23]
Co	Predominantly $Bi_{12}(Fe/Co)O_{20}$[11,24] type phase with $Bi_2Sn_2O_7$[23]

Table 5.26: *Summary of the phases formed in the synthetic attempts of the systems* $Bi_2Sn_{2/3}Fe_{2/3}X_{2/3}O_6$ *(X = Zn, Mg, Ni, Co) system trials.*

5.5.6 $Bi_{4/3}X_{2/3}Mn_{4/3}Ni_{2/3}O_6$ (X = Sr and Te)

Synthetic trials to substitute on the bismuth site $Bi_2Mn_{4/3}Ni_{2/3}O_6$ was attempted, Sr^{2+} and Te^{4+} were substituted for Bi^{3+} this was with the aim to form a pure Mn^{4+} material. Stoichiometric quantities of the relevant starting materials were taken, Bi_2O_3 (Alfa Aesar 99.9995%), $SrCO_3$, TeO_2 (Alfa 99.9995%), MnO_2 (Alfa Aesar 99.999%) and NiO (Alfa Aesar 99.998%) ground together and pelletized. The samples were then heated at 800°C for 12hours, 850°C for 12hours, 875°C for 12hours and finally 900°C for 12hours, using heating and cooling rates of 5 and 10°C per minute respectively.

The $Bi_{4/3}Sr_{2/3}Mn_{4/3}Ni_{2/3}O_6$ material formed a perovskite like phase that was indexed to a cubic cell with a cell parameter of 3.8726(17)Å. However the x-ray powder pattern did imply that a number of impurity phases were also present, Electron Dispersive Spectroscopy revealed that the composition of the perovskite forming was different to that expected ($Bi_{1.5}Sr_{0.5}Mn_{4/3}Ni_{2/3}O_6$). The composition of this new

phase was not a full Mn^{4+} material and so the decision to abandon this system was taken.

The $Bi_{4/3}Te_{2/3}Mn_{4/3}Ni_{2/3}O_6$ material formed no perovskite phase, only a mixture of Bi_4TeO_8[25], $Bi_2Mn_4O_{10}$[26] and starting materials. As the sample was heated further to try and drive the formation of other phases the material began to melt. As a result the decision to abandon this system also was taken.

5.7 Refences

(1) Brown, I. D. *Chemical Society Reviews* **1978**, *7*, 359-376.

(2) Brown; Altermatt *Acta Cryst.* **1985**, *B41*, 244-247.

(3) Allmann *Monatshefte Chem.* **1975**, *106*, 779.

(4) Ok, K. M.; Chi, E. O.; Halasyamani, P. S. *Chemical Society Reviews* **2006**, *35*, 710-717.

(5) Azuma, M.; Takata, K.; Saito, T.; Ishiwata, S.; Shimakawa, Y.; Takano, M. *J. Am. Ceram. Soc.* **2005**, *127*, 8889.

(6) Wood; Palenik *Inorg. Chem.* **1998**, *37*, 4149-4151.

(7) Azuma, M.; Kanda, H.; Belik, A. A.; Shimakawa, Y.; Takano, M. *J. Magnetism and Magnetic Materials* **2007**, *310*, 1177-1179.

(8) Achenbach; James; Gerson *J. Am. Ceram. Soc.* **1967**, *50*, 437.

(9) Wretblad *Z. Anorg. Chem.* **1930**, *189*, 331.

(10) Popel, P.; Basai, N.; Lushnikova, E. *Russ. J. Inorg. Chem. (Engl. Transl.)* **1990**, *35*, 1409.

(11) Koizumi; Niizeki; Ikeda *Jpn. J. Appl. Phys.* **1964**, *3*, 495.

(12) Dann, S. E.; Currie, D. B.; Weller, M. T.; Thomas, M. F.; Al Rawwas, A. D. *J. Solid State Chem.* **1994**, *109*, 134.

(13) Devi, P. S.; Rao, M. S. *J. Solid State Chem.* **1992**, *98*, 237.

(14) Li, J. B.; Rao G.H; Liang J.K; Liu Y.H; Luo J; Chen J.R *Applied Physics Letters* **2007**, *90*, 162513.

(15) Yamamoto, T.; Kanno, R.; Takeda, Y.; Yamamoto, O.; Takano, M. *J. Solid State Chem.* **1994**, *109*, 372.

(16) Delicat, U.; Radaev, S. F.; Troemel, M.; Behrens, P.; Kargin, Y. F.; Marin, A. A. *J. Solid State Chem.* **1994**, *110*, 66.

(17) Kirik, S. D.; Kutvitskij, V. A.; Koryagina, T. I. *Zh. Strukt. Khim.* **1985**, *26*, 90.

(18) Ramanan, A.; Gopalakrishnan, J.; Rao, C. *Mater. Res. Bull.* **1981**, *16*, 169.

(19) Hirata, T.; Yokokawa, T. *Solid State Commun.* **1997**, *104*, 673.

(20) Swindells, D. C. N.; Gonzalez, J. L. *Acta Crystallogr. Sec. B: Structural Science* **1988**, *44*, 12.

(21) Schmalle, H. W.; Williams, T.; Reller, A.; Linden, A.; Bednorz, J. G. *Acta Crystallogr. Sec. B: Structural Science* **1993**, *49*, 235.

(22) Ramanan, A.; Gopalakrishnan, J.; Rao, C. *Mater. Res. Bull.* **1981**, *16*, 169.

(23) Kahlenberg, V.; Zeiske, T. *Z. Kristallogr.* **1997**, *212*, 297.

(24) Mary, T. A.; Mackay, R.; Nguyen, P.; Sleight, A. W. *Eur. J. Solid State Inorg. Chem.* **1996**, *33*, 285.

(25) Frit, B.; Jaymes, M.; Hagenmuller, P. *Rev. Chim. Miner.* **1971**, *8*, 453.

(26) Niizeki, N.; Wachi, I. *Z. Kristallogr.* **1968**, *127*, 173.

Chapter 6: Synthesis and Characterisation of other structure types

6.1 Introduction

This chapter will deal with the further synthetic trials carried out in an attempt to prepare potential multiferroic materials. The focus of this chapter is the use of other structure types rather than concentrating on the perovskite system as mentioned in previous chapters. The structure types investigated were garnets and spinels. An introduction to each of these structures types and why they were selected was given in Chapter One.

6.2 Garnet Structure Type

6.2.1 Introduction

The garnet structure type, as discussed in *Chapter One,* was chosen due to the tendency of it to form materials with high ordering temperatures, because as shown in previous chapters, it has proven difficult in other structure types (perovskites) to couple a low temperature magnetic transition with a high temperature ferroelectric-like transition. Therefore by increasing the magnetic ordering temperature the overall aim will hopefully be overcome and promote the magnetic and the ferroelectric transitions to couple.

A number of garnet phases were taken with high ordering temperatures, $Y_3Fe_5O_{12}$ (T_c = 555K), $Er_3Fe_5O_{12}$ (T_c = 560K), $Lu_3Fe_5O_{12}$ (T_c = 530K) and $Yb_3Fe_5O_{12}$ (T_c = 550K)[1] and an attempt was made to dope bismuth onto the lanthanide site in order to introduce ferroelectricity into the material. Attempts to

substitute only a third of the lanthanide were made due to reports that the maximum substitution of bismuth for lanthanide in $Y_{3-x}Bi_xFe_5O_{12}$ was x = 1.2[2] via solid state synthesis. The pure bismuth phase $Bi_3Fe_5O_{12}$ reportedly requires the use of thin films[3]. Of the trials attempted only the doped phases $Y_2BiFe_5O_{12}$ and $Er_2BiFe_5O_{12}$ formed. Following on from this a literature study was carried out investigating the effect iron site substitutions has on the magnetic ordering temperature. Elements that resulted in an ordering temperature close to room temperature in the pure lanthanide garnet were selected for doping into the lanthanide-bismuth garnet. The elements that were selected were Sn, Ga, Ge, Sc, Zr and In; however only the materials $Y_2BiFe_4GaO_{12}$ and $Y_2BiFe_4ScO_{12}$ formed pure garnet phases.

6.2.2 Synthesis

6.2.2.1 $LN_2BiFe_5O_{12}$ synthetic attempts

Synthetic attempts to prepare lanthanide iron garnets doped with bismuth via the ceramic method were made; synthetic trials included $Y_2BiFe_5O_{12}$, $Er_2BiFe_5O_{12}$, $Lu_2BiFe_5O_{12}$ and $Yb_2BiFe_5O_{12}$. The two materials, $Y_2BiFe_5O_{12}$ and $Er_2BiFe_5O_{12}$, proved successful to synthesise and so the undoped materials were made in order for comparison experiments to be carried out. All trials were attempted on a 1g scale, in each case platinum foil was used to prevent reaction of the sample with the alumina crucible that the reaction was carried out in. Stoichiometric quantities of Fe_2O_3 (Alfa Aesar 99.998%), Bi_2O_3 (Alfa 99.9995%), Y_2O_3 (Alfa Aesar 99.999%), Er_2O_3(Alfa Aesar 99.999%), Lu_2O_3 (Alfa Aesar 99.999%) and Yb_2O_3 (Alfa Aesar 99.999%) were weighed out, and then thoroughly ground together using an agate pestle and mortar. The starting materials were then

pelletized, placed on top of platinum foil inside an alumina boat and then into the furnace for the specific temperatures and heating times (*table 6.1*). Samples containing bismuth were not heated above 950°C to prevent any bismuth loss from the material. Heating and cooling rates of 5 °C and 10°C per minute were used respectively.

Sample	Temperature of synthesis / °C (dwell times at temperature / hours)
$Y_2BiFe5O_{12}$	900°C (48 / 48 / 48 / 48), 925°C (48) and then 950°C (48 / 48)
$Er_2BiFe_5O_{12}$	900°C (48 / 48) then 950°C (24 / 24 / 24)
$Lu_2BiFe_5O_{12}$	900°C (12 /12 / 48 / 48 / 48)
$Yb_2BiFe_5O_{12}$	900°C (12 /12 / 48 / 48) then 950°C (12)
Y_3Fe5O_{12}	1200°C (48 / 48)[2]
$Er_3Fe_5O_{12}$	1200°C (48 / 20 / 20)[2]

Table 6.1: *Synthetic details of the attempts to make both bismuth doped and un-doped garnet phases.*

6.2.2.2 $(Y/Er)_2BiFe_4XO_{12}$ synthetic attempts (X = Sn; Ga; Ge; Sc; Zr; In)

All trials were attempted on a 1g scale; in each case platinum foil was used to prevent reaction of the sample with the alumina crucible that the reaction was carried out in. Stoichiometric quantities of Fe_2O_3 (Alfa Aesar 99.998%), Bi_2O_3 (Alfa 99.9995%), Y_2O_3 (Alfa Aesar 99.999%), Er_2O_3 (Alfa Aesar 99.999%), SnO_2 (Alfa Aesar 99.996%), Ga_2O_3 (Alfa Aesar 99.999%), GeO_2 (Fluka, 99.99%), Sc_2O_3 (Alfa Aesar 99.99%), ZrO_2 (Alfa Aesar 99.8%) and In_2O_3 (Alfa Aesar 99.999%) were weighed out, and then thoroughly ground together using an agate pestle and mortar. The starting materials were then pelletized, placed on top of platinum foil inside an alumina boat and then into the furnace. The samples were heated to 900°C for 60hours followed by two further firings at

950°C 60 hours each; heating and cooling rates of 5 °C and 10°C per minute were used respectively.

Only the materials $Y_2BiFe_4GaO_{12}$ and $Y_2BiFe_4ScO_{12}$ formed pure garnet phases, all other trials produced a mixture of garnet phases, various oxides and starting materials.

6.2.3 Characterisation

X-ray diffraction patterns of the pure phases formed were taken; the patterns were indexed and then compared with reference data of the compound or of similar compounds in order to draw conclusions.

Two bismuth doped pure iron garnets were made, $Y_2BiFe_5O_{12}$ and $Er_2BiFe_5O_{12}$; the indexing of the powder patterns of these two materials in comparison to the indexing of the un-doped phases led to the conclusion that pure phases had been formed with 33% of the lanthanide substituted for bismuth. However as the data was collected over a short timescale (~10 minutes), it was not of sufficient quality to carry out Rietveld analysis and obtain full structural parameters. Had more time been allocated to this project higher quality data would have been collected to allow full structural analysis to be carried out.

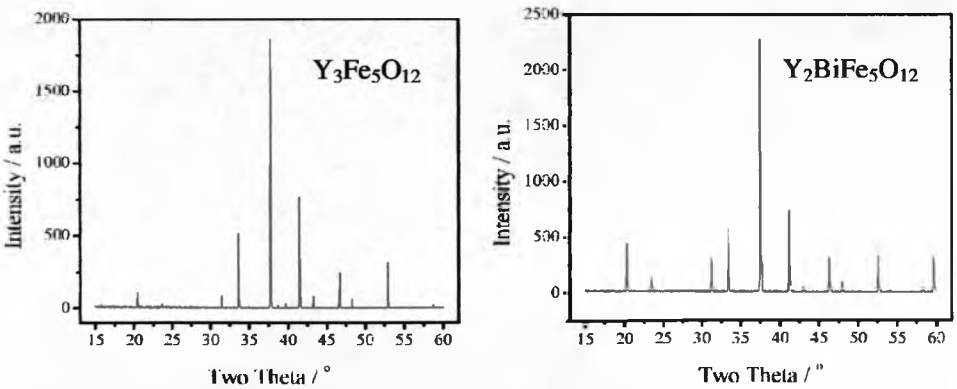

Figure 6.1: *X-ray diffraction patterns (λ = 1.788965Å (Co source)) collected on $Y_3Fe_5O_{12}$ and $Y_2BiFe_5O_{12}$. The $Y_3Fe_5O_{12}$ pattern was indexed to a cubic unit cell (space group, Ia-3d) with a = 12.3632(13)Å, this compared favourably to the reference data for this material (a = 12.376Å[4]). The $Y_2BiFe_5O_{12}$ pattern was indexed using the same space group with the cell parameters, a=12.4524(11)Å, the fact that the doped material has a larger unit cell is a positive sign that some yttrium has been substituted for the slightly larger bismuth atom.*

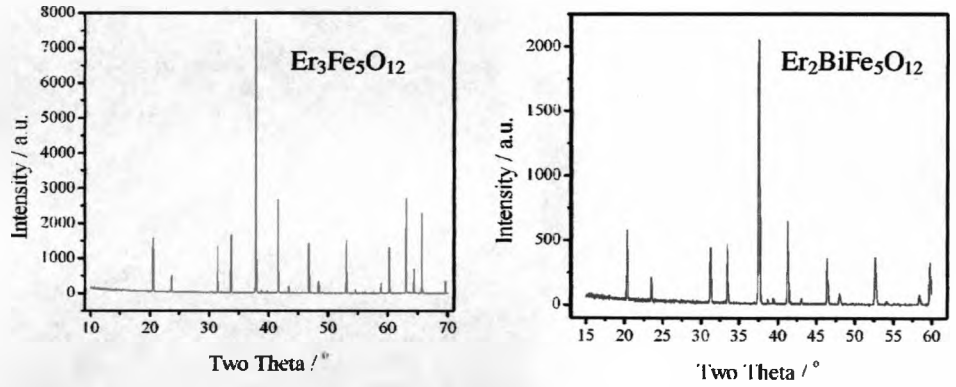

Figure 6.2: *X-ray diffraction patterns (λ = 1.788965Å (Co source)) collected on $Er_3Fe_5O_{12}$ and $Er_2BiFe_5O_{12}$. The $Er_3Fe_5O_{12}$ pattern was indexed to a cubic unit cell (space group, Ia-3d) with a = 12.3394(9)Å, this compared favourably to the reference data for this material (a = 12.347Å[1]). The $Er_2BiFe_5O_{12}$ pattern was indexed using the same space group with the cell parameters, a=12.436(14)Å, the fact that the doped material has a larger unit cell is a positive sign that some erbium has been substituted for the slightly larger bismuth atom.*

Attempts to substitute on the iron site of these doped garnets were also carried out with the aim of lowering the magnetic ordering temperature closer to room temperature. Cations were selected based on a literature search carried out, however the only pure garnet phases formed were $Y_2BiFe_4GaO_{12}$ and $Y_2BiFe_4ScO_{12}$, all other trials produced a mixture of garnet phases, various oxides and starting materials. Again diffraction data was not of sufficient quality to carry out Rietveld analysis and obtain full structural parameters. Conclusions were made based on the indexing of the patterns and comparison with reference data. Had more time been allocated to this project higher quality data would have been collected to allow full structural analysis to be carried out.

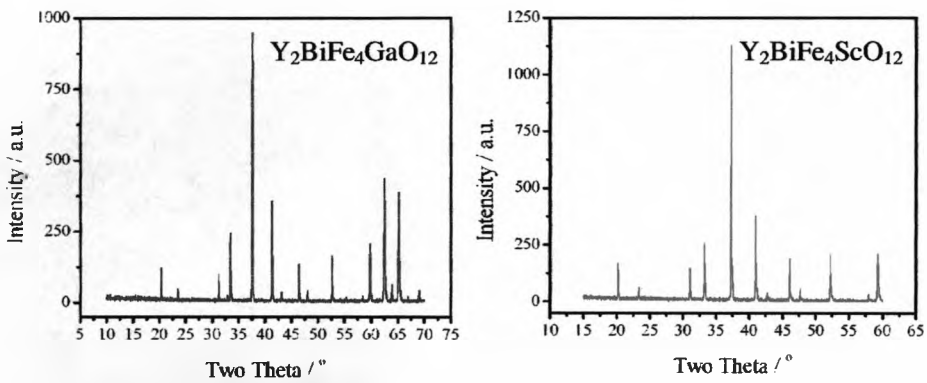

Figure 6.3: *X-ray diffraction patterns (λ = 1.788965Å (Co source)) collected on $Y_2BiFe_4GaO_{12}$ and $Y_2BiFe_4ScO_{12}$; the patterns was indexed to a cubic unit cell (space group, Ia-3d) with cell parameters of a = 12.4266(12)Å and a = 12.5229(20)Å respectively. Both materials have a larger unit cell than the parent $Y_2BiFe_5O_{12}$ material, which implies that both have formed a new phase with slightly larger cations incorporated on the iron site.*

6.2.4 Conclusion

As discussed in *Chapter One*, garnets were chosen because of their high magnetic ordering temperatures which were favourable as it would hopefully overcome the problems observed in the $Bi_{2-x}La_xMn_{4/3}Ni_{2/3}O_6$ (*Chapters Three and Four)* of a low magnetic transition and a high structural one. This section details how it was possible to introduce bismuth into the garnet structure and potentially ferroelectricity. The flexibility of the iron site was displayed in this section potentially opening up a method of varying the magnetic transition temperature like in the $Bi_{2-x}La_xMn_{4/3}Ni_{2/3}O_6$ case. However at this stage this is only speculation, further characterisation experiments required were not carried out on these materials due to time constraints. Full structural analysis is outstanding, along with magnetic studies, dielectric testing and variable temperature diffraction experiments. As such it is very difficult to draw conclusions from this part of the project, however a number of new doped garnet phases have been synthesised that have been designed specifically for use as multiferroics. As to whether they have the desired properties for use as a multiferroic remains in question.

6.3 Spinel Structure Type

6.3.1 Introduction

The spinel structure types as already discussed in *Chapter One* is attractive as a possibility of preparing a multiferroic material due to the tendency of this structure type to adopt spiral magnetic structures. Interest in spiral magnetic structures for use as multiferroics was inspired by a number of recent reviews that discuss the link between spiral magnetism and ferroelectricity[5-10]. The reviews state that the onset of the spiral magnetic ordering induces an electric polarisation, and so the magnetic and electrical properties are coupled making the material multiferroic.

A literature search was carried out on known spiral magnetic materials from this it was discovered that most spiral magnets have low ordering temperatures, typically 100K or less. Therefore if the overall aim of the project was to prepare a multiferroic material for use at room temperature, an attempt to raise the ordering temperature must be made. The idea was to take a known spiral magnet ($ZnFe_2O_4$ T_c ~ 100K[11]) and dope it with a material that exhibited ferromagnetic ordering with a much higher transition temperature ($NiFe_2O_4$ T_c ~ 850K[12]).

6.3.2 Synthesis

An attempt to prepare the spiral material, $ZnFe_2O_4$ and the 30% doped material, $Zn_{0.7}Ni_{0.3}Fe_2O_4$ was made. The ceramic method used to synthesis $ZnFe_2O_4$[13] on a 1g scale was selected for these trials. Stoichiometric quantities of NiO (Alfa Aesar 99.998%), ZnO (Alfa Aesar 99.99%), and Fe_2O_3 (Alfa Aesar 99.998%) were weighed out, and then thoroughly ground together using an agate pestle and

mortar. The starting materials were then pelletized, placed on top of platinum foil inside an alumina boat and then placed into the furnace at 1200°C for 120 hours. Heating and cooling rates of 2°C per minute were used.

6.3.3 Characterisation

6.3.3.1 Structural Characterisation

X-ray diffraction patterns of the two materials were taken and indexed to reference data[14] for the two materials. Good agreement between the reference parameters and the observed parameters led to the conclusion that the two desired phases had formed.

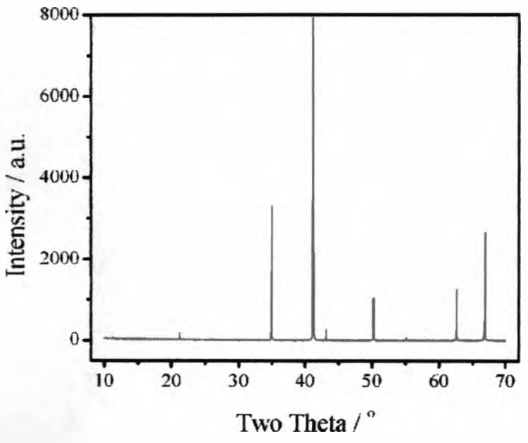

Figure 6.4: *X-ray diffraction pattern (λ = 1.788965Å (Co source)) collected on $ZnFe_2O_4$, the pattern was indexed to a cubic unit cell (space group, Fd-3m) with a = 8.4333(11)Å, this compared favourably to the reference data for this material (a = 8.439Å)[14].*

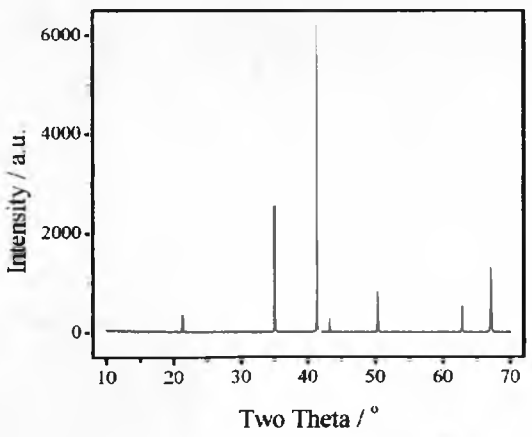

Figure 6.5: *X-ray diffraction pattern (λ = 1.788965Å (Co source)) collected on $Zn_{0.7}Ni_{0.3}Fe_2O_4$, the pattern was indexed to a cubic unit cell (space group, Fd-3m) with a = 8.4094(12)Å, this compared favourably to the reference data for this material (a = 8.421Å for x = 0.25)*[14].

Again, the data shown in the figures above were collected over a short timescale (~10 minutes), therefore the data was not of sufficient quality to carry out Rietveld analysis.

6.3.3.2 Magnetic Measurements

Magnetic susceptibility data were collected using a Quatum Design MPMS SQUID magnetometer. Each sample was loaded at room temperature and cooled in the absence of an applied field to 2K. A field of 100Oe was then applied and measurements were recorded between 2 and 300 or 400K. The systems were then cooled again to 2K in the applied field and the measurements between 2 and 300 or 400K were repeated.

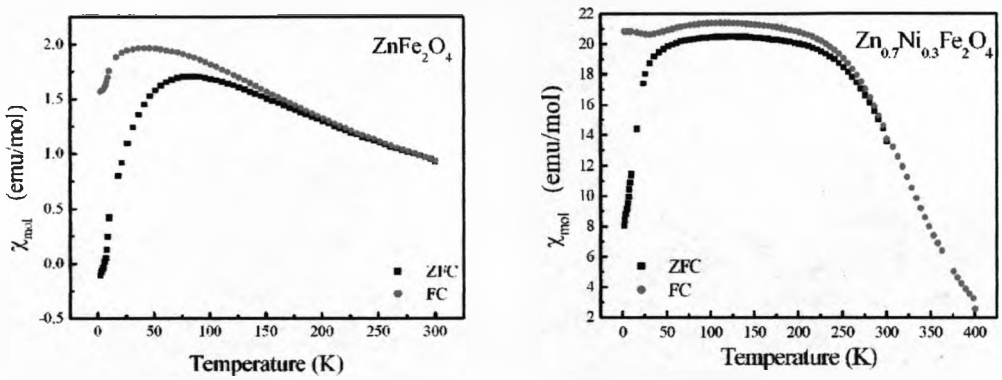

Figure 6.6: *ZFC-FC data collected on the $ZnFe_2O_4$ and $Zn_{0.7}Ni_{0.3}Fe_2O_4$ materials at 100Oe. The plots show that the magnetic ordering temperatures are ~ 200K and ~ 300K respectively.*

The magnetic susceptibilities showed a divergence between the zero-field-cooled and the field-cooled data at ~200K and ~300K for the $ZnFe_2O_4$ and $Zn_{0.7}Ni_{0.3}Fe_2O_4$ respectively. These were taken as the magnetic ordering temperatures. Although these results showed that the doping had the desired effect of increasing the magnetic ordering temperature, in order to investigate the effect of doping on the spiral magnetism and the ferroelectricity, the samples were sent away to Dr. Nataliá Belido at CRISMAT, Caen, France. To date the results of these tests had not been received and the experiments are ongoing.

The magnetic measurements carried out on these samples were carried out in the form of pressed pellets that were fixed into place by inverting the capsule. The diamagnetic correction for these samples was calculated as 78 x 10^{-6} emu/mol and 78.6 x 10^{-6} emu/mol for $ZnFe_2O_4$ and $Zn_{0.7}Ni_{0.3}Fe_2O_4$ respectively, these values were subtracted from all data recorded.

6.3.4 Conclusion

The section above has described the experiments out on the spinel structure type in the attempt to prepare a multiferroic material, this structure type has focused on the use of a spiral magnetic structure and its links to ferroelectricity. Two spinel materials were synthesised, a known spiral magnet, $ZnFe_2O_4$ and $Zn_{0.7}Ni_{0.3}Fe_2O_4$. Although no structural analysis was carried out on these materials in order to confirm that the desired materials had formed and that the doping had occurred, the diffraction patterns were indexed and the results matched reference data on the two materials. The experiments to determine whether the materials exhibited a spiral magnetic structure and if the magnetism did induce ferroelectricity within the samples are still ongoing. The materials were sent away to our collaborators in CRISMAT, Caen, France for testing, however to date no results have been received back. Although, it was shown that the magnetic transition temperature could be varied with nickel content in $Zn_{1-x}Ni_xFe_2O_4$ like in the $Bi_{2-x}La_xMn_{4/3}Ni_{2/3}O_6$ case *(chapters four)* opens up the possibility of tuning the magnetic properties. This is extremely desirable as the multiferroic transition temperature could then be varied if the results from Caen are positive.

6.4 Summary

In summary, different structure types have been investigated and reported in this chapter. The garnets and spinels were each selected as they exhibited favourable properties for use as potential multiferroic materials. It is difficult to summarise this chapter as it is still very much ongoing no real conclusions can or have been

made. The most important thing to take away from this chapter is that other structure types, apart from perovskites, show favourable properties that could be adapted and manipulated for use as multiferroic materials, and so this opens up the possibility of exploring many other structure types for the elusive room temperature multiferroic material.

6.5 References

(1) Landolt-Bornstein *Magnetic Properties of Non-Metallic Inorganic Compounds Based on Transition Elements: Garnets*, 1991; Vol. III / 27 / E

(2) Zhao, H.; Zhou, J.; Bai, Y.; Gui, Z.; Li, L. *J. Magnetism and Magnetic Materials* **2004**, *280*, 208 - 213.

(3) Lux, R.; Heinrich, A.; Leitenmeier, S.; Korner, T.; Herbort, M.; Stritzker, B. *Journal of Applied Physics* **2006**, *100*, 113511.

(4) Euler, F.; Bruce, J. A. *Acta Cryst.* **1965**, *19*, 971 - 978.

(5) Cheong, S.-W.; Mostovoy, M. *Nat Mater* **2007**, *6*, 13-20.

(6) Mostovoy, M. *Physical Review Letters* **2006**, *96*, 067601-4.

(7) Radaelli, P. G.; Chapon, L. C. *Condensed Matter* **2006**, 1 - 22.

(8) Heyer, O.; Hollmann, N.; Klassen, I.; Jodlauk, S.; Bohat, L.; Becker, P.; Mydosh, J. A.; Lorenz, T.; Khomskii, D. *Journal of Physics: Condensed Matter* **2006**, *18*, L471 - L475.

(9) Przenioslo, R.; M., R.; Sosnowska, I. *J Phys Soc Jpn* **2006**, *75*, 084718.

(10) Sergienko, I. A.; Dagotto, E. *Physical Review B (Condensed Matter and Materials Physics)* **2006**, *73*, 094434-5.

(11) Kamazawa, K.; Katano, S.; Tsunoda, Y. *Physica B* **2004**, *345*, 96 - 98.

(12) Joy, P. A.; Date, S. K. *Journal of Magnetism and Magnetic Materials* **2000**, *218*, 229-237.

(13) Henriet-Iserentant, C.; Robbrecht, G. *C.R. Academic Science, Series B* **1972**, *275*, 323.

(14) Mouallem-Bahout, M.; Bertrand, S.; Pena, O. *Journal of Solid State Chemistry* **2005**, *178*, 1080-1086.

Chapter 7: Conclusion

The aim of this thesis, as discussed in *Chapter One: Introduction*, was the design and synthesis of a multiferroic material. A number of approaches were taken when designing a multiferroic material. However the main approach taken was to incorporate two sets of elements, one favouring ferroelectricity and the other ferromagnetism. To generate ferroelectricity bismuth atoms were used; to generate ferromagnetism magnetically active transition metals were used. The primary focus of this thesis was on the perovskite structure type; details of the investigations performed using this structure type is given in chapters three, four and five.

Chapter Three details the synthesis and characterisation of a novel bismuth-base perovskite, $Bi_2(Mn^{4+})_{2/3}(Mn^{3+})_{2/3}(Ni^{2+})_{2/3}O_6$, under ambient conditions. To date only one other type of these materials is known to be synthesised under these conditions, $BiFeO_3$. What makes this material even more remarkable is that all other bismuth based perovskites require high pressure or thin film synthesis. The stability of this phase was assigned to the presence of three cation oxidation states on the B-site. Although initial experiments appeared promising that this material was going to be multiferroic, it was not. The lack of ferroelectricity was explained by the presence of a modulation within the structure that cancelled out any polarity within the material; and the lack of ferromagnetism was explained by the presence of other magnetic interactions between the three cations on the B-site of the perovskite. However this

was a unique material and did open the door for further exploration of potential multiferroics, as discussed in *Chapters Four* and *Five*.

Chapter Four details the full doping study carried out on $Bi_2Mn_{4/3}Ni_{2/3}O_6$ with lanthanum. Although as in the parent case a multiferroic material was not found, it showed that it is possible to vary both the structural transition and magnetic ordering temperatures with lanthanum content.

Chapter Five details the further substitution experiments that were carried out based on $Bi_2(Mn^{4+})_{2/3}(Mn^{3+})_{2/3}(Ni^{2+})_{2/3}O_6$. The chapter details the many attempts to prepare bismuth based perovskites with a range of cations on the B-site, however the only successful materials synthesised were through the substitution of Mn^{4+} ions for $Ti^{4+}$and Ni^{2+} with Co^{2+}, along with the preparation of $BiMn_{1-x}Fe_xO_3$. In the first case another novel bismuth based perovskite at ambient pressure $Bi_2(Ti^{4+})_{2/3}(Mn^{3+})_{2/3}(Ni^{2+})_{2/3}O_6$ was made, however again for this material no evidence was found to suggest any coupling between the structural transition observed and the magnetic transition. In the second case were Ni^{2+} was replaced with Co^{2+}, the material could only be synthesised if 50% or more doping of lanthanum was present, the pure bismuth phase proved impossible to form. Although this material exhibited true ferromagnetism with a favourably high ordering temperature, the material unfortunately adopted a non-polar structure. Finally, successful attempts to make a bismuth based perovskite containing both manganese and iron were also performed, however no electrical or magnetic property

measurements were carried out on this material to determine whether any coupling occurs.

Chapter six details the attempts to synthesise a multiferroic material from other structure types garnet and spinel; this chapter was still very much in progress and so making it difficult to draw any conclusions from it. Garnets were chosen because of their high magnetic ordering temperatures, and spinels because of recent reports suggesting coupling between a magnetic and structural transition observed in this structure type. Although some experiments were still ongoing and no real conclusions were made, this chapter shows how other structure types, apart from perovskites, display favourable properties that could be adapted and manipulated with doping for use as multiferroic materials, and so this opens up the possibility of exploring many other structure types for the elusive room temperature multiferroic material.

In summary, although no multiferroic material was synthesised during the course of this project, this thesis has made a number of novel bismuth containing perovskites at ambient pressure. It has also displayed how it was possible to tune the transition temperature of a material through a doping study and explored the possibility of using other structures, apart from perovskites, for use as multiferroics. This thesis has opened many doors for the further exploration of multiferroic materials.